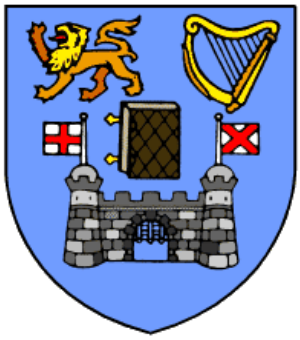

Growth and Characterisation of Nanocarbon Structures

By

Niall Mc Evoy

A thesis submitted for the degree of
Doctor of Philosophy
in the University of Dublin.

School of Physics,
Trinity College Dublin,

2010

Declaration

I declare that the work in this thesis has not been previously submitted as an exercise for a degree to this or any other university.

The work described herein is entirely my own, except for the assistance mentioned in the acknowledgements and the collaborative work mentioned in the list of publications.

I agree that Trinity College Library may lend or copy this thesis on request.

_____

Niall Mc Evoy

Acknowledgements

Thanks first and foremost to Prof. Werner Blau for giving me the opportunity to do a PhD and for all of the support over the years.

I would also like to sincerely thank Prof. Georg Duesberg for all of his help since his arrival in Crann. I'm very grateful for all of the advice you've provided me with and also for the access to equipment without which this work would've been impossible.

IRCSET Ireland and the School of Physics TCD provided the funding and I benefitted from the use of tools provided by SFI. I'd like to thank the staff in physics for all their help and in particular Jeanette Cummins, Marie Callanan and Robbie Gallagher.

Research is a collaborative effort and I owe thanks to many people for their assistance in providing samples, analysis and access to lab equipment.

Thanks to Tony Donnelly who supplied catalyst films in the early stages of my work as well as Prof. James Lunney and Dr. Satheesh Krishnamurthy for help with various matters. Aun-Shih Teo tried PECVD growth on NSL films. Dr. Rory Leahy assembled the Lindberg system used for growth in the early days. Dr. Nikos Peltekis performed extensive XPS measurements and was always available for discussion of various forms of spectroscopy, vacuum equipment, etc. Shishir (Sid) Kumar provided graphene samples and growth recipes, and was a constant source of help in the ASIN lab. Chris Murray provided assorted catalyst substrates, without which I'd have been lost. Dr. Gareth Keeley performed electrochemical characterisation and was a welcome source of football related banter in the lab. Hugo Nolan performed CV measurements on forests. Paul King provided Iljin SWNT films along with discussion on thin films and devices. Dr. Jing Jing Wang helped with scanning Raman measurements. Nealo Leddy in CMA and Dr. Markus Boese in AML both helped with various aspects of electron microscopy. Dr. Eddie Moore helped in various matters and dispensed plenty of sound advice.

On the equipment access front I'd like to thank Prof. Hugh Byrne of DIT for access to Raman equipment and Dr. Graham Cross for access to profilometry and sputter coating facilities.

I've had the pleasure of working with some fantastic people in the Blau, MI, Coleman and Duesberg groups. A full roll call may prove exhaustive but I'll give it a go;

Firstly, I have to mention Darren and Paula who've been along for the ride since the Physics B days……..9 more years?

Bu/Co Oldies (but goodies): Rory, Papa Blond, Denis, Emer, Djiango (my thesis beard almost beats yours), Valeria, Helen, Les, Umar (Khaaaaan!), Chris K, Strevens, Dr. Larkin, Jimmy, Yenny, Jun, Take, Rutsu, Javier, Shane, ZhenYu……..

Bu/Co Current: Paula, Daz (has more land than you), Sophie, Arlo, Ronan S (pup!), Pete (12ft monster), Paul, Phil, Rickard, Musty, Tuffy, Graeme, Phil, Will, Ronan H, Trev, Marguerite, Karen, Evelyn, Denise, Anna, Mad Dog, Ramesh, Sukante……

ASIN: Sid, Gar, Nick the Greek, Tarek (skier/monk/scientist), Kay, Hye-young, Zhimin, Chris, Hugo, Marcel, Jaume, Nick, Schreiber, Ehsan……

Many thanks to my proof-readers: Karen, Marguerite, Nikos, Arlene, Sid and Eddie

Thanks to all the footballers (as well as Darren and JP) who I've had the pleasure of playing 5-a-side with in TCD. Regular exercise (as well as sledging) helped to keep me somewhat sane over the past few years.

Thanks to Mick, BFT and Dar Duff at Tyre Bay Supplies. Bagging patches every summer in my youth kept me on the straight and narrow.

Thanks to my parents for their continued support over the years. Thanks also to my sisters Fiona, Orla, Niamh and Clodagh as well as Toby and Oscar.

Finally, congratulations to my grandfather Paddy who turned 101 last week (17/10/10).

Abstract

Nanocarbon materials have come to the forefront of research in recent years due to their outstanding properties and wide potential applications. Production of these materials by chemical vapour deposition (CVD) is preferable as it is scalable and compatible with existing semiconductor processing techniques. The work presented concerns the growth of carbon nanotubes, pyrolytic carbon (PyC) and graphene by thermal CVD.

The growth of vertically aligned multiwall nanotube (MWNT) forests on conducting substrates (Tantalum) has been demonstrated. This is crucial for applications such as supercapacitors, vias and field emission devices where an electrical contact is needed. The lengths and purity of these MWNTs were tuned by varying the reaction temperature and pressure. Samples produced were characterised using a combination of scanning electron microscopy (SEM), transmission electron microscopy (TEM) and Raman spectroscopy. Atomic force microscopy (AFM) analysis of annealed catalyst samples showed an increase in particle size with rising temperature. At temperatures greater than 750 ^{o}C the catalyst became non-uniform. Four different catalyst systems were investigated and a $Co_{90}Fe_{10}$ alloy was shown to give the highest purity growth. The use of a conductive carbon layer in place of Ta was also investigated. The structures grown on this catalyst system showed poor alignment and a broad diameter distribution.

The growth of single wall nanotubes (SWNTs) was performed using thinner catalyst films on Al_2O_3 layers. Through modification of the gas flow parameters these could be grown as films or aligned forests using the same catalyst material and thickness. High purity SWNTs with diameter distributions lower than those typically seen for commercially available materials were produced.

A process has been developed for the production of conducting thin films of pyrolytic carbon (PyC) on SiO_2 substrates by CVD. The CVD process developed allowed for fine tuning of the film thickness grown by varying the growth temperature and dwell time used. Films had resisitivities of ~ 2 x 10^{-5} Ωm and a conductivity ratio (σ_{DC}/σ_{op}) in the

range 0.8 – 1.1. Characterisation using Raman spectroscopy and x-ray photoelectron spectroscopy (XPS) highlighted the nanocrystalline nature of films grown.

Improved graphitic ordering of PyC films was achieved using a Ni catalyst and annealing treatments. Raman spectroscopy indicated the removal of amorphous carbon and an increase in crystallite size. XPS analysis indicated a removal of functional groups and improved graphitic order. Further, graphene films were grown by catalytic CVD on Ni substrates.

The use of a remote O_2 plasma for the functionalisation and etching of different CVD grown nanocarbons has been demonstrated. Back-etching (recess) is an important component for the integration of carbon structures in silicon technology. In the case of MWNTs forests this can be used for the introduction of controlled defect levels and under certain conditions unzips the MWNTs producing graphitic sheets. Plasma treatment of PyC films has been shown to introduce oxygenated functionalities to the surface of the films giving them enhanced electrochemical activity. Graphene films grown by catalytic CVD on Ni substrates were also subjected to plasma treatment. Raman analysis indicated a significant increase in the defect levels of graphene post etching and Raman mapping demonstrated that these defects were not confined to edges.

Table of Contents

Chapter 1

Introduction

1.1 Low Dimensional Carbons

In 1985 Kroto and Smalley were conducting laser ablation experiments on graphite in an attempt to recreate conditions found near stars. On examining the structures formed they found that the dominant species was a cluster of sixty carbon atoms[1]. Further analysis showed the structure to be a truncated icosahedron, much like that of a football. This consists of a spherical cage composed of twenty hexagons and twelve pentagons with carbon atoms at each of the vertices (see Figure 1.1(a)). This zero-dimensional molecule was named Buckminsterfullerene (or buckyballs) after the American architect R. Buckminster Fuller.

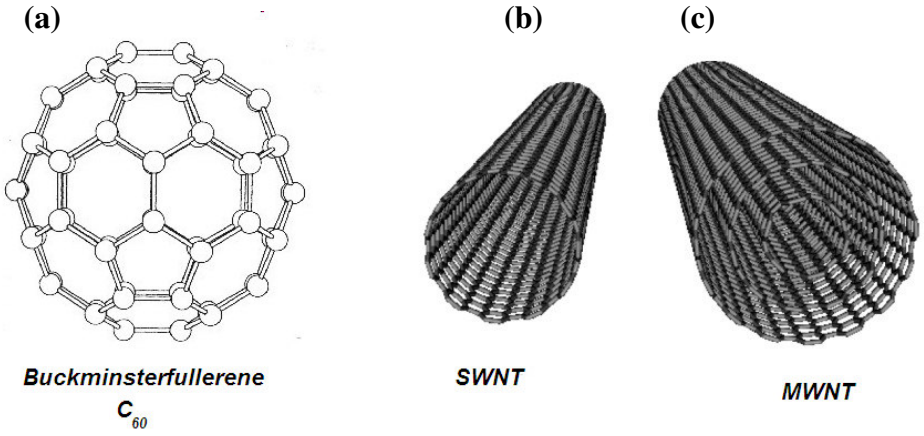

Figure 1.1 *Structure of (a) Buckminsterfullerene (C_{60}) and (b) single and (c) multiwall CNTs.*

Heightened interest in carbon materials led to the discovery of carbon nanotubes (CNTs). Iijima, an expert electron microscopist, imaged the products of a graphite electrode arc discharge experiment and showed what he referred to as "helical microtubules of carbon" [2]. Graphitic tubes with diameters in the range of 4 to 30 nm were imaged and their helical structure was inferred. These tubes correspond with what are now known as multiwall carbon nanotubes (MWNTs). These consist of a series of concentric shells (see Figure 1.1(c)). Two years later Iijima reported the synthesis of

single walled nanotubes (SWNTs)[3]. These can be considered as purely one-dimensional structures.

The discovery of two-dimensional carbon nanostructures followed in 2004 when Geim and Novoselov produced single isolated graphitic layers known as graphene by mechanical exfoliation[4]. Up to this point graphene was thought to be unstable and was considered as a purely academic material with widespread usage in theoretical modelling. It can be thought of as the building block from which all other graphitic materials are constructed. This discovery led to the awarding of the Nobel prize in physics in 2010.

The nanoscale architecture and low dimensional nature of CNTs and graphene endow them with outstanding properties (to be discussed in chapter 2). This has led to an explosion of activity in the research community, particularly in the area of materials science. CNTs are seen as promising candidates for extending the lifetime of existing processes and also for the production of completely novel devices and materials[5]. At present, the primary stumbling block to implementation of these materials in applications is their production and assembly in a controllable and scalable manner.

1.2 Chemical Vapour Deposition

Chemical vapour deposition (CVD) is a versatile technique which uses a chamber of reactive gases to synthesise high purity solid materials. CVD processes were first used in a practical sense in the 1880s for the coating of filaments in incandescent bulbs with metal or carbon. In the 1960s CVD techniques gained widespread usage in semiconductor fabrication facilities for the production of many different component layers.

CVD allows for uniform deposition over large areas and control over deposition rates and thicknesses through modification of reaction parameters. These techniques are scalable and allow for the production of patterned samples. CVD is well established in industry making it the most probable route for implementation of new materials in existing processes.

1.3 Thesis Outline

Work in this thesis concerns the growth of three different nanostructured carbon materials by CVD methods. These include the aforementioned CNTs and graphene as well as Pyrolytic carbon (PyC).
PyC is a nanocrystalline material produced by gas phase dehydrogenation of hydrocarbons. CNTs and graphene have a higher degree of crystalline perfection due to the use of carefully designed catalysts.

The main aims of this thesis were as follows

- To demonstrate and optimise the growth of aligned MWNTs on conducting substrates.
- To develop flexible growth recipes for the production of films and forests of SWNTs.
- To investigate the growth of thin films of PyC.
- To investigate the effect of plasma treatment on different nanocarbon films.
- To extensively characterise the materials grown using an assortment of spectroscopic and microscopic techniques.
- To assess the suitability of materials produced for assorted applications.

This thesis consists of seven chapters:

- Chapter 2 gives an overview of relevant literature. The properties of carbon nanotubes along with CVD growth and applications are reviewed. The production and properties of graphene are discussed briefly. An overview of Raman scattering from graphitic materials is also included.

- Chapter 3 presents an overview of experimental techniques and parameters used in this work. The furnaces used for CVD growth are described in detail.

- Chapter 4 describes the growth of nanotubes on different catalyst materials by CVD. Flexible growth recipes for the production of films and forests of

MWNTs and SWNTs are developed. In particular the growth of MWNT forests on conducting substrates is demonstrated. Patterned growth is achieved through the use of nanosphere lithography.

- Chapter 5 describes the growth of PyC films by CVD. The suitability of this material as a thin electrode and as a coating for SWNT films is assessed. Further graphitisation of this material through the use of a Ni catalyst and heat treatments is presented.

- Chapter 6 presents results on the plasma treatment of products described in previous chapters. The use of O_2 plasma for etching and functionalisation purposes is demonstrated. The growth of high quality graphene films by CVD methods is also introduced.

- Chapter 7 reviews the main findings of this thesis and suggests a future direction for the work.

References

1. Kroto, H.W., et al., *C-60 - Buckminsterfullerene.* Nature, 1985. **318**(6042): p. 162-163.
2. Iijima, S., *Helical Microtubules of Graphitic Carbon.* Nature, 1991. **354**(6348): p. 56-58.
3. Iijima, S. and T. Ichihashi, *Single-shell carbon nanotubes of 1-nm diameter.* Nature, 1993. **363**(6430): p. 603-605.
4. Novoselov, K.S., et al., *Electric field effect in atomically thin carbon films.* Science, 2004. **306**(5696): p. 666-669.
5. Baughman, R.H., A.A. Zakhidov, and W.A. de Heer, *Carbon Nanotubes--the Route Toward Applications.* Science, 2002. **297**(5582): p. 787-792.

Chapter 2

Background and Literature Review

2.1 Allotropes of Carbon

Conventional Allotropes

Carbon can be considered unique amongst the elements due to its ability to form many different compounds and allotropes. Carbon has the electronic configuration $1s^2 2s^2 2p_x^1 2p_y^1$ and is capable of forming *sp*, sp^2 and sp^3 hybrid bonds. The two conventional allotropes of carbon are graphite and diamond respectively.

In graphite the *2s* orbital mixes with two *2p* orbitals to give three sp^2 hybridised orbitals. In this configuration each carbon atom is strongly bonded to three others forming planar sheets. The empty p_z orbitals form weak Van Der Waals bonds between different layers. The (C-C) sp^2 bond has a length of 0.142 nm whereas the interlayer spacing is 0.335 nm.

In diamond the *2s* orbital mixes with three *2p* orbitals forming sp^3 hybridised orbitals. Each carbon atom is bonded to four others in a tetrahedral fashion with a bond length of 0.156 nm.

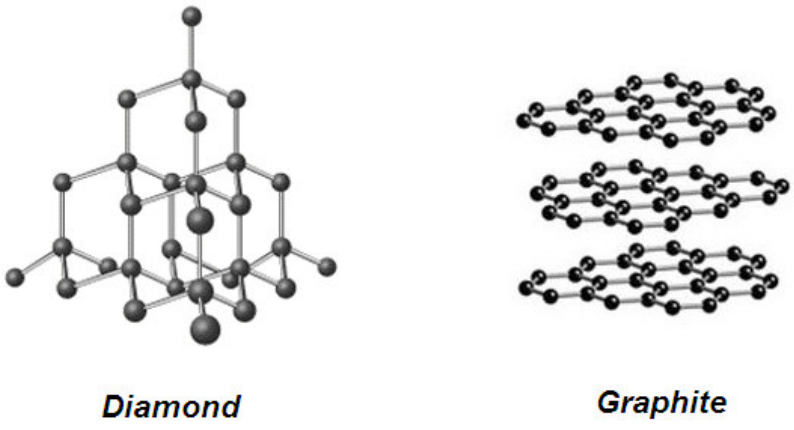

Figure 2.1 *Structure of diamond and graphite.*

The different properties of these two materials can be linked to their bonding. Graphite conducts electricity due to the delocalised nature of electrons in the p_z orbital, whereas

diamond is an insulator due to the absence of delocalised electrons. The in-plane bond length for graphite is shorter than the bonds found in diamond, and as such the bonding is stronger. However, the interlayer bonding is weak. Diamond is an incredibly tough material due to its rigid structure whereas slipping between different layers makes graphite very soft. The electrons in diamond are tightly bound within σ bonds between carbon atoms and do not absorb visible light. Electrons within the π bonds in graphite are free to interact with light giving it a black colour.

Pyrolytic carbon (PyC) has a structure similar to that of graphite in which graphene layers are stacked roughly parallel to each other (c direction) but with disorder in the graphitic (a-b) plane. This can be classed as a turbostratic carbon and has a random translation parallel to the graphene plane. The growth and characterisation of this material is discussed in detail in chapter 5.

Recently Discovered Allotropes

Buckyballs, discovered in 1985 have a truncated icosahedron structure[1]. In this system each carbon atom is bonded to three others. The bonding is primarily sp^2 but there is some sp^3 character due to curvature-induced effects.

Graphene is a 2D single atomic layer of carbon atoms arranged into a honeycomb lattice[2]. Like graphite this is sp^2 hybridised with bonding occurring exclusively in the graphene plane. Conceptually, the rolling up of a graphene sheet produces a carbon nanotube. The structure of this is discussed in the next section.

2.2 Physical and Electronic Structure of Carbon Nanotubes

An individual SWNT can be considered as a graphene sheet rolled into a cylinder and capped at both ends by the introduction of pentagons (similar to half a buckyball). MWNTs are similar but consist of a series of concentric shells with an inter-shell spacing slightly higher than the interlayer spacing in graphite. Typically SWNT diameters are in the range 0.7 – 2 nm whereas MWNT diameters can be up to ~ 30 nm. Lengths tend to be of the order of microns but can be much longer, giving CNTs a massive aspect ratio.

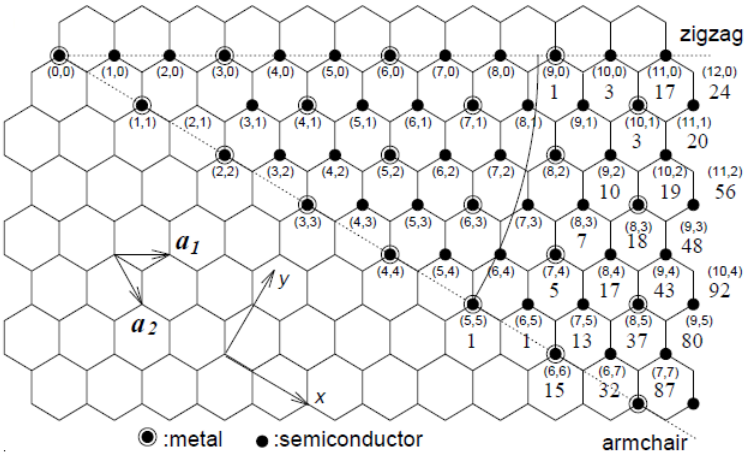

Figure 2.2 *Schematic representation of a graphene sheet showing the (n,m) values and unit vectors which define different chiralities of SWNTs. Dashed lines indicate regions for zigzag and armchair SWNTs. Solid dots represent semiconducting SWNTs and encircled dots represent metallic SWNTs*[3].

Many different types of SWNTs are possible depending on the angle at which the graphene sheet is rolled up; these are referred to as different chiralities. This is best described mathematically by expressing the circumference in terms of a chiral vector joining two equivalent points on the graphene lattice. This chiral vector, $\vec{C}$ is defined by a pair of integer numbers (*n*, *m*) with $0 \le m \le n$ and the lattice vectors for graphene $\hat{a}_1$ and $\hat{a}_2$.

$$\vec{C} = n\hat{a}_1 + m\hat{a}_2 \qquad \textit{Equation 2.1}$$

As the chiral vector defines the circumference it can be used to calculate the diameter of different SWNT chiralities.

$$d = \frac{\left|\vec{C}\right|}{\pi} = \frac{a(m^2 + mn + n^2)^{1/2}}{\pi} \qquad \textit{Equation 2.2}$$

where *a* is the lattice constant for graphene, $a = \alpha_{C-C}\sqrt{3} = 0.249\,nm$.

The chirality can also be expressed in terms of a chiral angle θ.

$$\theta = \tan^{-1}\left(\frac{\sqrt{3n}}{2m+n}\right)$$ *Equation 2.3*

Two particular high symmetry constructs are possible with this chiral vector, armchair SWNTs where $n = m$ ($\theta = 30^o$) and zigzag SWNTs where $m = 0$ ($\theta = 0^o$). All other SWNTs are described as chiral ($0^o < \theta < 30^o$).

It is found that all armchair SWNTs are metallic and zigzag SWNTs where $(m - n)$ is divisible by three are also metallic. In general the condition for metallic conductivity is given by;

$$\frac{(2m+n)}{3} = integer$$ *Equation 2.4*

This relation was predicted theoretically[4] and later verified experimentally[5].

The electrical properties of nanotubes are dictated by π and π^* bands produced by the mixing of p_z orbitals. The bands produced by mixing of the sp^2 orbitals, σ and σ^* lie far from the Fermi level and play no part in the electronic properties of nanotubes.

P.R. Wallace used a tight binding model which considered only nearest neighbour interactions to describe 2D graphite (graphene) and arrived at an expression for the energy dispersion[6];

$$E_{2D}(k_x k_y) = \pm\gamma_0\left\{1 + 4\cos\left(\frac{\sqrt{3}k_x a}{2}\right)\cos\left(\frac{k_y a}{2}\right) + 4\cos^2\left(\frac{k_y a}{2}\right)\right\}$$ *Equation 2.5*

where k_x and k_y are the wavevectors, a is the lattice constant (0.246 nm) and γ_0 is the nearest neighbour overlap integral. The expression produces π and π^* bands which touch at six corners (K points) of a hexagonal Brillouin zone. Representative Brillouin zones are shown in Figure 2.3.

SWNTs have macroscopic dimensions along the tube axis and atomic dimensions in the circumferential direction. Because of this there are many allowed electronic states along the axis but a discrete number in the circumferential direction. 1D energy bands for SWNTs can be obtained by applying periodic boundary conditions to the graphene energy dispersion, thereby restricting it to quantised k states.

$$\vec{C}.\vec{k} = 2\pi a \qquad \textit{Equation 2.6}$$

By substituting allowed *k* values into Equation 2.5 dispersion relations can be calculated for different nanotube chiralities as shown in Figure 2.4. This quantisation means that allowed electronic states for SWNTs are lines on the 2D graphene energy dispersion separated by $2\pi / \vec{C}$. A SWNT will only be metallic if one of these lines intersects with a K point on the graphene Brillouin zone. As stated previously, the condition for metallic conductivity is related to the chirality, thus all armchair tubes have *k* state lines which intersect with a K point whereas only one third of zigzag and chiral tubes do.

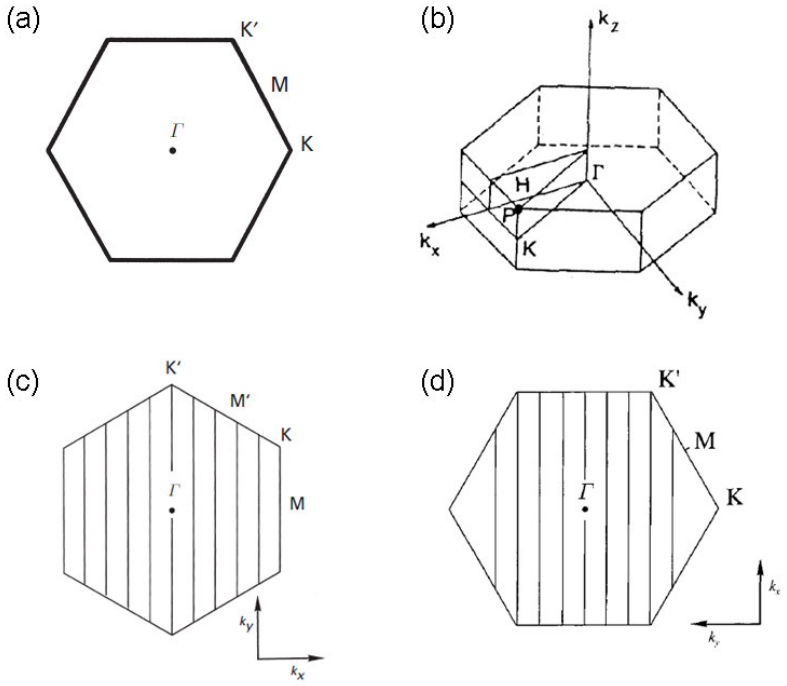

Figure 2.3 Brillouin zones for (a) Graphene or 2D graphite (b) 3D graphite with a hexagonal pancake structure due to band formation in the z-direction (c, d) Metallic (5, 5) and (9, 0) SWNTs with *k* state lines intersecting with a K point. Adapted from [7].

The electronic density of states (DOS) can be determined by combining the dispersion relation with the number of states per wavevector[4]. The 1D nature of SWNTs leads to spikes in the density of states known as van Hove singularities[10] (Figure 2.5). These were predicted by tight binding models and have been observed experimentally [5, 11].

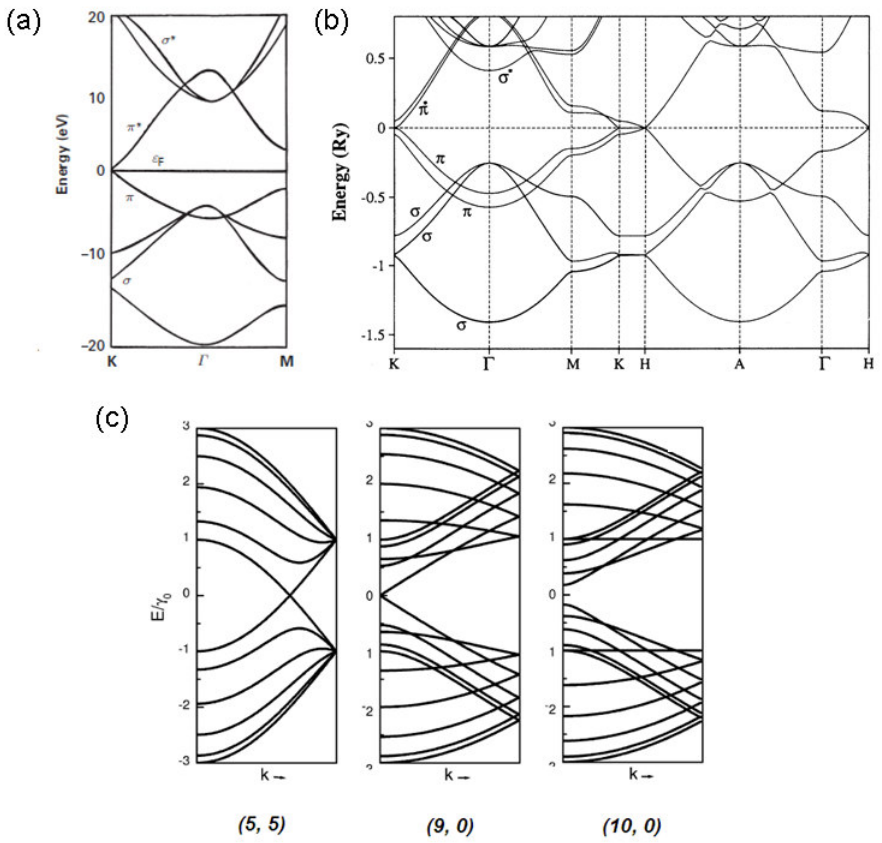

Figure 2.4 *Dispersion relations for (a) graphene as well as (b) graphite[8] and (c) metallic (5, 5) and (9, 0) and semiconducting (10, 0) SWNTs[9].*

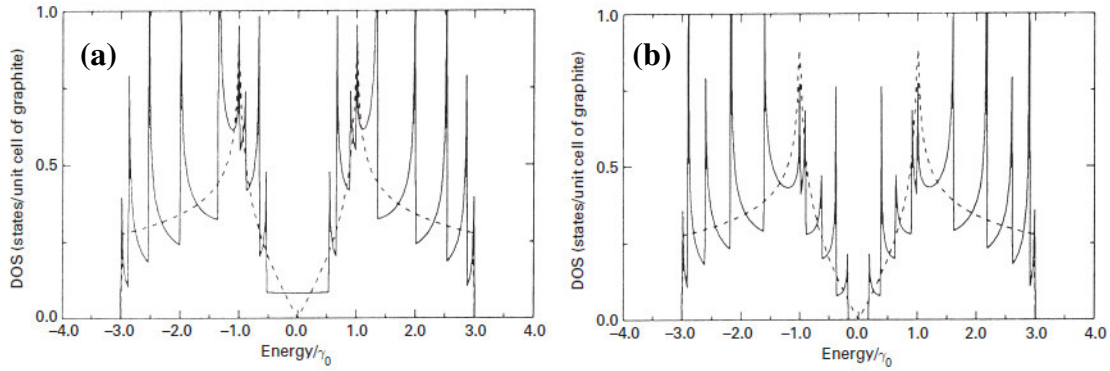

Figure 2.5 *Density of states for (a) (10, 0) and (b) (9, 0) SWNTs with van Hove singularities. The dashed line represents graphene.*

2.3 CVD Growth of Carbon Nanotubes

2.3.1 Introduction

Chemical vapour deposition (CVD) is a technique in which one or more gaseous species are decomposed forming reactive species, which deposit onto a substrate forming a film or particles. The typical steps in a basic CVD process are as follows;

- A mixture of reactant and carrier gases is introduced into the reaction chamber.
- These gases are directed towards the substrate(s).
- Reactants get adsorbed on the surface of the substrate.
- Products are formed by chemical reactions at the surface of the substrate. This step is catalysed in some cases.
- By-products are desorbed and evacuated from the reaction chamber.

CVD processes are often used for the deposition of resistant coatings. They are also widely used in the semiconductor industry for the growth of different layers including polycrystalline Si, SiO_2 and Si_3N_4.

Different types of CVD processes can be classed based on the process parameters used. Common variants include thermally assisted CVD, low pressure CVD (LPCVD), and plasma enhanced CVD (PECVD). In thermally assisted CVD, heat is used to activate the chemical reaction. LPCVD involves evacuating the reaction chamber to pressures below atmosphere. This increases the mean free path of gaseous molecules used ensuring molecular flow. The pumping action also serves to accelerate the gas flow. PECVD involves the use of plasma within the reaction chamber. This plasma can ionise reactant species leading to higher reaction/deposition rates and lower reaction temperatures.

Carbon based CVD processes include pyrolysis of hydrocarbons for the production of pyrolytic carbon (PyC), high pressure production of diamond like carbons (DLC) and thin diamond layers[12] as well as the catalytic production of carbon nanofibers (CNFs)[13] and carbon nanotubes (CNTs).

Growth of CNTs by CVD involves decomposing a hydrocarbon feedstock at elevated temperatures in the vicinity of a metallic nanoparticle catalyst. Typical growth models

(see Figure 2.6) entail the hydrocarbon precursor decomposing at high temperatures forming a solid solution with the catalyst. The nanoparticle becomes saturated with carbon leading to the precipitation of tubular crystalline graphite. Growth terminates either when the hydrocarbon supply ceases or if the catalyst becomes inactive. Base and tip growth methods (see Figure 2.7) have both been reported depending on the strength of interaction between the catalyst material and the surface. A collection of some of the key publications in the area of CVD growth of CNTs is shown in Table 2.1.

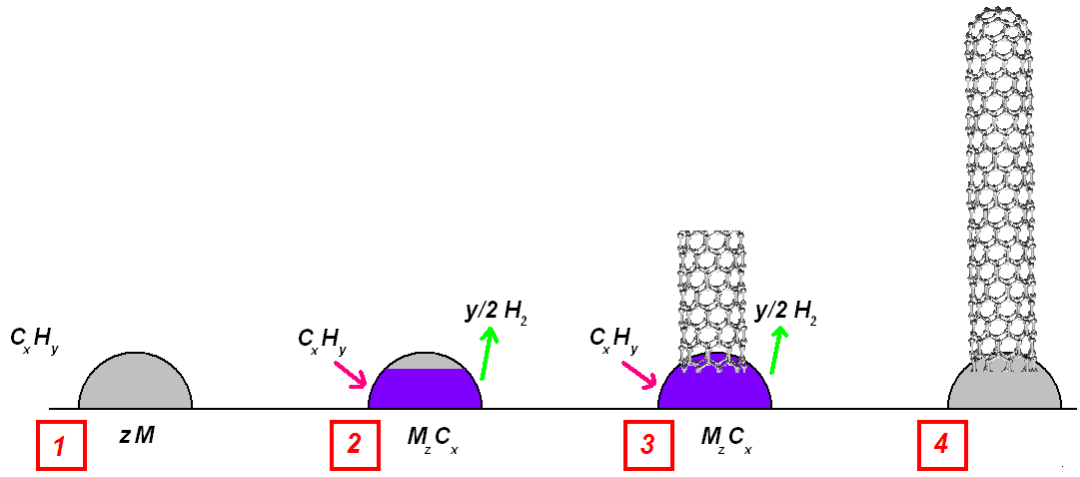

Figure 2.6 *Growth mechanism for CNTs. (1) A hydrocarbon precursor comes into the vicinity of a metallic nanoparticle. (2) The hydrocarbon decomposes forming a metastable carbide. (3) Carbon saturation occurs and tubular crystalline graphite is precipitated from the nanoparticle. (4) Growth terminates when the hydrocarbon supply ceases or if the catalyst becomes inactive.*

Common growth temperatures are in the range 600 – 800 ^{o}C but this can be lowered using techniques such as PECVD. A wide variety of different hydrocarbon gases can be used as feedstock including C_2H_2, C_2H_4, CH_4 and CO. Liquid precursors such as C_2H_5OH are also commonly used. Typically nanoparticles of transition metals such as Fe, Co and Ni are used as the catalyst and act as nucleation sites; these can be prepared by physical (sputtering, evaporation) or chemical methods. The diameter of the CNTs produced is related to the diameter of the catalyst[14-15] used and so catalysts must be finely tuned in order to produce SWNTs, MWNTs or even double wall nanotubes (DWNTs). The following section will give an overview of different approaches to CVD growth of nanotubes along with some recent advances in the field.

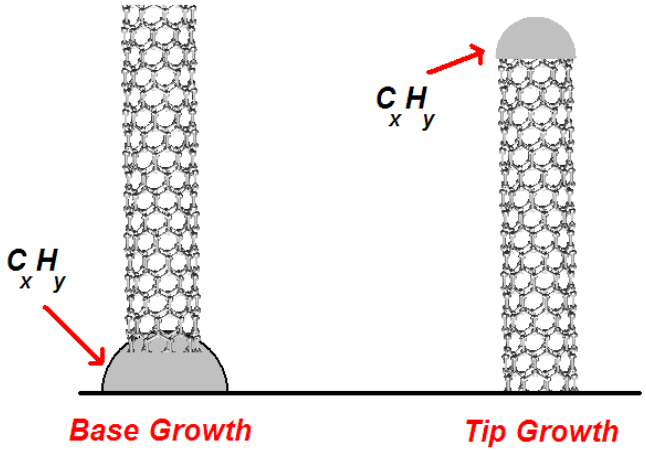

Figure 2.7 *Diagram of base- and tip-growth mechanisms. In base growth the metallic nanoparticle interacts strongly with the substrate and remains pinned during growth. In tip-growth the substrate interaction is weaker and the metallic nanoparticle is pushed upwards in the direction of the tube growth.*

2.3.2 Early Growth of CNTs

Preliminary work in the field of nanotube research focused on products formed by arc discharge[16-19] and laser vaporisation[20] methods. Both of these methods are capable of producing relatively large amounts of material. However, this material is in the form of a powder and controlled growth at defined sites is not possible.

The production of MWNTs by catalytic CVD was first reported by Ivanov et al. in 1994. Nanotubes with outer diameters in the range 15 – 20 nm were formed by the decomposition of C_2H_2 on Co nanoparticle catalysts[21]. Two years later, Honjie Dai, working in the Smalley group in Rice University, reported CVD growth of SWNTs by decomposition of CO over Mo, Co and Fe particles at 1200 ^{o}C[22]. The link between nanotube diameter and catalyst particle diameter was established by transmission electron microscopy (TEM). Further papers soon followed showing increased production volume and higher purity [23-25].

2.3.3 Patterned Growth of CNTs

Jing Kong (working under Dai in Stanford) outlined one of the primary advantages of CVD growth of CNTs in 1999[26], that is, the ability to grow nanotubes at well-defined sites on substrates. Electron beam lithography (EBL) was used to pattern islands with diameters of 3 – 5 μm in PMMA on Si. A liquid catalyst solution containing iron nitrates and alumina nanoparticles was dropped on the substrates which were then annealed, followed by removal of the non-patterned PMMA. Methane was used as the hydrocarbon feedstock and growth took place at 1000 ^{o}C. Individual SWNTs with measured diameters in the range 1 – 3 nm and lengths up to 20 μm grew exclusively from the patterned catalyst islands.

Many advances have been made in the growth of nanotubes on patterned substrates. Ren et al. demonstrated PECVD growth of aligned carbon structures on individual Ni dots defined by EBL[27], however, the tubes in this case had diameters of ~150 nm and were probably closer to carbon nanofibres (CNFs) than highly crystalline CNTs. Teo et al. showed similar growth with better defined patterning and smaller catalyst size[28]. Growth from nanoholes created in SiO_2 by optical lithography was reported by Duesberg et al.[29]. The diameter of the tubes grown was directly related to the size of the hole with bundles of MWNTs growing from holes > 60 nm diameter and individual tubes growing from holes of 20 – 60 nm. For holes in the range 20 – 60 nm the tube diameter was related to the size of the hole, for larger holes the tube diameter was found to be 12 nm due to the catalyst breaking into clusters. Growth in nanoholes has also been demonstrated using channels in porous alumina templates[30-32].

An alternative approach to catalyst patterning was proposed by Huang et al. who used an AFM tip with an applied voltage to selectively oxidise nanoscale dots on a thin Ni film[33]. Unoxidised Ni was removed by wet etching and CVD growth then occurred exclusively from the oxidised dots. Nanosphere lithography (NSL) is another non-conventional lithographic technique which has been used to pattern catalyst sites for horizontal growth[34] and aligned arrays[35-36].

2.3.4 Vertically Aligned Arrays

Control of growth in the vertical direction is of great importance as aligned arrays are of interest for a number of different applications. As mentioned previously,

confinement of catalyst to defined channels is one approach to this, however, such confinement is not always a requirement for aligned growth. Fan et al. demonstrated the growth of large horizontal arrays of patterned MWNTs 240 μm in length on patterned porous silica with a shadow mask evaporated Fe catalyst using C_2H_2 at 700 ^oC as the reactive species[37-38]. The horizontal alignment observed was attributed to van der Waals interactions between the outer shells of adjacent tubes. A parametric study on similarly produced nanotube arrays was carried out by Brokinowski et al. who were able to exercise precise control over tube lengths by modifying reaction time or pressure[39]. Similar growth conditions were used by Zhu et al. who achieved heights of up to 420 μm[40], whereas Hart et al. reported arrays with heights up to 2 mm[41]. The influence of catalyst pattern geometry was investigated by Jeong et al. who discovered that larger catalyst areas led to longer tubes as in smaller areas an oversupply of carbon led to the formation of a growth terminating carbon coating[42].

2.3.5 Horizontally Directed Growth

A number of approaches have been taken to controlling growth in the horizontal direction which is important for many interconnect applications. Franklin et al. prepared silicon pillars by EBL and used contact printing to deposit catalyst material solely at the top of these[43]. CVD growth was carried out at 900 ^oC with an acetylene feedstock. SWNTs were seen to nucleate only at tower tops where the catalytic material was located. The growth model suggested, was that as the SWNTs were growing they were kept waving in the "wind" due to differential gas flow velocities between the tower tops and tower. Thus the growth could be considered flow-directed.

Another approach to controlling the horizontal direction of growth is by the application of an electric field as described by Zhang et al.[44] Patterned trenches consisting of two middle poly Si lines and two outer poly Si pads were prepared by depositing a poly Si film on a quartz wafer and then patterning by photolithography and plasma etching. A liquid catalyst was deposited on the etched trenches by contact printing. CVD growth was carried out at 900 ^oC in a methane/hydrogen mix whilst a voltage was applied to the outer poly Si pads. It was observed that in the presence of the electric field the nanotube growth was highly directional whereas in its absence it was random. This is because the large induced dipole moments lead to large aligning torques on the

nanotubes. Other approaches to horizontally directed growth have involved the use of surface modified substrates[45] or substrates such as sapphire with defined trenches[46].

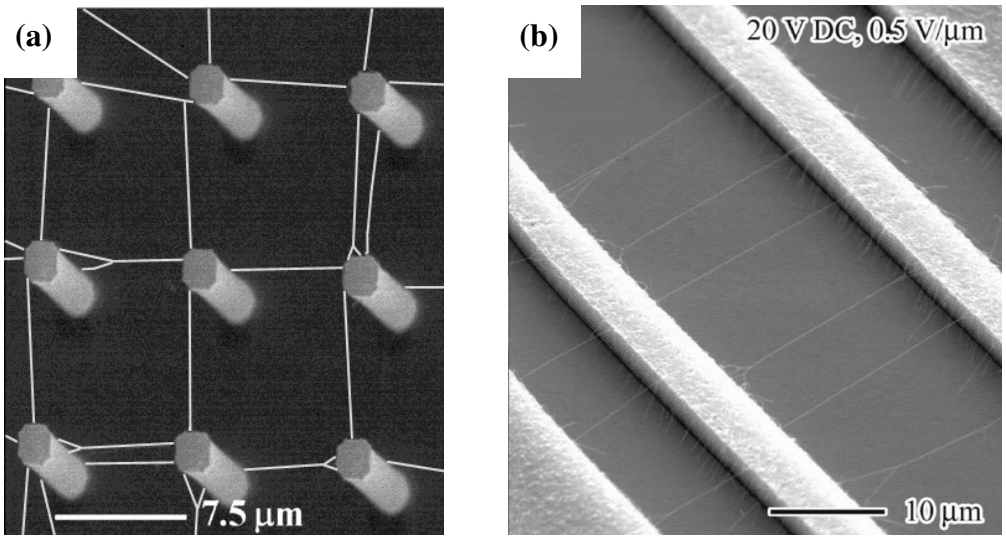

Figure 2.8 *(a) Flow directed growth across pillars as reported by Franklin et al.[43] (b) Electric field directed growth as reported by Zhang et al.[44]*

2.3.6 Supergrowth

A major advance in CVD growth of SWNTs was reported by Hata et al. in 2004[47]. It was shown that the incorporation of water vapour increased both the activity and lifetime of sputtered metal catalysts by oxidising amorphous carbon which would normally form on the surface of the tubes and poison catalyst sites. C_2H_4 was used as the hydrocarbon feedstock with a mix of Ar and H_2 as carrier gases and a small controlled amount of water vapour. Aligned arrays up to 2.5 mm in height were produced and photoluminescence studies exhibited a wide range of nanotube chiralities and signified that the nanotubes were not present in bundles. This method was dubbed "supergrowth" due to the massive increase in height it offered. Supergrowth of vertically aligned MWNTs 4 mm in height was reported soon afterwards[48].

Futaba from the Iijima group performed a systematic and thorough study on aligned SWNTs from the supergrowth method and made a number of interesting discoveries[49]. Firstly, a catalytic activity of 84% was reported which is much higher than typical values of a few %. Secondly, the average SWNT diameter was measured to be ~ 3 nm

which is rather large. Lastly a density of 5.2 x 10^{11} tubes/cm^2 was measured; this corresponds to SWNTs occupying only 3.6% of the total volume (despite looking very dense optically). This sparse population is thought to be vital for efficient growth.

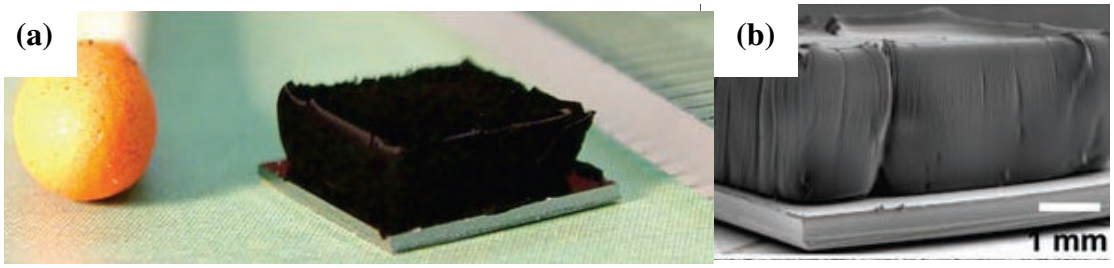

Figure 2.9 *(a) Optical and (b) SEM images of SWNT forests produced by supergrowth*[47].

2.3.7 CVD Growth of Junctions

A number of different branch and junction-like structures are achievable through fine-tuning of growth conditions. Li et al. first illustrated this possibility by growing Y-junction nanotubes in a Y-branched nano-channel template[50]. These three pronged structures are of interest for molecular switches. Other nanotube junctions involve the use of two-step CVD processes. Jin et al. demonstrated MWNT/SWNT junctions grown on a Fe-Mo catalyst[51]. In the first step MWNTs were grown at 750 ^{o}C using C_2H_2 as feedstock. In the second step the temperature was ramped to 950 ^{o}C and CH_4 was used as feedstock leading to SWNTs growing from the tips of the MWNTs. The morphology of the junctions was controllable by varying process parameters, in particular by introducing a cooling step between the two growth steps. This idea was extended by Yao et al. who introduced intermolecular junctions in SWNTs by oscillating the growth temperature between 890 ^{o}C and 950 ^{o}C during growth[52]. The sudden change in temperature mid growth led to a change in diameter (and thus chirality) of the SWNTs producing structures of great interest for nanoscale electronics.

2.3.8 Catalytic Material and Mechanism

The catalytic activity of transition metals in carbon based processes was studied long before CNTs were first reported. In different forms transition metal catalysts have been used for growth of PyC[53] and CNFs[13] by CVD. Knowledge in these areas has led to the use of similar catalysts for the CVD growth of CNTs and more recently graphene.

The growth of CNTs was linked to the solubility of carbon in the catalyst material by Deck et al.[54] Successful catalysts (Ni, Co, Fe) all exhibited some carbon solubility (~ 1 at.%) in the solid solution and didn't form substantial quantities of stable carbides. Other materials including Cr, Mn, Zn, Cd, Zr, La and V were shown to be unsuitable for catalytic growth of CNTs and instead formed soot like deposits under typical CNT growth conditions. This failure was due to either poor solubility of carbon in the material or the formation of stable carbides which prevented graphitic precipitation.

A thorough study on the catalytic activity of different metals for CNT growth was presented by Esconjauregui et al.[55] It was surmised that transition metals with few *d* orbital vacancies (Ni, Co, Fe) gave rise to metastable carbides and were capable of precipitating carbon thus making them ideal for CNT growth. In addition, by looking at the enthalpy of formation of different gaseous species and the carbides formed with metals, it was determined that C_2H_2 gave the largest change in Gibbs free energy.

Hofmann et al. investigated the state of catalyst nanoparticles using x-ray photo-electron spectroscopy (XPS) and environmental TEM. It was established that for Fe and Ni nanoparticles the active state of the catalyst was crystalline metal rather than oxides[56].

Matching of catalyst materials to growth precursors may also be of importance. Mizuno et al. demonstrated that Fe and Co exhibited selectively enhanced growth when using ethylene and ethanol respectively[57]. This was attributed to differing growth mechanisms with different precursors. Ago et al. investigated the conversion of methane by different catalysts and found an activity order Fe > Co > Ni[58].

A number of non-traditional catalysts have been reported in recent years including Pd and Cu catalysts doped with Mo and W[59], SiC, Si and Ge semiconductor nanoparticles[60] and even catalyst free growth on SiO_2 substrates[61].

2.3.9 Catalyst Size

A number of authors have shown a link between the diameter of CNTs grown and the diameter of catalyst particle used. Cheung et al. used monodisperse Fe nanoclusters with diameters of 3, 9 and 13 nm and showed that CNTs with diameters 3, 7 and 12 nm respectively were formed[14]. Similar results were obtained by Dai and coworkers using Fe nanoparticles derived from ferritin[15] and by Kukovitsky et al. using evaporated Ni catalysts[62]. However, Harutyunyan et al. observed no direct correlation between catalyst size and CNT diameter for large particles[63].

The density and roughness of catalyst films can also impact on the CNTs grown as shown by Signore et al. who reported an increase in forest height and decrease in diameter with decreasing cluster density[64].

2.3.10 Temperature Effects

The growth temperature used has a number of effects on the CNTs produced. In general an increase in growth temperature is seen to produce more crystalline CNTs with fewer defects as seen in improved Raman spectra [65-67]. Increasing the growth temperature has been seen to increase the growth rate for MWNT forests[68]. This can be linked with increased decomposition of the precursor gas and increased carbon solubility in the catalyst nanoparticles. Higher growth temperatures can lead to an increase in CNT diameters [69-70]. This can be attributed to increased catalyst mobility and agglomeration of metallic nanoparticles.

Table 2.1 *Key publications in the field of CVD growth of CNTs.*

Notes	Year	Author	Type	Diameter (nm)	Length	Alignment	T (^{o}C)	Reactive Species	Catalyst Type	Catalyst
First CVD MWNTs	1994	Ivananov[21]	MWNTs	15 – 20	300 µm	N/A	700	C_2H_2	Chemical	Co
First CVD SWNTs	1996	Dai[22]	SWNTs	1 – 5	~1 µm	N/A	1200	CO	Chemical	Ni/Co
Patterned SWNT growth	1999	Kong[26]	SWNTs	1 – 3	20 µm	N/A	1000	CH_4	Chemical	$FeNO_3$
Vertically Aligned MWNTs	1999	Fan[37]	MWNTs	16	240 um	Vertical	700	C_2H_2	Physical	Fe
HipCO Process	1999	Nikolaev[24]	SWNTs	0.7 – 1.4	~1um	N/A	1200	CO	Chemical	$FeCO_5$
Growth Across Pillars	2000	Franklin [43]	SWNTs		~150 µm	Horizontal	900	CH_4	Chemical	$FeCl_3$
Electric Field Aligned	2001	Zhang[44]	SWNTs		~10 µm	Horizontal	900	CH_4	Chemical	
Patterned growth on 4" wafers	2001	Franklin [71]	SWNTs	1 – 3	~10 µm	N/A	900	CH_4	Chemical	Fe/Mo
Low Temp Ethanol Growth	2002	Maruyama[72]	SWNTs	0.8 – 1.2		N/A	550-900	C_2H_5OH, CH_3OH	Chemical	FeMo, CoMo
Patterned Growth on 6" wafers	2002	Kreupl[73]	MWNTs	12	50 µm	Vertical	700	C_2H_2	Physical	Fe
Water Assisted SWNTs	2004	Hata[47]	SWNTs	1 – 3	2.5 mm	Vertical	750	C_2H_4	Physical	Fe/Co
Ultralong individual tubes	2004	Zheng[74]	SWNTs	1.4	4 cm	N/A	900	C_2H_5OH	Chemical	$FeCl_3$

2.4 Applications of Carbon Nanotubes

The structure of CNTs engenders unique electrical, mechanical, thermal and optical properties. A summary of some of these properties is given in Table 2.2. This in combination with their massive aspect ratio makes nanotubes potentially suitable for a wide range of applications. In some cases, this involves incorporating CNTs into existing processes. In others, exciting new approaches are envisaged which are only possible through the exploitation of nanotube properties. Approaches towards utilising nanotubes in different applications have been published in high impact journals[75]. This section will look in particular at the applicability of vertical aligned and thin film CNTs grown by CVD. Other nanotube applications will be discussed briefly.

Property	***CNTs***	***Comparison***
Density	*1.33 – 1.4 g/cm^3*	*Al: 2.7 g/cm^3*
Maximum Current Density	*10^9 A/cm^2[76]*	*Cu wires: 10^6A/cm^2*
Thermal Conductivity	*MWNT: 3000 W/m.K[77]* *SWNT: 3500 W/m.K [78]*	*Copper: 401 W/m.K* *Diamond: ~2000 W/m.K*
Maximum Tensile Strength	*~ 30 GPa[79]*	*Reinforced Steel: 2 GPa*

Table 2.2 *Physical properties of carbon nanotubes.*

2.4.1 Vertically Grown Arrays

Traditionally metals, such as copper, have been used for vertical interconnects (vias) in the back end of integrated circuit processing. Carbon nanotubes theoretically offer higher thermal conductivities and maximum current densities making them a high interest material in this field. MWNTs are preferable over SWNTs in this case due to their purely metallic nature. Kreupl et al. were the first to demonstrate this by growing MWNTs in vias and contact holes on 6" wafers in a microelectronic compatible process[73]. The temperature used, however, was 700 ^oC which is too high for Si large scale integration (LSI) processing techniques. Li et al. took a slightly different approach

to fabricating vias by growing arrays of aligned CNTs by PECVD and then using TEOS CVD to deposit SiO_2 around the tubes, followed by a planarisation step. The resistance of the MWNTs was measured using current sensing AFM and was found to be 200 kΩ per tube, which is much higher than the theoretically predicted value. This discrepancy was attributed to the defective nature of the tubes produced and contacting issues. A number of groups have attempted to reduce the growth temperature of CNT vias in order to meet the requirements of LSI processing. Nihei et al. grew CNT via interconnects at 450 ^{o}C in 2 μm diameter holes, the interconnects consisted of ~ 1000 tubes with a resistance of 5 Ω[80]. Yokoyama et al. further lowered the growth temperature to 390 ^{o}C and produced vias with a resistance of 0.9 Ω in 2 μm diameter holes. This resistance was lowered to 0.6 Ω by a hydrogen annealing treatment[81]. Kawabata et al. showed that MWNTs could be grown at temperatures as low as 365 ^{o}C, furthermore they established that 160 nm diameter MWNT via interconnects grown at 400 ^{o}C could sustain a high current density for 100 hours without any degradation in performance[82]. In order for MWNTs to be successfully used in via interconnect applications obstacles concerning growth temperature, nanotube quality and packing density still have to be overcome, but they remain promising candidates.

The high aspect ratio of nanotubes and efficient electron emission makes them of interest for use as field emitters [83-88] and CVD techniques allow for precise positioning of such emitters. This was first demonstrated by de Heer et al. in 1995 who reported a current density of 100 $mAcm^{-2}$ with an applied field of 14 $kV\mu m^{-1}$ from a CVD grown aligned CNT film[83]. This value has been improved on since by using PECVD growth on patterned substrates. This produces aligned CNTs which are spaced apart in order to minimise shielding effects, with Milne et al. reporting current densities of 0.7 Acm^{-2} with an applied field of 21 $V\mu m^{-1}$[85]. Wang et al. fabricated a basic flat panel display lit by the emission from a CNT-epoxy composite[87] and several companies have built large prototype displays in recent years. However, the cost of such displays compared with LCD devices has proved prohibitive. Field emission from CVD grown nanotubes has also been used in x-ray tubes and offers an improvement in the longevity, energy efficiency, mobility and resolution over conventional thermal filaments[89].

The massive surface area and good electrical properties of CNTs has led to their usage as electrodes in supercapacitors. These devices have specific energies and specific powers which lie between those of batteries and traditional capacitors and are expected to play a pivotal role in future energy storage applications. The use of MWNTs as

supercapacitor electrodes was first reported by Niu et al. who measured a power density of 8 kW/kg[90]. Futaba et al. demonstrated improved performance through the usage of densified SWNT forests[91]. For further improvement it is desirable to have dense aligned forests grown directly on conducting substrates.

Aligned CNT forests have also been incorporated into novel biomimetic applications, such as dry adhesives similar to gecko's feet[92]. Geckos have sticky feet due to a series of aligned microscopic hairs which bond via van der Waals forces to surfaces. Mechanical studies showed that aligned SWNT forests have adhesive forces three times that of Gecko's feet. The SWNT forests also displayed a thermal stability greater than scotch tape or superglue making them applicable for higher temperature adhesive applications.

2.4.2 Thin Films and Networks

CVD growth can be used to fabricate thin films of CNTs as well as positioned individual CNTs. These are of interest for their use in field effect transistors (FETs), network transistors and gas sensors.

A number of approaches have been adopted for the production of FETs and related devices based on individual SWNTs. Franklin et al. demonstrated the growth of individual SWNTs from one electrode to another in etched/suspended and flat geometries[93]. Arrays of such devices were fabricated and individual metallic and semiconducting SWNTs were probed electrically. Individual suspended semiconducting tubes displayed p-type behaviour and had an on-state resistance of 0.1 – 1 MΩ. Individual metallic SWNTs displayed resistances as low as 20 kΩ. Javey et al. further extended such devices by using multiple SWNT FETs to perform a series of different logic operations[94].

Rosenblatt et al. produced similar CVD produced FET devices but employed an electrolyte as the gate[95]. These were shown to have a transconductance of 7 μS/nm, suggesting the possibility of single molecule detection.

Thin film transistors based on SWNT networks involve less processing steps than FETs based on individual SWNTs and as such are easier to fabricate. Snow et al. demonstrated such a device, with source and drain electrodes 1 – 25 μm apart patterned on CVD grown SWNT networks[96]. The electrical properties of such devices depended

on the density of the SWNTs grown with low density networks behaving like a p-type semiconductor and high density networks behaving like a narrow band gap semiconductor with a high off-state current. Seidel et al. reported a similar approach with the source contact located inside the drain contact with a gap of 100 nm between the two[97], the application of a high bias was used to eliminate the metallic SWNTs and the transistors produced were shown to be capable of controlling macroscopic devices. Cao et al. used CVD growth followed by a transfer process to produce SWNT integrated circuits based on network transistors on transparent flexible substrates [98]. The transistors were shown to have high mobilities and on/off ratios.

Horizontally aligned SWNTs were grown on patterned metallic catalyst stripes by Kang et al. who subsequently deposited source and drain contacts between the stripes[99]. The aligned SWNTs behaved as a p-type transistor but could also be switched to n-type by the application of a thin layer of polyethyleneimine. The transistors produced had mobilities and on/off ratios making them feasible for use in integrated electronics.

SWNTs contacted in transistor-like configurations can also be used as gas sensors. Kong et al. demonstrated that when a semiconducting SWNT is exposed to a Lewis acid or base, charge transfer occurs changing the resistance[100]. Sensitivities of ppb levels have been reported[101-102] and enhanced selectivity has been shown by measuring the change in the dielectric constant of the SWNT[103-104] rather than the resistance or by polymer functionalisation[101, 105].

2.4.3 Other Nanotube Applications

One niche, to which CNTs are uniquely suited to, is as tips for scanning probe microscopy (SPM). This possibility was first illustrated by a low throughput method of transferring CNTs onto Si tips[106]. Production of SPM tips using CVD methods to grow CNTs on catalyst patterned Si tips[107] has also been demonstrated. This method offers better throughput and repeatability.

Other CNT applications involve the use of powders, dispersions and other post growth processing. In these cases CNTs produced by other techniques (e.g. arc discharge) are also feasible but CVD based techniques (e.g. HipCO) are often used. Such applications include strong composite materials[108-111], conductive fibres[112], drug delivery[113-114], improvement of Li batteries[115], actuators[116-117], thin film loudspeakers[118],

membranes for energy storage[119] and desalination[120], transparent conductive films[121], electrochemical sensors and biosensors[122-124] and electroluminescent devices[125-127] to name but a few.

2.5 Graphene

The 2D nature of graphene infers a number of interesting properties. In pristine samples electron and hole mobilities have been shown to exceed 15,000 cm^2/Vs[128]. The charge carriers satisfy Dirac's equation in quantum mechanics and are known as massless Dirac Fermions. This unique situation arises due to interactions with the periodic potential of the honeycomb lattice. These massless Dirac Fermions can be considered as electrons which have lost their rest mass. This in combination with other novel effects such as the room temperature quantum Hall effect[129], high thermal conductivity[130] and tunable band gaps[131] make graphene potentially useful for innovative approaches to electronic devices and other applications.

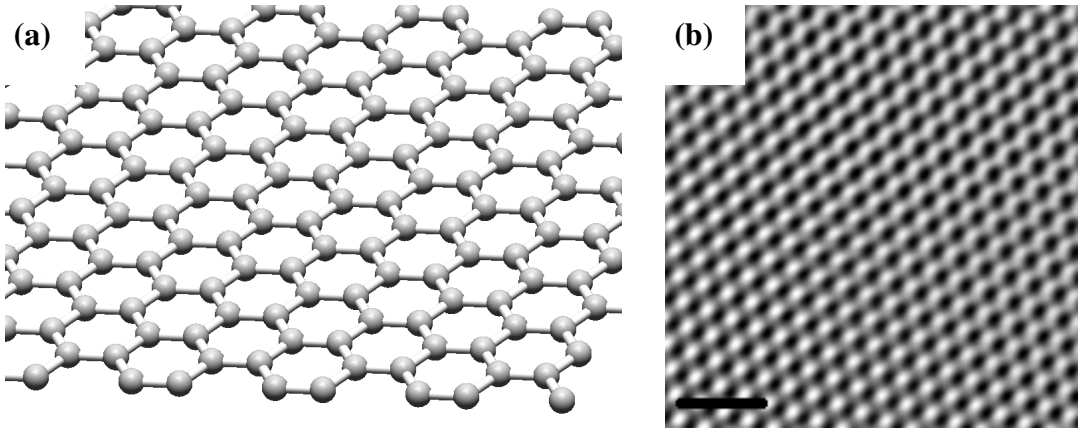

Figure 2.10 *(a) Graphic representation of a graphene sheet. (b) High resolution TEM image of graphene lattice[132], scale bar is 1 nm.*

Already applications such as liquid crystal devices[133], solar cells[134], field effect transistors[135] and highly sensitive gas sensors[136] have been illustrated. For these to be fully realised, scalable and reproducible growth methods are required.

One can imagine graphene being produced through the breaking of van der Waals bonds between graphitic planes. The first graphene reported was produced by the

mechanical exfoliation technique[2]. This entails using sticky tape to repeatedly peel a graphite surface. High purity graphene is produced but at a very low yield and so whilst it is of great interest for original lab-based experiments it is not well suited to large scale production.

Liquid phase exfoliation of graphite in organic solvents[137] and surfactant stabilised solutions[138] marked a major advance in the scalability and processability of graphene making composite materials and thin films readily attainable. However, the weight percentage of mono and bilayer graphene produced by this technique is rather low and it is not directly compatible with standard electronics processing steps.

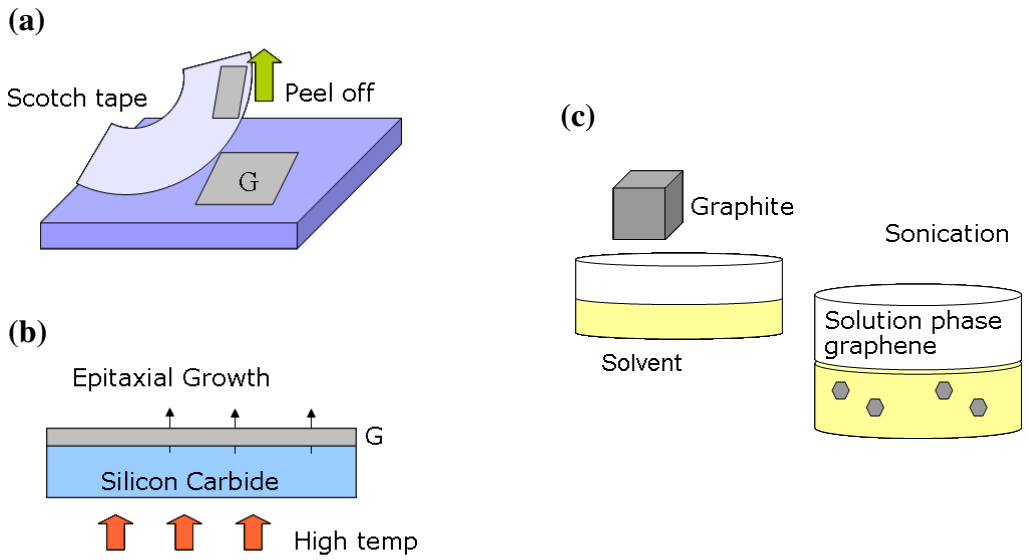

Figure 2.11 *Schematics for different graphene production methods (a) Mechanical exfoliation (b) Epitaxial growth on SiC (c) Liquid phase exfoliation.*

Other growth methods involve the growth or assembly of graphene rather than exfoliation of bulk graphite. Epitaxial growth of graphene on SiC surfaces by thermal desorption of Si was demonstrated by the de Heer group in 2004[139]. This technique produces ultrathin (~nm) graphitic films. However very high temperatures are involved (> 1200 ^{o}C) and the films are generally non uniform[140]. Furthermore, the electrical properties are adversely affected when compared with graphene produced by mechanical exfoliation. Epitaxial growth has subsequently been demonstrated on metallic surfaces including Ir[141] and Ru[142] but again, this involves very high temperatures.

The production of ultrathin (~ 1.5 nm) graphitic films on Ni substrates by CVD was reported by Obraztsov in 2007[143]. A growth temperature of 950 ^{o}C was used with a CH_4:H_2 gas mixture. The proposed growth mechanism suggested heteroepitaxial growth of graphene sheets on the Ni surface. The recently reported production of graphene on Ni[144] and Cu[145] by CVD methods offers improvement over other methods in terms of scalability, integration and uniformity. Furthermore, the growth temperature is considerably lower than epitaxial methods[146] and gas phase processing allows for doping during growth.

Alternative graphene production methods include reduction of graphene oxide[147], chemical[148] and plasma treatment of CNTs[149] and chemical assembly from small molecules[150].

2.6 Raman Spectroscopy of CVD Grown Nanocarbons

Raman spectroscopy is a powerful characterisation tool for investigating the physical properties and quality of assorted materials. It is widely used in the study of different carbon materials and is used throughout this thesis to probe the CVD nanocarbons grown. The following section gives a quick overview of the technique with particular focus on the features seen in the spectra of graphitic materials. The equipment used will be discussed in chapter 3.

2.6.1 Introduction to Raman Spectroscopy

When monochromatic light interacts with a sample the majority of photons are elastically (Rayleigh) scattered. However a small portion (~ 1 in 10^7) is shifted in wavelength through interactions with the sample material. This effect was first reported by Sir C.V. Raman in 1928[151], for which he was later awarded the Nobel prize in physics in 1930.

First and Second Order Raman Scattering

The first order Raman effect is described in Equation 2.7. An incident photon with a frequency ω_1 creates an electron-hole pair. This scatters inelastically with the emission of a phonon ω_{ph} and then recombines with the emission of a scattered photon ω_2. Energy and momentum are conserved.

$$\hbar\omega_1 = \hbar\omega_2 \pm \hbar\omega_{ph} \qquad \textit{Equation 2.7}$$

$$q_1 = q_2 \pm q_{ph}$$

This process can be simply envisaged looking at energy level diagrams such as that shown in Figure 2.12 whereby interaction with the incident photon promotes a molecule to a virtual state. If the molecule returns to a higher energy level then the photon will have lost energy on interaction with the molecule. The emitted photon will have less energy and a longer wavelength. This is known as Stokes Raman scattering. If the molecule returns to a lower energy level than the one it started in, the photon will have gained energy on interaction with the molecule and the emitted photon will be of higher energy and shorter wavelength than the incident photon. This is known as anti-Stokes Raman scattering.

In general the Stokes Raman intensity is much higher than anti-Stokes Raman intensity. This is due to the fact that Stokes Raman scattering intensity is proportional to the number of molecules in the lowest vibrational energy level whereas anti Stokes Raman scattering intensity is proportional to the number of molecule in the next highest vibrational energy level. The relative population of vibrational energy levels is governed by the Boltzmann distribution which dictates that the majority of modes are in the ground state at room temperature.

$$\frac{N_2}{N_1} = \frac{g_2}{g_1}\exp\left[\frac{-(E_2 - E_1)}{kT}\right] \qquad \textit{Equation 2.8}$$

where N_1 and N_2 are the number of molecules in the ground and first excited energy level respectively, g is the degeneracy of the levels, T is the temperature and E is the energy of the vibrational levels.

Second order Raman scattering occurs through a similar process, however in this case two scattering processes occur giving an increase in the energy observed.

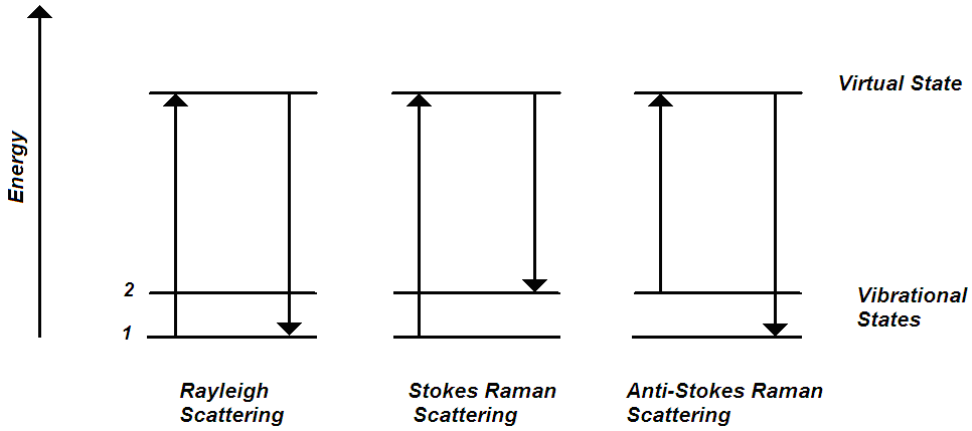

Figure 2.12 *Energy level diagram for Rayleigh scattering and Stokes and anti-Stokes Raman scattering.*

Resonant and Double Resonant Conditions

Resonant Raman scattering occurs when the excitation energy used matches or is close to that of an electronic transition. Under these conditions the Raman scattering intensity is greatly enhanced.

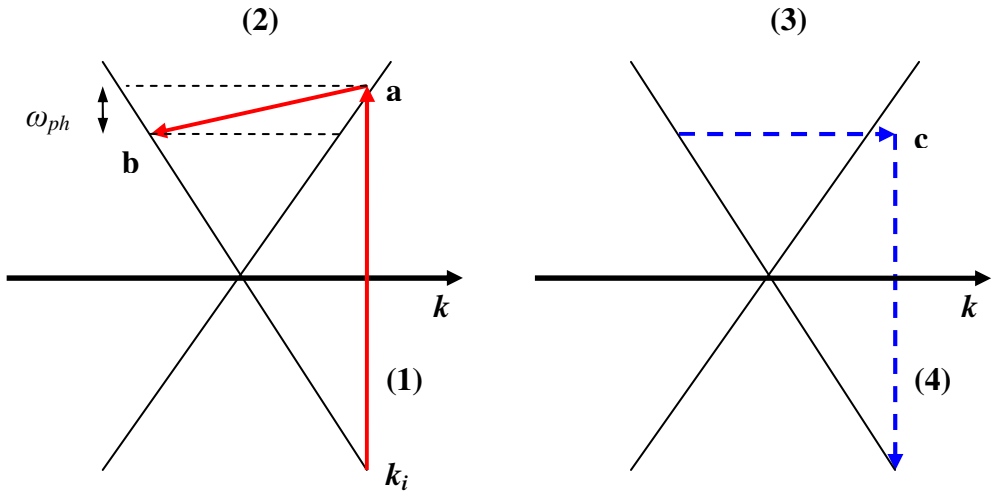

Figure 2.13 *Double resonant Raman scattering.*

If two of the intermediate states for the exciton in the second order process correspond to real electronic states then the condition for double resonance is satisfied. A schematic representation of this process is shown in Figure 2.13. The following steps are involved; (1) Incident light resonantly scatters an electron at wavevector k_i. (2) This electron is resonantly scattered from *a* to *b* by a phonon. (3) Through interaction with a

second phonon or a defect the electron is scattered back to *c*, where (4) it recombines with a hole.

Raman Spectra

A Raman spectrum is a plot of Raman scattering intensity (or number of scattered photons detected) versus the Raman shift in wavenumbers. The Raman shift is described as;

$$\nu = 1/\lambda_i - 1/\lambda_s \qquad \textit{Equation 2.9}$$

Where ν = Raman shift in cm^{-1}, λ_i = wavelength of incident light and λ_s = wavelength of scattered light.

The Raman shift associated with a given vibration or bond is a measure of the energy of that vibration. For example the *G* band for graphitic materials is typically found at 1580 cm^{-1} with a 632.8 nm excitation wavelength, this corresponds to emitted light of wavelength ~ 703 nm. Raman spectroscopy can be used as a tool for fingerprinting materials as each peak in a Raman spectrum corresponds to a vibrational mode in the sample.

When incident photons interact with a molecule's electron cloud, the strength of the interaction depends on the polarisability of the molecule. For a sample to be Raman active its polarisability must change on interaction with an external field. Molecules with distributed electron clouds such as pi-bonds which are easily polarised are very strong Raman scatterers and so Raman spectroscopy is a particularly useful characterisation technique for a wide array of nanocarbon materials.

Raman spectroscopy is a powerful tool for investigating different allotropes of carbon and has traditionally been used for characterisation of graphite[152], diamond[153] and amorphous carbon materials[154]. The bonds in sp^2 and sp^3 type carbon materials are highly Raman active and give rise to intense spectra with clearly-defined features. With the emergence of novel allotropes of carbon, Raman has come to the forefront of analysis techniques and has been invaluable in the characterisation and structural understanding of fullerenes[155], carbon nanotubes and most recently graphene.

2.6.2 Raman Spectroscopy of Graphite and Graphitic Materials

The Raman spectrum of graphite has three principal features, these are the *D*, *G* and *2D* (or *G'*) bands seen at ~1340 cm^{-1}, ~1580 cm^{-1} and ~2700 cm^{-1} respectively. The *G* band is due to a first order process whereas the *D* and *2D* bands originate from double resonance processes.

D and G Bands

The *D* band is related to defects and disorder in sp^2 hybridised carbon materials. This transition is forbidden in perfect graphitic systems and requires a defect for its activation. The *D* band stems from a double resonance process involving a phonon and a defect and can be considered as a breathing mode of A_{1g} symmetry. This double resonance process also leads to the *D* band being strongly dispersive with excitation laser energy[156].

Structural defects (such as edges, missing atoms or dopants) are generally the cause of the *D* band but it can also be due to the presence of residual amorphous carbon. In highly defective materials there are a number of additional *D* band contributions as described by Sadezky[157].

The *G* band stems from in plane vibrations and has E_{2g} symmetry; this is observed in all sp^2 carbon systems. In graphite the *G* band can be fitted with a single Lorentzian peak and can be assigned to an in-plane tangential optical phonon.

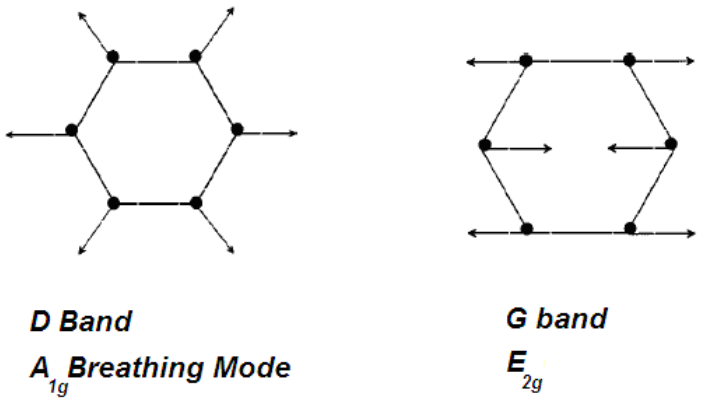

Figure 2.14 *Graphic representation of the vibrations giving rise to D and G bands seen in Raman spectra of graphitic systems.*

D/G Ratio and Crystallite Size

Because of its reliance on the presence of defects, the relative intensity of the *D* band is directly related to average crystallite size (L_a) [152]. Cancado et al. formulated an equation linking the ratio of the integrated area of the *D* and *G* bands to the crystallite size[158]. This is dependent on the energy of the excitation laser used (E_l). Typically broadening of the *D* and *G* bands is associated with increasing disorder.

$$L_a\left(nm\right)=\frac{560}{E_l^4}\left(\frac{A_D}{A_G}\right)^{-1} \qquad \textit{Equation 2.10}$$

2D Band

The 2D band (referred to as *G'* by some authors) is an overtone of the *D* band. Like the *D* band it stems from a double resonance process. However, it does not require a defect for activation and instead involves scattering from a second phonon.

The *2D* band is linked to 3D stacking in graphitic materials or uniformity in the graphitic plane where the presence of defects would lead to a reduction in intensity. For graphitic materials with a very small crystallite size, the *2D* band merges with other nearby bands forming a broad bump[157]. A relative increase in the *2D* band intensity can be linked to increasing graphitisation[159].

2.6.2 Raman Characterisation of CNTs

In addition to *D*, *G* and *2D* bands observed for graphite, SWNTs have peaks in the range 100 – 400 cm^{-1} known as radial breathing modes (RBMs). The use of each of these peaks in characterising CNTs will be outlined in the following section.

Radial Breathing Modes

RBMs are caused by all the atoms in the tube vibrating coherently in the radial direction. Such peaks are generally not seen in MWNTs due to their large diameters and damping between concentric shells. The wavenumber of these modes (ω_{RBM}) varies inversely with the tube diameter (d) as given in the equation;

$$\omega_{RBM} = \frac{A}{d} + B$$ *Equation 2. 11*

This relation was used by Duesberg et al. in 1999[160] to characterise isolated SWNTs and was later refined by other groups[161-163]. In these studies the RBM positions were used to ascertain the diameter of the SWNTs being probed and the possible tube chiralities were then calculated. Different values of A and B have been reported in the literature depending on the excitation wavelength being used and the environment of the tubes. A table of these values has been collated by Reich et al.[164].

Due to their unique density of states (DOS), different diameters/chiralities of nanotubes will be in resonance with different excitation wavelengths. This is best illustrated using a so called "Kataura plot", which is named after Hiromichi Kataura who related the gaps between symmetrical spikes in the DOS of SWNTs to their diameter in 1997[165]. A representative Kataura plot is shown in Figure 2.15. Detailed calculations on the DOS were later carried out by Saito et al.[166] and were in good agreement with Kataura's work. As different tubes are in resonance with different excitation wavelengths it is advantageous to use a number of different lasers or indeed a tunable laser in order to get information on the chirality/diameter distribution in nanotube samples as has been performed by a number of groups.[161, 167-168] Due to the powerful resonant RBM signal it is possible to image individual nanotubes using scanning Raman spectroscopy[169]. This can be extended to map chirality changes in individual nanotubes as shown by Anderson et al.[170].

As well as giving information on diameter and chirality the RBM modes can also be used to investigate functionalisation[171-172] and doping[173].

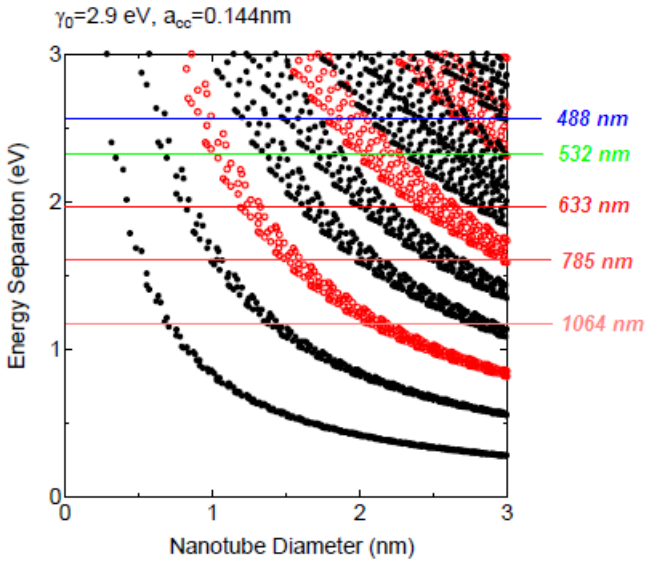

Figure 2.15 *A Kataura plot with lines drawn in showing resonance regions for some conventional excitation wavelengths. Black and red indicate semiconducting and metallic tubes respectively. Adapted from*[174].

G Band

The *G* band in MWNTs is a single peak and is very similar to that of graphite. A shoulder on the *G* band at 1620 cm^{-1} is seen in defective nanotubes. This is known as the *D'* band. In the case of SWNTs the *G* band becomes a little more complicated as it is seen to split into two peaks referred to as G^- and G^+. Quantum confinement along the circumferential direction leads to the graphite *G* band phonon splitting into longitudinal optical (LO) and transverse optical (TO) modes. In the case of isolated SWNTs metallic and semiconducting tubes have very different shaped *G* bands, semiconducting tubes display sharp G^- and G^+ peaks, whereas metallic tubes have a broadened and downshifted G^-[175] as shown in Figure 2.16. Piscanec et al. recently clarified the phonon association for these peaks and showed that in semiconducting SWNTs the G^- and G^+ peaks were linked to the TO and LO phonons respectively and that the opposite assignment applied to metallic SWNTs[176]. The position of the G^+ peak is sensitive to dopant species whereas the position of both G^+ and G^- peaks show diameter dependence[177]. Spectra of bulk SWNT samples contain metallic and semiconducting contributions. The overall shape of the *G* band will change depending on the method

used to prepare the tubes and the relative population of semiconducting and metallic species[178].

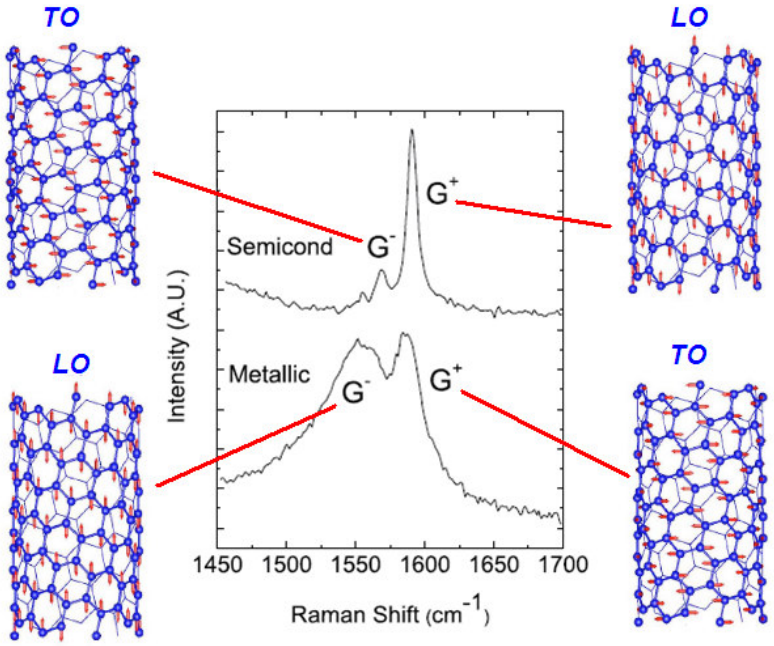

Figure 2.16 *G band splitting for individual semiconducting and metallic SWNTs, adapted from[176].*

D/G Ratio

The intensity ratio of *D* to *G* peaks (I_D/I_G) is seen to scale with decreasing crystallite size[152, 156]. As such, I_D/I_G is often used as a means of determining the impurity levels or degree of functionalisation in nanotube samples.

Osswald et al. used a combination of Raman and FTIR spectroscopy to show the effect of both thermal and chemical oxidation of MWNT samples[179]. The oxidation treatment showed a linear increase in I_D/I_G in the case of isothermal, flash and chemical oxidation. This was coupled with the emergence of OH and COOH groups in the FTIR spectra.

Di Leo et al. also used relative intensity ratios of Raman peaks to investigate the purity of MWNTs[180]. In their experiments MWNTs were mixed with a set amount of nanocarbon and calibration curves were fitted to the intensity ratios obtained for different purity levels.

Qian et al. examined mixed samples of MWNTs and SWNTs with Raman and were able to correlate the mol% of MWNTs present to I_D/I_G and also to the frequencies of these bands (ω_D and ω_G)[181].

In the process of functionalising SWNTs, Dyke et al. showed that the *D* band increased considerably upon functionalisation and then diminished when the sample was annealed, thus removing functionalities[182]. Strano et al. functionalised SWNTs with diazonium salts and were able to link the increase in I_D to the relative number of functional groups present[172].

Sato-Berru et al. employed principal component analysis (PCA) in tandem with Raman spectroscopy to detect subtle changes in the spectra of MWNTs upon functionalisation[183].

2D Band

The 2D band is less investigated than the RBMs, *D* and *G* bands in CNTs. However, its intensity has been linked with the metallicity of the tubes being probed[184].

2.6.3 Raman Characterisation of Graphene

The Raman spectrum of graphene is similar to that of graphite in two respects. Firstly a single Lorentzian *G* band is observed and secondly defects are indicated by the presence of a *D* band. The spectrum differs greatly though with respect to the *2D* band. The *2D* band is a single narrow Lorentzian peak (FWHM ~ 30 cm^{-1}) in monolayer graphene, a combination of four peaks in bilayer graphene, and approaches a standard graphite *2D* band after 5 – 10 layers, as first described by Ferrari et al.[185]. The intensity ratio I_{2D}/I_G is approximately 4 for monolayer graphene and decreases with the addition of subsequent layers, thus making it possible to estimate the thickness of graphene layers from Raman spectra.

Scanning Raman spectroscopy is particularly useful for graphene as it allows for direct imaging of defects and edges (I_D/I_G)[186-187] and also layer thickness (I_{2D}/I_G)[187] over large areas. This technique can also be used to investigate the effects of strain on graphene materials, with a downward shift in peak widths for both the *G* and *2D* bands ($\Delta\omega_G$ and $\Delta\omega_{2D}$) seen when strain is applied to graphene deposited on PET[188-189]. This red shift is attributed to a stretching of bonds.

Bruna et al. investigated the effect of doping on the Raman spectrum of different thicknesses of graphene by using a CHF_3 plasma to introduce F atoms[190]. They observed a blue-shifted *G* band for odd numbered layers and splitting of the *G* band was seen for even numbered layers. Lin et al. carried out similar studies on NH_3 plasma treated graphene and observed the *G* band splitting and shifts as well as an increase in I_D and a decrease in I_{2D}/I_G[191].

References

1. Kroto, H.W., et al., *C-60 - Buckminsterfullerene.* Nature, 1985. **318**(6042): p. 162-163.
2. Novoselov, K.S., et al., *Electric field effect in atomically thin carbon films.* Science, 2004. **306**(5696): p. 666-669.
3. Dresselhaus, M.S., G. Dresselhaus, and R. Saito, *Physics of carbon nanotubes.* Carbon, 1995. **33**(7): p. 883-891.
4. Saito, R., et al., *Electronic Structure of Chiral Graphene Tubules.* Applied Physics Letters, 1992. **60**(18): p. 2204-2206.
5. Wilder, J.W.G., et al., *Electronic structure of atomically resolved carbon nanotubes.* Nature, 1998. **391**(6662): p. 59-62.
6. Wallace, P.R., *The Band Theory of Graphite.* Physical Review, 1947. **71**(9): p. 622.
7. Harris, P.J.F., *Carbon Nanotube Science*. 2009: Cambridge University Press.
8. Ahuja, R., et al., *Electronic structure of graphite: Effect of hydrostatic pressure.* Physical Review B, 1995. **51**(8): p. 4813.
9. Popov, V.N., *Carbon nanotubes: properties and application.* Materials Science and Engineering: R: Reports, 2004. **43**(3): p. 61-102.
10. Van Hove, L., *The Occurrence of Singularities in the Elastic Frequency Distribution of a Crystal.* Physical Review, 1953. **89**(6): p. 1189.
11. Kim, P., et al., *Electronic density of states of atomically resolved single-walled carbon nanotubes: Van Hove singularities and end states.* Physical Review Letters, 1999. **82**(6): p. 1225-1228.
12. May, P.W., *Diamond thin films: a 21st-century material.* Philosophical Transactions of the Royal Society of London Series a-Mathematical Physical and Engineering Sciences, 2000. **358**(1766): p. 473-495.
13. De Jong, K.P. and J.W. Geus, *Carbon nanofibers: Catalytic synthesis and applications.* Catalysis Reviews-Science and Engineering, 2000. **42**(4): p. 481-510.
14. Cheung, C.L., et al., *Diameter-Controlled Synthesis of Carbon Nanotubes.* The Journal of Physical Chemistry B, 2002. **106**(10): p. 2429-2433.
15. Li, Y., et al., *Growth of Single-Walled Carbon Nanotubes from Discrete Catalytic Nanoparticles of Various Sizes.* The Journal of Physical Chemistry B, 2001. **105**(46): p. 11424-11431.
16. Bethune, D.S., et al., *Cobalt-Catalyzed Growth of Carbon Nanotubes with Single Atomic-Layer Walls.* Nature, 1993. **363**(6430): p. 605-607.

17. Ebbesen, T.W. and P.M. Ajayan, *Large-Scale Synthesis of Carbon Nanotubes.* Nature, 1992. **358**(6383): p. 220-222.
18. Iijima, S., *Helical Microtubules of Graphitic Carbon.* Nature, 1991. **354**(6348): p. 56-58.
19. Iijima, S. and T. Ichihashi, *Single-shell carbon nanotubes of 1-nm diameter.* Nature, 1993. **363**(6430): p. 603-605.
20. Thess, A., et al., *Crystalline ropes of metallic carbon nanotubes.* Science, 1996. **273**(5274): p. 483-487.
21. Ivanov, V., et al., *The study of carbon nanotubules produced by catalytic method.* Chemical Physics Letters, 1994. **223**(4): p. 329-335.
22. Dal, H.J., et al., *Single-wall nanotubes produced by metal-catalyzed disproportionation of carbon monoxide.* Chemical Physics Letters, 1996. **260**(3-4): p. 471-475.
23. Hafner, J.H., et al., *Catalytic growth of single-wall carbon nanotubes from metal particles.* Chemical Physics Letters, 1998. **296**(1-2): p. 195-202.
24. Nikolaev, P., et al., *Gas-phase catalytic growth of single-walled carbon nanotubes from carbon monoxide.* Chemical Physics Letters, 1999. **313**(1-2): p. 91-97.
25. Cassell, A.M., et al., *Large Scale CVD Synthesis of Single-Walled Carbon Nanotubes.* J. Phys. Chem. B, 1999. **103**(31): p. 6484-6492.
26. Kong, J., et al., *Synthesis of individual single-walled carbon nanotubes on patterned silicon wafers.* Nature, 1998. **395**(6705): p. 878-881.
27. Ren, Z.F., et al., *Growth of a single freestanding multiwall carbon nanotube on each nanonickel dot.* Applied Physics Letters, 1999. **75**(8): p. 1086-1088.
28. Teo, K.B.K., et al., *Uniform patterned growth of carbon nanotubes without surface carbon.* Applied Physics Letters, 2001. **79**(10): p. 1534-1536.
29. Duesberg, G.S., et al., *Growth of Isolated Carbon Nanotubes with Lithographically Defined Diameter and Location.* Nano Lett., 2003. **3**(2): p. 257-259.
30. Li, J., et al., *Highly-ordered carbon nanotube arrays for electronics applications.* Applied Physics Letters, 1999. **75**(3): p. 367-369.
31. Jeong, S.-H. and K.-H. Lee, *Fabrication of the aligned and patterned carbon nanotube field emitters using the anodic aluminum oxide nano-template on a Si wafer.* Synthetic Metals, 2003. **139**(2): p. 385-390.
32. Sklar, G.P., et al., *Pulsed electrodeposition into AAO templates for CVD growth of carbon nanotube arrays.* Nanotechnology, 2005. **16**(8): p. 1265-1271.
33. Huang, J.-H., et al., *Selective growth of carbon nanotubes on nickel oxide templates created by atomic force microscope nano-oxidation.* Diamond and Related Materials, 2005. **14**(3-7): p. 744-748.
34. Ryu, K.M., et al., *Synthesis of aligned single-walled nanotubes using catalysts defined by nanosphere lithography.* Journal of the American Chemical Society, 2007. **129**(33): p. 10104-10105.
35. Huang, Z.P., et al., *Growth of large periodic arrays of carbon nanotubes.* Applied Physics Letters, 2003. **82**(3): p. 460-462.
36. Tsai, T.Y., et al., *The fabrication of a carbon nanotube array using a catalyst-poisoning layer in the inverse nano-sphere lithography method.* Nanotechnology, 2009. **20**(30).
37. Fan, S., et al., *Self-Oriented Regular Arrays of Carbon Nanotubes and Their Field Emission Properties.* Science, 1999. **283**(5401): p. 512-514.

38. Fan, S., et al., *Carbon nanotube arrays on silicon substrates and their possible application.* Physica E: Low-dimensional Systems and Nanostructures, 2000. **8**(2): p. 179-183.
39. Bronikowski, M.J., *CVD growth of carbon nanotube bundle arrays.* Carbon, 2006. **44**(13): p. 2822-2832.
40. Zhu, L., et al., *Growth and electrical characterization of high-aspect-ratio carbon nanotube arrays.* Carbon, 2006. **44**(2): p. 253-258.
41. Hart, A.J. and A.H. Slocum, *Rapid growth and flow-mediated nucleation of millimeter-scale aligned carbon nanotube structures from a thin-film catalyst.* Journal of Physical Chemistry B, 2006. **110**(16): p. 8250-8257.
42. Jeong, G.H., et al., *Effect of catalyst pattern geometry on the growth of vertically aligned carbon nanotube arrays.* Carbon, 2009. **47**(3): p. 696-704.
43. Franklin, N.R. and H. Dai, *An Enhanced CVD Approach to Extensive Nanotube Networks with Directionality.* Advanced Materials, 2000. **12**(12): p. 890-894.
44. Zhang, Y., et al., *Electric-field-directed growth of aligned single-walled carbon nanotubes.* Applied Physics Letters, 2001. **79**(19): p. 3155-3157.
45. Yoshihara, N., et al., *Horizontally Aligned Growth of Single-Walled Carbon Nanotubes on a Surface-Modified Silicon Wafer.* Journal of Physical Chemistry C, 2009. **113**(19): p. 8030-8034.
46. Han, S., X. Liu, and C. Zhou, *Template-Free Directional Growth of Single-Walled Carbon Nanotubes on a- and r-Plane Sapphire.* Journal of the American Chemical Society, 2005. **127**(15): p. 5294-5295.
47. Hata, K., et al., *Water-assisted highly efficient synthesis of impurity-free single-waited carbon nanotubes.* Science, 2004. **306**(5700): p. 1362-1364.
48. Yun, Y.H., et al., *Growth mechanism of long aligned multiwall carbon nanotube arrays by water-assisted chemical vapor deposition.* Journal of Physical Chemistry B, 2006. **110**(47): p. 23920-23925.
49. Futaba, D.N., et al., *84% Catalyst Activity of Water-Assisted Growth of Single Walled Carbon Nanotube Forest Characterization by a Statistical and Macroscopic Approach.* The Journal of Physical Chemistry B, 2006. **110**(15): p. 8035-8038.
50. Li, J., C. Papadopoulos, and J. Xu, *Nanoelectronics: Growing Y-junction carbon nanotubes.* Nature, 1999. **402**(6759): p. 253-254.
51. Jin, Z., et al., *Direct growth of carbon nanotube junctions by a two-step chemical vapor deposition.* Chemical Physics Letters, 2006. **432**(1-3): p. 177-183.
52. Yao, Y.G., et al., *Temperature-mediated growth of single-walled carbon-nanotube intramolecular junctions.* Nature Materials, 2007. **6**(4): p. 283-286.
53. Wada, H., et al., *The Formation of Pyrolytic Carbon on a Nickel Sheet.* Japanese Journal of Applied Physics Part 2-Letters, 1989. **28**(2): p. L284-L286.
54. Deck, C.P. and K. Vecchio, *Prediction of carbon nanotube growth success by the analysis of carbon-catalyst binary phase diagrams.* Carbon, 2006. **44**(2): p. 267-275.
55. Esconjauregui, S., C.M. Whelan, and K. Maex, *The reasons why metals catalyze the nucleation and growth of carbon nanotubes and other carbon nanomorphologies.* Carbon, 2009. **47**(3): p. 659-669.
56. Hofmann, S., et al., *State of Transition Metal Catalysts During Carbon Nanotube Growth.* The Journal of Physical Chemistry C, 2009. **113**(5): p. 1648-1656.

57. Mizuno, K., et al., *Selective Matching of Catalyst Element and Carbon Source in Single-Walled Carbon Nanotube Synthesis on Silicon Substrates.* J. Phys. Chem. B, 2005. **109**(7): p. 2632-2637.
58. Ago, H., et al., *Gas analysis of the CVD process for high yield growth of carbon nanotubes over metal-supported catalysts.* Carbon, 2006. **44**(14): p. 2912-2918.
59. O'Byrne, J.P., et al., *Growth of Carbon Nanotubes from Heterometallic Palladium and Copper Catalysts.* The Journal of Physical Chemistry C, 2010. **114**(18): p. 8115-8119.
60. Takagi, D., et al., *Carbon Nanotube Growth from Semiconductor Nanoparticles.* Nano Lett., 2007. **7**(8): p. 2272-2275.
61. Liu, H., et al., *The growth of single-walled carbon nanotubes on a silica substrate without using a metal catalyst.* Carbon, 2010. **48**(1): p. 114-122.
62. Kukovitsky, E.F., et al., *Correlation between metal catalyst particle size and carbon nanotube growth.* Chemical Physics Letters, 2002. **355**(5-6): p. 497-503.
63. Harutyunyan, A.R., et al., *Evolution of catalyst particle size during carbon single walled nanotube growth and its effect on the tube characteristics.* Journal of Applied Physics, 2006. **100**(4).
64. Signore, M.A., et al., *Role of iron catalyst particles density in the growth of forest-like carbon nanotubes.* Diamond and Related Materials, 2008. **17**(11): p. 1936-1942.
65. Liu, Q., et al., *Effects of argon flow rate and reaction temperature on synthesizing single-walled carbon nanotubes from ethanol.* Physica E: Low-dimensional Systems and Nanostructures, 2009. **41**(7): p. 1204-1209.
66. Kwok, C.T.M., et al., *Temperature and time dependence study of single-walled carbon nanotube growth by catalytic chemical vapor deposition.* Carbon, 2010. **48**(4): p. 1279-1288.
67. Nerushev, O.A., et al., *The temperature dependence of Fe-catalysed growth of carbon nanotubes on silicon substrates.* Physica B: Condensed Matter, 2002. **323**(1-4): p. 51-59.
68. Liu, K., et al., *A growth mark method for studying growth mechanism of carbon nanotube arrays.* Carbon, 2005. **43**(14): p. 2850-2856.
69. Siegal, M.P., et al., *Linear Behavior of Carbon Nanotube Diameters with Growth Temperature.* The Journal of Physical Chemistry C, 2010. **114**(35): p. 14864-14867.
70. Zhu, Y.B., et al., *Theoretical analysis of external diameter distributions of carbon nanotubes by CVD.* Diamond and Related Materials. **12**(10-11): p. 1862-1866.
71. Franklin, N.R., et al., *Patterned growth of single-walled carbon nanotubes on full 4-inch wafers.* Applied Physics Letters, 2001. **79**(27): p. 4571-4573.
72. Maruyama, S., et al., *Low-temperature synthesis of high-purity single-walled carbon nanotubes from alcohol.* Chemical Physics Letters, 2002. **360**(3-4): p. 229-234.
73. Kreupl, F., et al., *Carbon nanotubes in interconnect applications.* Microelectronic Engineering, 2002. **64**(1-4): p. 399-408.
74. Zheng, L.X., et al., *Ultralong single-wall carbon nanotubes.* Nat Mater, 2004. **3**(10): p. 673-676.
75. Baughman, R.H., A.A. Zakhidov, and W.A. de Heer, *Carbon Nanotubes--the Route Toward Applications.* Science, 2002. **297**(5582): p. 787-792.

76. Wei, B.Q., R. Vajtai, and P.M. Ajayan, *Reliability and current carrying capacity of carbon nanotubes.* Applied Physics Letters, 2001. **79**(8): p. 1172-1174.
77. Kim, P., et al., *Thermal Transport Measurements of Individual Multiwalled Nanotubes.* Physical Review Letters, 2001. **87**(21): p. 215502.
78. Pop, E., et al., *Thermal Conductance of an Individual Single-Wall Carbon Nanotube above Room Temperature.* Nano Letters, 2005. **6**(1): p. 96-100.
79. Yu, M.-F., et al., *Tensile Loading of Ropes of Single Wall Carbon Nanotubes and their Mechanical Properties.* Physical Review Letters, 2000. **84**(24): p. 5552.
80. Nihei, M., et al., *Electrical properties of carbon nanotube bundles for future via interconnects.* Japanese Journal of Applied Physics Part 1-Regular Papers Short Notes & Review Papers, 2005. **44**(4A): p. 1626-1628.
81. Yokoyama, D., et al., *Electrical properties of carbon nanotubes grown at a low temperature for use as interconnects.* Japanese Journal of Applied Physics, 2008. **47**(4): p. 1985-1990.
82. Kawabata, A., et al. *Robustness of CNT via interconnect fabricated by low temperature process over a high-density current*. in *2008 IEEE International Interconnect Technology Conference, IITC, June 1, 2008 - June 4, 2008*. 2008. Burlingame, CA, United states: Inst. of Elec. and Elec. Eng. Computer Society.
83. Deheer, W.A., A. Chatelain, and D. Ugarte, *A Carbon Nanotube Field-Emission Electron Source.* Science, 1995. **270**(5239): p. 1179-1180.
84. Jang, H.S., H.-R. Lee, and D.-H. Kim, *Field emission properties of carbon nanotubes with different morphologies.* Thin Solid Films, 2006. **500**(1-2): p. 124-128.
85. Milne, W.I., et al., *Carbon nanotubes as field emission sources.* Journal of Materials Chemistry, 2004. **14**(6): p. 933-943.
86. Murakami, H., et al., *Field emission from well-aligned, patterned, carbon nanotube emitters.* Applied Physics Letters, 2000. **76**(13): p. 1776-1778.
87. Wang, Q.H., et al., *A nanotube-based field-emission flat panel display.* Applied Physics Letters, 1998. **72**(22): p. 2912-2913.
88. Zhu, W., et al., *Large current density from carbon nanotube field emitters.* Applied Physics Letters, 1999. **75**(6): p. 873-875.
89. Yue, G.Z., et al., *Generation of continuous and pulsed diagnostic imaging x-ray radiation using a carbon-nanotube-based field-emission cathode.* Applied Physics Letters, 2002. **81**(2): p. 355-357.
90. Niu, C., et al., *High power electrochemical capacitors based on carbon nanotube electrodes.* Applied Physics Letters, 1997. **70**(11): p. 1480-1482.
91. Futaba, D.N., et al., *Shape-engineerable and highly densely packed single-walled carbon nanotubes and their application as super-capacitor electrodes.* Nature Materials, 2006. **5**(12): p. 987-994.
92. Qu, L. and L. Dai, *Gecko-Foot-Mimetic Aligned Single-Walled Carbon Nanotube Dry Adhesives with Unique Electrical and Thermal Properties.* Advanced Materials, 2007. **19**(22): p. 3844-3849.
93. Franklin, N.R., et al., *Integration of suspended carbon nanotube arrays into electronic devices and electromechanical systems.* Applied Physics Letters, 2002. **81**(5): p. 913-915.
94. Javey, A., et al., *Carbon nanotube transistor arrays for multistage complementary logic and ring oscillators.* Nano Letters, 2002. **2**(9): p. 929-932.

95. Rosenblatt, S., et al., *High performance electrolyte gated carbon nanotube transistors.* Nano Letters, 2002. **2**(8): p. 869-872.
96. Snow, E.S., et al., *Random networks of carbon nanotubes as an electronic material.* Applied Physics Letters, 2003. **82**(13): p. 2145-2147.
97. Seidel, R., et al., *High-Current Nanotube Transistors.* Nano Lett., 2004. **4**(5): p. 831-834.
98. Cao, Q., et al., *Medium-scale carbon nanotube thin-film integrated circuits on flexible plastic substrates.* Nature, 2008. **454**(7203): p. 495-U4.
99. Kang, S.J., et al., *High-performance electronics using dense, perfectly aligned arrays of single-walled carbon nanotubes.* Nature Nanotechnology, 2007. **2**(4): p. 230-236.
100. Kong, J., et al., *Nanotube molecular wires as chemical sensors.* Science, 2000. **287**(5453): p. 622-625.
101. Qi, P., et al., *Toward Large Arrays of Multiplex Functionalized Carbon Nanotube Sensors for Highly Sensitive and Selective Molecular Detection.* Nano Lett., 2003. **3**(3): p. 347-351.
102. Valentini, L., et al., *Sensors for sub-ppm NO2 gas detection based on carbon nanotube thin films.* Applied Physics Letters, 2003. **82**(6): p. 961-963.
103. Chopra, S., et al., *Selective gas detection using a carbon nanotube sensor.* Applied Physics Letters, 2003. **83**(11): p. 2280-2282.
104. Robinson, J.A., E.S. Snow, and F.K. Perkins, *Improved chemical detection using single-walled carbon nanotube network capacitors.* Sensors and Actuators A: Physical, 2007. **135**(2): p. 309-314.
105. Star, A., et al., *Sensing with Nafion coated carbon nanotube field-effect transistors.* Electroanalysis, 2004. **16**(1-2): p. 108-112.
106. Nishijima, H., et al., *Carbon-nanotube tips for scanning probe microscopy: Preparation by a controlled process and observation of deoxyribonucleic acid.* Applied Physics Letters, 1999. **74**(26): p. 4061-4063.
107. Marty, L., et al., *Self-assembled single wall carbon nanotube field effect transistors and AFM tips prepared by hot filament assisted CVD.* Thin Solid Films, 2006. **501**(1-2): p. 299-302.
108. Blond, D., et al., *Enhancement of Modulus, Strength, and Toughness in Poly(methyl methacrylate)-Based Composites by the Incorporation of Poly(methyl methacrylate)-Functionalized Nanotubes.* Advanced Functional Materials, 2006. **16**(12): p. 1608-1614.
109. Blond, D., et al., *Toughening of artificial silk by incorporation of carbon nanotubes.* Biomacromolecules, 2007. **8**(12): p. 3973-3976.
110. Coleman, J.N., et al., *Small but strong: A review of the mechanical properties of carbon nanotube-polymer composites.* Carbon, 2006. **44**(9): p. 1624-1652.
111. Lahiff, E., et al., *Physical properties of novel free-standing polymer-nanotube thin films.* Carbon, 2006. **44**(8): p. 1525-1529.
112. Dalton, A.B., et al., *Super-tough carbon-nanotube fibres - These extraordinary composite fibres can be woven into electronic textiles.* Nature, 2003. **423**(6941): p. 703-703.
113. Lacerda, L., et al., *Carbon nanotubes as nanomedicines: From toxicology to pharmacology.* Advanced Drug Delivery Reviews, 2006. **58**(14): p. 1460-1470.
114. Liu, Z., et al., *Drug delivery with carbon nanotubes for in vivo cancer treatment.* Cancer Research, 2008. **68**(16): p. 6652-6660.
115. Endo, M., et al., *Recent development of carbon materials for Li ion batteries.* Carbon, 2000. **38**(2): p. 183-197.

116. Baughman, R.H., et al., *Carbon nanotube actuators.* Science, 1999. **284**(5418): p. 1340-1344.
117. Fraysse, J., et al., *Carbon nanotubes acting like actuators.* Carbon, 2002. **40**(10): p. 1735-1739.
118. Xiao, L., et al., *Flexible, Stretchable, Transparent Carbon Nanotube Thin Film Loudspeakers.* Nano Letters, 2008. **8**(12): p. 4539-4545.
119. Che, G., et al., *Carbon nanotubule membranes for electrochemical energy storage and production.* Nature, 1998. **393**(6683): p. 346-349.
120. Corry, B., *Designing carbon nanotube membranes for efficient water desalination.* Journal of Physical Chemistry B, 2008. **112**(5): p. 1427-1434.
121. Wu, Z.C., et al., *Transparent, conductive carbon nanotube films.* Science, 2004. **305**(5688): p. 1273-1276.
122. Keeley, G.P. and M.E.G. Lyons, *The Effects of Thin Layer Diffusion at Glassy Carbon Electrodes Modified with Porous Films of Single-Walled Carbon Nanotubes.* International Journal of Electrochemical Science, 2009. **4**(6): p. 794-809.
123. Lin, Y.H., et al., *Glucose biosensors based on carbon nanotube nanoelectrode ensembles.* Nano Letters, 2004. **4**(2): p. 191-195.
124. Maehashi, K., et al., *Label-free protein biosensor based on aptamer-modified carbon nanotube field-effect transistors.* Analytical Chemistry, 2007. **79**(2): p. 782-787.
125. Fournet, P., et al., *Enhanced brightness in organic light-emitting diodes using a carbon nanotube composite as an electron-transport layer.* Journal of Applied Physics, 2001. **90**(2): p. 969-975.
126. Kazaoui, S., et al., *Near-infrared electroluminescent devices using single-wall carbon nanotubes thin flms.* Applied Physics Letters, 2005. **87**(21).
127. Zhang, D.H., et al., *Transparent, conductive, and flexible carbon nanotube films and their application in organic light-emitting diodes.* Nano Letters, 2006. **6**(9): p. 1880-1886.
128. Novoselov, K.S., et al., *Two-dimensional gas of massless Dirac fermions in graphene.* Nature, 2005. **438**(7065): p. 197-200.
129. Novoselov, K.S., et al., *Room-Temperature Quantum Hall Effect in Graphene.* Science, 2007: p. 1137201.
130. Balandin, A.A., et al., *Superior Thermal Conductivity of Single-Layer Graphene.* Nano Letters, 2008. **8**(3): p. 902-907.
131. Melinda, Y.H., et al., *Energy Band-Gap Engineering of Graphene Nanoribbons.* Physical Review Letters, 2007. **98**(20): p. 206805.
132. Kumar, S., et al., *Gas phase controlled deposition of high quality large-area graphene films.* Chemical Communications, 2010. **46**(9): p. 1422-1424.
133. Blake, P., et al., *Graphene-Based Liquid Crystal Device.* Nano Letters, 2008. **8**(6): p. 1704-1708.
134. Wang, X., L. Zhi, and K. Mullen, *Transparent, Conductive Graphene Electrodes for Dye-Sensitized Solar Cells.* Nano Letters, 2008. **8**(1): p. 323-327.
135. Meric, I., et al., *Current saturation in zero-bandgap, top-gated graphene field-effect transistors.* Nat Nano, 2008. **3**(11): p. 654-659.
136. Schedin, F., et al., *Detection of individual gas molecules adsorbed on graphene.* Nature Materials, 2007. **6**(9): p. 652-655.
137. Hernandez, Y., et al., *High-yield production of graphene by liquid-phase exfoliation of graphite.* Nature Nanotechnology, 2008. **3**(9): p. 563-568.

138. Lotya, M., et al., *Liquid Phase Production of Graphene by Exfoliation of Graphite in Surfactant/Water Solutions.* Journal of the American Chemical Society, 2009. **131**(10): p. 3611-3620.
139. Berger, C., et al., *Ultrathin epitaxial graphite: 2D electron gas properties and a route toward graphene-based nanoelectronics.* Journal of Physical Chemistry B, 2004. **108**(52): p. 19912-19916.
140. Taisuke, O., et al., *Morphology of graphene thin film growth on SiC(0001).* New Journal of Physics, 2008(2): p. 023034.
141. Johann, C., et al., *Growth of graphene on Ir(111).* New Journal of Physics, 2009(2): p. 023006.
142. Sutter, P.W., J.-I. Flege, and E.A. Sutter, *Epitaxial graphene on ruthenium.* Nat Mater, 2008. **7**(5): p. 406-411.
143. Obraztsov, A.N., et al., *Chemical vapor deposition of thin graphite films of nanometer thickness.* Carbon, 2007. **45**(10): p. 2017-2021.
144. Reina, A., et al., *Large Area, Few-Layer Graphene Films on Arbitrary Substrates by Chemical Vapor Deposition.* Nano Letters, 2009. **9**(1): p. 30-35.
145. Li, X., et al., *Large-Area Synthesis of High-Quality and Uniform Graphene Films on Copper Foils.* Science, 2009. **324**(5932): p. 1312-1314.
146. Kumar, S., et al., *Low Temperature Graphene Growth.* ECS Transactions, 2009. **19**(5): p. 175-181.
147. Stankovich, S., et al., *Synthesis of graphene-based nanosheets via chemical reduction of exfoliated graphite oxide.* Carbon, 2007. **45**(7): p. 1558-1565.
148. Kosynkin, D.V., et al., *Longitudinal unzipping of carbon nanotubes to form graphene nanoribbons.* Nature, 2009. **458**(7240): p. 872-876.
149. Jiao, L., et al., *Narrow graphene nanoribbons from carbon nanotubes.* Nature, 2009. **458**(7240): p. 877-880.
150. Yang, X., et al., *Two-Dimensional Graphene Nanoribbons.* Journal of the American Chemical Society, 2008. **130**(13): p. 4216-4217.
151. Raman, C., *A New Radiation.* Indian J. Phys., 1928. **2**: p. 387.
152. Tuinstra, F. and J.L. Koenig, *Raman Spectrum of Graphite.* The Journal of Chemical Physics, 1970. **53**(3): p. 1126-1130.
153. Nemanich, R.J., et al., *Raman scattering characterization of carbon bonding in diamond and diamond like thin films.* Journal of Vacuum Science & Technology a-Vacuum Surfaces and Films, 1988. **6**(3): p. 1783-1787.
154. Ferrari, A.C. and J. Robertson, *Interpretation of Raman spectra of disordered and amorphous carbon.* Physical Review B, 2000. **61**(20): p. 14095.
155. Dresselhaus, M.S., G. Dresselhaus, and P.C. Eklund, *Raman scattering in fullerenes.* Journal of Raman Spectroscopy, 1996. **27**(3-4): p. 351-371.
156. Sato, K., et al., *D-band Raman intensity of graphitic materials as a function of laser energy and crystallite size.* Chemical Physics Letters, 2006. **427**(1-3): p. 117-121.
157. Sadezky, A., et al., *Raman microspectroscopy of soot and related carbonaceous materials: Spectral analysis and structural information.* Carbon, 2005. **43**(8): p. 1731-1742.
158. Cancado, L.G., et al., *General equation for the determination of the crystallite size L-a of nanographite by Raman spectroscopy.* Applied Physics Letters, 2006. **88**(16).
159. Lee, Y.-J., *The second order Raman spectroscopy in carbon crystallinity.* Journal of Nuclear Materials, 2004. **325**(2-3): p. 174-179.

160. Duesberg, G.S., et al., *Experimental observation of individual single-wall nanotube species by Raman microscopy.* Chemical Physics Letters, 1999. **310**(1-2): p. 8-14.
161. Alvarez, L., et al., *Resonant Raman study of the structure and electronic properties of single-wall carbon nanotubes.* Chemical Physics Letters, 2000. **316**(3-4): p. 186-190.
162. Jorio, A., et al., *Structural (n, m) determination of isolated single-wall carbon nanotubes by resonant Raman scattering.* Physical Review Letters, 2001. **86**(6): p. 1118-1121.
163. Strano, M.S., et al., *Assignment of (n, m) Raman and Optical Features of Metallic Single-Walled Carbon Nanotubes.* Nano Letters, 2003. **3**(8): p. 1091-1096.
164. Reich, S., C. Thomsen, and M. Janina, *Carbon Nanotues: Basic Concepts and Physical Properties.* Wiley-VCH, 2004.
165. Kataura, H., et al., *Optical properties of single-wall carbon nanotubes.* Synthetic Metals, 1999. **103**(1-3): p. 2555-2558.
166. Saito, R., G. Dresselhaus, and M.S. Dresselhaus, *Trigonal warping effect of carbon nanotubes.* Physical Review B, 2000. **61**(4): p. 2981.
167. Doorn, S.K., et al., *Resonant Raman excitation profiles of individually dispersed single walled carbon nanotubes in solution.* Applied Physics a-Materials Science & Processing, 2004. **78**(8): p. 1147-1155.
168. Son, H.B., et al., *Characterizing the chirality distribution of single-walled carbon nanotube materials with tunable Raman spectroscopy.* physica status solidi (b), 2006. **243**(13): p. 3161-3165.
169. Mews, A., et al., *Raman Imaging of Single Carbon Nanotubes.* Advanced Materials, 2000. **12**(16): p. 1210-1214.
170. Anderson, N., A. Hartschuh, and L. Novotny, *Chirality Changes in Carbon Nanotubes Studied with Near-Field Raman Spectroscopy.* Nano Letters, 2007. **7**(3): p. 577-582.
171. Müller, M., et al., *Raman spectroscopy of pentyl-functionalized carbon nanotubes.* physica status solidi (RRL) - Rapid Research Letters, 2007. **1**(4): p. 144-146.
172. Strano, M.S., et al., *Electronic structure control of single-walled carbon nanotube functionalization.* Science, 2003. **301**(5639): p. 1519-1522.
173. Kavan, L., et al., *Electrochemical Doping of Chirality-Resolved Carbon Nanotubes.* The Journal of Physical Chemistry B, 2005. **109**(42): p. 19613-19619.
174. Maruyama, S. *http://www.photon.t.u-tokyo.ac.jp/~maruyama/kataura/kataura.html*.
175. Brown, S.D.M., et al., *Origin of the Breit-Wigner-Fano lineshape of the tangential G-band feature of metallic carbon nanotubes.* Physical Review B, 2001. **63**(15): p. 155414.
176. Piscanec, S., et al., *Optical phonons in carbon nanotubes: Kohn anomalies, Peierls distortions, and dynamic effects.* Physical Review B, 2007. **75**(3).
177. Jorio, A., et al., *G-band resonant Raman study of 62 isolated single-wall carbon nanotubes.* Physical Review B, 2002. **65**(15): p. 155412.
178. Li, Z.R., et al., *Spectroscopic Characteristics of Differently Produced Single-Walled Carbon Nanotubes.* Chemphyschem, 2009. **10**(13): p. 2296-2304.

179. Osswald, S., M. Havel, and Y. Gogotsi, *Monitoring oxidation of multiwalled carbon nanotubes by Raman spectroscopy.* Journal of Raman Spectroscopy, 2007. **38**(6): p. 728-736.
180. DiLeo, R.A., B.J. Landi, and R.P. Raffaelle, *Purity assessment of multiwalled carbon nanotubes by Raman spectroscopy.* Journal of Applied Physics, 2007. **101**(6): p. 064307.
181. Qian, W., et al., *Quantitative Raman characterization of the mixed samples of the single and multi-wall carbon nanotubes.* Carbon, 2003. **41**(9): p. 1851-1854.
182. Dyke, C.A. and J.M. Tour, *Solvent-free functionalization of carbon nanotubes.* Journal of the American Chemical Society, 2003. **125**(5): p. 1156-1157.
183. Sato-Berrú, R.Y., E.V. Basiuk, and J.M. Saniger, *Application of principal component analysis to discriminate the Raman spectra of functionalized multiwalled carbon nanotubes.* Journal of Raman Spectroscopy, 2006. **37**(11): p. 1302-1306.
184. Kim, K.K., et al., *Dependence of Raman spectra G ' band intensity on metallicity of single-wall carbon nanotubes.* Physical Review B, 2007. **76**(20).
185. Ferrari, A.C., et al., *Raman Spectrum of Graphene and Graphene Layers.* Physical Review Letters, 2006. **97**(18): p. 187401.
186. Casiraghi, C., et al., *Raman Spectroscopy of Graphene Edges.* Nano Letters, 2009. **9**(4): p. 1433-1441.
187. Graf, D., et al., *Spatially Resolved Raman Spectroscopy of Single- and Few-Layer Graphene.* Nano Letters, 2007. **7**(2): p. 238-242.
188. Ni, Z.H., et al., *Uniaxial Strain on Graphene: Raman Spectroscopy Study and Band-Gap Opening.* ACS Nano, 2008. **2**(11): p. 2301-2305.
189. Yu, T., et al., *Raman mapping investigation of graphene on transparent flexible substrate: The strain effect.* Journal of Physical Chemistry C, 2008. **112**(33): p. 12602-12605.
190. Bruna, M. and S. Borini, *Observation of Raman G-band splitting in top-doped few-layer graphene.* Physical Review B. **81**(12): p. 7.
191. Lin, Y.C., C.Y. Lin, and P.W. Chiu, *Controllable graphene N-doping with ammonia plasma.* Applied Physics Letters, 2010. **96**(13).

Chapter 3

Experimental Methods

This chapter gives an overview of the materials preparation, growth furnaces and analysis techniques used in this thesis.

3.1 Catalyst Preparation

This section outlines the different deposition techniques used to prepare catalyst films for CVD growth of CNTs and graphene. The use of nanosphere lithography to create patterned catalysts is also described.

3.1.1 Metal Deposition

Thin metallic catalyst films were prepared by a number of different physical deposition methods. These were deposited on SiO_2 (300 nm) on Si substrates. A layer of Al_2O_3 was first deposited for SWNT catalysts. Typically deposition thicknesses were 3 nm for MWNT catalysts and < 1 nm for SWNT catalysts. The following section will give a brief overview of these techniques and provide details on the apparatus and conditions used.

Pulsed Laser Deposition (PLD)

The PLD process takes place in an ablation chamber and involves an excimer laser striking a metal target forming a plasma plume, which then deposits onto a substrate [1-2]. A schematic of this apparatus is shown in Figure 3.1.

Fe films were prepared using this method in collaboration with the laser and plasma applications group in Trinity College Dublin. Vacuum conditions were used which typically entailed a pressure of 6 x 10^{-5} mbar. The laser used was a 248 nm KrF laser with a pulse width of 26 ns, a repetition rate of 10 Hz and a fluence of 1 Jcm^{-2}. The deposition was controlled using a quartz crystal microbalance (QCM) to monitor thickness and an ion probe to ensure plasma reproducibility. The QCM measures the

change in the resonant frequency of a piezoelectric upon material deposition. This change is related to the mass and hence thickness of the material deposited through the Sauerbrey equation[3].

The area of uniform deposition for this setup was approximately 2.5 cm^2 and so the number of catalyst substrates produced per run was very small.

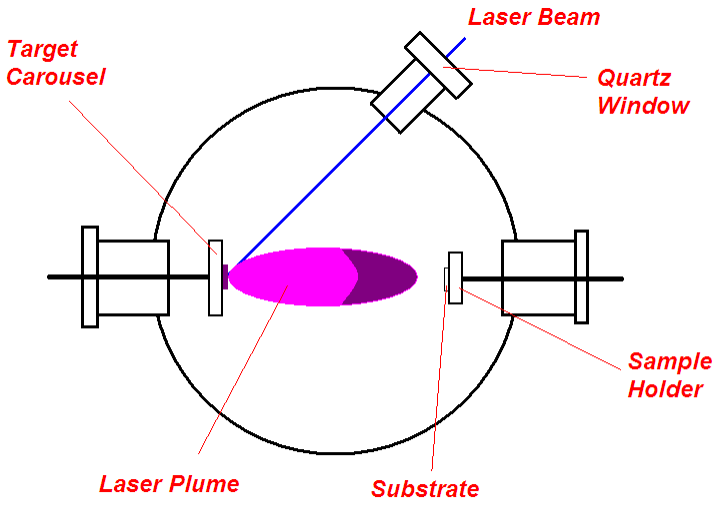

Figure 3.1 *Schematic diagram of PLD setup.*

Thermal Evaporation

Thermal evaporation involves heating a metal source so that it evaporates onto an unheated substrate placed above it. This is carried out under vacuum conditions to ensure molecular flow. The heating can be applied through resistive means (current applied across a filament/boat) or by using an electron beam to heat the source directly.

An Auto Edwards 306 resistive heating thermal evaporator was used to prepare thin metal films. A schematic of this apparatus is shown in Figure 3.2. Metallic pellets (Fe/Co) or wire (Ni) were used as the source material and Tungsten boats were used as the heating elements. The chamber was pumped out to a pressure of ~ 2 x 10^{-6} mbar by a diffusion pump backed by a rotary pump. A current of ~2 A was used across the boat to evaporate the metal. This gave a steady controllable deposition rate in the case of wires (Ni), however for pellets (Fe/Co) the initial deposition rate when the pellet melted was too high for the production of very thin films. A QCM was used to control the thickness deposited. Uniform deposition was possible over an area of ~ 16 cm^2.

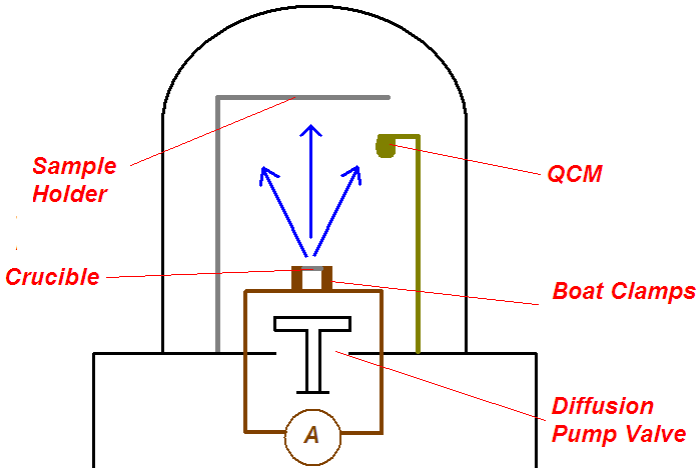

Figure 3.2 *Schematic diagram of thermal evaporator based on resistive heating.*

Sputter Coating

A standard sputter coating setup consists of a chamber under vacuum with a target material attached to a cathode placed opposite a deposition substrate. A well defined pressure of Ar is introduced into the chamber. Free electrons are accelerated away from the cathode and collide with the Ar atoms forming Ar^+ ions. The ions in turn are then attracted towards the cathode where they collide with the target liberating target atoms and further electrons. These electrons further fuel the formation of Ar^+ ions and the target atoms are deposited on the substrate.

Magnetron sputtering offers improvements by placing a magnet behind the cathode. This creates a magnetic field which traps free electrons above the target. This prevents stray electrons from bombarding the deposition substrate. Furthermore the induced helical trajectory enhances Ar ionisation probability and endows the Ar ions with a high kinetic energy.

Catalyst films were prepared using a number of different sputtering systems including a Cressington HR coating system for small substrates and a wafer scale DC magnetron system for larger samples. Typical deposition conditions involved a pressure of 1.3×10^{-3} mbar and a power of 100 W which lead to a deposition rate of 0.1 nm s^{-1}. This allowed for fine control of the thickness deposited which was measured using a QCM.

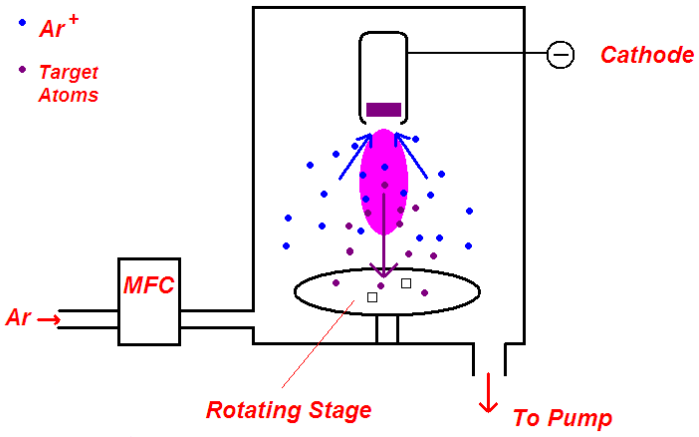

Figure 3.3 *Basic schematic of sputtering apparatus*

3.1.2 Nanosphere Lithography

Nanosphere lithography (NSL) was used for patterning catalyst dots for CNT growth and also to form shadow masks for plasma etching. Polystyrene nanospheres of different diameters (202 nm and 362 nm) were purchased from polysciences Inc. Monolayers of these spheres were prepared on different substrates using a modified version of the procedure described by Hulteen et al[4]. This involved further diluting the purchased sphere solutions on a 1:1 basis with a 400:1 solution of methanol:triton x-100. The surfactant was used for enhanced wetting of substrates.

For the preparation of catalyst dots SiO_2 substrates were cut into pieces 1 cm^2 in area and then cleaned with a base piranha solution (5:1:1, H_2O:NH_4OH:H_2O_2). The nanosphere solution was then drop cast (2 µL) or spin coated (10 µL) onto the SiO_2 substrates to create a monolayer over large portions of the substrates. After the solution had dried metals were deposited in the interstitial sites by physical deposition methods. The perpendicular bisector of the particle formed (a) and the interparticle spacing (i) are related to the diameter (d) of the spheres used by the following relationships.

$$a = \frac{3}{2}\left(\sqrt{3} - 1 - \frac{1}{\sqrt{3}}\right)d = 0.233d \qquad \textit{Equation 3.1}$$

$$i = \frac{d}{\sqrt{3}} = 0.577d \qquad \textit{Equation 3.2}$$

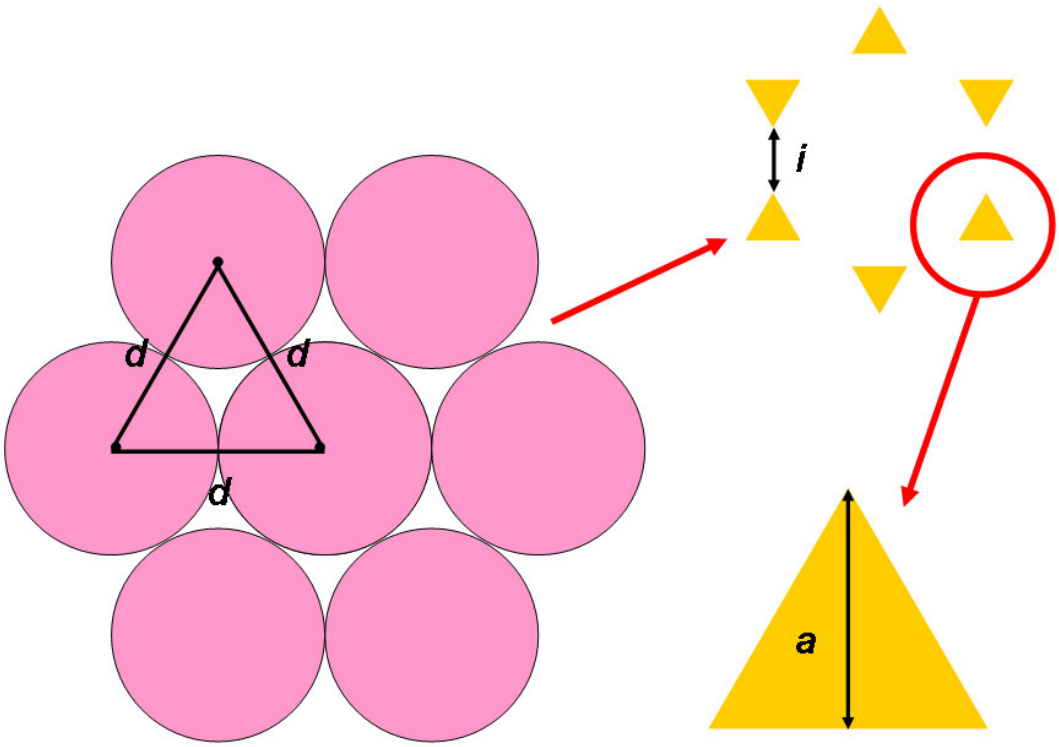

Figure 3.4 *NSL monolayer with metal deposited at interstitial sites. Sphere diameter (d), perpendicular bisector of nanoparticle (a) and inter-particle spacing (i) are highlighted.*

Measured values are shown in Table 3.1 for Au and Ni particles prepared using 362 nm spheres. The spheres were removed from substrates by mild sonication in dichloromethane (DCM).

Au Nanoparticles	***a* (nm)**	***i* (nm)**
Measured	*103*	*159*
Predicted	*84.35*	*208.87*
Ni Nanoparticles	***a* (nm)**	***i* (nm)**
Measured	*97*	*167*
Predicted	*84.35*	*208.87*

Table 3.1 *Measured and predicted values for perpendicular bisector and inter-particle spacing of Au and Ni particles prepared by NSL.*

3.2 CVD Furnaces

The use of CVD processes to produce CNTs and other materials was discussed in chapter 2; as such, this section will only consider the equipment used in this thesis.
Two different CVD setups were used for the growth presented in this work. These are referred to as the Lindberg and Gero systems and are named in accordance with the furnaces at the centre of each system. The following section describes the systems and outlines their differences.

3.2.1 Lindberg Furnace CVD System

This setup was based around a Lindberg blue mini-mite horizontal tube furnace. This is a compact furnace with exterior dimensions of 38.1 cm x 27.9 cm x 40.6 cm allowing for bench top setup. The maximum operating temperature was 1100 ^{o}C and the heating zone had a length of ~ 25 cm. The furnace was fitted with a hinge and could be opened up for fast cooling.

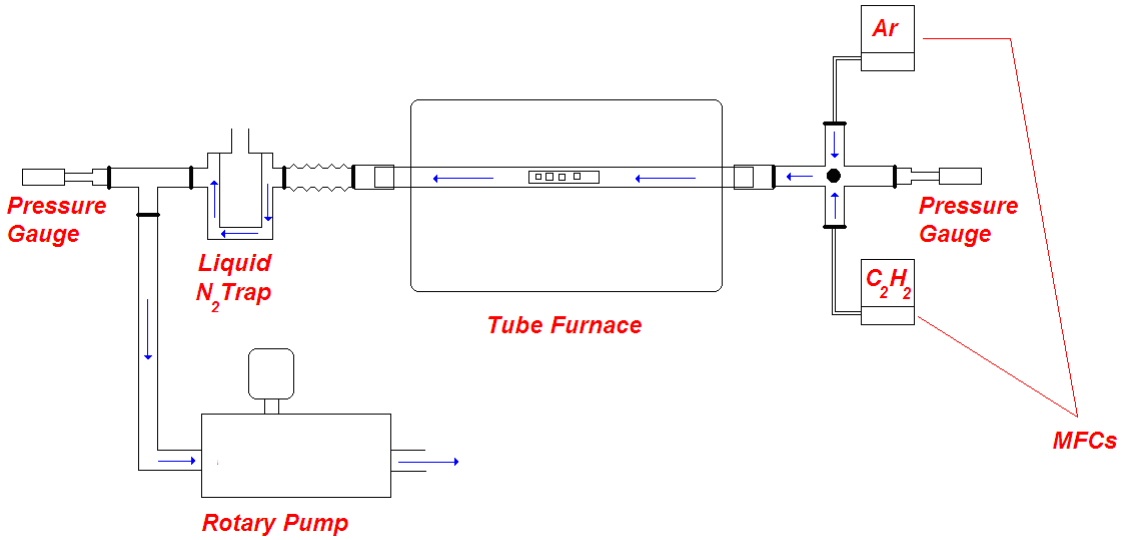

Figure 3.5 *Schematic diagram of Lindberg furnace CVD setup.*

The furnace was fitted with a quartz work tube with an outer diameter of 2.54 cm and length 1 m. Samples were placed in the centre of this tube, typically in ceramic boats. This region thus could be considered as the reaction chamber. Process gases were directed into the reaction chamber using a combination of stainless steel tubing, KF fittings and mass flow controllers (MFCs). The MFCs used were MKS 1479 units

controlled by a central controller (MKS digital supply and readout type PR4000A). The principal component of these MFCs is a small tube with resistance and thermometer elements. A small proportion of the gas flows through this tube and is heated by the elements. The measured temperature differential is dependent on the gas flow; this is converted into a voltage signal which drives a control valve.

The system consisted of two MFCs connected to Ar and C_2H_2 gas lines; these were calibrated for flow rates in the range 100 – 50000 sccm and 10 – 5000 sccm respectively. The layout of the setup prohibited further gas lines being added to the system.

An Edwards RV12 single phase rotary vane pump was used to evacuate ambient gases from the reaction chamber; this has a maximum vacuum of 1×10^{-3} mbar but was typically used to pump the reaction chamber to a pressure of 2×10^{-2} mbar (1.5×10^{-2} Torr). The system was fitted with a liquid N_2 cooled trap before the pump for trapping debris (particularly from powder based samples) before it reached the pump. Pirani gauges were located at either end of the system to ensure uniform pressure and also for leak checking.

3.2.2 Gero Furnace CVD System

This setup was based around a Gero F-series tube furnace. The furnace had exterior dimensions of 50 cm x 120 cm x 84 cm; furthermore it included a separate controller unit with dimensions 56 cm x 50 cm x 40 cm, thus making it a far bulkier system than the Lindberg. The maximum operating temperature was 1350 ^{o}C and the heating zone had a length of 50 cm.

The furnace was fitted with a quartz work tube with an outer diameter of 10 cm and a length of 65.5 cm. Quartz rails were placed in the centre of the heated zones and samples could be placed in this region by putting them on a quartz shovel which was then propped up on the rails. This shovel allowed for larger samples than those possible in the Lindberg furnace and also made sample loading and unloading much easier allowing for a higher sample throughput.

Like the Lindberg setup, process gases were introduced into the reaction chamber using stainless steel tubing, KF fittings and mass flow controllers; however there were some notable differences. Firstly, the geometry of the inlet allowed for the incorporation of up to five process gases in any run greatly extending the growth recipes possible. The

default configuration had C_2H_2, CH_4, Ar, N_2 and H_2 lines but this could be easily altered. This setup involved the use of five manual gas flow valves located ahead of the sample inlet as shown in Figure 3.7 and also included a rough pressure gauge.

Another advantage of the Gero setup was the availability of H_2 for one of the gas lines. As mentioned previously, the number of gas lines connected to the Lindberg setup was restricted; however, a H_2 generator was readily incorporated into the Gero setup. This produced high purity H_2 by electrolysis without any of the safety concerns associated with a H_2 cylinder. H_2 acts as a strong reducing agent and is important in many CNT growth recipes and other CVD processes.

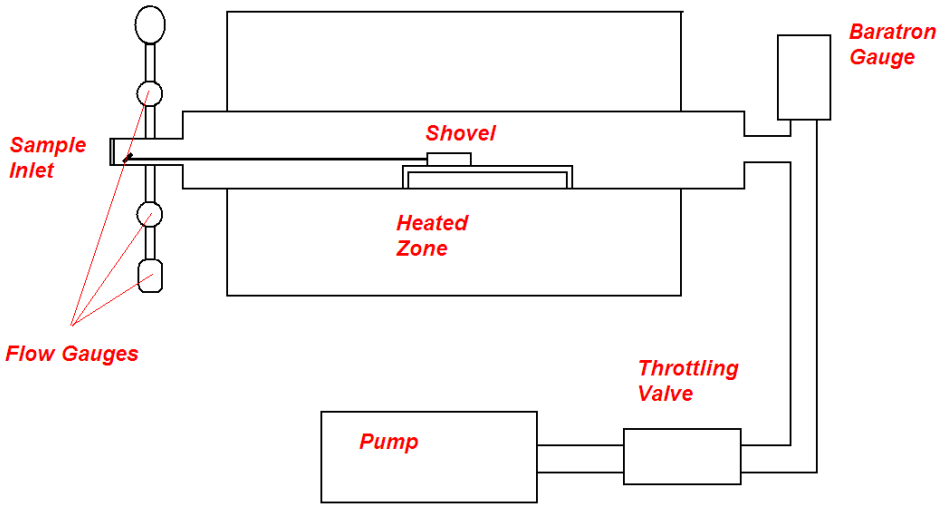

Figure 3.6 *Schematic diagram of Gero furnace CVD setup.*

The system was evacuated using a Leybold Trivac rotary vane pump. The reaction chamber was typically evacuated to a pressure of <10 mTorr (1.3 x 10^{-2} mbar) before the introduction of any process gases. The pressure was monitored using a baratron gauge and the operating capacity of the pump was controlled using a throttling valve. These were both connected to a MKS 655A controller which allowed for growth to be carried out at defined pressures for different gas flow rates.

Overall the Gero system offered a number of advantages over the Lindberg system: a comparison of some of the key features is shown in Table 3.2.

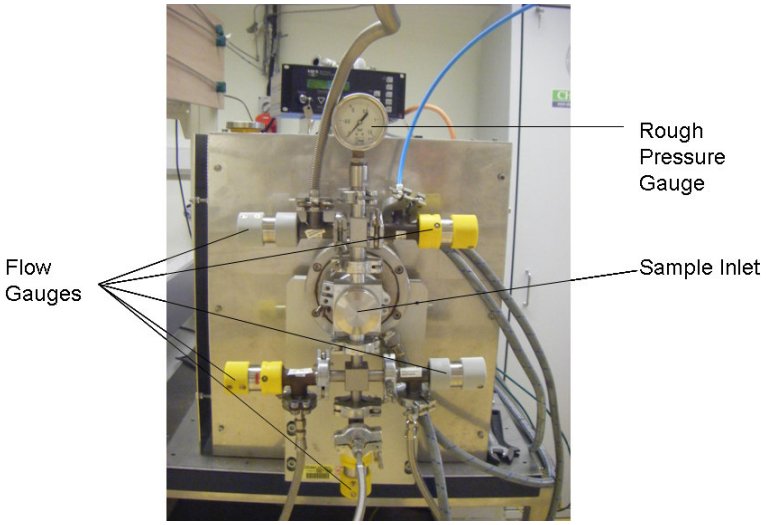

Figure 3.7 *Front of Gero setup showing loading area and gas lines.*

	Lindberg	**Gero**
Max Temperature	*1100 °C*	*1300 °C*
Heating Zone	*25 cm*	*50 cm*
Furnace Dimensions	*38 cm x 28 cm x 41 cm*	*50 cm x 120 cm x 84 cm*
Reactor Volume	*430 cm^3*	*1625 cm^3*
Work Tube Diameter	*2.54 cm*	*10 cm*
Maximum Sample Size	*~1 cm^2*	*~ 3 x 3 cm*
Base Pressure	*~ 2 x 10^{-2} mbar*	*~1.3 x 10^{-2} mbar*
Flow Control	*MFCs*	*Manual Flow Valves*
Number of Gas Lines	*2*	*5+*
H_2	*No*	*Yes*
Pressure Gauge	*Pirani*	*Baratron*
Pressure Control	*No*	*Yes – Throttling Valve*
Cooling Rate	*Fast*	*Slow*

Table 3.2 *Comparison of the Lindberg and Gero CVD setups.*

3.3 Plasma Treatment

A plasma can be described as an assembly of ions, neutral atoms and electrons which exhibit collective effects. These can be formed by ionising a specific proportion of molecules in a gas at specific pressures. Plasmas can carry electrical currents and generate magnetic fields.

Sputter coating as described in section 3.2.1 involves the use of an Ar plasma to dislodge atoms from a target. Plasmas have many other uses including etching, functionalisation, displays and PECVD.

Plasma treatment of films was carried out using a R^3T TWR 2000T microwave radical generator. This system had a maximum operating power of 2000 W (at 2.450 GHz) and a pressure range of 0.3 – 5.0 Torr. O_2, H_2, N_2 and Ar remote plasmas were generated using the same gas lines as those used in the Gero CVD setup. Gas flows were controlled using a series of MKS MFCs connected to a custom built controller. An Edwards rotary vane pump was used to evacuate the chamber.

O_2 plasmas were used for etching and functionalising a series of different nanocarbon films. Typical treatment conditions involved O_2 flows rates in the range 10 – 50 sccm and plasma powers of 300-1000 W.

3.4 Analysis Techniques

This section describes the different techniques used to characterise the samples produced in this work. These include electron and probe microscopies, spectroscopic techniques and electrical characterisation.

3.4.1 Raman Spectroscopy

The fundamental principals of Raman spectroscopy were covered in chapter 2 so this section will only be concerned with instrumentation.

The majority of Raman spectra in this thesis were obtained using a Jobin Yvon Labram HR. This system is based on 180^o scattering. That is, laser light is delivered through a collector lens and scattered light is then directed back through it. The scattered light is passed through a notch filter which removes the majority of Rayleigh scattered contributions. The radiation is then directed to a monochromator which separates out different energies of Raman scattered light which are then focused on a charge coupled device (CCD) detector.

A HeNe laser with excitation wavelength of 632.8 nm was used for most scans; this has a maximum power of 12 mW and was used with a diffraction grating with 600 lines/mm. A 100x long working distance objective lens was used giving a spatial

resolution of 3 – 5 μm. The instrument has a quoted resolution of 0.3 cm^{-1} when properly calibrated. In practice the lower cut-off afforded by the notch filter was ~100 cm^{-1}.

Acquisition times and cycles were set so that peaks of interest had a high signal to noise ratio and high overall intensity. Where possible, at least five spectra were taken per sample to establish the degree of uniformity. The system was calibrated using a Si reference before use. A small number of spectra were taken using a similar spectrometer with 473 nm and 785 nm excitation wavelengths.

Raman mapping was performed on a Renishaw inVia Raman microscope. This also involved a HeNe 632.8 nm excitation wavelength. Maps were taken over area up to 100 x 100 μm^2 with scans taken in steps of < 500 nm in the x any y direction.

3.4.2 X-ray Photoelectron Spectroscopy (XPS)

XPS involves measuring the energy of core level electrons emitted from a sample irradiated with an x-ray beam under UHV conditions. When a photon of energy *hv* penetrates the surface of a sample it is absorbed by a core electron of binding energy E_B. This electron is then emitted into the vacuum with a kinetic energy (E_K) given by;

$$E_K = h\nu - E_B - (E_{vac} - E_F) \qquad \textit{Equation 3.3}$$

where E_{vac} and E_F are the vacuum and Fermi levels respectively.

Thus, the energy distribution of the emitted electrons can be directly correlated with the electron states in the surface of the sample being probed. An XPS spectrum consists of a plot of binding energy versus intensity. Different elements show different spectral "fingerprints" allowing XPS to probe and identify the elemental composition of the surface. Furthermore, the binding energy varies for electrons in the same elemental core due to factors like the valence of the atom and the local chemical and physical environment. These variations are manifested on an XPS spectrum in the form of

chemical shifts and imbue the technique with the ability to distinguish between atoms of the same species in different environments.

All XPS measurements in this thesis were performed by Dr. Nikos Peltekis of the ASIN group, CRANN, Trinity College Dublin. An Omicron ESCA system was used with an EA 125 Analyser and XM1000MK II monoenergetic x-ray source. The Al $K\alpha$ x-ray source gave a 2 mm x-ray spot. The analyser was operated with a pass energy (E_p) of 50 eV for wide scans and 20 eV for fine scans leading to an instrumental resolution of ~ 1.25 eV for the wide scan and 0.65 eV for the fine scans.

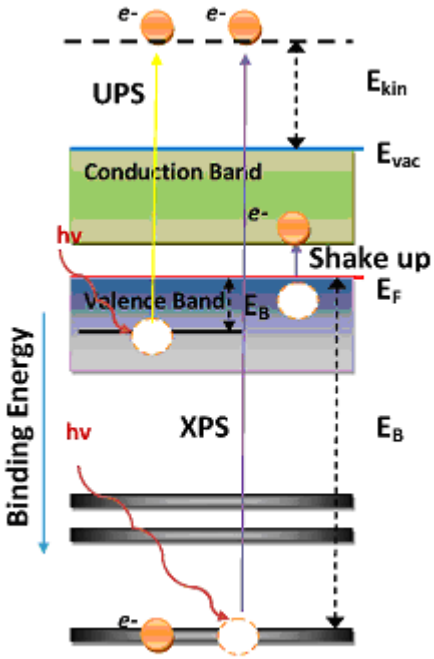

Figure 3.8 *Schematic of core level electron emission probed by XPS*

3.4.3 UV-Vis-NIR Absorption Spectroscopy

When radiation interacts with molecules if the energy of the radiation is close to that of molecular electronic transitions the light can be absorbed by the molecule. Absorption spectroscopy involves measuring the portion of radiation absorbed by a sample as a function of the radiation frequency. This is typically carried out by scanning over a range of frequencies. UV and visible and near-IR light are used as their energies

correspond to promotion of electrons from the highest occupied molecular orbital (HOMO) to the lowest unoccupied molecular orbital (LUMO).

The transmittance, *T*, can be defined as the ratio of the transmitted to incident light intensity and is described by the Beer Lambert equation.

$$T = \frac{I}{I_0} = e^{-\alpha l} \qquad \textit{Equation 3.4}$$

where I and I_0 are the incident and transmitted intensities respectively, l is the path length and α is the absorption coefficient.

Transmittance measurements were carried out on thin films using a Cary Varian 6000i UV-Vis-NIR spectrometer. This gave information on the portion of light absorbed in the range 200 – 1800 nm.

3.4.4 Electron Microscopy

Scanning electron microscopy (SEM) uses a focused and accelerated beam of electrons for imaging and analysis at a resolution far beyond that possible with light microscopy.

A basic SEM schematic is shown in Figure 3.9. Electrons are emitted from a filament by cold field emission or thermal field emission depending on the type of filament used. The electrons are accelerated by an anode and condensed by a lens (or series of lenses) which reduce the spot size to a couple of nm. The beam is rastered across the sample by varying the current in coils in the x and y direction. The entire setup is kept under vacuum to ensure that a sufficient portion of the electron beam reaches the sample.

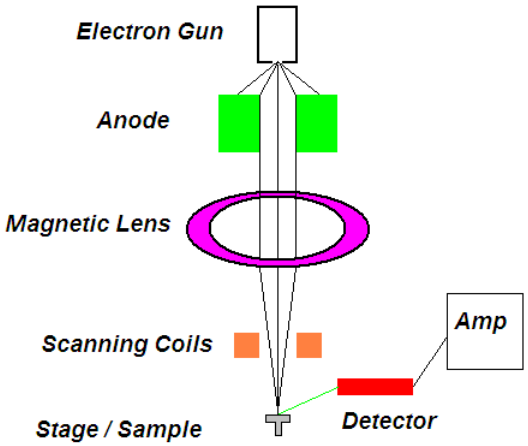

Figure 3.9 *Basic schematic diagram of SEM system.*

When the beam of electrons interacts with a sample it can undergo different scattering events forming secondary products. These scattering events occur in an interaction volume which has a pear like shape due to broadening. The exact size and shape of this depends on the accelerating voltage of the electron beam and the constituent materials in the sample being probed. The two primary types of electrons involved in SEM imaging are secondary electrons (SE) and backscattered electrons (BSE). Collectors are positioned in different parts of the system to selectively collect these different types of electrons. These collectors have a scintillator layer which generates flashes when hit by electrons; these flashes are directed towards a photomultiplier tube and then converted into an electrical signal.

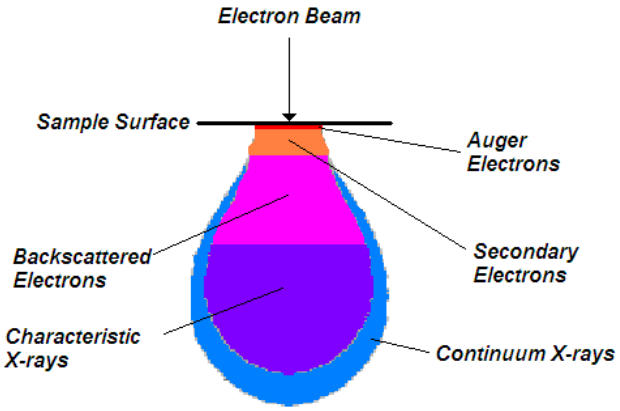

Figure 3.10 *Diagram of electron interaction volume illustrating the depth of secondary and backscattered electrons.*

Secondary electrons are produced by inelastic scattering between the incident electrons and the material being imaged. These are low energy electrons (< 50 eV) with a small mean free path and so stem from regions near the surface of the material (a few nm deep). Because of this SE images give good topographical information. Higher energy electrons are classed as backscattered electrons (BSE) and are produced by elastic collisions deeper in the interaction volume. BSE carry information on chemical composition as materials with higher atomic numbers are better scatterers and thus appear brighter on BSE images.

The incident electron beam can also cause the material being probed to emit characteristic X-rays. This occurs when an incident electron knocks an electron from the inner-shell of the specimen material creating a hole which is subsequently filled by an electron from a higher shell. The difference in energy between the higher and lower energy levels can be emitted in the form of an X-ray which carries information on chemical composition. The probing of these X-rays is known as energy dispersive X-ray spectroscopy (EDX) and requires a further specialised detector inside the SEM apparatus.

The majority of SEM analysis in this work was carried out on a Zeiss Ultra Plus FE SEM. This is fitted with in-lens and Everhardt Thornley detectors for SE imaging and an energy and angle selective detector for BSE imaging. Samples were mounted on carbon tabs and typically imaged with an accelerating voltage of 1-5 kV. The SEM was also fitted with an INCA system from Oxford instruments for EDX analysis. A number of samples were imaged using a Hitachi S4300 FE SEM under similar conditions (but without an in lens detector)

Transmission electron microscopy (TEM) operates in a similar manner to SEM but rather than collecting backscattered and secondary electrons, the electrons transmitted through a sample are used to form the image. Ultrathin samples with a high degree of electron transparency are required for this. As the electrons must pass through the sample to form an image the accelerating voltages used are higher than those used for SEM imaging.

TEM measurements were carried out on a JEOL-JEM 2100 system. Samples were prepared by dropping ~μL of dispersions onto 400 mesh holey carbon grids from Agar. These were imaged using an accelerating voltage of 200 kV and a beam current of ~ 105 μA.

3.4.5 Atomic Force Microscopy

Atomic force microscopy (AFM) is a very high resolution probe technique with a sub-nanometre resolution. A basic schematic of an AFM is shown in Figure 3.11. The probe consists of a microscale cantilever of known spring constant with a nanoscale tip attached to its end. When the tip is brought within atomic level distances of the sample being probed it experiences strong repulsive forces due to orbital overlap. These forces cause deflection of the cantilever in accordance with Hooke's law. The deflection is measured indirectly using a laser which is shone on the back of the cantilever. The reflected beam is projected onto a stage of photodiodes, the output of which can be converted back into cantilever deflection by processing software.

Samples are mounted on a piezo tube which moves the sample in the x and y direction. Scanning in these directions, whilst measuring the cantilever deflection, gives a 3D map of the sample.

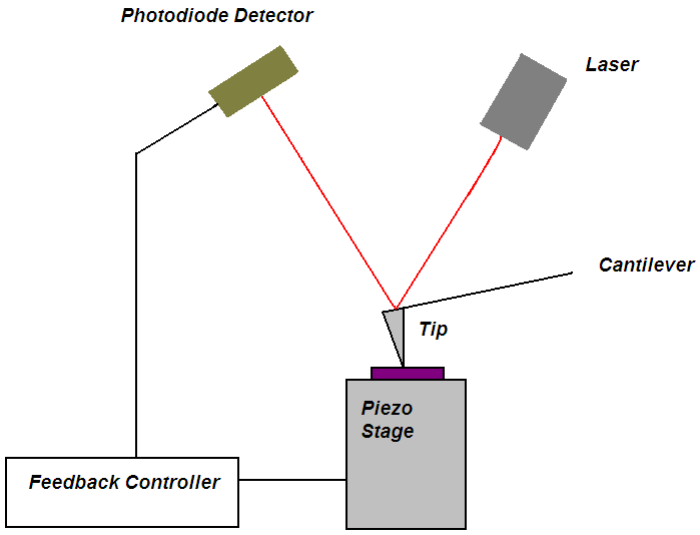

Figure 3.11 *Basic schematic diagram of AFM apparatus.*

The most common modes of AFM used are contact and tapping mode. Contact mode involves dragging the tip across the surface of the sample. A feedback loop maintains a constant cantilever deflection by adjusting the cantilever-sample distance. Lateral forces between the tip and substrate are incredibly strong and the constant contact between tip and sample can lead to tip damage (and resulting tip artefacts). Because of these problems tapping mode is more commonly used. However, extensions of contact

mode, including AFM lithography and nanoindentation have gained popularity in recent years.

In tapping mode the tip is oscillated at its resonant frequency (with an amplitude of ~100 nm) so that it is only in contact with the sample for a small proportion of the scan time. This means that the tip experiences less shear force and is less likely to become damaged or dirty. Constant oscillation amplitude is maintained by a feedback loop which in turn provides information on tip-sample interactions.

In general AFM is far more sensitive to changes in the z direction than those in the x and y directions; this is due to a phenomenon known as tip convolution. If the tip has a radius of curvature comparable with or larger than features being examined the resulting image will be broadened: this is because the sides of the tip interact with the sample as well as the apex. This effect can be minimised by using tips with a very small radius of curvature. A similar but more serious effect is sometimes observed with dirty tips. Double tipping occurs when a piece of debris attached to the tip acts as a second tip, this results in the formation of a second image which is superimposed with an offset on top of the original.

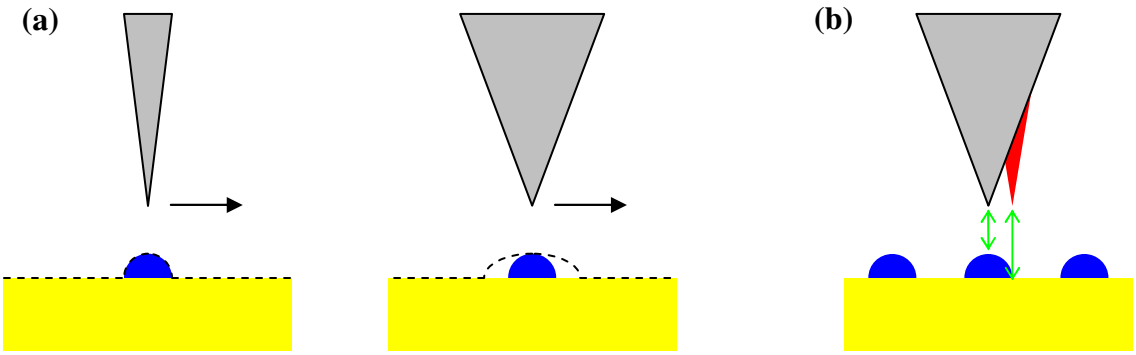

Figure 3.12 *Diagrams illustrating (a) tip convolution and (b) double tipping effects*

In this work a Digital Instruments multimode SPM with a Nanoscope IIIa controller was used. This was operated in tapping mode to image CNT catalysts and other thin films. The probes used were fabricated from Si and consisted of a cantilever 125 μm in length with a resonant frequency of 320 kHz. The tip had a height of 10 μm and a radius < 8 nm. Processing software allowed for the calculation of the average (R_a) and the root mean square (R_q) roughness of films.

$$R_a = \frac{1}{n}\sum_{i=1}^{n}|y_i| \qquad \textit{Equation 3.5}$$

$$R_q = \sqrt{\frac{1}{n}\sum_{i=1}^{n} y_i^2} \qquad \textit{Equation 3.6}$$

3.4.6 Profilometry

The thicknesses of films (PyC predominantly) on SiO_2 substrates were measured using a Dektak 6M profilometer. The profilometer operates in a similar manner to an AFM in contact mode but on a larger scale. A stylus is brought into contact with a substrate and then gently dragged across the surface. Changes in the sample height are then recorded by a feedback loop allowing values for step heights and roughness to be obtained. The manufacturer specified measurement accuracy is 1 nm; however considerations such as noise mean that it is somewhat higher in practice (~3 nm).

The procedure for film thickness measurements entailed using a fine blade to expose the underlying substrate (without digging into the substrate itself) and then running the profilometer stylus across the exposed region to give the film height. At least ten measurements were made in different regions for each sample investigated.

3.4.7 Electrical Measurements

In a regular three dimensional conductive material the resistance (R) is given by the formula;

$$R = \rho\frac{L}{A} = \rho\frac{L}{Wt} \qquad \textit{Equation 3.7}$$

where ρ is the resistivity, L is the length, W is the width and t is the thickness.

When working with uniform thin films it is convenient to group the resistivity and thickness together in what is known as the sheet resistance, R_s.

$$\rho = R_s t \qquad \textit{Equation 3.8}$$

$$R = \frac{\rho}{t}\frac{L}{W} = R_S \frac{L}{W}$$ *Equation 3.9*

This has the same dimensions as resistance but is generally expressed in terms of ohm/square (Ω/□) to avoid confusion with bulk resistance.

The majority of electrical measurements in this work were four point probe sheet resistance measurements on thin films. These were carried out using a Jandel four point probe head connected to a Keithley 2400 sourcemeter.

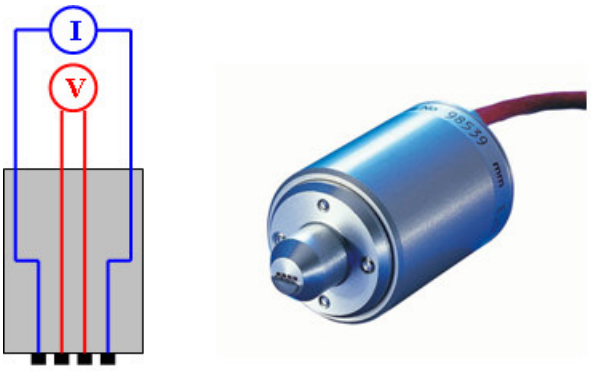

Figure 3.13 *Four point probe head.*

The Jandel head consists of four collinear probes with a radius of 100 μm and a spacing of 1 mm. The head is mounted and brought into contact with films so that all four probes make good contact with the film. The voltage is measured across the inner two probes and the current is measured across the outer probes. The sheet resistance R_s is then given by the formula;

$$R_S = \frac{V}{I} \times CF$$ *Equation 3.10*

CF is a correction factor which depends on the dimensions of the sample being probed and the inter probe spacing. For samples with thicknesses much less than the spacing between probes and lateral dimensions much larger than the spacing between probes a correction factor of (π/ln2) is suitable[5].

References

1. Dolbec, R., et al., *Growth dynamics of pulsed laser deposited Pt nanoparticles on highly oriented pyrolitic graphite substrates.* Physical Review B (Condensed Matter and Materials Physics), 2004. **70**(20): p. 201406-4.
2. Donnelly, T., et al., *Pulsed laser deposition of nanoparticle films of Au.* Applied Surface Science, 2007. **254**(4): p. 1303-1306.
3. Sauerbrey, G., *Verwendung von Schwingquarzen zur Wägung dünner Schichten und zur Mikrowägung.* Zeitschrift für Physik A Hadrons and Nuclei, 1959. **155**(2): p. 206-222.
4. Hulteen, J.C. and R.P. Van Duyne, *Nanosphere lithography: A materials general fabrication process for periodic particle array surfaces.* Journal of Vacuum Science & Technology A: Vacuum, Surfaces, and Films, 1995. **13**(3): p. 1553-1558.
5. Smits, F.M., *Measurement of sheet resistivities with four-point probe.* Bell System Technical Journal, 1958. **37**(3): p. 711-718.

Chapter 4

CVD Growth of Carbon Nanotubes

4.1 Introduction

The growth of carbon nanotubes by CVD is probably the most promising production technique, as it is scalable and allows for growth at predefined locations. Many different catalyst systems and growth recipes are possible depending on the type of nanotubes desired. This chapter presents results on the growth of MWNTs and SWNTs as thin films and forests. The effects of varying the catalyst type, catalyst thickness, growth temperature, growth pressure, gas flow rates and the growth furnace used have been investigated.

The growth process entails introducing thin catalyst films into the growth furnace at high temperatures. Upon annealing catalyst nanoparticles are formed by coagulation. Growth is achieved by passing a precursor gas over these nanoparticles. Important considerations include catalytic efficiency, generation of radicals from the precursor and adhesion of the catalyst to the substrate.

4.2 MWNT Growth

MWNTs consist of a series of concentric graphitic tubes and grow from larger catalyst particles than those used for the growth of SWNTs. Suitable catalyst particles can typically be produced using films with thicknesses greater than 1 nm.

A number of different catalyst systems were investigated for MWNT growth. Pulsed laser deposition was used to produce Fe catalysts on native oxide Si substrates. MWNTs of different types were grown on these catalysts through tuning of the growth conditions.

The use of a thin Ta layer between the substrate and catalyst was proposed for the production of MWNT forests on conducting substrates. Growth conditions for this setup were modified in order to obtain aligned forests of high quality nanotubes.

The use of nanosphere lithography to create defined catalyst sites was also considered.

4.2.1 MWNT Growth on PLD Films

4.2.1.1 Growth on PLD Films: Lindberg System

Initial MWNT growth was carried out in the Lindberg CVD system using Fe catalyst films prepared on native oxide Si (<100>) substrates (~ 1 cm^2 in area) by pulsed laser deposition (PLD) [1-3]. The advantage of PLD over other physical deposition methods lies in the high kinetic energy of the generated species which result in a superior adhesion.

Vacuum conditions were used for PLD catalyst preparation with a typical pressure of 6 x 10^{-5} mbar. The laser used was a 248 nm KrF laser with a pulse width of 26 ns, a repetition rate of 10 Hz and a fluence of 1 J/cm^2. The deposition was controlled using a quartz crystal monitor to measure film thickness and an ion probe to ensure plasma reproducibility.

Prior to CVD growth the nanoparticle films were characterised by atomic force microscopy (AFM). These AFM images give an indication of the size, distribution and morphology of the nanoparticle films (see Figure 4.1). A uniform distribution of well defined catalyst nanoparticles was observed. In comparison, sputtered and evaporated films would not be expected to produce such well defined nanoparticles without a subsequent annealing step. A mixture of C_2H_2 and Ar was used for growth. The active gas flow rate and growth temperature were varied to produce films or forests of MWNTs of varying quality, under typical growth pressures of 5 – 10 mbar.

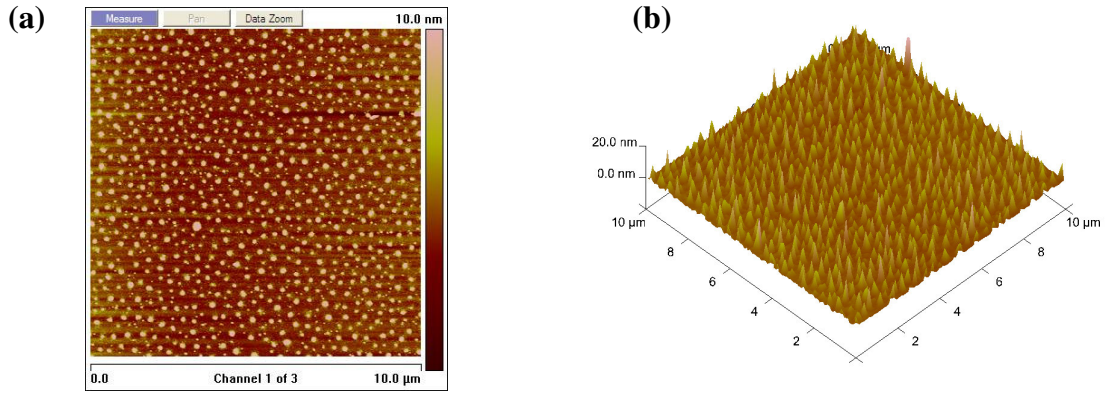

Figure 4.1 *Typical AFM image of 5 nm Fe PLD film showing metallic islands with measured values of roughness R_a = 1.4 nm, R_q = 2.3 nm. (a) Top down view (b) 45 ^{o} pitch. Scale is 10 x 10 µm.*

Greater surface coverage was observed with increasing active gas flow times; however more interesting results were produced by varying the active gas flow rate. Using a 50 sccm flow of C_2H_2 a mat of carbon nanotubes was formed on the substrate (Figure 4.2(a)). In the case of a 300 sccm flow of C_2H_2 long entangled arrays ~20 μm in height grew perpendicular to the substrate surface (Figure 4.2(b)). This increase in growth rate with increasing active gas flow rate is consistent with results reported by other groups[4]. A growth rate of 4 μm/min was implied assuming linear growth (without catalyst poisoning). In both cases SEM images indicated nanotube diameters in the range 25 – 30 nm.

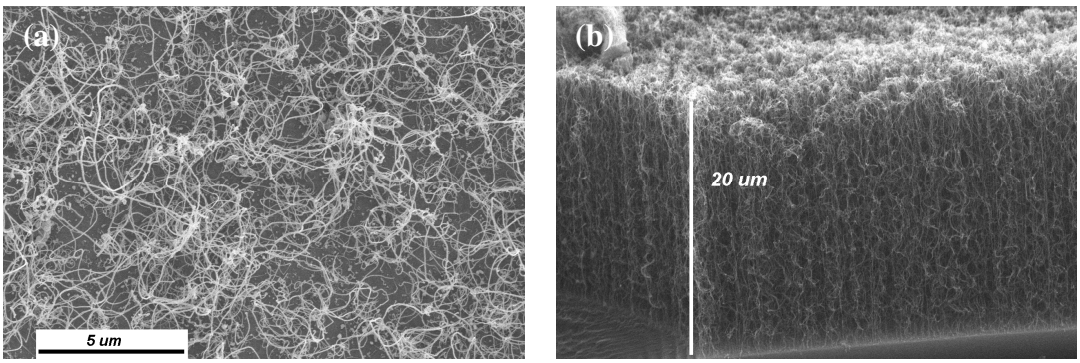

Figure 4.2 *SEM images of MWNTs grown on 5 nm thick Fe PLD films with (a) 50 sccm flow of C_2H_2 (scale bar 5 μm) and (b) 300 sccm flow of C_2H_2 (scale bar 20 μm). Both samples were grown at 700 ^oC with a growth time of 5 minutes.*

Increasing the growth temperature had a significant effect on the quality of nanotubes produced. Raman spectroscopy indicated a linear decrease in I_D/I_G with increasing growth temperature indicating a greater crystallinity at higher temperatures (Figure 4.3).

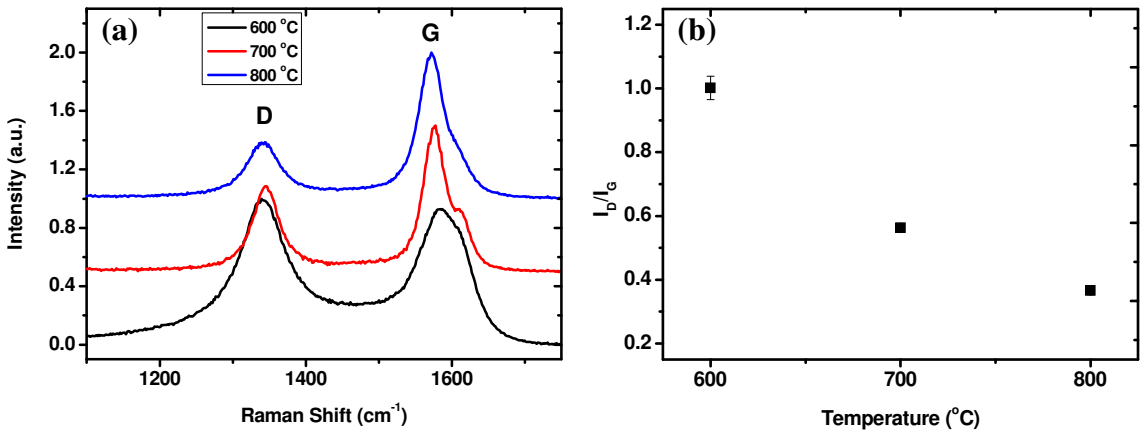

Figure 4.3 *(a) Raman spectra for different growth temperatures showing a decrease in the D band with increasing temperature. (b) Decrease in I_D/I_G is highlighted.*

4.2.1.2 Hydrogen Assisted MWNT Growth

The Gero tube furnace CVD system, used for the majority of growth processes in this thesis, offers a number of advantages over the Lindberg furnace used for growth in the previous section. Perhaps the most important of these is the incorporation of additional gas lines in the CVD setup, in particular a H_2 line. The addition of H_2 to nanotube growth recipes has been shown to enhance the growth; this can be attributed to H_2 reducing the catalyst material[5]. Hofmann et al. verified this using XPS and real time TEM to monitor the growth of CNTs on Fe and Ni nanoparticles[6]. They showed that oxidised metals were incapable of forming a graphitic network under standard growth conditions. The addition of H_2 also plays a role in gas phase kinetics, i.e. in preventing the deposition of amorphous carbon[7].

MWNT growth was carried out on Fe PLD substrates in the Gero furnace at a temperature of 750 °C. A 10 minute H_2 pre-treatment was used to reduce the Fe clusters and the growth step involved passing a mixture of H_2 and C_2H_2 over the clusters for 10 minutes at a pressure of 10 Torr. SEM was used to characterise the films thus grown and the forest heights measured were greater than 400 μm (Figure 4.4), suggesting a tenfold increase in the growth rate. These tubes looked denser and better aligned when compared with those grown in the Lindberg furnace (counting across an image, > 18 tubes/μm are in focus). This suggests that a greater proportion of catalyst particles were active during growth. Diameters in the range 20 – 30 nm were measured and metallic

particles were visible at the tips of tubes indicating a tip growth mechanism. This was supported by the fact that the tubes were seen to be peeling from the substrate implying a weak interaction therewith.

Raman spectra taken of such forests exhibited a larger I_D/I_G than those produced under similar conditions using the Lindberg furnace. This is initially surprising as overall one would expect fewer defects/disorder to be present due to H_2 removing amorphous carbon deposits during growth. However, this increased I_D/I_G can possibly be attributed to the large density of tips which inevitably contain defects at the top of the forest on which the Raman laser was focused. A Raman sampling depth of ~30 nm for carbon based materials has been reported previously[8]. A larger sampling depth would be expected in the case of MWNT forests due to their porosity.

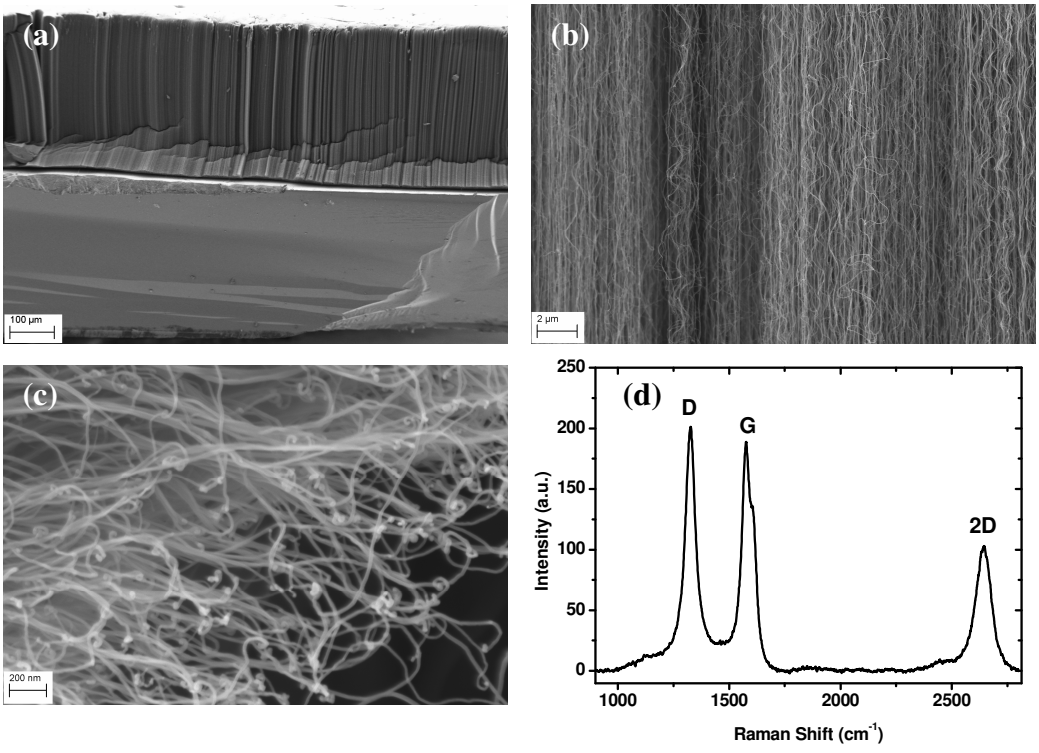

Figure 4.4 *Different magnification SEM images of MWNTs grown on Fe PLD film (a) Heights of > 400 µm. (b) Alignment in the vertical direction. (c) Catalyst particles visible at the tips, suggesting tip growth mechanism; MWNTs have a measured mean diameter of 26 nm. (d) Raman spectrum of MWNT Forest.*

4.2.1.3 Conclusions

Successful growth of films and forests of MWNTs was achieved using Fe films produced by PLD. Varying the temperature and flow rates used allowed for control over the quality and density of the tubes produced. The incorporation of H_2 into growth recipes was seen to enhance the growth producing much longer MWNT forests with lengths greater than 400 μm. SEM images showed catalyst particles present at the tips of the forest implying a tip-growth mechanism.

4.2.2 MWNT Forest Growth on Conductive Substrates

The growth of nanotubes on conducting substrates is of interest for a wide array of applications including vias, field emission devices and supercapacitors. A variety of approaches to growing CNTs on conducting substrates have been adopted. Growth using a Ni catalyst on a Cu substrate was reported by Atthipalli et al. However, the CNTs in this case showed no alignment and were of poor quality[9]. Delzeit et al. reported the growth with a Fe catalyst on Ir and Al underlayers but these were only 10 nm thick and became discontinuous during growth[10]. The use of different metal underlayers (NiV, Ir, Ag, Pt, W, Ta) with diffusion PECVD was investigated by Kim et al.[11] who showed the production of thin films of defective CNTs. Recently Robertson and co-workers described the use of a CoS_2 underlayer and produced dense forests with good alignment[12].

This section presents data obtained using a thin layer of Ta sputtered onto SiO_2 films on Si substrates. Catalyst layers were then sputtered on top of the Ta layer. The Ta layer remained intact during and post growth thus producing MWNT forests on a conducting substrate.

Initial Studies

Initial studies centred on a catalyst system consisting of a catalytic layer (3 nm Co) on top of a conducting layer (30 nm Ta) on SiO_2 films (300 nm) on Si (<100>) substrates (henceforth referred to as SiO_2 substrates). A randomised series of runs (Table 4.1) were carried out on this catalyst. The CNTs produced in each run were assessed using Raman spectroscopy and SEM.

Every run was preceded by a 10 minute pre-treatment in H_2 (60 sccm, 5 Torr). Well-aligned forests of MWNTs (Figure 4.5(a)) were produced in each case. Mean diameters were determined using SEM, measuring more than 50 tubes in each case. These were seen to be in the range 15 – 20 nm and seemed to become larger with increasing growth temperature (Figure 4.5(b)). An increase in tube diameter with increasing growth temperature has previously been reported [13-14]. This was attributed to the effect of temperature on catalyst particles with larger diameter particles forming at higher temperatures due to increased nanoparticle mobility. However, in this case the increases observed were not much larger than the errors in the measurements.

Run	Temp (°C)	Pressure (Torr)	Flow (sccm)	Carrier Gas (Ar/H_2)
1	*675*	*15*	*60*	*H_2*
2	*675*	*15*	*180*	*Ar*
3	*725*	*5*	*60*	*Ar*
4	*700*	*10*	*120*	*Ar*
5	*725*	*5*	*180*	*H_2*
6	*675*	*5*	*60*	*H_2*
7	*675*	*5*	*180*	*Ar*
8	*725*	*15*	*60*	*Ar*
9	*725*	*15*	*180*	*H_2*
10	*700*	*10*	*120*	*H_2*

Table 4.1 *Different growth conditions for runs on Co/Ta catalyst.*

Forest heights were also measured using SEM and it was clear that using Ar as the carrier gas for the precursor produced longer forests (Figure 4.5(d)). This can be explained by considering the action of H_2 in the growth recipe. Whilst the incorporation of H_2 can prolong the catalyst lifetime by reduction of amorphous carbon deposited. It also causes a shift in the chemical equilibrium making the decomposition of C_2H_2 less likely. This reduces the number of radicals available for nanotube growth resulting in shorter forests.

Raman analysis suggested a decrease in I_D/I_G with increasing growth temperature (Figure 4.5 (c)). However, the spread of values in this case was rather large.

Overall these runs suggested certain trends; however, the spread in values meant further experiments were required to establish relationships between growth parameters and measurable nanotube outputs.

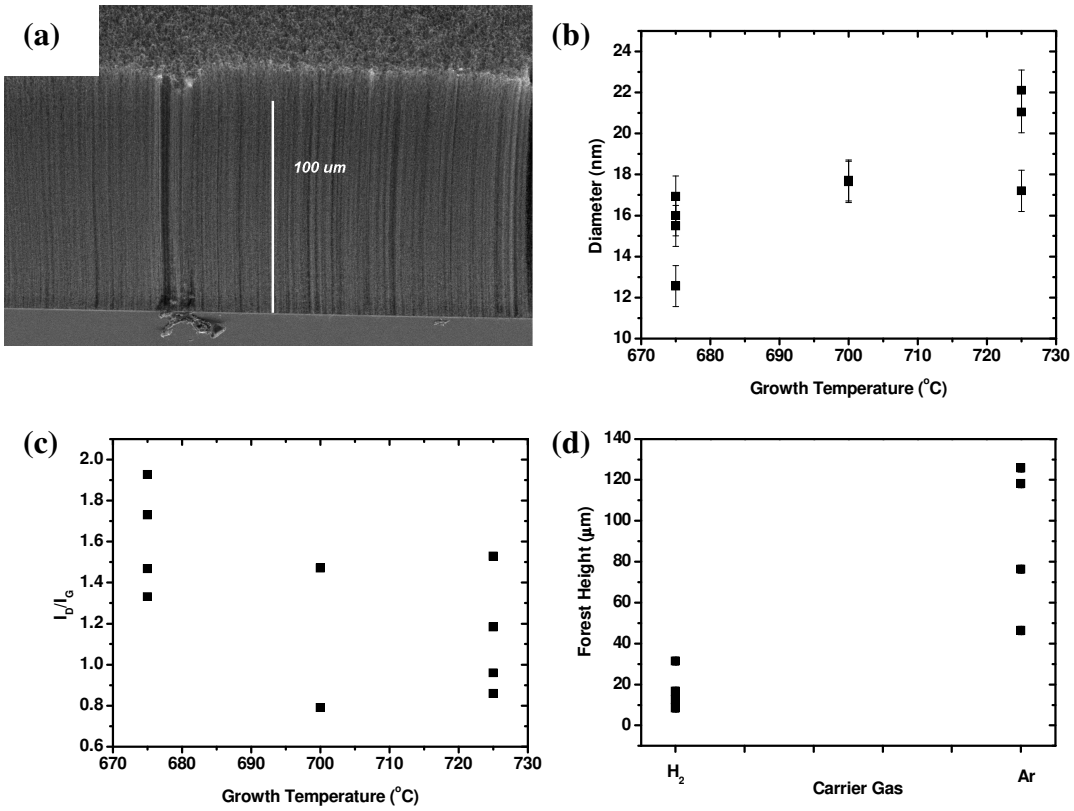

Figure 4.5 *(a) SEM image of vertically aligned MWNT forest (b) Relationship between growth temperature and tube diameter (c) Relationship between growth temperature and Raman I_D/I_G ratio. (d) Relationship between carrier gas used and forest height.*

Extended Study

In order to better appraise the trends an extensive series of runs comprising four different pressures (1, 5, 10 and 20 Torr) and six different temperatures (550, 600, 650, 700, 750, 800 ^{o}C) were carried out. A catalyst layer of 3 nm $Co_{90}Fe_{10}$ on 30 nm Ta on SiO_2 substrates was used. In each case a ten minute pre-treatment in H_2 (60 sccm, 5 Torr) was performed. The reactant mixture used was 60 sccm each of C_2H_2 and Ar with a growth time of 10 minutes for every run.

Raman spectroscopy was again used to assess the purity of the tubes grown. SEM was used to measure forest heights, TEM was used to measure tube diameters and AFM was used to investigate the catalyst.

$Co_{90}Fe_{10}$ was chosen for the catalytic layer as a series of experiments indicated that it yielded better purity CNTs than pure Co under the same conditions. Flahaut et al. previously demonstrated the use of alloys of Fe and Co for CNT growth and observed

enhanced yields compared with pure metals[15]. Through measurement of the surface area of the catalyst pre- and post-growth they also showed that increasing Co content in Fe-Co catalysts led to improved CNT quality.

4.2.2.1 AFM Characterisation of Catalyst

Catalyst films were subjected to a 10 minute H_2 treatment at each growth temperature and then removed from the furnace without any growth (C_2H_2/Ar) step. This was performed under the same conditions as the H_2 pre-treatment used in this work in order to replicate the condition of the catalyst immediately prior to the growth step. These samples were characterised using AFM to measure the roughness and image the catalyst particles. Representative AFM images are shown in Figure 4.6. It is clear that the catalyst particle size increases with increasing H_2 treatment temperature.

Values for roughness (arithmetic average, *Ra* and root mean square, *Rq*) were obtained from AFM images and plotted as a function of temperature (Figure 4.7). The roughness was seen to increase with increasing growth temperature but drops between 750 ^{o}C and 800 ^{o}C. This can be understood by looking at the AFM images. Whilst the cluster size at 800 ^{o}C is on average larger, the film is patchy and non uniform at this temperature. This could be attributed either to clustering of the metallic nanoparticles or removal of the catalyst from the surface of the substrate.

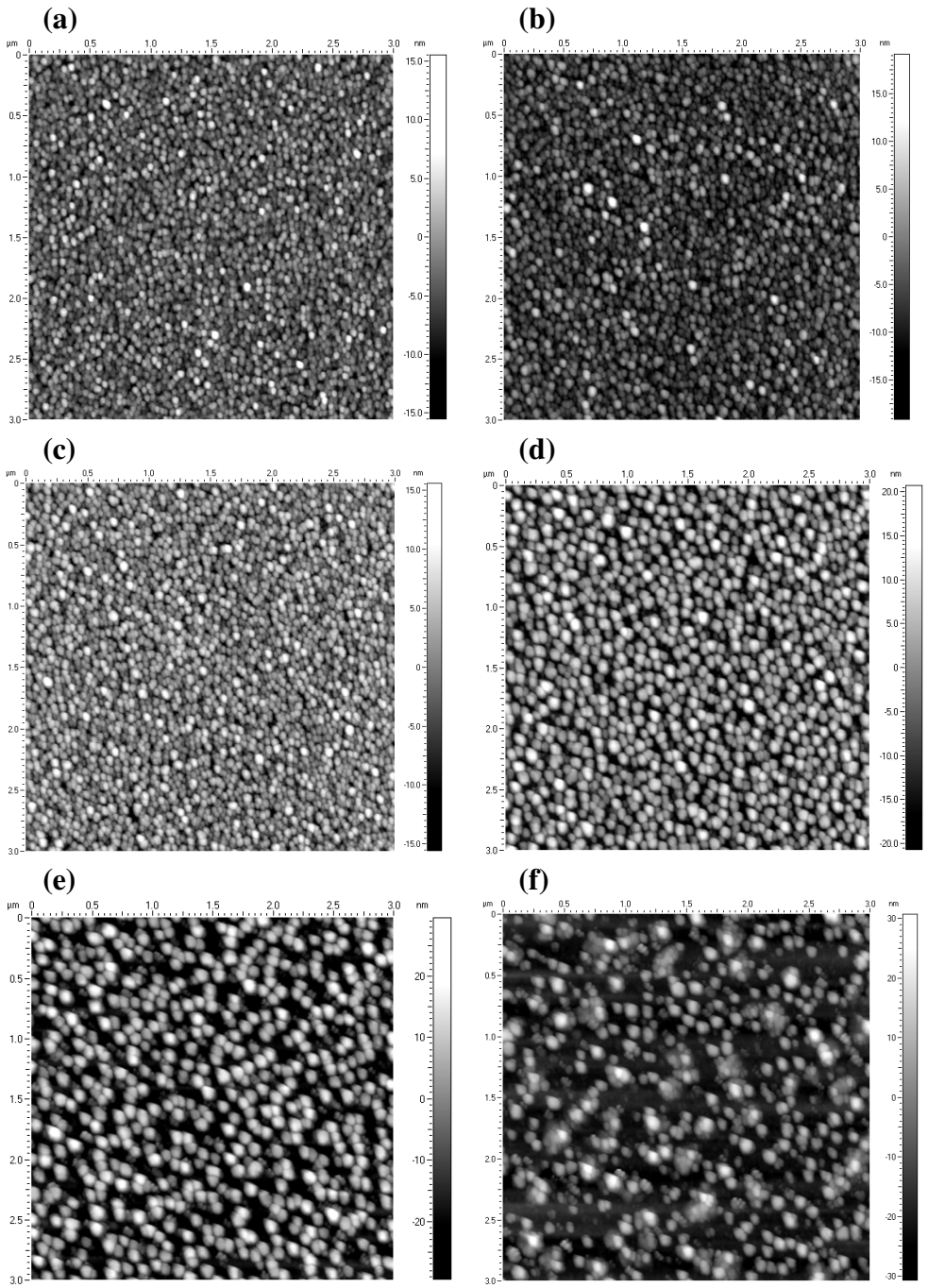

Figure 4.6 *AFM images of catalyst films (3nm CoFe on 30nm Ta) treated at different temperatures in H_2 at (a) 550 ^oC (b) 600 ^oC (c) 650 ^oC (d) 700 ^oC (e) 750 ^oC (f) 800 ^oC. Scale 3 x 3 μm in each case.*

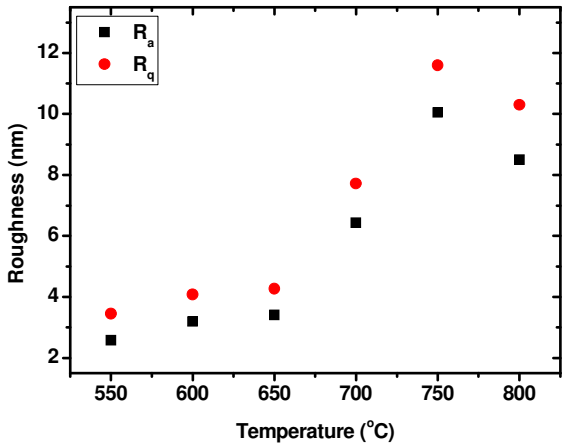

Figure 4.7 *Catalyst film roughness as a function of treatment temperature.*

4.2.2.2 SEM Analysis

SEM analysis was used to measure the heights of the forests produced. This entailed making a scratch near the centre of the sample and then measuring the height in the vicinity of the scratch by tilting the SEM stage to 45°. Heights were also measured from the side and these closely matched those in the middle of the samples indicating good uniformity. Representative SEM images of forests grown at 550 °C and 700 °C are shown in Figure 4.9. A plot of forest height versus growth temperature is shown in Figure 4.8.

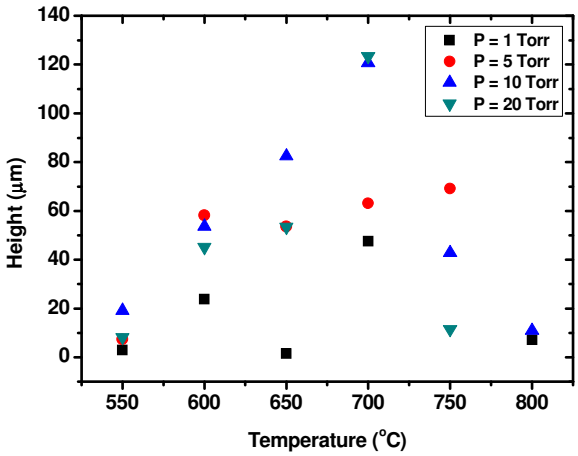

Figure 4.8 *MWNT Forest heights as a function of temperature for different growth pressures.*

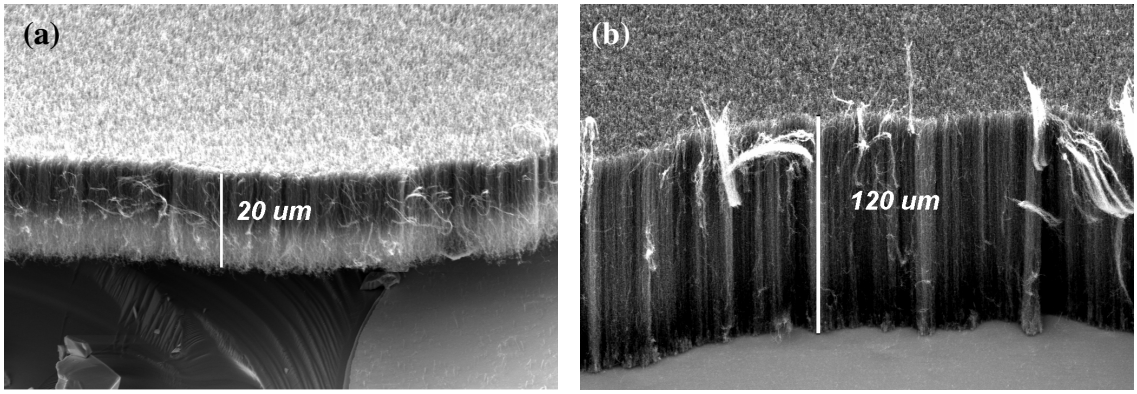

Figure 4.9 *SEM images with 45^o tilt (a) Short forest produced at 550 ^{o}C and 10 Torr. (b) Long forest produced at 700 ^{o}C and 10 Torr.*

From this plot it is seen that the tallest forests were produced at a temperature of 700 ^{o}C at high growth pressures. This is consistent with the results of Liu et al. who reported increased growth rates with rising growth temperatures (and increasing C_2H_2 pressure) for the production of MWNT forests on a Fe/Si catalyst in the temperature range 600 – 680 ^{o}C[16].

Missing data points indicate that the sample was too short to measure the height (< 1 μm). In this case the sample could be considered to be a thin film or carpet of tubes rather than a forest. This was the case for two of the samples grown at 800 ^{o}C. In general, the shortest forests were produced at the lower (550 ^{o}C) and higher (800 ^{o}C) end of the growth temperatures used. The poor growth at 800 ^{o}C can be attributed to the patchy nature of the catalyst film at this temperature as observed by AFM. The poor growth at 550 ^{o}C is most likely related to the low concentration of carbon radicals and also the lower solubility of carbon in the catalyst particles at this temperature. Similar results on optimal temperatures for CNT growth have been reported by other authors[17].

4.2.2.3 TEM Analysis

TEM analysis was used to measure the diameter of the nanotubes and also to investigate their structure. Forests grown at different temperatures (all at P = 20 Torr) were placed in vials containing isopropanol (IPA) and exposed to mild sonication to detach the tubes from their substrate. Samples for TEM imaging were prepared by dropping ~ 50 μL of suspended MWNTs onto lacey carbon grids. Images were taken

for each sample and diameter distributions were determined by using image processing software (Image J) to measure more than 120 tubes for each sample.

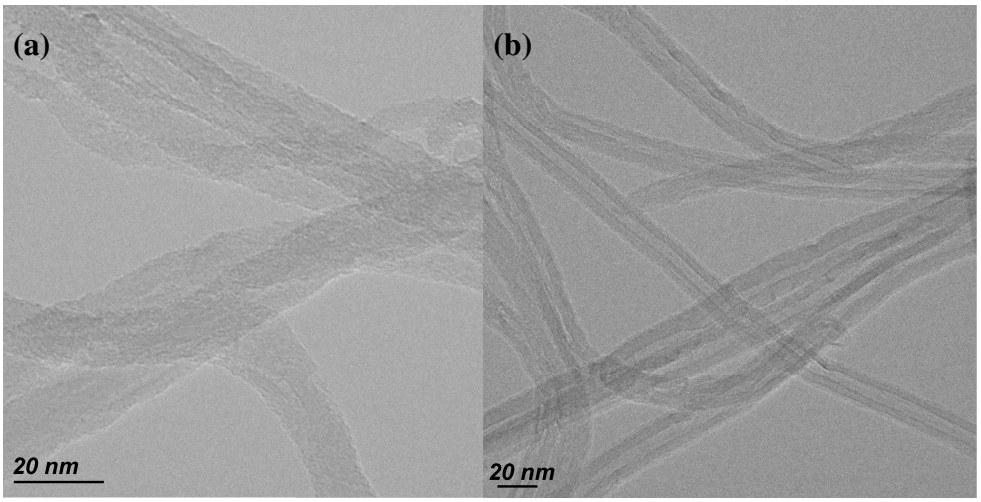

Figure 4.10 *TEM images of MWNTs grown at (a) 550 ^{o}C and (b) 650 ^{o}C. Scale bar is 20 nm for both images.*

TEM images of MWNTs grown at 550 ^{o}C and 650 ^{o}C are shown in Figure 4.10. These images indicate that MWNTs grown at 550 ^{o}C were defective with poorly defined walls. For all higher growth temperatures (represented here by 650 ^{o}C) the concentric nature of the tubes was apparent, with well defined inner and outer diameters visible. Histograms of measured outer tube diameter distributions are shown in Figure 4.11. These indicate that for temperatures in the range 500 ^{o}C – 750 ^{o}C the mean diameter does not vary much and is in the range 15 – 16 nm. This is surprising as earlier SEM studies indicated a slight upshift in diameter with increasing growth temperature. However TEM is a higher resolution technique than SEM and these generated histograms involved a large sample population.

The MWNTs grown at 800 ^{o}C have a mean diameter about twice as large (30.19 nm) and a much larger spread in diameter overall, with tubes > 70 nm in diameter observed. This can be understood by looking at the AFM images shown in section 4.2.2.1. At 800 ^{o}C a considerably larger cluster size is seen; such clusters act as nucleation sites for larger diameter tubes.

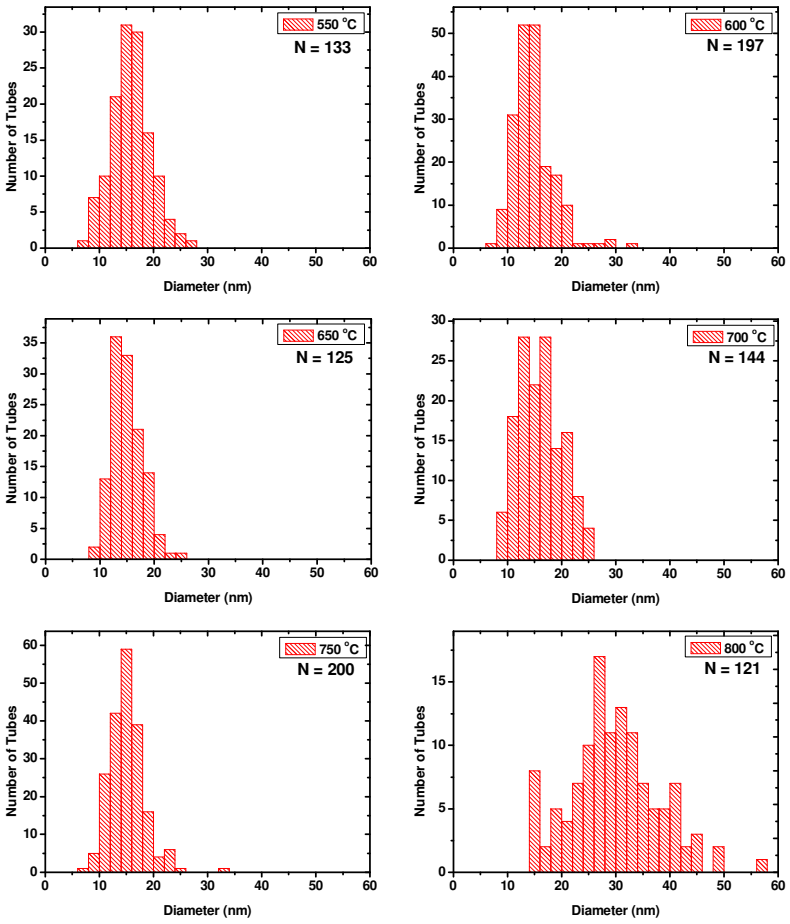

Figure 4.11 *TEM measured diameters for MWNTs grown at different temperatures*

4.2.2.4 Raman Analysis

All of the samples grown were characterised by Raman spectroscopy using a 633 nm excitation wavelength. For each sample spectra were taken from five spots and then averaged to give a representative signal. Typically negligible differences were observed between spectra. These plots are shown in Figure 4.12. In each case *D*, *G* and *2D* bands are observed confirming the presence of a graphitic deposit.

The CNTs grown at 550 ^{o}C display features indicative of highly defective growth, i.e. high *D* band intensity, low *2D* band intensity and broad peaks. The spectra change markedly with increasing growth temperature implying a change in the structure of the CNTs grown. The spectra of CNTs grown at 800 ^{o}C have sharper peaks and in general suggest the growth of much higher quality CNTs.

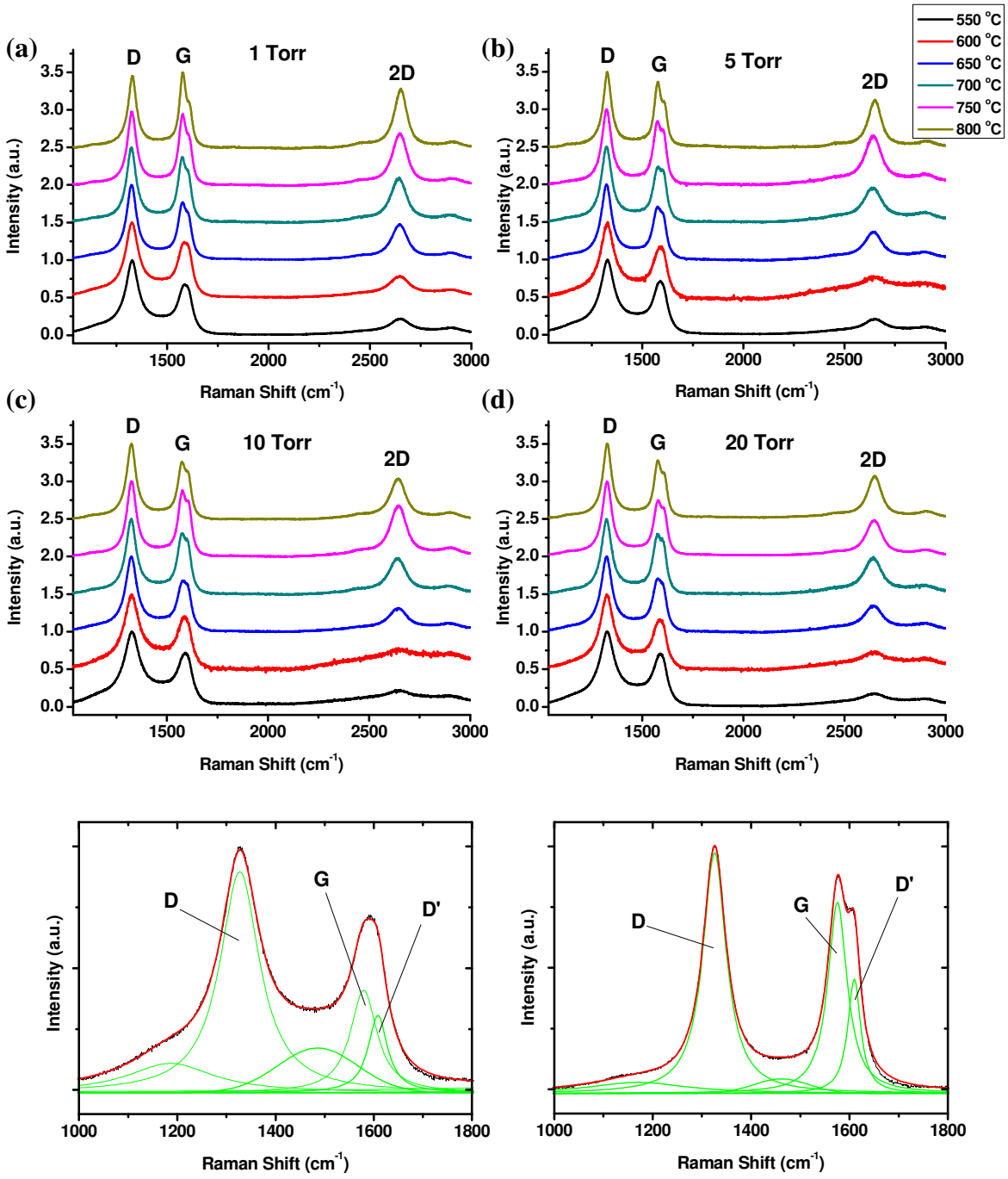

Figure 4.12 *Raman spectra of CNTs grown on 3nm CoFe on 30 nm Ta at different temperatures at (a) 1 Torr (b) 5 Torr (c) 10 Torr (d) 20 Torr. Fits are shown for growth at 10 Torr at (e) 550 °C and (f) 750 °C.*

In order to better examine the features of the spectra, peak fitting was carried out. Lorentzian peaks were fitted for the *D*, *G*, *D'* and *2D* bands. For highly disordered samples, a Gaussian feature related to the presence of amorphous carbon was fitted at ~

1500 cm^{-1}. From these fits peak intensity ratios, integrated area ratios and widths were determined.

The intensity of the *D* band for graphitic materials is directly related to the crystallite size and so it reflects on the presence of defects and edges. The ratio of the *D* to *G* band intensity (I_D/I_G) is often used as a figure of merit for CNT quality. A plot of this ratio against growth temperature is shown in Figure 4.13(a). It is evident that increasing growth temperature leads to an improvement in CNT quality (or a reduction in defect levels). This is supported by the trend seen for the ratio of *2D* to *G* band intensity (I_{2D}/I_G) which is seen to increase with rising growth temperature (Figure 4.13(b)). The *2D* band represents a double resonant two phonon scattering process and is related to spatial uniformity in the graphitic plane or 3D ordering in graphite based crystallites. Its intensity is suppressed in the presence of defects, thus a high I_{2D}/I_G further implies good quality growth.

The effect of growth pressure on CNT quality is less obvious; however, the lowest I_D/I_G and highest I_{2D}/I_G are seen with a growth pressure of 1 Torr. The higher defect levels at higher growth pressures can be accounted for by considering the deposition of other carbon species. Whilst a higher CNT growth rate is expected (and observed) at higher pressures, the probability of the carbon radicals formed recombining is also greater, increasing the deposition rate of amorphous carbon.

The peak widths of the *D* and *G* bands have also been linked to the graphitic quality or crystallite size[18]. Broadened *D* and *G* bands are typically seen in highly disordered sp^2 carbon systems. Here, the peak widths of the *D* and *G* bands ($\Delta\omega_D$ and $\Delta\omega_G$) are seen to narrow considerably with increasing growth temperature, further establishing that the quality of the CNTs grown improves (Figure 4.13(c, d)).

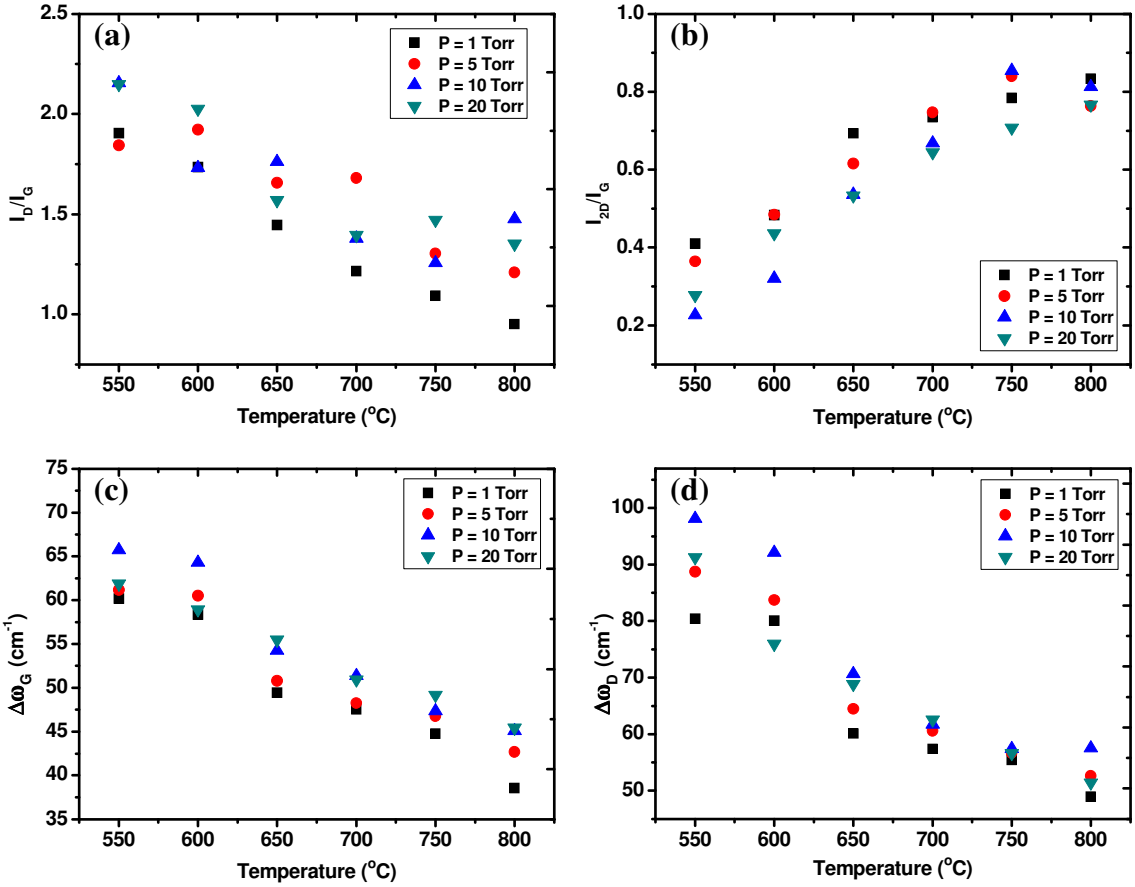

Figure 4.13 *Growth temperature dependence of (a) I_D/I_G ratio and (b) I_{2D}/I_G ratio (c) $\Delta\omega_G$ (d) $\Delta\omega_D$*

4.2.2.5 Effect of catalyst composition

In order to investigate the effect of varying the composition of the catalyst on the quality of the nanotubes grown three additional catalysts were used for a series of runs, and the nanotubes thus produced were compared to those detailed above. The catalysts were 3 nm of $Co_{90}Fe_{10}$ on SiO_2 substrates without a Ta underlayer, 3 nm of $Co_{50}Fe_{50}$ on 30 nm Ta on SiO_2 substrates and 3 nm $Co_{40}Fe_{40}B_{20}$ on 30 nm Ta on SiO_2 substrates respectively.

Runs were carried out at different temperatures using the same gas flow conditions as for the $Co_{90}Fe_{10}$ films, at a growth pressure of 10 Torr. Plots of A_D/A_G and I_{2D}/I_G for each of these catalysts are shown in Figure 4.14. It is clear from the plots that the best and worst I_{2D}/I_G ratios are seen for the $Co_{90}Fe_{10}$ catalysts with and without a 30 nm Ta underlayer respectively. This suggests that the addition of the Ta layer improves the

quality of CNTs grown. (Data is presented in chapter 5 which indicates that the deposition rate of carbon is much lower on Ta than on SiO_2 substrates). The $Co_{50}Fe_{50}$ catalyst exhibited the 2nd best I_{2D}/I_G ratio and the $Co_{40}Fe_{40}B_{20}$ catalyst had slightly lower values. Less variation was seen among the A_D/A_G ratios, but overall the $Co_{90}Fe_{10}$ catalyst had the lowest values implying that it produced the best quality tubes for a given growth temperature.

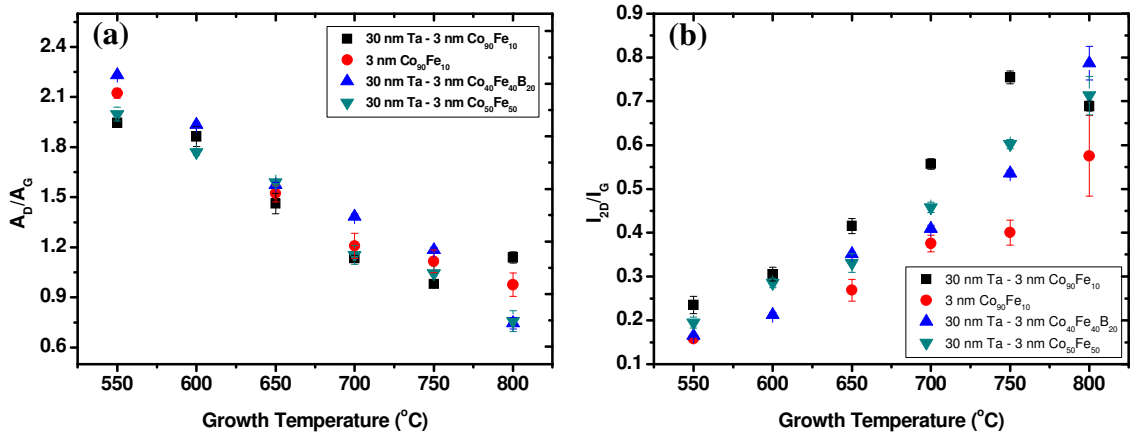

Figure 4.14 *(a) A_D/A_G and (b) I_{2D}/I_G versus growth temperature for an assortment of different MWNT catalysts.*

4.2.2.6 CNT growth on conductive carbon layers

The use of Ta as a conducting underlayer for MWNT growth was demonstrated in the preceding sections. An alternative approach was adopted using pyrolysed photoresist films (PPF)[19-20] as the conductive support layer. These were prepared by annealing thin layers of photoresist at high temperatures to produce conductive glassy carbon layers. Such films can withstand the high temperatures and processing conditions used for the growth of MWNTs.

PPFs were prepared using the procedure previously described by Schreiber et al[20]. In brief, this entailed spin coating a film of the resist AZ nLOF onto SiO_2 substrates and then annealing at 1000 °C in a forming gas (Ar/H_2) environment. The annealing step leads to an 80% reduction in film thickness and the formation of a conductive glassy carbon film with a resistivity of 6.25 x 10^{-5} Ωm.

Conductive carbon films with a thickness of ~ 100 nm were prepared by this method and subsequently coated with a 3 nm Ni catalyst layer by sputtering. These films were then employed as substrates for CVD growth using recipes established with standard MWNT catalysts (Ar + C_2H_2, P = 5 Torr, Flow = 120 sccm).

Raman studies on such films indicated that a strong degree of graphitisation occured on subjecting the films to CVD conditions (see Figure 4.15). Before growth PPFs exhibited an intense and broad *D* band and high I_D/I_G ratio, as expected for a nanocrystalline glassy carbon material. Post-growth the *D* and *G* bands had both narrowed, the I_D/I_G ratio decreased, and a clear *2D* band emerged at ~2655 cm^{-1}. An improved I_D/I_G was seen with increasing growth temperature. These features point towards the crystallite size increasing or the carbon material becoming better ordered.

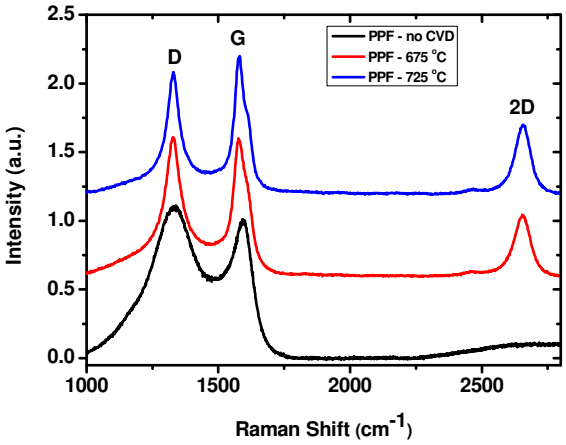

Figure 4.15 *Raman spectra of PPF films pre and post CVD growth, showing graphitisation on growth.*

In order to investigate what was causing the changed Raman signal SEM analysis was carried out. This showed that structures similar to the CNTs seen previously had formed (Figure 4.16). These structures exhibited a larger spread and mean for diameters than MWNTs produced on conventional substrates. Typical diameters in the range 40 – 80 nm and lengths of ~ 10 μm were observed. The broad spread suggests a very different interaction between the catalyst and PPF layer compared with SiO_2 or Ta.

The tubes grown were not well aligned and as such not of much use for vias and other electrical applications. However, the unique nature of the carbon-carbon contact between the PPF layer and the grown structures could be of interest for applications

where a conductive material with high surface area is desirable such as electrochemical electrodes and sensors.

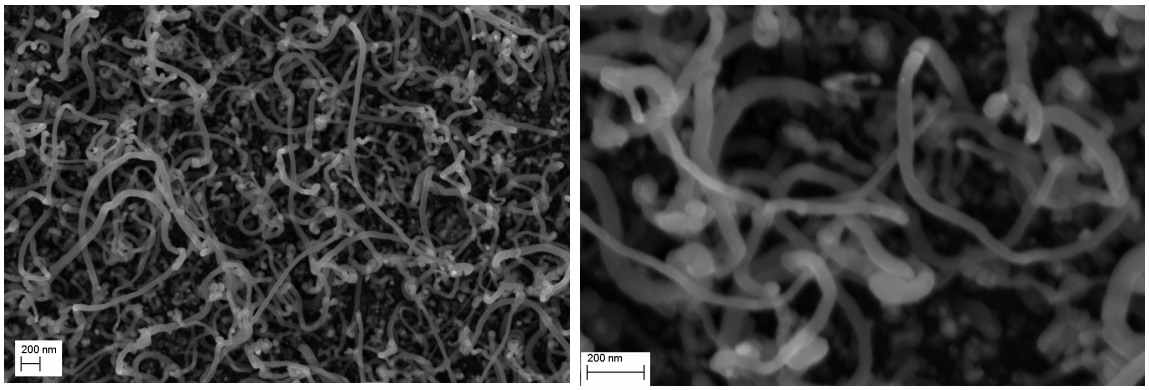

Figure 4.16 *SEM images of the structures grown on PPF films. These have larger diameters with a bigger spread than other catalysts (40 – 80 nm). Scale bar 200 nm.*

4.2.2.7 Conclusions

MWNT Forests have been grown on a series of catalysts consisting of a thin catalytic layer deposited on a conductive Ta underlayer. The MWNTs grown exhibited better quality and alignment when compared with other groups attempts at growth on Ta layers[11]. Optimal growth conditions for the production of long forests were found to involve temperatures in the range 700 – 750 ^{o}C and high pressures. Raman spectroscopy indicated that the quality of MWNTs produced improved with increasing growth temperature. AFM analysis showed a roughening of catalyst films with increasing growth temperature up to ~ 750 ^{o}C after which point, catalyst particles were seen to cluster. TEM analysis indicated similar outer diameter ranges for all MWNTs grown except for those grown at 800 ^{o}C. Comparative runs were undertaken using different alloys as the catalyst layer; these suggested that $Co_{90}Fe_{10}$ produced higher quality MWNTs than other alloys under the growth conditions used. The use of a conductive carbon layer in the place of Ta was briefly investigated. This led to the formation of CNF like structures with a broad diameter distribution.

4.2.4 Patterned Growth of MWNTs

4.2.4.1 Nanosphere Lithography

For applications from field emission to vias, the patterned growth of vertically aligned nanotubes is important. Conventional optical lithography has a resolution limit related to the wavelength of light used by the Rayleigh equation[21]. E-beam lithography involves a much smaller beam size and wavelength and can be used for defining nanoscale features. However, it is an expensive and low throughput technique. One alternative approach to defining small feature sizes is nanosphere lithography (NSL) as first described by Deckman[22]. This technique uses nanoscale polystyrene spheres of uniform diameter prepared by chemical methods[23] to form hexagonally close packed monolayers on the surface of flat substrates. The monolayer can then be used as a shadow mask for material deposition for the preparation of hexagonal arrays of triangular nanoparticles. These particles can also be used as catalyst sites[24-25], quantum dots[26], periodic magnetic arrays[27] as well as being employed in surface enhanced Raman scattering (SERS) and other plasmonic studies[28]. The monolayer can alternatively be used as an etch mask for the production of nanopillars[29] and, by extension, nanoimprinting moulds[30].

Hexagonal arrays of triangular metallic nanoparticles were prepared by this method using polystyrene nanospheres of diameter 362 nm. AFM and SEM images of representative films are shown in Figure 4.17. Fe and Ni catalyst films were prepared by thermal evaporation of 10 nm of these metals onto NSL monolayers. CVD growth was then carried out in the Lindberg furnace using conditions similar to those used for PLD films.

Raman analysis was first used on these films to confirm the presence of CNTs (see Figure 4.20, overleaf). SEM was then used to investigate the geometry of the tubes grown. In the case of Ni particles it was found that short tubes (1 – 2 μm) were seen but only nucleated at a small proportion of catalyst sites, with a large number of particles remaining inactive or showing small buds of growth (Figure 4.18(a, b)) . A similar situation was observed for Fe particles but the tubes grown were much longer (~100 μm) (Figure 4.18(c, d)).

The poor catalytic activity observed can be attributed to either amorphous carbon forming on the particle surface (also known as catalyst poisoning) or due to oxidation

of the catalyst. As there was no H_2 line available for the Lindberg furnace there was no obvious route for incorporating a reducing agent in these runs.

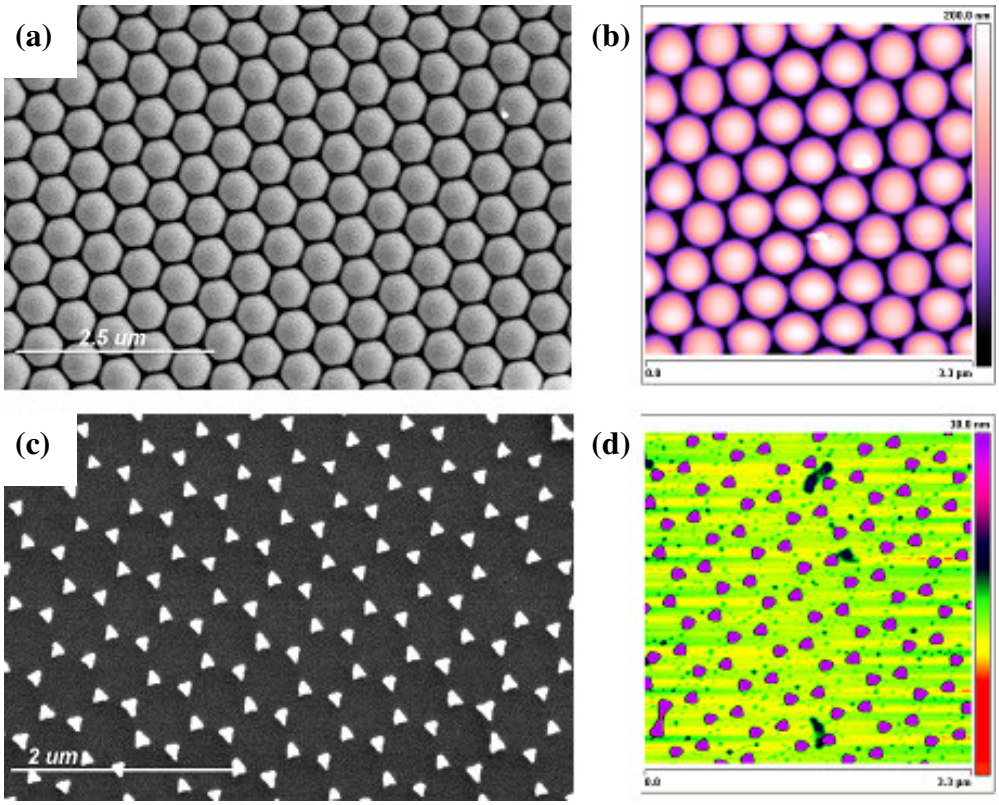

Figure 4.17 *AFM and SEM images showing monolayers of polystyrene spheres (a, b) and arrays of hexagonal triangular particles (c, d) produced by NSL. AFM x-y scale is 3.3 x 3.3 μm.*

Growth was next attempted on such films in the Gero furnace setup with H_2 added to the growth recipe. It was seen that tubes nucleated at the majority of catalyst sites. However, this had drawbacks, with the tubes collapsing onto the substrate with negligible alignment. This can be explained by considering the distance between catalyst sites (~ 100 nm). Alignment in nanotube forests grown by thermal CVD has been linked to van der Waal's forces between adjacent tubes[31]. In the case of these NSL films, however individual tubes were seen to grow at each catalyst site and the distance between these sites was too large for alignment to be induced by van der Waal's forces. The use of larger spheres would produce larger catalyst sites, which in turn produce aligned bunches of MWNTs. Recent studies have shown improved field emission from arrays produced in this manner [32].

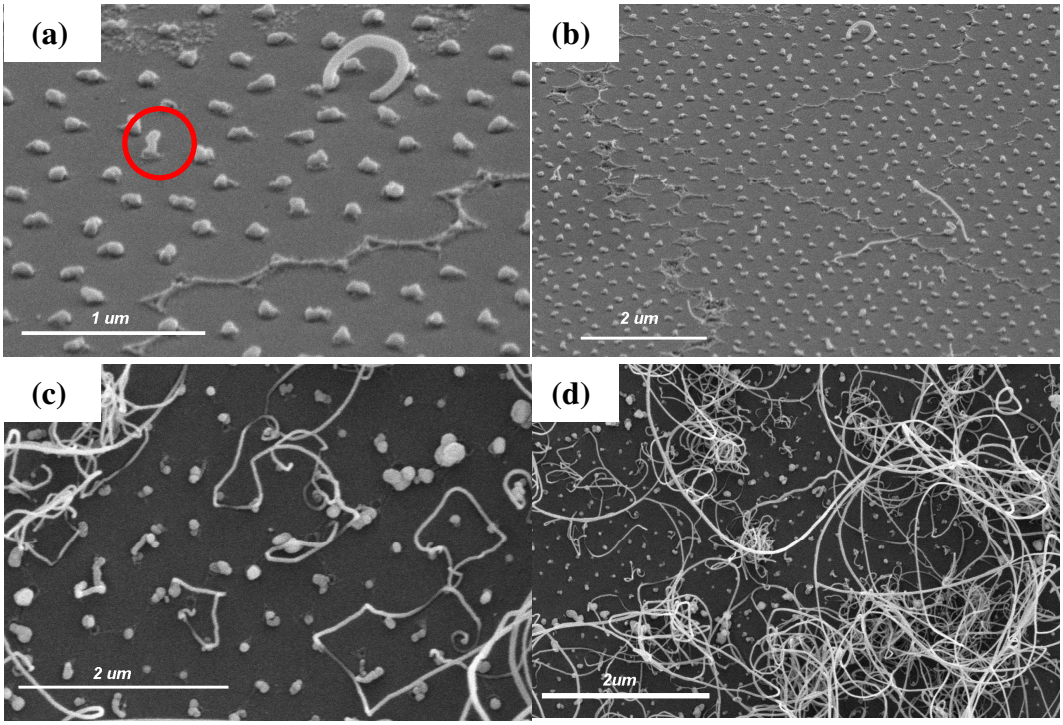

Figure 4.18 *(a & b) Nanotubes grown on Ni NSL films with a small bud circled. (c & d) Growth on Fe NSL films showing longer tubes but a similarly poor activity of catalyst sites.*

With a view towards achieving better alignment and catalyst activity, a series of Ni samples were prepared for collaborators in Cambridge for PECVD growth. The growth conditions involved a 4:1 mixture of NH_3:C_2H_2, whereby the NH_3 acted as a reducing agent. The growth temperature was 725 ^oC and a 620 V plasma was used for improved tube alignment. Structures were seen to nucleate from almost all nanoparticle sites under these conditions and exhibited good vertical alignment (Figure 4.19). SEM analysis indicated diameters of ~ 50 nm which is smaller than the measured perpendicular bisector of the triangular catalyst particles (97 nm). The spacing between adjacent structures was in the range 190 – 200 nm. The length was ~ 1 µm with good site to site uniformity.

Raman analysis indicated that the structures were highly defective with no appreciable *2D* band (see Figure 4.20). Furthermore, the diameter was larger than that generally expected for crystalline graphitic nanotubes. These observations suggested that the structures grown were most likely some form of carbon nanofibre (CNF) with a

different structure to the concentric shells expected for graphitic nanotubes. This type of structure is quite common for PECVD processes[33].

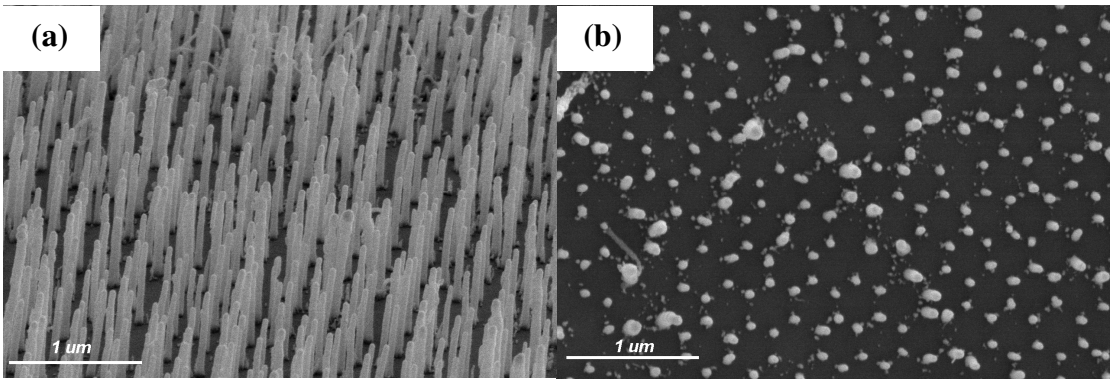

Figure 4.19 *(a) Tilted and (b) top down view of tubes grown by PECVD on Ni NSL film. Hexagonal arrangement of tubes is obvious as is high catalytic activity.*

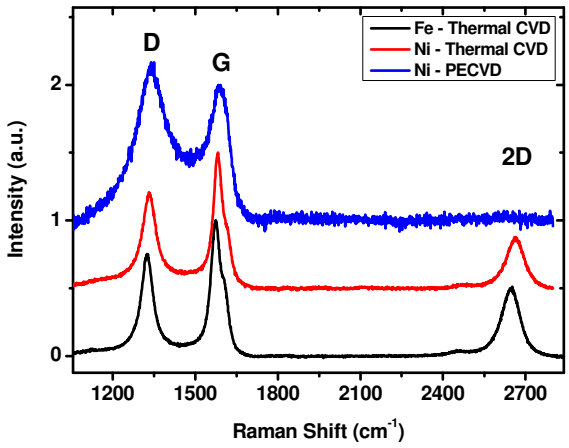

Figure 4.20 *Raman spectra of CNTs grown by different CVD methods on NSL films. The high I_D/I_G ratio and band shape highlight the defective nature of those produced by PECVD.*

In summary, the NSL technique was employed to prepare hexagonal arrays of catalytic nanoparticles for the production of CNTs. Growth in the Lindberg system showed poor catalytic activity. The Gero system allowed for a much higher catalytic activity but the tubes grown showed no alignment. PECVD growth was then carried out on these arrays by collaborators. Structures with uniform heights and spacing and good vertical

alignment were produced. Raman spectroscopy showed that these were highly defective. Future field emission studies on such samples are of interest, here the size of nanospheres used could be modified to change tube spacing and reduce screening effects.

4.2.4.2 Conventional Patterning

Patterned growth through conventional lithographic methods was achieved in the Gero furnace. Alignment markers patterned by optical lithography were used to create catalyst stacks consisting of a Ta underlayer with a Fe catalyst top layer. CVD Growth on such samples (700 ^{o}C, 10 mins) produced columns of MWNTs from the crosses which were greater than 100 μm long. These were visible by optical microscopy using a 100x objective lens as shown in Figure 4.21(a). SEM characterisation of such samples showed that they consisted of bundles ~ 7 μm in diameter.

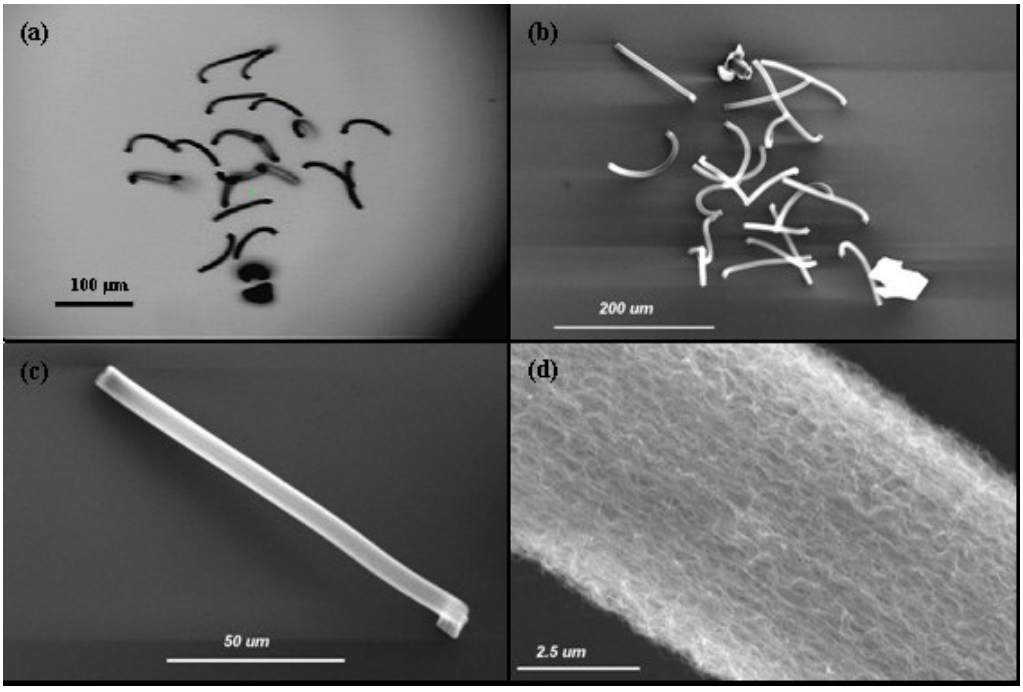

Figure 4.21 *(a) Optical microscopy image of MWNT bundles (b, c, d) Different magnification SEM images showing bundle lengths and diameters as well as individual tubes.*

4.3 SWNT Growth

The diameter of nanotubes grown by CVD is directly related to the diameter of catalyst particles used [34-35]. Very small particles of well controlled diameter are required for the growth of single wall nanotubes (SWNTs). Typically very thin films (< 1nm) prepared by physical deposition methods or nanoparticles prepared by chemical methods are used as catalyst materials.

This section deals with the growth of both thin films and forests of SWNTs on thin sputtered catalysts. The growth of SWNT thin films is of interest for electrodes and thin film devices such as network transistors and gas sensors. SWNT forests, by comparison, are potentially useful for via and supercapacitor applications. Forest growth also offers a route for bulk production of SWNTs longer than those commercially available.

4.3.1 SWNT Network Growth

4.3.1.1 Importance of Al_2O_3 Layer

The addition of an alumina catalyst support layer is seen to be favourable for SWNT growth; this is due to deposited catalyst metals forming smaller and denser particles on alumina, compared to silica substrates. This effect is attributed to alumina reducing the surface diffusion and agglomeration of metals[36].

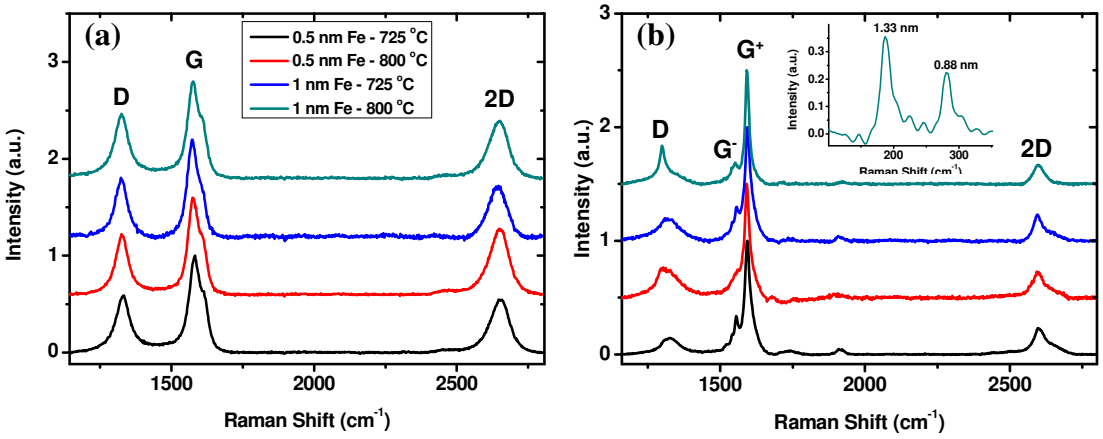

Figure 4.22 *Raman spectra of CNTs grown on Fe catalyst films prepared on (a) SiO_2 substrates and (b) Al_2O_3 films on SiO_2 substrates; inset shows RBM modes.*

A comparison between different substrates was undertaken by sputtering 0.5 nm and 1 nm of Fe onto SiO_2 and Al_2O_3 substrates (simultaneously). These substrates were subjected to identical growth conditions at 800 ^oC and 725 ^oC in the Lindberg furnace (i.e. no H_2). Flow rates of 300 sccm of C_2H_2 and 1000 sccm of Ar were used with a dwell time of 15 mins. Raman spectroscopy (Figure 4.22) indicated that the Al_2O_3 substrates gave rise to SWNTs (both RBMs and *G* band splitting were observed), whereas the SiO_2 substrates gave rise to MWNTs. This confirmed the importance of an Al_2O_3 layer for the production of SWNTs. Fe films thicker than 1 nm led to the growth of MWNTs on both SiO_2 and Al_2O_3 substrates. SEM imaging of the tubes grown indicated that they were very short (< 1 μm, see Figure 4.23) suggesting a termination of growth due to catalyst poisoning.

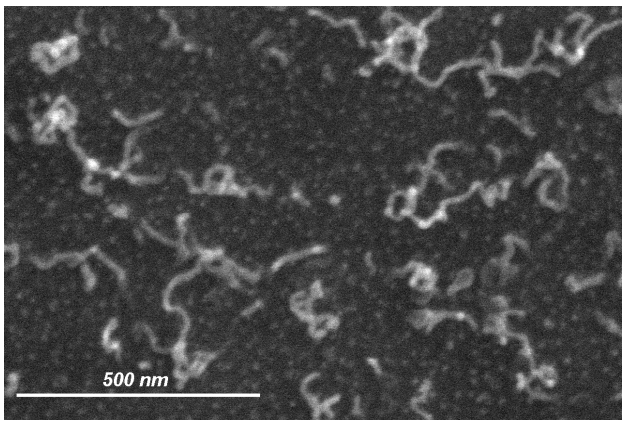

Figure 4.23 *SEM image of SWNTs grown on Fe/Al_2O_3 substrates in Lindberg furnace*

4.3.1.2 Gero growth – Denser Networks

Thin catalyst films (0.4 nm Co, 0.4 nm $Co_{40}Fe_{40}B_{20}$ and 0.4 nm $Ni_{80}Fe_{20}$ respectively) on alumina were prepared by sputtering. These were used in the Gero system with the addition of H_2 to the growth recipe in order to obtain denser networks of higher quality SWNTs. Typical conditions used entailed a growth temperature of 800 ^oC, a 10 minute H_2 pre-treatment (120 sccm, 5 Torr) and growth for 10 minutes at 10 Torr with a 50:50 mix of C_2H_2:H_2 (60 sccm each).

Raman spectra for films grown under these conditions are shown in Figure 4.24. All the catalysts exhibited similar RBM frequencies and similar I_D/I_G ratios, implying similar diameter distributions (for the SWNTs in resonance with the excitation wavelength) and similar defect levels respectively. The $Co_{40}Fe_{40}B_{20}$ catalyst exhibits a stronger

relative contribution from larger diameter SWNTs. This is in agreement with recent results reported by Inoue et al., who showed that Fe/Ni based catalysts gave a smaller relative contribution of large diameter SWNTs when compared with Fe/Co catalysts[37].

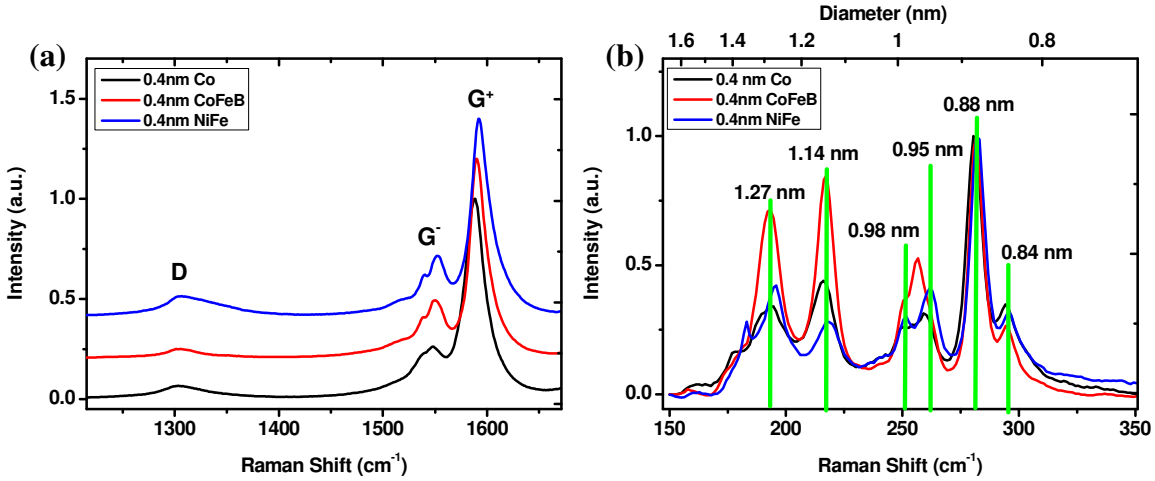

Figure 4.24 *Raman spectra of SWNTs produced on 0.4nm Co, CoFeB and NiFe catalysts (a) D and G bands (b) RBM region.*

The *G* band shape, meanwhile, suggests that a large proportion of the tubes excited by the beam are semiconducting due to the relatively small G^- band. I_D/I_G ratios as low as 0.05 were measured which marks a significant improvement over those obtained at lower temperatures. RBM peaks were observed at frequencies suggesting diameters of 1.27, 1.14, 0.98, 0.95, 0.88 and 0.84 nm respectively. Comparing the RBM region of these tubes with commercially available CVD and arc-discharge based nanotubes (HiPCO and Iljin) shows some overlapping peaks but importantly, these CVD grown nanotubes have some higher energy peaks which are missing from the commercial nanotube spectra (see Figure 4.25). This demonstrates that the CVD process presented here produces quantities of smaller diameter SWNTs.

Spectra were taken of a sample grown on the 0.4 nm CoFeB catalyst using a number of different excitation wavelengths to get a better indication of the spread of nanotube diameters. Raman spectra showing the RBM modes and *D*, *G* and *2D* bands are shown in Figure 4.26. The RBM modes identify additional SWNT diameters not seen using the 633 nm excitation alone. A table of diameter values is given in Table 4.2. The *D* and *G* band regions of the spectrum are also of interest. The frequency of the *D* band

rises with increasing excitation energy due to its dispersive nature (as discussed in Chapter 2). The frequency upshifts from ~ 1292 cm^{-1} for 785 nm excitation, to ~ 1306 cm^{-1} for 633 nm up to ~ 1351 cm^{-1} for 485 nm. The shape of the *G* band also changes considerably due to the different fractions of semiconducting and metallic SWNTs in resonance with the beam.

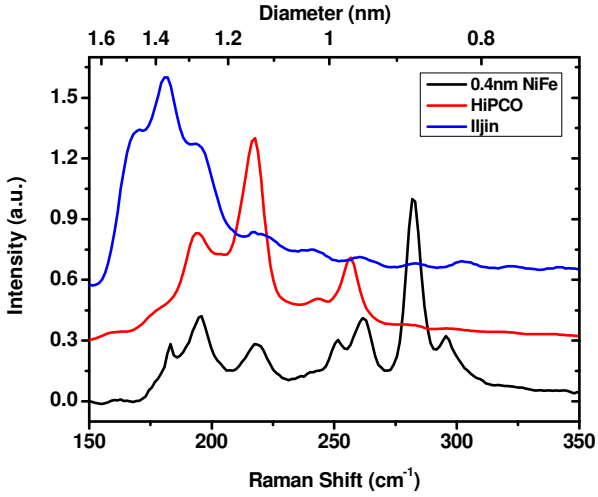

Figure 4.25 *Raman spectra comparing the RBM region of SWNTs grown on NiFe catalyst with those of HiPCO and Iljin SWNTs.*

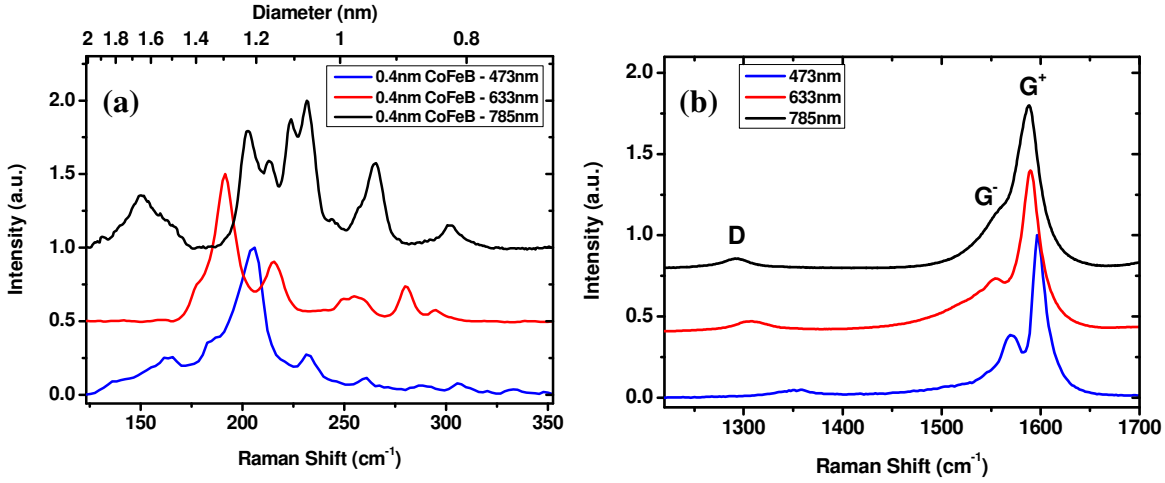

Figure 4.26 *Raman spectra of (a) RBM region and (b) D and G bands of SWNTs grown on CoFeB catalyst with three different excitation wavelengths.*

d (nm) at λ=473 nm	d (nm) at λ=633 nm	d (nm) at λ=785 nm
1.51	*1.27*	*1.64*
1.34	*1.14*	*1.23*
1.21	*0.98*	*1.17*
1.07	*0.95*	*1.11*
0.95	*0.88*	*1.07*
	0.84	*0.94*

Table 4.2 *SWNT diameters observed for CoFeB catalyst using different excitation wavelengths*

SEM analysis showed uniform thin films of SWNTs growing horizontally. These were clearly above the percolation threshold over a large area. Film thicknesses were of the order of 10-100 nm as shown in Figure 4.27.

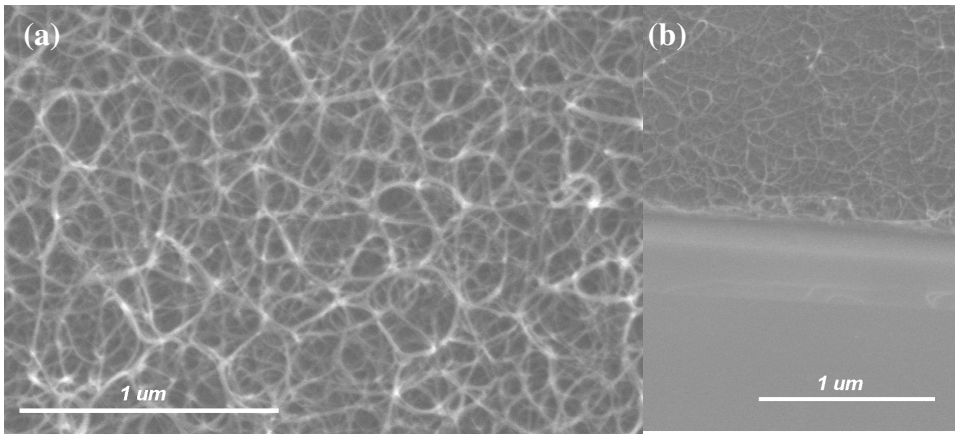

Figure 4.27 *SEM images of SWNTs grown on 0.4nm Co catalyst (a) High magnification (b) Tilt view showing film thickness.*

A number of runs were carried out at a higher temperature (900 ^{o}C) on the 0.4 nm Co catalyst keeping other conditions constant. The effect of increasing the growth temperature was best seen by examining the RBM region of the Raman spectrum (Figure 4.28) which showed a strong signal for low frequency modes but suppressed high frequency modes thus suggesting a reduced population of smaller diameter

SWNTs. This can be linked with the increased size of catalyst particles at this elevated temperature.

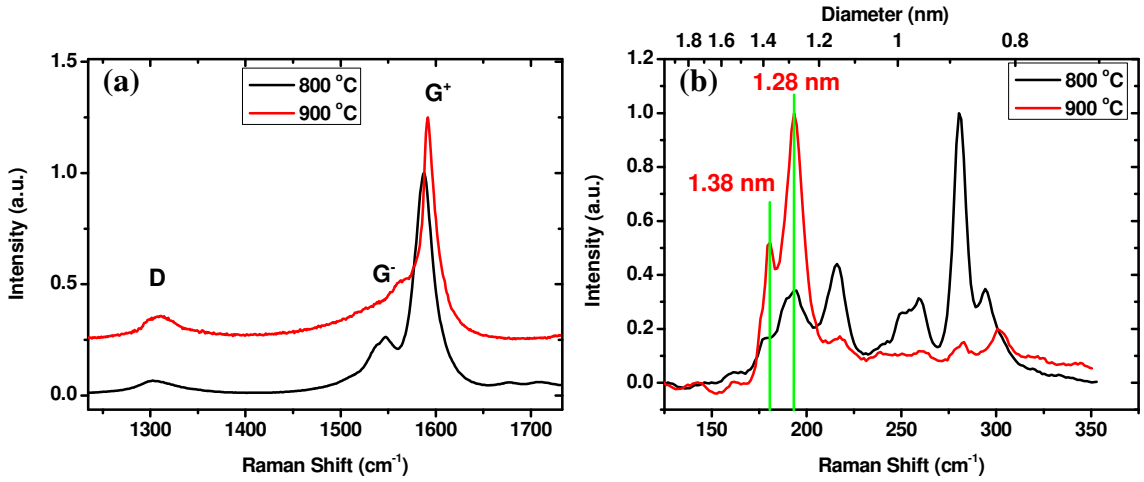

Figure 4.28 *(a) D and G bands and (b) RBM modes for SWNTs grown at 800 °C (black) and 900 °C (red).*

4.3.2 SWNT Forest Growth

In an attempt to change the SWNTs grown from thin films to forests, changes were made to the CVD growth recipes. In particular, the overall gas flow was increased and the growth mixture was diluted by the incorporation of Ar. The use of Ar as a carrier gas was seen to increase the height for MWNT forests in section 4.2.2. Furthermore, increased carbon yields have been reported upon the dilution of carbon feedstocks[38].

The catalyst used was created by sputtering and consisted of 0.4 nm $Co_{90}Fe_{10}$ on Al_2O_3 on SiO_2 substrates. H_2 pretreatment was carried out in the same manner as described for MWNTs grown on Ta backed catalyst layers (H_2, 60 sccm, 5 Torr, 10 mins). The gas composition used for the growth step was typically 120 sccm H_2, 120 sccm Ar and 45 sccm C_2H_2, with growth temperatures in the range of 650 – 950 °C and pressures of 5 and 10 Torr.

Forests of nanotubes have dense black coverage and so optical inspection alone can give a good indication as to whether or not a forest has been grown (This can later be confirmed using SEM). Samples grown were thus split into the categories of “forest” if dense black coverage was observed and “film” if lesser or no colour change was noted.

Raman spectroscopy was used to establish the type of deposit present and then assess the purity.

4.3.2.2 Characterisation

The outputs from these growth runs are summarised in Table 4.3. Good quality SWNT growth was observed for all temperatures greater than 700 ^{o}C. A growth pressure of 10 Torr gave dense growth for temperatures in the range 700 – 850 ^{o}C. Films grown at 950 ^{o}C did not display forest growth but gave a strong SWNT Raman signal.

T (^{o}C)	P (Torr)	Sample Morphology	Raman Signal
650	5	Film	Defective
700	5	Forest	Defective
750	5	Film	SWNTs
800	5	Forest	SWNTs
850	5	Film	SWNTs
950	5	Film	SWNTs
650	10	Film	Defective
700	10	Forest	Defective
750	10	Forest	SWNTs
800	10	Forest	SWNTs
850	10	Forest	SWNTs
950	10	Film	SWNTs

Table 4.3 *Summary of growth outputs for attempts at SWNT forest growth on CoFe catalyst*

Raman spectra for these runs showing the *D*, *G* and *2D* band are shown in Figure 4.29. The defective nature of the deposit formed at temperatures < 750 ^{o}C is evident in the high I_D/I_G ratio seen. The shape and width of the *D* band suggest contributions from amorphous carbon. At higher temperatures, splitting of the *G* band and a high I_D/I_G ratio, both indicative of good quality SWNTs, are seen. An increase in the relative *2D* band intensity with temperature is also seen giving further indication of improved quality.

A plot of I_D/I_G is shown in Figure 4.30. At low growth temperatures (650 ^{o}C, 700 ^{o}C) this suggests higher purity at a growth pressure of 10 Torr. This can be understood by looking at the Raman plots and noticing the noise level in the 5 Torr plots in this temperature range. The incredibly noisy signal obtained points to minimal deposition. For all higher growth temperatures, a growth pressure of 5 Torr gives a better quality

Raman signal. This, however, is somewhat misleading, as all of the films grown at 10 Torr are forest-like meaning a high concentration of defective tips in the region on which the Raman laser is focused.

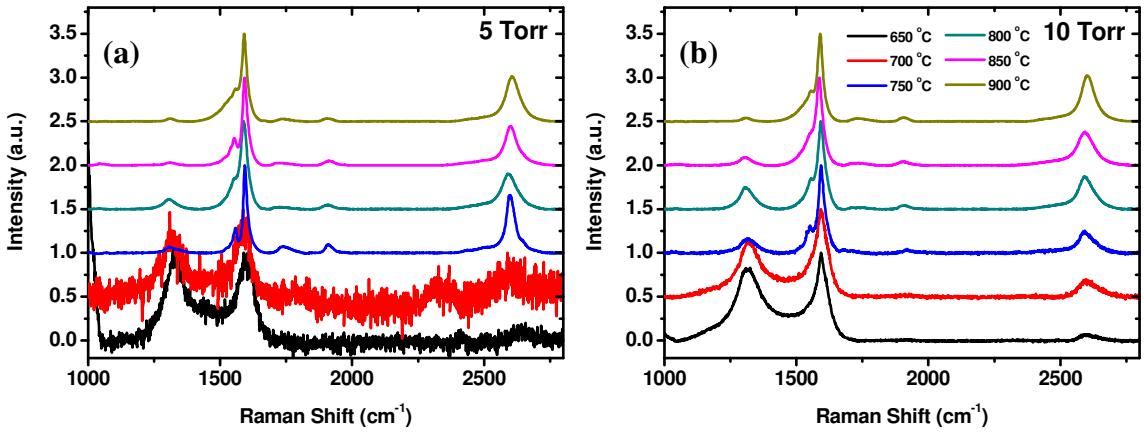

Figure 4.29 *Raman spectra for growth on CoFe SWNT catalyst at different growth temperatures with a growth pressure of (a) 5 Torr and (b) 10 Torr*

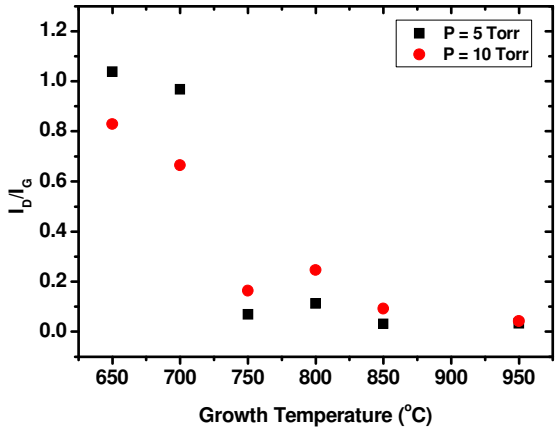

Figure 4.30 *I_D/I_G as a function of growth temperature for SWNT growth on CoFe catalyst*

A Raman plot of the RBM modes for temperatures in the range 750 – 950 °C is shown in Figure 4.31. This suggests the suppression of lower diameter contributions at high temperatures. In the temperature range 750 – 850 °C, the contribution of smaller diameter tubes (< 1 nm) is greater than that typically seen for water assisted growth[39]

and is comparable with that seen for growth on Co-Mo catalysts using alcohol precursors[40].

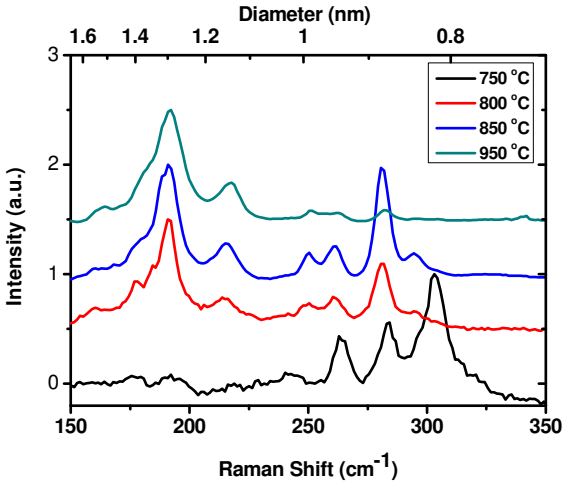

Figure 4.31 *RBM region for SWNTs grown on CoFe catalyst at different temperatures*

The optimum conditions for the production of SWNT forests were found to be a temperature of 850 °C and a pressure of 10 Torr. These conditions repeatedly yielded dense, aligned forests of high purity SWNTs with a length greater than 100 μm. The largest samples possible based on the furnace geometry were 3 x 3 cm in area. An optical image of such samples is shown in Figure 4.32(a). A SEM image of such a sample is shown, illustrating the length and alignment of the forest.

The transfer of SWNT films and forests was achieved through immersion of the growth substrates in HF. This dissolved the SiO_2 from the substrate leaving untethered SWNTs which could then be dredged onto arbitrary substrates. SEM images of films and forests transferred to PET by this technique are shown in Figure 4.33. Whilst the film remains intact and unchanged the forest sample undergoes densification upon drying outlining the low density of the aligned SWNTs. Such densification was also observed by dropping small volumes of solvents on top of forests. This technique has been used by other authors to produce "SWNT solids" for supercapacitor electrodes[41].

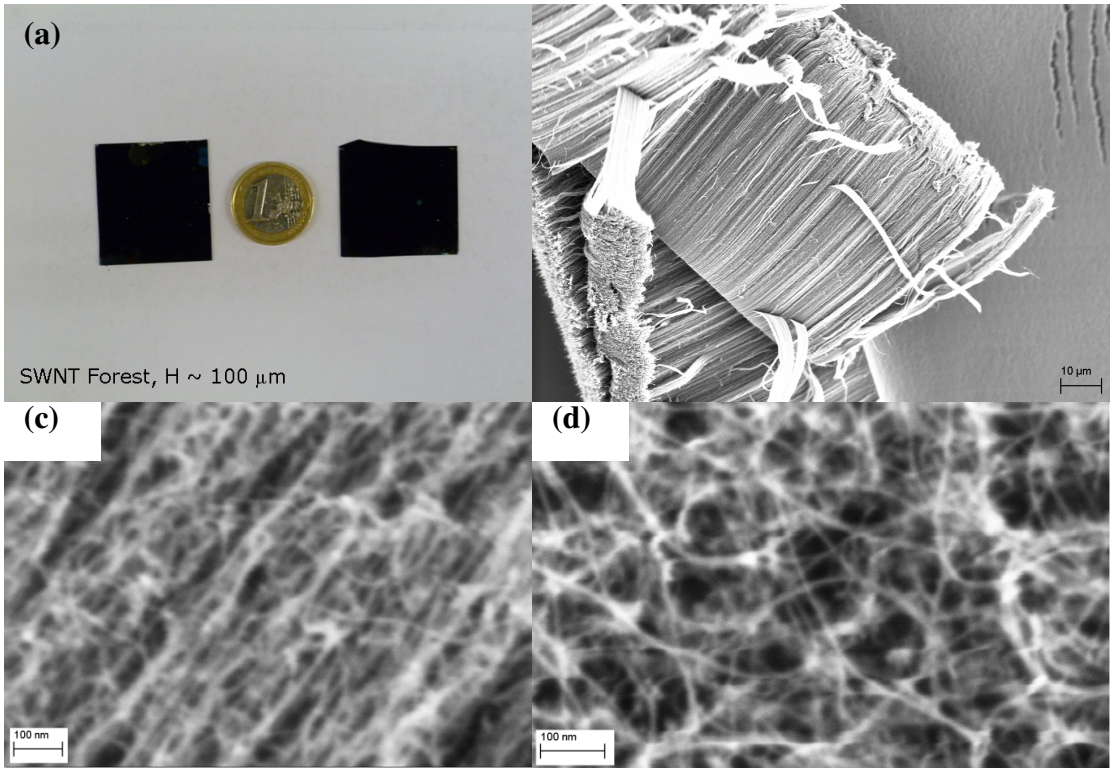

Figure 4.32 *(a) Image of SWNT forests on 3 x 3 cm substrates (b) SEM of SWNT forests showing vertical alignment and tube lengths of ~ 100 µm (c) High-mag SEM image in tilted mode (d) High-mag SEM image, top-down on forest.*

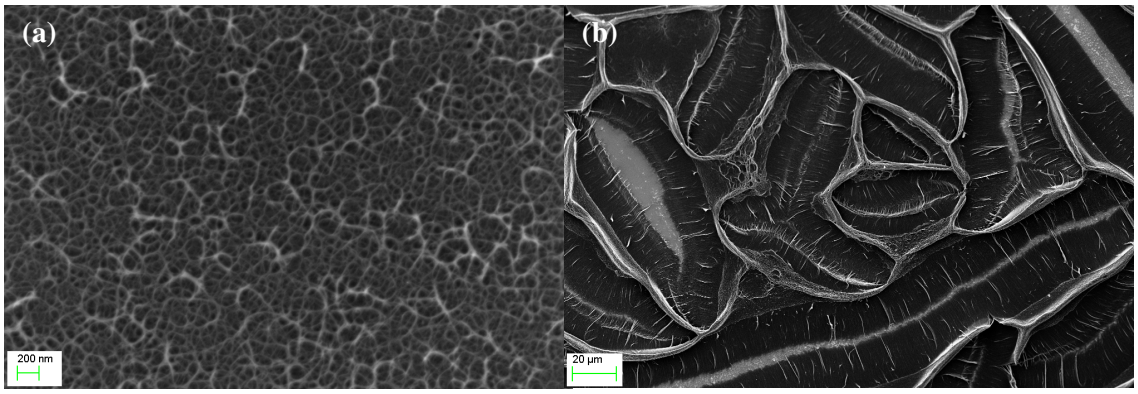

Figure 4.33 *(a) SWNT film and (b) SWNT forest transferred to PET by immersion in HF*

4.4 Conclusions

Thin Fe films produced by PLD were shown to be an effective catalyst for the growth of MWNT forests. Through modification of the temperature and gas flow the quality and alignment of the MWNTs grown could be varied. Incorporation of H_2 into the growth recipes greatly enhanced growth.

In order to obtain MWNT forests on a conducting substrate, films with a Ta layer between the SiO_2 substrate and the catalytic layer were used as growth substrates. Conditions were optimised for the production of long aligned forests of high quality MWNTs. Raman spectroscopy showed an increase in quality with increasing growth temperature, as seen in the ratios and peak widths of *D* and *G* bands in particular. Different alloy catalysts were also investigated and $Co_{90}Fe_{10}$ was seen to give the best quality growth.

The use of PPF as a conductive underlayer was investigated. This was seen to produce larger diameters of MWNTs with a bigger spread in diameters than seen for Ta underlayers. It was hypothesised that such structures could be of interest for modified electrochemical electrodes.

The use of NSL to define catalyst sites for MWNT growth was demonstrated. This offers a cheaper alternative to conventional lithography steps. PECVD allows for the production of well aligned CNF structures which are of interest for further field emission studies.

By reducing the thickness of the sputtered catalyst used, SWNTs were grown in film and forest geometries. Raman analysis indicated that the SWNTs grown were of high purity and comparable with those available commercially. Investigation of the RBM modes showed different distributions through the use of different catalysts. Furthermore, RBM modes indicative of small diameter tubes not seen in common commercial SWNTs were observed.

Conditions for the growth of well aligned SWNT forests were determined. Compared with thin film growth, this involved further dilution of the C_2H_2 feedstock and a higher overall gas flow. Changes in the growth temperature had a large impact on the quality of SWNTs grown. Optimal conditions were found at a growth temperature of 850 ^oC and a pressure of 10 Torr. Films and forests could both be transferred to arbitrary substrates by immersion in HF.

References

1. Dolbec, R., et al., *Growth dynamics of pulsed laser deposited Pt nanoparticles on highly oriented pyrolitic graphite substrates.* Physical Review B (Condensed Matter and Materials Physics), 2004. **70**(20): p. 201406-4.
2. Donnelly, T., B. Doggett, and J.G. Lunney, *Pulsed laser deposition of nanostructured Ag films.* Applied Surface Science, 2006. **252**(13): p. 4445-4448.
3. Donnelly, T., et al., *Pulsed laser deposition of nanoparticle films of Au.* Applied Surface Science, 2007. **254**(4): p. 1303-1306.
4. Liu, K., et al., *A growth mark method for studying growth mechanism of carbon nanotube arrays.* Carbon, 2005. **43**(14): p. 2850-2856.
5. Murakami, Y., et al., *Characterization of single-walled carbon nanotubes catalytically synthesized from alcohol.* Chemical Physics Letters, 2003. **374**(1-2): p. 53-58.
6. Hofmann, S., et al., *State of Transition Metal Catalysts During Carbon Nanotube Growth.* The Journal of Physical Chemistry C, 2009. **113**(5): p. 1648-1656.
7. Franklin, N.R., et al., *Patterned growth of single-walled carbon nanotubes on full 4-inch wafers.* Applied Physics Letters, 2001. **79**(27): p. 4571-4573.
8. Alsmeyer, Y.W. and R.L. McCreery, *Surface enhanced Raman examination of carbon electrodes: effects of laser activation and electrochemical pretreatment.* Langmuir, 1991. **7**(10): p. 2370-2375.
9. Atthipalli, G., et al. *Growth of carbon nanotubes on copper substrates using a nickel thin film catalyst*. in *2009 MRS Fall Meeting, November 30, 2009 - December 4, 2009*. 2010. Boston, MA, United states: Materials Research Society.
10. Delzeit, L., et al., *Multilayered metal catalysts for controlling the density of single-walled carbon nanotube growth.* Chemical Physics Letters, 2001. **348**(5-6): p. 368-374.
11. Kim, S.M. and L. Gangloff, *Growth of carbon nanotubes (CNTs) on metallic underlayers by diffusion plasma-enhanced chemical vapour deposition (DPECVD).* Physica E: Low-dimensional Systems and Nanostructures, 2009. **41**(10): p. 1763-1766.
12. Zhang, C., et al., *Growth of vertically-aligned carbon nanotube forests on conductive cobalt disilicide support.* Journal of Applied Physics, 2010. **108**(2).
13. Hofmann, S., et al., *In situ Observations of Catalyst Dynamics during Surface-Bound Carbon Nanotube Nucleation.* Nano Letters, 2007. **7**(3): p. 602-608.
14. Siegal, M.P., et al., *Linear Behavior of Carbon Nanotube Diameters with Growth Temperature.* The Journal of Physical Chemistry C, 2010. **114**(35): p. 14864-14867.
15. Flahaut, E., et al., *Synthesis of single-walled carbon nanotubes using binary (Fe, Co, Ni) alloy nanoparticles prepared in situ by the reduction of oxide solid solutions.* Chemical Physics Letters, 1999. **300**(1-2): p. 236-242.
16. Liu, Q., et al., *Effects of argon flow rate and reaction temperature on synthesizing single-walled carbon nanotubes from ethanol.* Physica E: Low-dimensional Systems and Nanostructures, 2009. **41**(7): p. 1204-1209.
17. Khedr, M.H., K.S. Abdel Halim, and N.K. Soliman, *Effect of temperature on the kinetics of acetylene decomposition over reduced iron oxide catalyst for the*

production of carbon nanotubes. Applied Surface Science, 2008. **255**(5, Part 1): p. 2375-2381.
18. Nakamura, K., M. Fujitsuka, and M. Kitajima, *Disorder-induced line broadening in first-order Raman scattering from graphite.* Physical Review B, 1990. **41**(17): p. 12260.
19. Benjamin, Y.P., et al., *Electrical Properties and Shrinkage of Carbonized Photoresist Films and the Implications for Carbon Microelectromechanical Systems Devices in Conductive Media.* Journal of The Electrochemical Society, 2005. **152**(12): p. J136-J143.
20. Schreiber, M., et al., *Transparent ultrathin conducting carbon films.* Applied Surface Science, 2010. **256**(21): p. 6186-6190.
21. Ito, T. and S. Okazaki, *Pushing the limits of lithography.* Nature, 2000. **406**(6799): p. 1027-1031.
22. Deckman, H.W. and J.H. Dunsmuir, *Natural lithography.* Applied Physics Letters, 1982. **41**(4): p. 377-379.
23. Shim, S.E., et al., *Size control of polystyrene beads by multistage seeded emulsion polymerization.* Journal of Applied Polymer Science, 1999. **71**(13): p. 2259-2269.
24. Fan, H.J., et al., *Well-ordered ZnO nanowire arrays on GaN substrate fabricated via nanosphere lithography.* Journal of Crystal Growth, 2006. **287**(1): p. 34-38.
25. Kyung Ho, P., et al., *Advanced nanosphere lithography for the areal-density variation of periodic arrays of vertically aligned carbon nanofibers.* Journal of Applied Physics, 2005. **97**(2): p. 024311.
26. Pacifico, J., D. Gómez, and P. Mulvaney, *A Simple Route to Tunable Two-Dimensional Arrays of Quantum Dots.* Advanced Materials, 2005. **17**(4): p. 415-418.
27. Rybczynski, J., U. Ebels, and M. Giersig, *Large-scale, 2D arrays of magnetic nanoparticles.* Colloids and Surfaces A: Physicochemical and Engineering Aspects, 2003. **219**(1-3): p. 1-6.
28. Zhang, X.Y., C.R. Yonzon, and R.P. Van Duyne, *Nanosphere lithography fabricated plasmonic materials and their applications.* Journal of Materials Research, 2006. **21**(5): p. 1083-1092.
29. Cheung, C.L., et al., *Fabrication of nanopillars by nanosphere lithography.* Nanotechnology, 2006. **17**(5): p. 1339.
30. Wang, B., et al., *Formation of nanoimprinting mould through use of nanosphere lithography.* Journal of Crystal Growth, 2006. **288**(1): p. 200-204.
31. Fan, S., et al., *Self-Oriented Regular Arrays of Carbon Nanotubes and Their Field Emission Properties.* Science, 1999. **283**(5401): p. 512-514.
32. Mathur, A., et al., *Growth of carbon nanotube arrays using nanosphere lithography and their application in field emission devices.* Diamond and Related Materials, 2010. **19**(7-9): p. 914-917.
33. Milne, W.I., et al., *Carbon nanotubes as field emission sources.* Journal of Materials Chemistry, 2004. **14**(6): p. 933-943.
34. Cheung, C.L., et al., *Diameter-Controlled Synthesis of Carbon Nanotubes.* The Journal of Physical Chemistry B, 2002. **106**(10): p. 2429-2433.
35. Li, Y., et al., *Growth of Single-Walled Carbon Nanotubes from Discrete Catalytic Nanoparticles of Various Sizes.* The Journal of Physical Chemistry B, 2001. **105**(46): p. 11424-11431.

36. Ohno, H., et al., *Growth of vertically aligned single-walled carbon nanotubes on alumina and sapphire substrates.* Japanese Journal of Applied Physics, 2008. **47**(4): p. 1956-1960.
37. Inoue, S., Y. Kikuchi, and Y. Matsumura, *Effect of catalyst combination on growth of single-walled carbon nanotubes.* Diamond and Related Materials, 2008. **17**(11): p. 1888-1890.
38. McCaldin, S., et al., *The effect of processing conditions on carbon nanostructures formed on an iron-based catalyst.* Carbon, 2006. **44**(11): p. 2273-2280.
39. Hata, K., et al., *Water-assisted highly efficient synthesis of impurity-free single-waited carbon nanotubes.* Science, 2004. **306**(5700): p. 1362-1364.
40. Maruyama, S., et al., *Low-temperature synthesis of high-purity single-walled carbon nanotubes from alcohol.* Chemical Physics Letters, 2002. **360**(3-4): p. 229-234.
41. Futaba, D.N., et al., *Shape-engineerable and highly densely packed single-walled carbon nanotubes and their application as super-capacitor electrodes.* Nature Materials, 2006. **5**(12): p. 987-994.

Chapter 5

CVD Growth of Pyrolytic Carbon

5.1 Introduction

Pyrolytic carbon (PyC) can be formed through gas phase dehydrogenation (or pyrolysis) of hydrocarbons and subsequent deposition on surfaces. This is non-catalysed and can be thought of as a pure CVD process. PyC is mostly sp^2 hybridised and can be considered as disordered nanocrystalline graphite. PyC belongs to the family of turbostratic carbons due to slipped or randomly oriented basal planes of crystallites. Gas phase deposition means that PyC can be deposited onto many different substrates in a conformal fashion. Infiltration of porous materials and fibres is also possible.
Depending on the growth parameters used, the orientation of deposited crystals with respect to the growth substrate can vary between isotropic and laminar. The orientation of crystals has been characterised using techniques such as selected area electron diffraction (SAED), polarised light microscopy and polarised Raman spectroscopy [1-4].

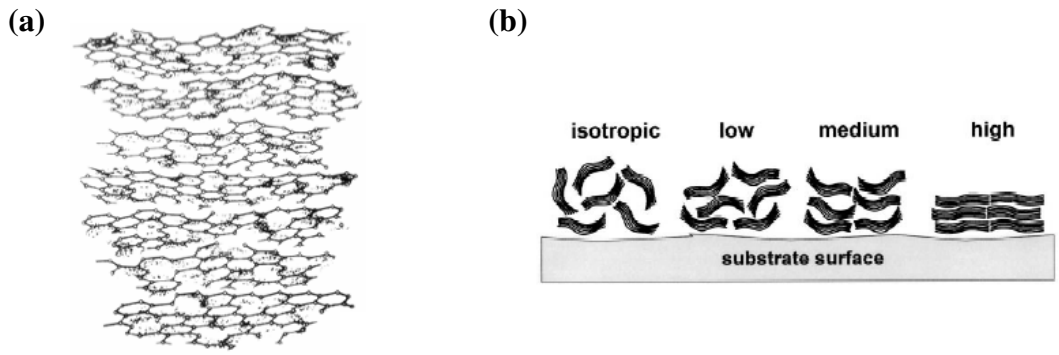

Figure 5.1 *(a) Nanocrystalline structure of PyC (b) Different orientations of PyC adapted from[5].*

PyC exhibits good thermal and electrical conductivity as well as high durability and chemical and wear resistance. The thermal and mechanical properties have led to usage as a coating for individual pebbles in pebble bed reactors[6] and rocket nozzles[7] as well as electronic thermal management applications including heat spreaders[8].

PyC is biocompatible and thromboresistant and has been investigated as a coating for heart valves and other forms of prosthesis[9-10]. Chemical vapour infiltration (CVI) has been used with CNFs to form assorted carbon felt materials [11-12]. It has also been used to coat optical fibres making them more resistant to harsh environmental conditions[13]. Deposition into pores and trenches has been demonstrated by using PyC as a liner for trench capacitors in DRAM applications[14]. PyC can be readily patterned making it suitable for other microelectronics applications including vias and wires[15] and gate electrodes[16].

The pyrolysis of hydrocarbons is a very complicated process with a large number of different reaction pathways. The chemistry and kinetics of PyC formation from different hydrocarbons has been extensively investigated by the Huttinger group [17-21]. In the case of acetylene[17], it was shown that it was very reactive in PyC deposition and that ethylene, benzene and methane were all formed upon pyrolysis but at low partial pressures, thus suggesting direct deposition from C_2H_2. Higher deposition rates were observed with longer reaction times indicating the formation of consecutive products with higher reactivity after a short period of time (0.11 - 0.33 s).

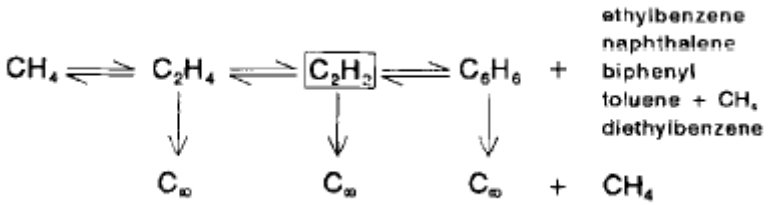

Figure 5.2 *Reaction pathways for PyC formation from C_2H_2 [17].*

This chapter deals with the production of thin films of PyC on substrates by CVD. The effect of varying growth parameters was investigated in order to achieve fine control over the thickness, sheet resistance and morphology of the films grown. The films produced were extensively characterised using various forms of spectroscopy and microscopy.

The feasibility of using such a process for depositing thin coatings on films of SWNTs for the production of all carbon composite materials is considered. The use of a Ni catalyst and annealing treatments to improve the graphitisation of PyC films was also investigated.

5.2 Pyrolytic Carbon Production

A series of PyC films were grown on SiO_2 substrates (300 nm SiO_2 on Si <100>) in the Gero furnace system. C_2H_2 was used as the hydrocarbon source at a flow rate of 180 sccm. No other process gases were used. Temperatures in the range of 850 – 1100 ^oC were used with pressures in the range of 5 – 20 Torr. The thickness of the films grown was measured by stylus profilometry and the sheet resistance was measured using the four point probe technique.

5.2.1 Temperature Dependence

PyC films were grown at temperatures in the range of 850 – 1100 ^oC with different deposition times, whilst keeping all other growth parameters constant (P = 20 Torr, flow = 180 sccm). Films grown at 950 ^oC and 20 Torr show an increase in thickness with increasing growth time as seen in Figure 5.3. This trend was verified by profilometry. At 850 ^oC the deposition rate becomes slow e.g. 30 minutes results in a thickness of 23 ± 3 nm. For higher growth temperatures the thickness of films grown was seen to increase in a linear fashion with deposition time Figure 5.4. Becker et al. reported an increase in deposition rate with deposition time in similar experiments[17]. However, this was with much shorter deposition times (~ 1s) and so is not directly comparable.

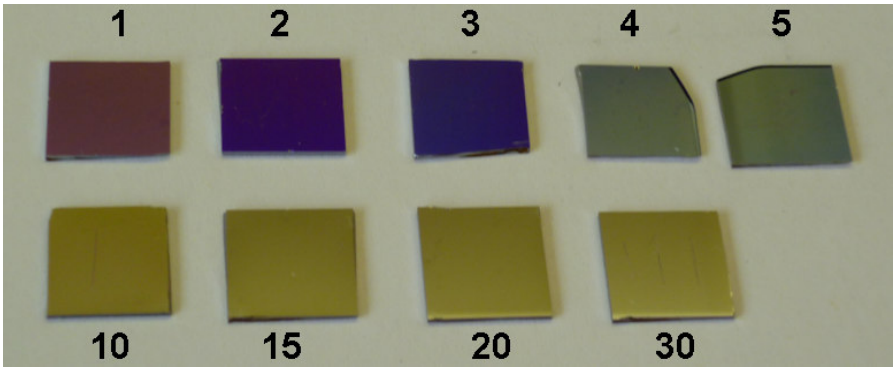

Figure 5.3 *Different thicknesses of PyC grown on SiO_2 substrates with different deposition times (numbers indicate deposition time in minutes) at T = 950 ^oC and P = 20 Torr.*

The deposition rate was obtained from the slope of these linear plots and was seen to vary from 3.72 ± 0.23 nm/min at 900 ^{o}C to 168.2 ± 9.70 nm/min at 1100 ^{o}C, where the error stems from the standard error in the linear fits. Thus precise control over film deposition rate and thickness was possible through growth temperature variation. A plot of deposition rate versus growth temperature is shown in Figure 5.4(f).

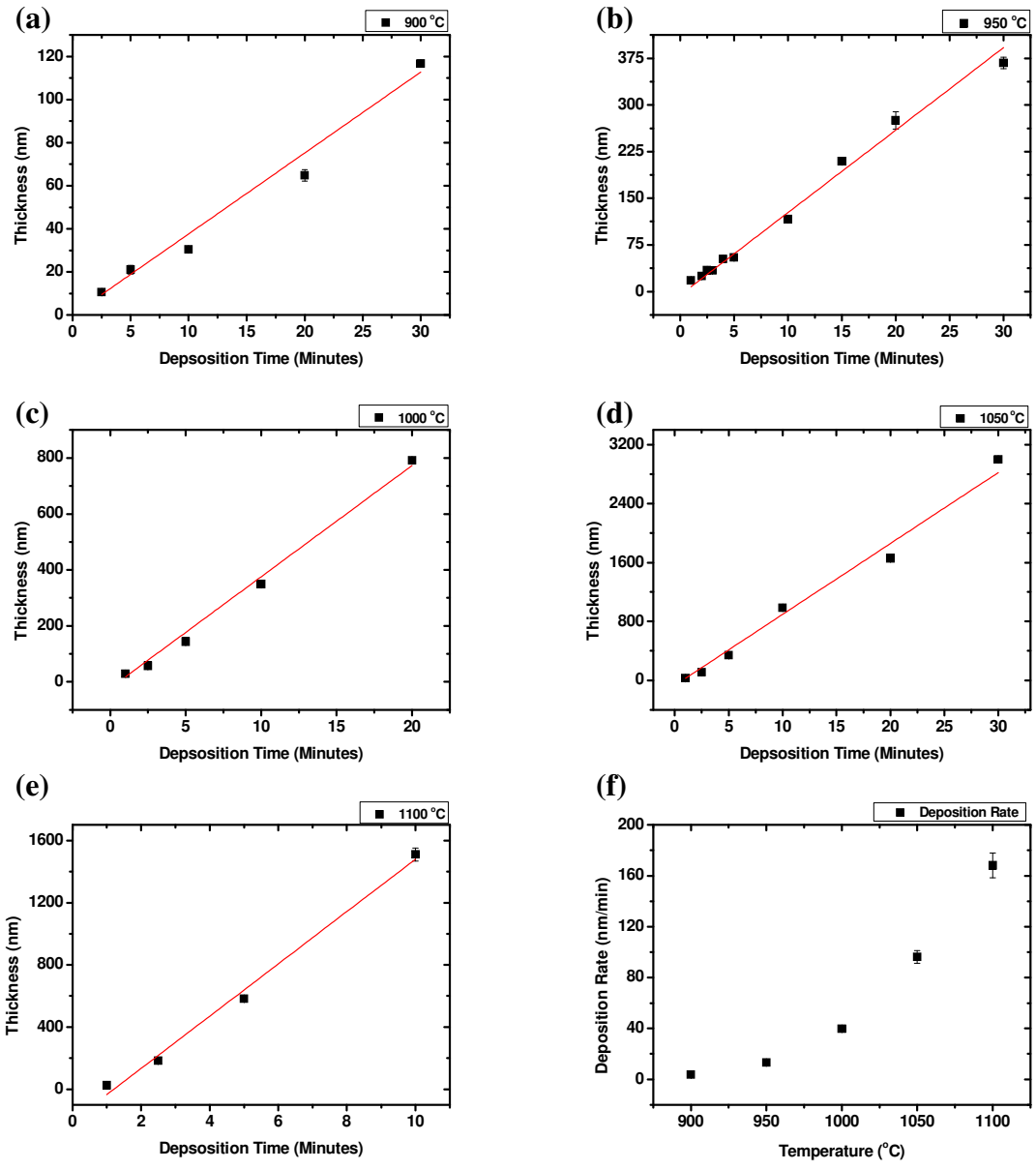

Figure 5.4 *(a – e) PyC film thickness as a function of deposition time for different deposition temperatures (f) Deposition rate as a function of temperature.*

The deposition rate was seen to increase in an exponential fashion with increasing growth temperature. This suggested a thermally activated process which can be described by the Arrhenius equation. A plot of the natural log of the deposition rate against the inverse of the deposition temperature as shown in Figure 5.5 verifies this. From the slope an activation energy of 2.68 ± 0.15 eV (259 ± 15 kJ/mol) was calculated. For comparison acetylene has an enthalpy of formation of 226.7 kJ/mol.

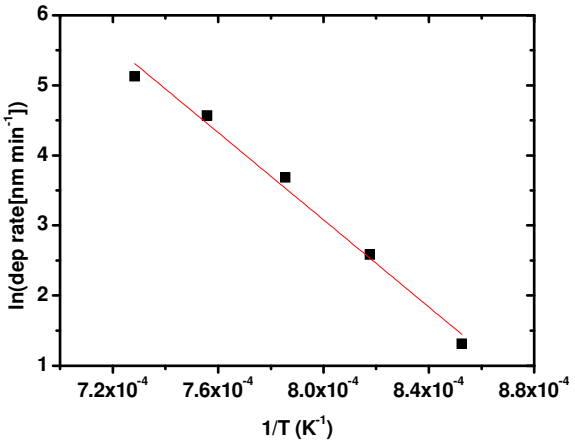

Figure 5.5 *Arrhenius plot, natural log of PyC deposition rate versus the reciprocal temperature.*

5.2.1 Pressure Dependence

PyC films were grown at different growth pressures whilst keeping all other growth parameters constant (T = 950 ^{o}C, C_2H_2 flow = 180 sccm). The film thicknesses for different growth pressures are shown in Figure 5.6. The growth pressure was seen to have a big impact on film thickness with a pressure of 20 Torr giving a deposition rate of 13.32 ± 0.66 nm/min, 10 Torr giving a deposition rate of 2.49 ± 0.28 nm/min and 5 Torr giving a deposition rate of 0.61 ± 0.10 nm/min. So, for fine control over thickness low pressures can be used as well as/instead of low temperatures.

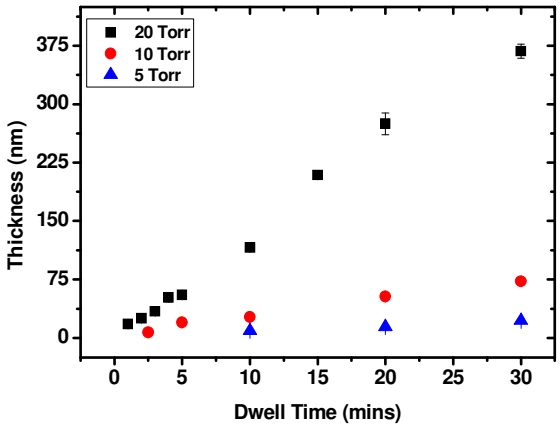

Figure 5.6 *PyC film thickness as a function of time for different growth pressures.*

5.2.3 Sheet Resistance Measurements

The sheet resistance of all PyC samples grown was measured using the four point probe technique. Typically ten sites near the centre of each sample were measured. The sheet resistance as a function of deposition time obtained at 950 ^{o}C and 20 Torr are shown in Figure 5.7 on the same axis as the thickness measurements.

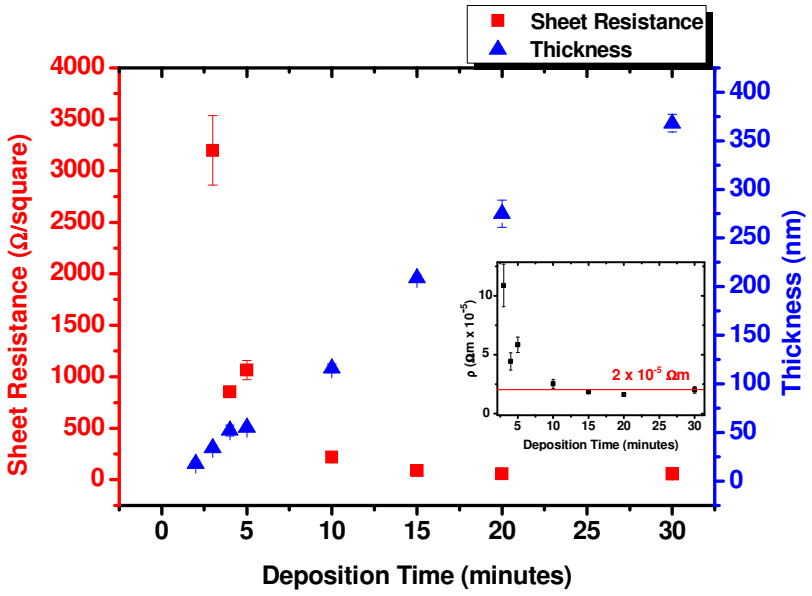

Figure 5.7 *Film thickness and sheet resistance as a function of deposition time for T = 950 ^{o}C and P = 20 Torr. Inset: Resistivity values for different deposition times.*

Using the thickness values obtained from profilometry and the sheet resistances measured by the four point probe technique the resistivity (ρ) could be calculated using equation 3.5. The calculated value for PyC films produced at 950 ^{o}C and 20 Torr with 30 mins deposition was (2.02 ± 0.28) x 10^{-5} Ωm. Deposition times of 10 minutes and greater gave rise to similar resistivities. For deposition times less than 10 minutes (t < 100 nm) the resistivity was seen to increase suggesting a lack in uniformity for very thin films.

The measured value of ρ for films of thickness > 100 nm is larger than that of graphite[22] (1.4 x 10^{-5} Ωm), pristine CNT films[23] (~4 x 10^{-6} Ωm) and CVD graphene[24] (10^{-7}-10^{-8} Ωm) but less than that of pyrolysed photoresist films (PPF)[25] (6.25 x 10^{-5} Ωm) or liquid phase graphene based thin films[26] (6.67 x 10^{-5} Ωm).

5.2.4 Transmittance Measurements

A series of PyC samples were grown on fused quartz substrates (pure SiO_2, no underlying Si) with different growth times in order to measure transmittance of films of different thicknesses. Growth conditions involved a temperature of 950 ^{o}C and a pressure of 20 Torr.

Transmittance and absorbance spectra for different dwell times are shown in Figure 5.8. These show an increase in absorbance in the visible range with increasing film thickness. A peak in the absorbance is seen in the UV region at ~ 255 nm. This corresponds to an energy of ~4.86 eV. This peak is seen in a wide variety of graphite like materials and is assigned to interband absorption between π bands near the *M* point in the Brillouin zone[27].

The transmittance at 550 nm was shown to be 93 % for 2 minutes of PyC deposition and < 1 % for 15 minutes deposition. Transmission values were compared with the sheet resistances for an extended series of different deposition times as shown in Figure 5.9. The contribution of PyC deposited on the underside of the quartz substrates had to be factored into the overall sheet resistance. This was not considered for SiO_2 films on Si substrates as the underside of the substrate was unimportant.

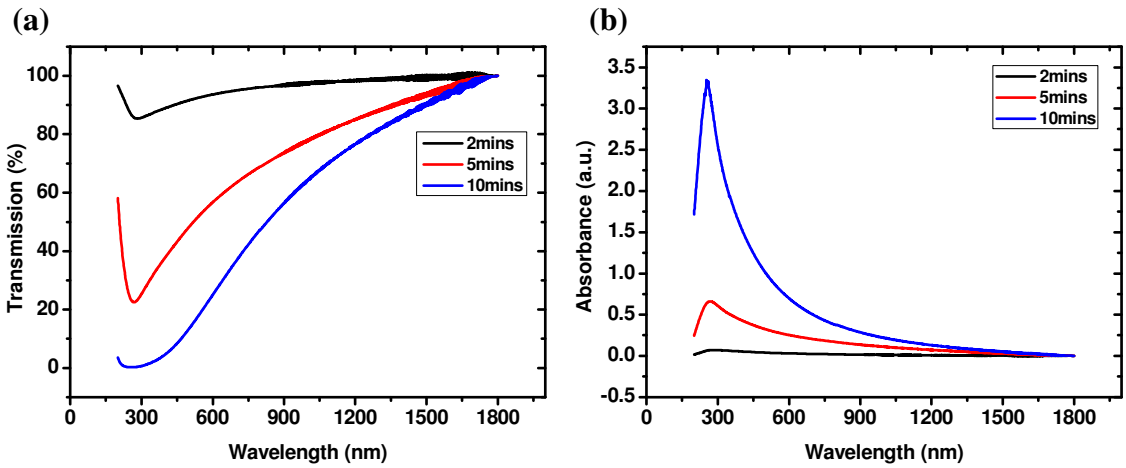

Figure 5.8 *(a) Transmission and (b) Absorbance spectra of PyC films prepared with different growth times.*

For transparent electrode materials, a combination of high electrical conductivity and high optical transmittance is required. In practice, a combination of 90% transmittance in the visible range and a sheet resistance of < 200 Ω/□ is desirable. To examine this it is convenient to use a figure of merit given by the ratio of the DC electrical conductivity (σ_{DC}) to the optical conductivity (σ_{op}). The DC electrical conductivity governs the response of electrons to constant applied fields whereas the optical conductivity governs the response of electrons to optical fields. The optical conductivity is related to the absorption coefficient, α, by $\sigma_{op} \approx 2\alpha/Z_{0,}$[28-29] where Z_0 is the impedance of free space (377 Ω).

For industry standard transparent conductors a minimum value of 35 is required. For films where the transmittance (T) and sheet resistance (R_s) are known the conductivity ratio can be calculated using the equation;

$$T = \left(1 + \frac{Z_0}{2R_S}\frac{\sigma_{op}}{\sigma_{DC}}\right)^{-2} \qquad \textit{Equation 5.1}^{[30]}$$

Using Equation 5.1, values in the range 0.8 – 1.1 are obtained for PyC films which fall short of required industry standard. This value is better than that of the majority of graphene films produced by liquid phase processing(0.001 – 0.7)[31] but below that of pristine SWNT networks (13.0)[23] and Ag nanowire networks (500)[32].

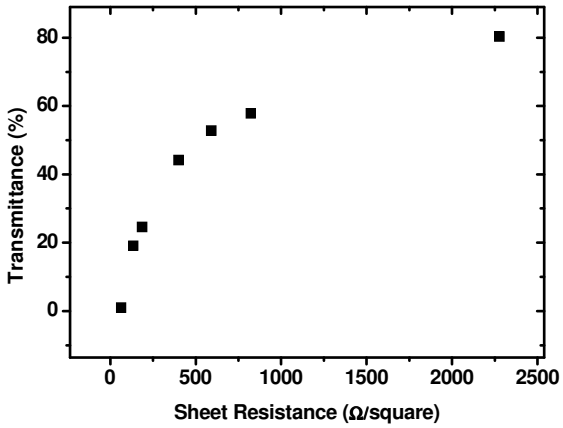

Figure 5.9 *Sheet resistance versus transmittance for PyC films of different thickness*

5.2.5 AFM Analysis

AFM images were taken for different deposition times for T = 950 ^{o}C and P = 20 Torr and showed little difference in roughness. A plot of roughness as a function of deposition time and a typical AFM image are shown in Figure 5.10. In all cases the roughness was less than 1 nm illustrating the smooth surface of the PyC films.

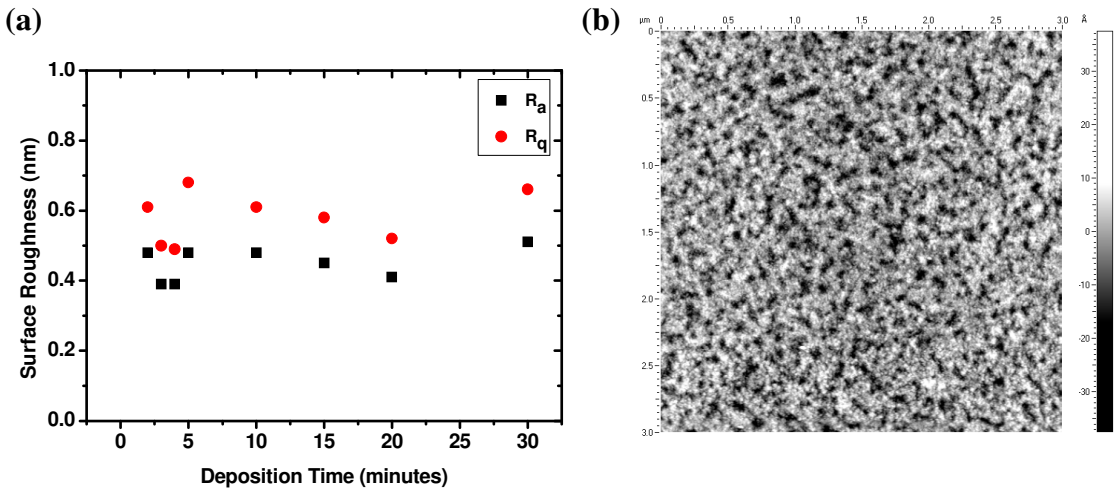

Figure 5.10 *(a) Roughness values obtained by AFM for PyC films with different deposition times (all T = 950 ^{o}C, P = 20 Torr) (b) AFM image of PyC film with a deposition time of 10 minutes (scale, 3 x 3 μm).*

Whilst the measured roughness was constant for different deposition times at 950 ^{o}C/20 Torr it was seen to increase with increasing growth temperatures. Films grown at 1000 ^{o}C exhibited roughnesses > 1 nm and films grown at 1100 ^{o}C were very rough (Ra > 10 nm). AFM images of films grown at 1050 ^{o}C and 1100 ^{o}C are shown in Figure 5.11. In both cases globular structures were observed. These have heights in the range 10 – 60 nm for 1050 ^{o}C and up to 150 nm for 1100 ^{o}C. Thus, for smooth (preferable for coatings) and thin films, lower deposition temperatures are required. This observation is consistent with SAED measurements performed by Meadows et al. who showed an increase in isotropy with increasing deposition temperature[33]. The increased roughness can be attributed to the rapid growth and nucleation of crystals (which occurs at higher temperatures).

(a)

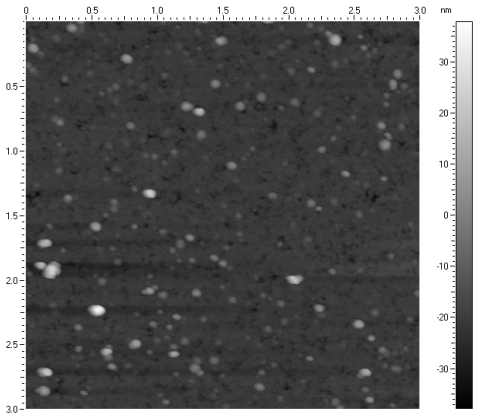

(b)

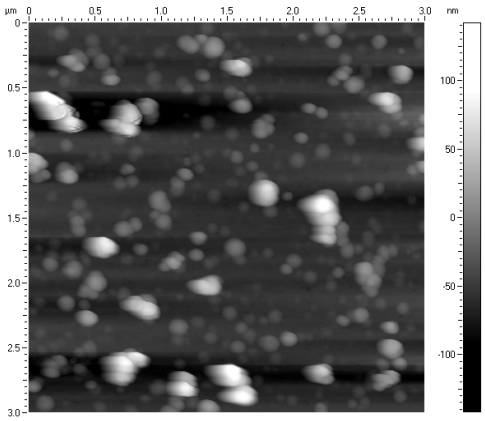

(c)

T (^{o}C)	Ra (nm)	Rq (nm)
1000	1.02	1.35
1050	1.83	3.8
1100	14.93	22.3

Figure 5.11 *AFM images of PyC films grown at (a) 1050 ^{o}C and (b) 1100 ^{o}C (scale 3 x 3 μm) (c) a table of associated roughness values.*

5.2.6 Raman Analysis

Raman spectra of the PyC films grown showed broad *D* and *G* bands with a high A_D/A_G ratio indicative of the nanocrystalline nature of PyC[34-35]. The second order bands in graphitic materials are related to spatial uniformity in the graphitic plane or uniformity of the interlayer spacing. The spectra obtained suggest that the PyC grown is laminar or

highly textured as the *2D* band is weak and forms a bump with surrounding bands[36]. Spectra taken for PyC deposited at different temperatures are shown in Figure 5.12(a). There is little change in the *G* and *D* band shape or intensity ratios suggesting the disorder levels and crystallite size are similar and the growth mechanism doesn't vary in the temperature range used. A small peak was observed at ~950 cm^{-1} for the sample grown at 850 ^{o}C. This stems from the SiO_2 substrate and is due to the fact that the thickest samples grown at this temperature were thinner than the penetration depth of the Raman laser in carbon (~ 30 nm).

The deposition of PyC was not limited to just SiO_2 on Si and pure quartz substrates. Films were grown on a series of different catalytically inert substrates at 950 ^{o}C. Raman spectra of these films grown are shown in Figure 5.12(b). The *D* and *G* band shape and intensities are independent of the substrate used suggesting that the PyC deposited is structurally identical.

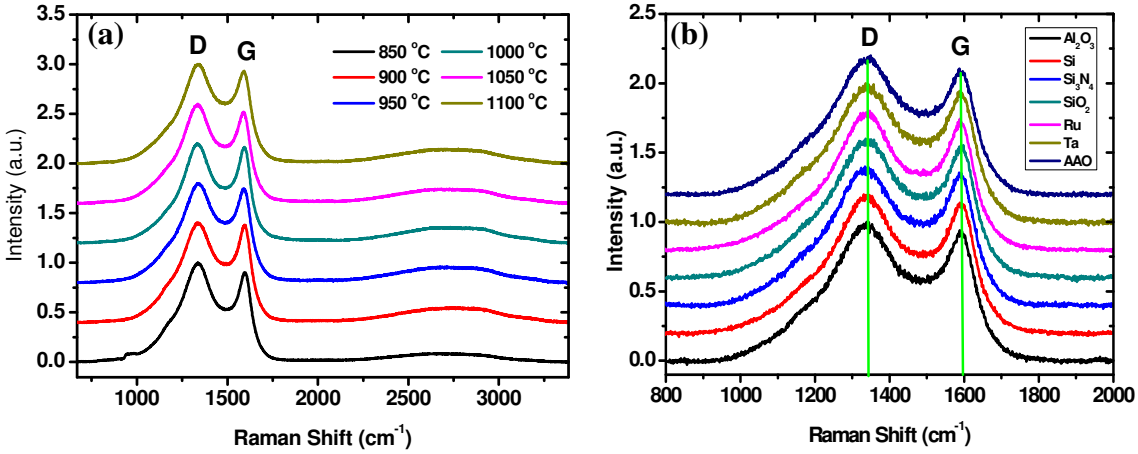

Figure 5.12 *Raman spectra of PyC films grown exhibiting broad D and G bands (a) at different temperatures and (b) on different substrates.*

The spectrum was deconvoluted as described previously by Vallerot et al[3]. This entailed the fitting of additional bands associated with nanocrystalline graphitic materials as well as the standard *D*, *G* and *D'* bands. These additional bands are labelled *I* and *D''* and are found at ~ 1180 cm^{-1} and ~ 1500 cm^{-1} respectively. The *I* band has been linked with disorder in the graphitic lattice, sp^2-sp^3 bonds[37] or the presence of polyenes[38] whereas the *D''* band is generally thought to stem from the presence of amorphous carbon[39]. Both of these peaks were fitted with Gaussian

functions. A deconvoluted plot is shown in Figure 5.13. An estimate of the crystallite size (L_a) was calculated using the integrated intensities of the *D* and *G* bands with equation 2.8. This gave a value of ~ 8 nm.

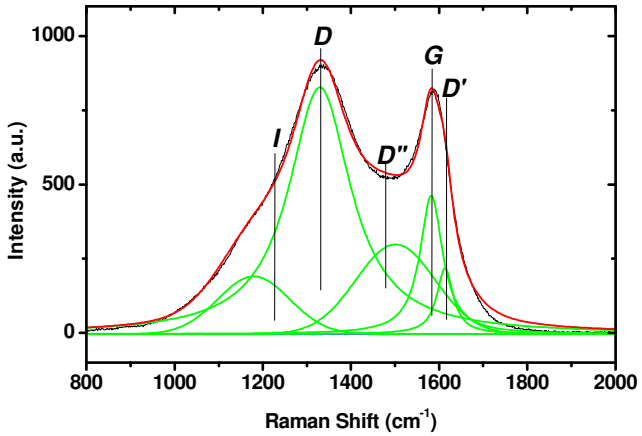

Figure 5.13 *Deconvoluted Raman spectrum of as grown PyC showing D, G, D', D'' and I bands*

5.2.7 XPS Analysis

XPS was used to probe the surface of thick (~ 400 nm) and thin (~ 20 nm) PyC films grown at 950 ^{o}C. High resolution C_{1s} core level spectra are shown in Figure 5.14(a). An asymmetric peak centred at 284.2 eV is seen. This has a tail which extends into the higher energy region. This peak is indicative of polyaromatic or graphitic structures with sp^2 hybridisation and delocalised π electrons. The asymmetry is associated with metallic systems and gives a good indication of conductivity [40-41].

A wide scan of these films is shown in Figure 5.14(b). Traces of O, N and F species are seen. These are likely to stem from contaminants incorporated during or after the growth process. Deconvolution of the C_{1s} spectrum is shown in Figure 5.14(c). The main peak located at 284.14 eV has been fitted with a Doniach-Sunjic function[42] which accounts for the asymmetry in the high energy end. This is an intrinsic property of the system based on the many-electron interaction[43-44]. The function used for fitting was of the form;

$$DS(E) = \beta \frac{\cos\left\{\pi\frac{\alpha}{2} + (1-\alpha)\arctan\left(\frac{E-E_0}{\beta}\right)\right\}}{\left[(E-E_0)^2 + \beta^2\right]^{\frac{1-\alpha}{2}}}$$

Equation 5.2

where β corresponds to half of the full width at half maximum height (FWHM), E_0 is the peak position and α is an asymmetry factor. The function transforms into a Lorentzian in the limit $\alpha \rightarrow 0$, as is seen for insulating systems which have symmetric peaks.

The asymmetry factor can be thought of as a measure of the screening of the core hole which depends on the delocalisation of the valence band. Highly defective (or nanocrystalline) graphitic systems display large asymmetry factors as they have a high density of edges and defect sites which leads to differential charging and the creation of excitonic states[45]. Highly crystalline graphitic materials have a higher delocalisation of electrons and so display a smaller asymmetry factor. The magnitude of α, thus gives an indication of the in-plane order and level of defects in the graphitic lattice and in turn the electrical conductivity. Fitting the PyC C_{1s} spectrum gave an extrapolated value for α of 0.191 which is in good agreement with literature values[45].

Peak fitting of the C_{1s} level also indicated the presence of aliphatic species (284.67eV) and assorted functional groups, C-OH (285.8 eV), C-CF & C-N (286.82 eV), CF-C (288.1 eV) and COOH/COOR (288.79 eV) [40-41, 46-48]. Of particular interest is the peak seen at 283.73 eV which is associated with extensive carbon doping of SiO_2[49]. The combination of this peak and the position of the Si_{2p} peak (101.5 eV, Figure 5.14(d)) suggests the presence of SiOC:H[49-51]. This is a highly porous low κ dielectric material. It is proposed that a thin layer is formed due to the dissolution of carbon in the SiO_2 substrate. Additional experiments and analysis are required to investigate the formation of this layer further.

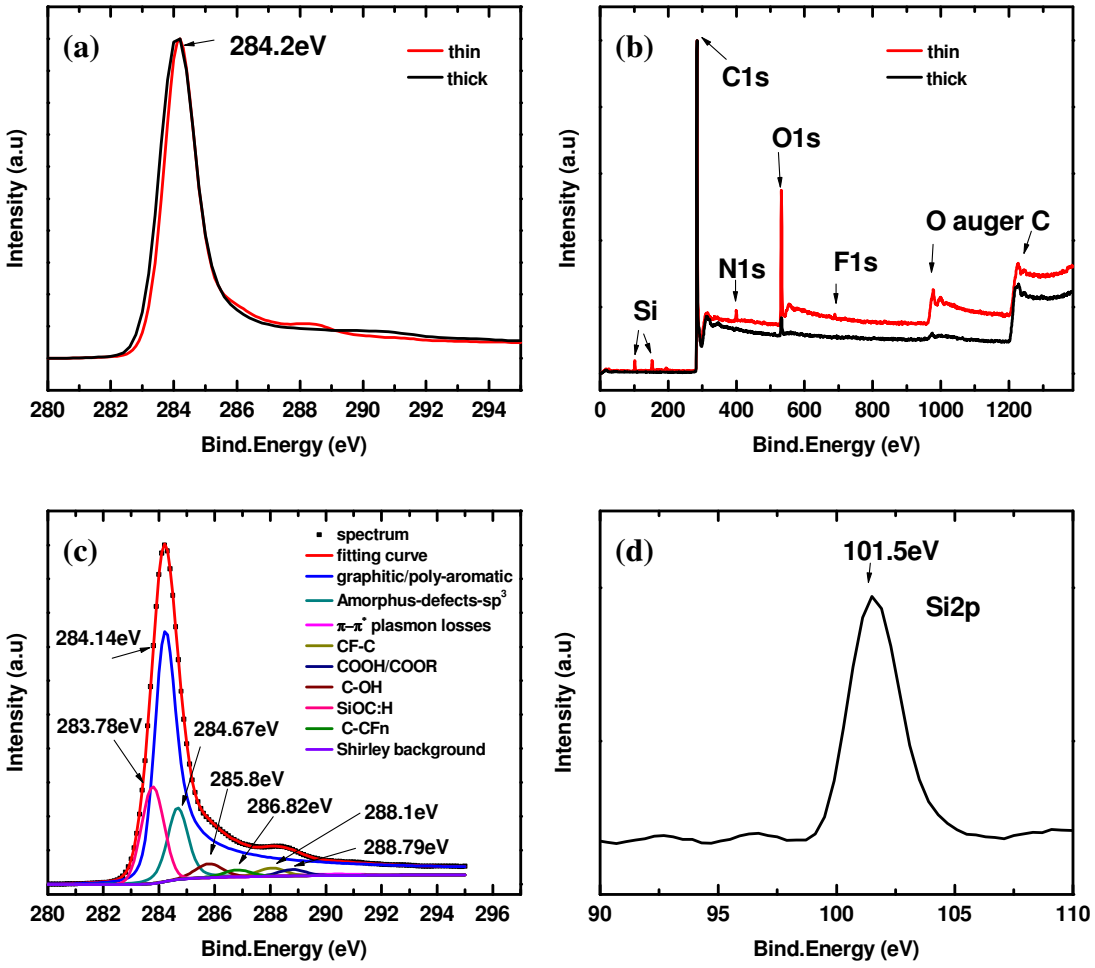

Figure 5.14 *(a) High resolution XPS spectrum of the C_{1s} core level for thick and thin PyC films. (b) Wide range scan of the same films (c) Peak fitting of the C_{1s} core level for the thin film. (d) Si_{2p} peak for the thin PyC sample. The peak position is indicative of SiOC:H.*

5.2.8 Conclusions

Thin films of PyC were grown on various substrates by CVD. The thickness and roughness of these films could be controlled by varying the temperature, pressure and deposition time used. AFM analysis showed that smooth films could be produced (R_a < 0.5 nm) and Raman spectroscopy verified their nanocrystalline nature. XPS analysis indicated the presence of various functional groups on the surface and suggested the formation of an SiOC:H layer between the SiO_2 and the PyC.

The films had a resistivity of ~ 2 x 10^{-5} Ωm and a conductivity ratio (σ_{DC}/σ_{op}) in the range 0.8 - 1.1. These values were better than those typically seen for thin films of PPF and liquid processed graphene but still fall short of the required industry standard for thin transparent conductors.

5.3 PyC/SWNT Composites

Chemical vapour infiltration (CVI) has been extensively used to create carbon-carbon composites consisting of CNFs as filler material in a matrix of PyC [11-12, 52]. These materials have a wide range of applications including aircraft brake disks and missile nose cones[53]. A number of authors have also demonstated CVI processes for the densification of MWNT forests. Allouche et al. used a two step CVD process to first grow MWNT forests and then deposit PyC[54]. This led to the formation of different morphologies of fibres with thicknesses in the μm range. Li et al. carried out similar experiments but demonstrated control over deposition thicknesses in the densification of MWNT forests[55].

Here, a carbon composite material was prepared using PyC to coat thin films of SWNTs. Such films are of interest for electrode applications and also for heat dissipation. Arc discharge SWNTs (Iljin) were used as they have been shown to exhibit excellent electrical properties[23]. Thin films were made from surfactant (SDS) stabilised dispersions of these SWNTs by vacuum filtration onto cellulose membranes. The films were then by transferred onto SiO_2 by dissolution of the membrane in acetone. Films with a thickness of 50 nm were obtained from collaborators and used as a scaffold for PyC deposition. The films were placed in the furnace at room temperature and the temperature was then ramped up to 950 ^{o}C under H_2 flow (60 sccm). PyC deposition was carried out using C_2H_2 at 10 Torr with a 180 sccm flow for different deposition times. After deposition the furnace was cooled to room temperature under H_2. A reference run was carried out without the deposition step. Samples were characterised pre and post deposition by SEM and Raman spectroscopy. Reference SiO_2 samples were included in each run, these showed PyC thicknesses of 61, 35 and 20 nm for 20, 10 and 5 minute depositions respectively.

5.3.1 Raman Analysis

Raman spectra of SWNT films pre and post PyC deposition using a 633 nm excitation wavelength are shown in Figure 5.15. The spectrum of the pristine SWNTs shows a *G* band shape indicative of mostly metallic SWNTs in resonance, this is further supported by the strong *2D* band intensity[56].

Raman spectra of the *D*, *G* and *2D* bands for pristine CNTs, H_2 annealed CNTs and those with PyC deposition are shown in Figure 5.15(a). It is clear from these spectra that the I_D/I_G ratio increases with increasing PyC deposition time. Some of this can be attributed to the H_2 anneal which leads to an increase in the *D* band intensity. In this case the *D* band remains narrow with a FWHM of 30 – 40 cm $^{-1}$ and the peak position remains the same at ~ 1318 cm^{-1}. This is a surprising result as in general such a high temperature anneal would be expected to de-dope the tubes and reduce the *D* band intensity [57-58]. The increased defect signal could be due to impurities from the furnace walls.

With the addition of PyC the *D* band upshifts with increasing PyC deposition up to ~ 1344 cm^{-1} for 20 minutes deposition, highlighting the mixing of the PyC and SWNT Raman signals. Furthermore the FWHM of the *D* band increases up to > 250 cm^{-1}.

The effect of PyC deposition on the *G* band is shown in Figure 5.15(b). The *G* band is seen to broaden with PyC deposition, again some of this can be attributed to the H_2 anneal but the effect is more pronounced with longer PyC deposition times. There is also an upshift in the *G* band frequency (not seen for the H_2 anneal) of ~ 5 cm^{-1} consistent with mixing of the PyC and CNT signals.

The *2D* band is shown in Figure 5.15(c). In this case the band is reduced in intensity and upshifts due to mixing with the PyC *2D* band. The H_2 anneal has negligible effect on the band. This implies that impurities introduced from the furnace are responsible for the increase in *D* band intensity as defects on the SWNTs would reduce the *2D* band intensity.

The RBM frequencies are shown in Figure 5.15(d). The three most prominent peaks are seen at 167-168 cm^{-1}, 178-180 cm^{-1} and 194-196 cm^{-1}. These peaks suggest CNT diameters of 1.48 nm, 1.39 nm and 1.27 nm respectively. The deposition of PyC has no observable effect on the position of the RBM peaks; however the relative intensities change post H_2 annealing (and for PyC deposition) suggesting a larger relative contribution from the 1.48 nm SWNTs. The signal in this region becomes considerably noisier with increasing PyC deposition.

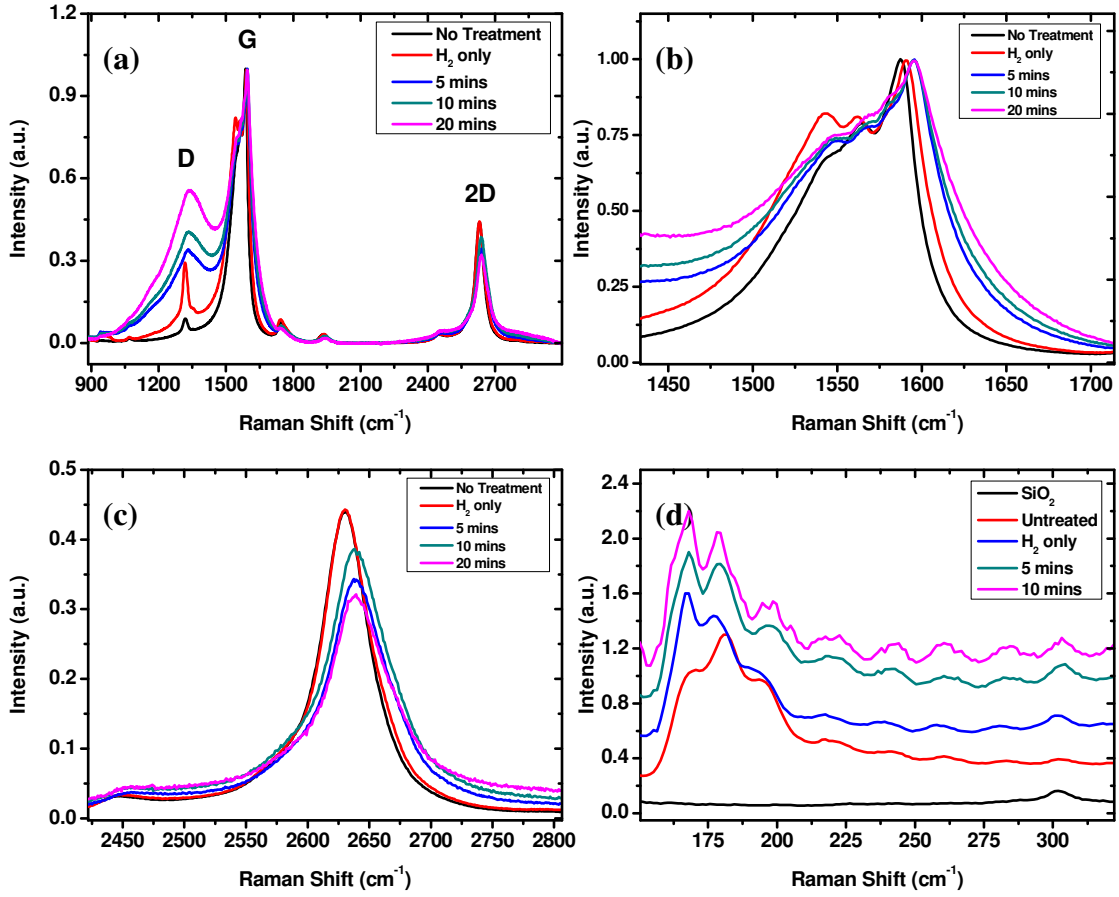

Figure 5.15 *Raman spectra of Iljin CNTs and PyC/CNT films (a) D, G and 2D bands (b) G band (c) 2D band (d) RBM modes.*

5.3.2 SEM Analysis

SEM was used to image both H_2 annealed films and those with PyC deposition. Figure 5.16 shows representative images of films prepared under different deposition conditions. For a pristine film, a bundle diameter of ~ 20nm is expected [23]. Here the H_2 annealed film exhibits an average bundle diameter close to this and the diameter is seen to increase with increasing PyC deposition time.

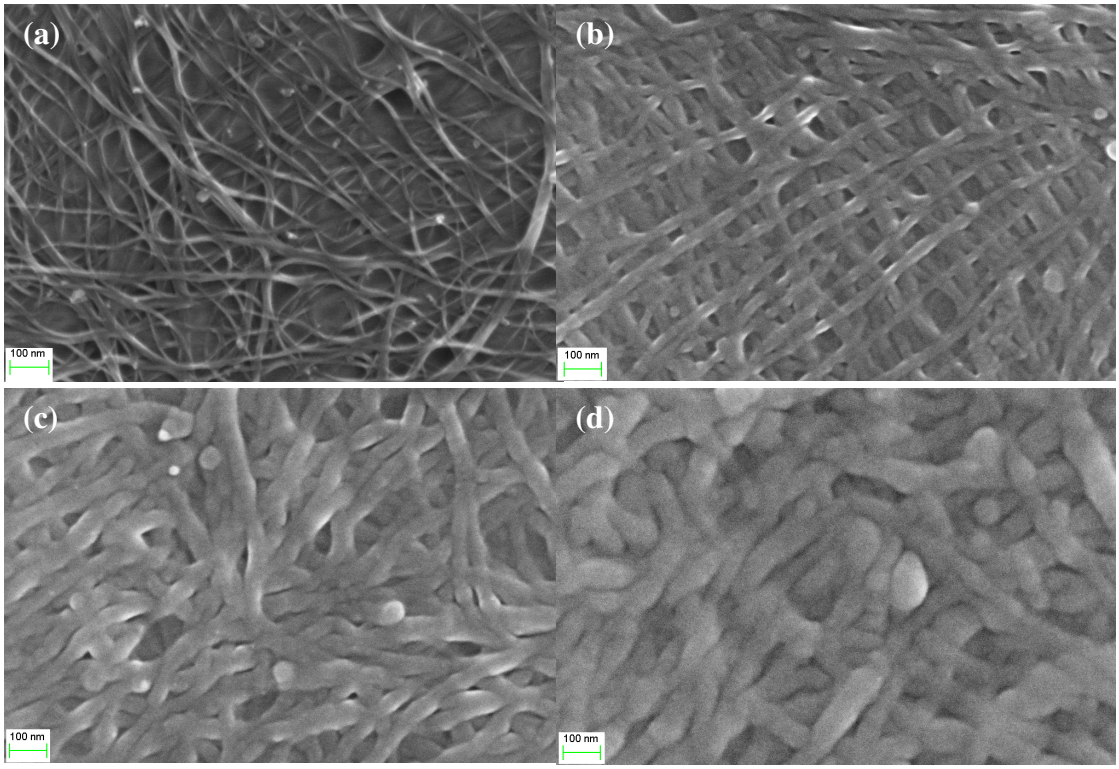

Figure 5.16 *SEM images of (a) H_2 treated Iljin SWNT film (b) 5 minutes PyC deposition (c) 10 minutes PyC deposition (d) 20 minutes PyC deposition. Scale bar 100 nm.*

Histograms of the diameter distribution obtained from SEM images are shown in Figure 5.17. It is observed that the mean bundle diameter increases from 18 nm in the case of the H_2 film to 38 nm, 61 nm and 84 nm for 5, 10 and 20 minute depositions respectively. This is not consistent with the linear deposition rate observed on SiO_2 but can be explained by considering that after 20 minutes deposition the bundles have considerable overlap thus skewing the diameter measurements.

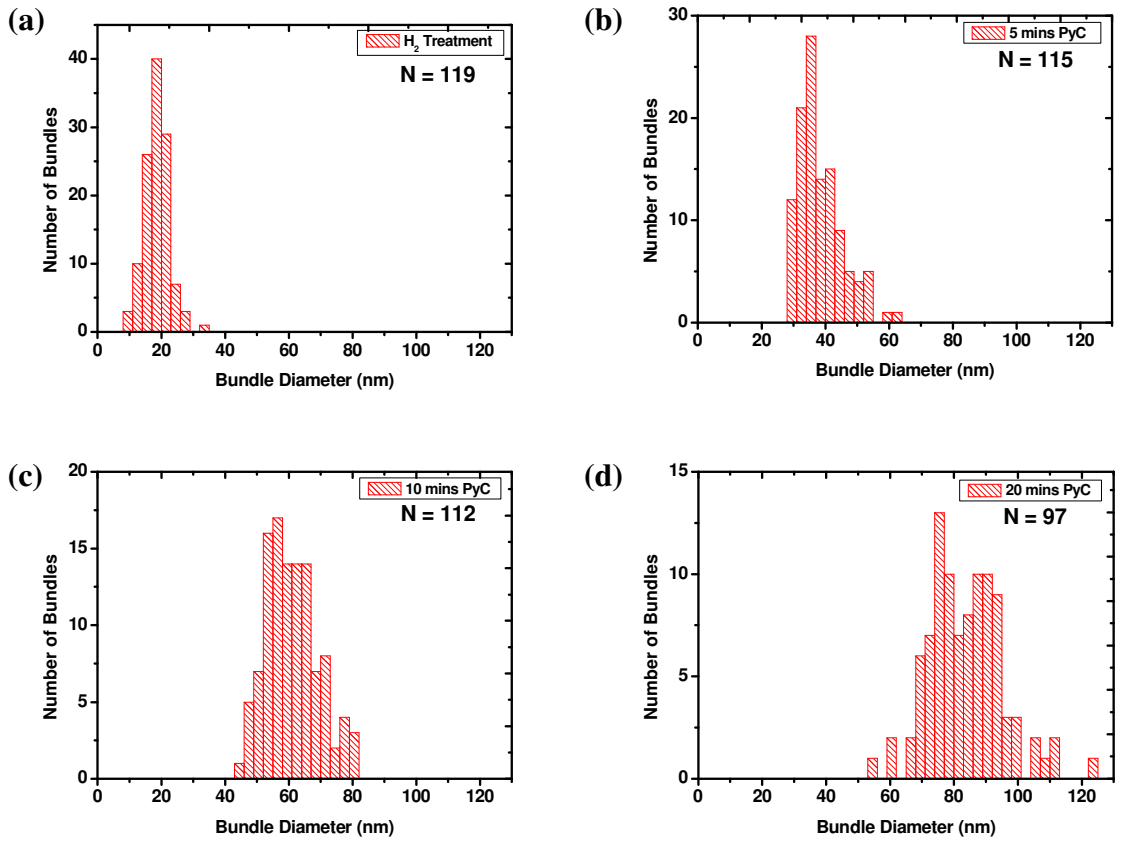

Figure 5.17 *Bundle diameter distribution for PyC/SWNT films prepared with (a) H_2 anneal only (b) 5 minutes PyC deposition (c) 10 minutes PyC deposition (d) 20 minutes PyC deposition.*

5.3.3 Electrical Characterisation

The electrical properties of all films were measured using the four point probe technique. The sheet resistance decreased with increasing deposition time and was seen to be considerably lower than that of PyC alone. Sheet resistances were measured by the four point probe technique and found to be 809, 294 and 193 Ω/□ for 5, 10 and 20 minute depositions respectively. These values represent an improvement over pure PyC but are not as good as similar pure SWNT films. Part of this disimprovement can be attributed to the role of the H_2 anneal in worsening junction resistances between SWNTs[59].

5.3.4 Conclusions

The deposition of controlled amounts of PyC onto thin films of SWNTs was demonstrated. This coated the SWNTs in a conformal fashion increasing the average bundle diameter. Raman analysis showed a mixing of PyC and SWNT signals. As expected the PyC signal became more prominent with increasing deposition time. PyC deposition led to a disimprovement in the electrical properties of the films compared with similar pure SWNT films. Further investigation into the mechanical and thermal properties of such films is of interest.

5.4 Graphitisation of PyC

The level of graphitisation in PyC can be improved by heat treatments. Matuyama et al. demonstrated this showing that curing of buckled layers occurred at a temperature of 1800 ^{o}C and that full graphitisation occurred at temperatures in the range 2000 – 3000 ^{o}C[60]. Such high temperature treatments have been shown to decrease the interlayer spacing and thus improve the electrical and mechanical performance of PyC films [61-62]. Increases in the crystallite size and optical anisotropy as well as an improved Raman signal have also been reported [3, 63].

It is well known that end transition metals, especially Ni, are catalytic agents for graphitic growth of carbon. This has been exploited for the production of CNFs, CNTs and most recently graphene. The effect of the presence of Ni on heat treatments of PyC was investigated by Shiota et al. in 1973[64]. This was carried out by electroplating films of Ni (0.8 μm) onto thick PyC films (1.5 mm) and then performing heat treatments. The Ni was seen to diffuse through the PyC and graphitise the carbon through which it passed. Shortly afterwards Derbyshire demonstrated the graphitisation of carbon films evaporated onto Ni foils and subjected to heat treatments [65], proposing a dissolution-precipitation mechanism.

Here the effect of heat treatments on PyC films with thin layers of Ni (3 nm) is investigated. Improved graphitisation would be expected to provide an improved in plane conductivity, making the films more suitable for thin film devices. Understanding of the role of Ni in catalysing graphitisation is of interest for other carbon CVD processes including growth of graphene.

5.4.1 Sample Preparation

Thin layers of Ni (3 nm) were sputtered onto PyC films (grown at T = 950 ^{o}C, P = 20 Torr, dwell time = 30 mins, t~400 nm) in order to investigate potential graphitisation. These films were then annealed at different temperatures (700 ^{o}C - 950 ^{o}C) in different gaseous environments (H_2 and $H_2 + C_2H_2$) for 10 minutes. All runs were carried out at a pressure of 5 Torr with a total gas flow of 60 sccm. Reference PyC films without any sputtered metals were included in each of these runs. The effect of these treatments was investigated using Raman spectroscopy, XPS and SEM.

5.4.1 Raman Analysis

Raman spectra were analysed by fitting Lorentzian peaks to the *D*, *G*, *D'* and *2D* bands and Gaussian peaks to the *I* and *D''* bands as described in section 5.2.6. Raman spectra showed a massive change in the structure of Ni/PyC films following annealing (see Figure 5.18). The heat treatment was seen to lead to a reduction in the relative integrated intensity of the *D* band and other defect related bands (*D'', I*) as well the emergence of a strong *2D* band. The Raman sampling depth is in the range 13 – 29 nm for carbon materials[66] meaning that more than just the surface layers are probed.

Peak Ratios – A_D/A_G and I_{2D}/I_G

The Raman signal of PyC as grown shows broad *D* and *G* bands with a high A_D/A_G ratio indicative of the high level of disorder (and small crystallite size) of the material as discussed in section 5.2.5. The *2D* band forms a modulated bump with surrounding bands and has a very low intensity. A large *D''* is also seen suggesting the presence of significant amounts of amorphous carbon.

All heat treatments produced an improvement in the graphitic order of the film as seen in a decrease in the A_D/A_G ratio and an increase in the I_{2D}/I_G ratio. These indicate an increase in the average crystallite size and improved spatial uniformity in the graphitic lattice respectively.

The lowest temperature anneals were carried out at 700 ^{o}C. Under these conditions a small *2D* band is seen to emerge at ~ 2650 cm^{-1} (I_{2D}/I_G ~ 0.2). The ratio of peak intensities I_D/I_G undergoes minimal change; however the *D* band narrows significantly

and as such there is a significant decrease in the ratio of the areas (A_D/A_G) suggesting an increase in crystallite size (Equation 2.8).

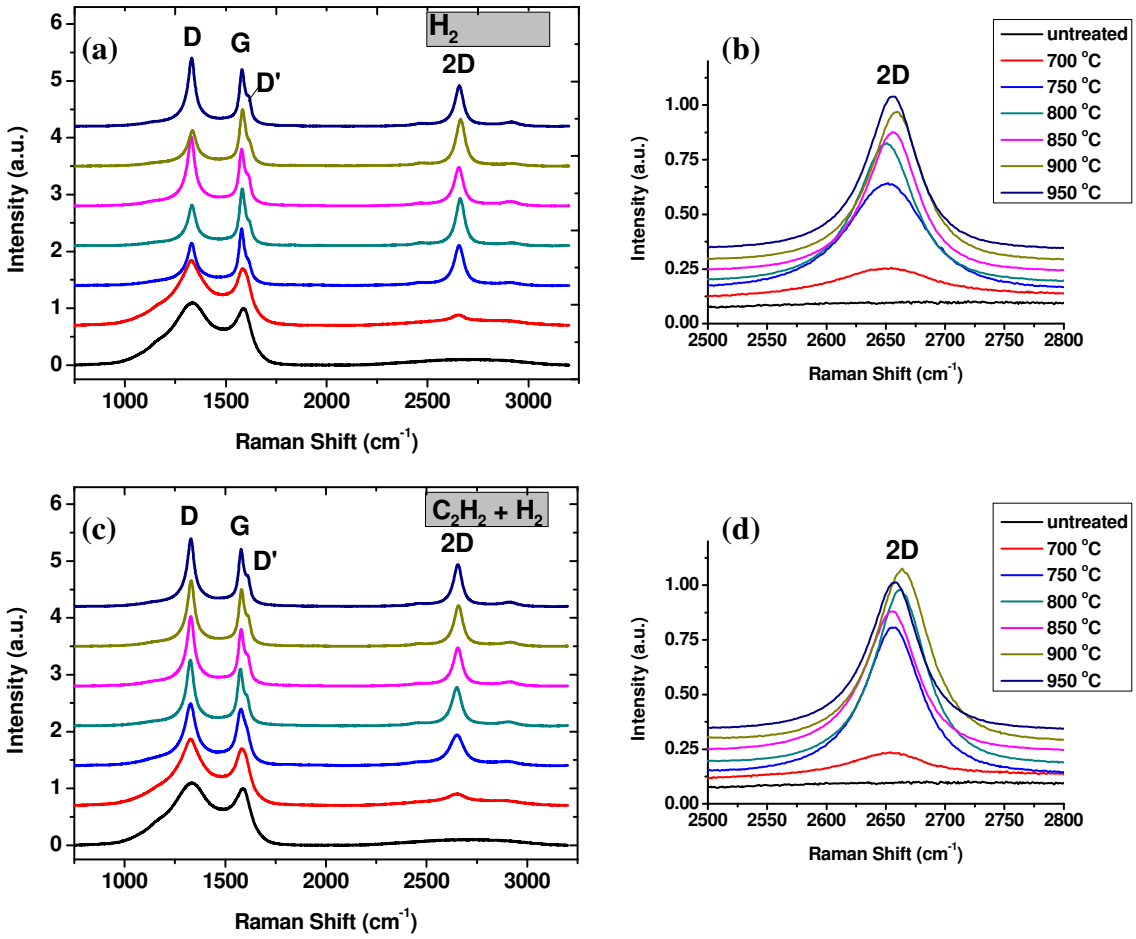

Figure 5.18 Raman spectra for Ni/PyC films (a, b) Annealed in H_2 (c, d) Annealed in a 50:50 C_2H_2:H_2 mix.

Increasing the annealing temperature up to 750 °C prompted further narrowing of the *D* and *G* bands and an associated increase in the peak area ratios. The *2D* band also increased dramatically in intensity (I_{2D}/I_G ~ 0.5–0.8 depending on annealing atmosphere). A similar improvement was seen using an annealing temperature of 800 °C, however both A_D/A_G and I_{2D}/I_G levelled off using annealing temperatures higher than this suggesting no further improvement.

Plots of A_D/A_G and I_{2D}/I_G as a function of annealing temperature are shown in Figure 5.19. These further demonstrate the improvement in defect levels (and by association crystallite size in accordance with equation 2.10) and spatial uniformity.

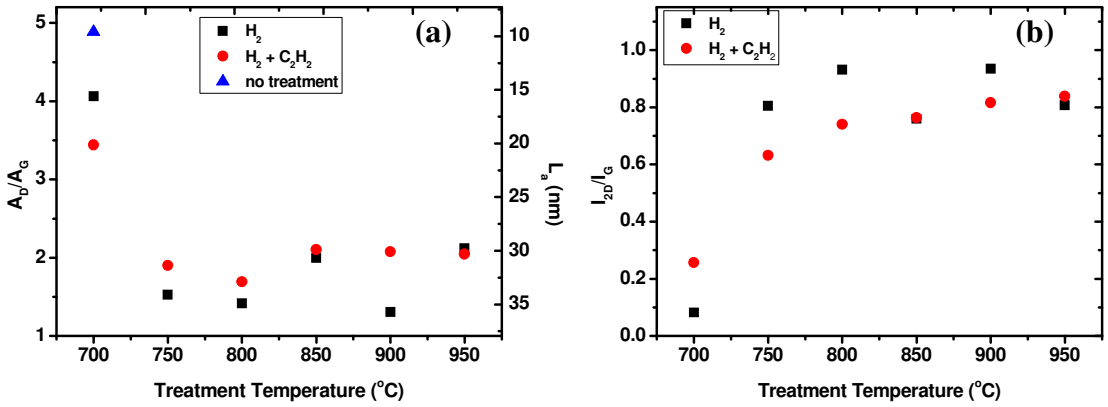

Figure 5.19 *(a) A_D/A_G with estimated crystallite size and (b) I_{2D}/I_G as a function of annealing temperature.*

Peak Widths – $\Delta\omega_D$, $\Delta\omega_G$, $\Delta\omega_{2D}$

The effect of treatment temperature on the FWHM of the standard graphitic peaks is shown in Figure 5.20. It is clear from this that the peaks narrow considerably with the heat treatments. It is generally accepted that the narrowing of these bands indicates improved levels of graphitisation. Lespade et al. correlated a decrease in the peak widths $\Delta\omega_G$ and $\Delta\omega_{2D}$ with a decrease in the interlayer spacing[67] whereas Nakamura et al. showed that the crystallite size scaled linearly with $\Delta\omega_D$ and $\Delta\omega_G$[68]. The narrowest FWHM values for $\Delta\omega_G$ seen here (~ 30 cm^{-1}) suggest an interlayer spacing of 0.3418 nm compared to 0.335 nm for graphite[69].

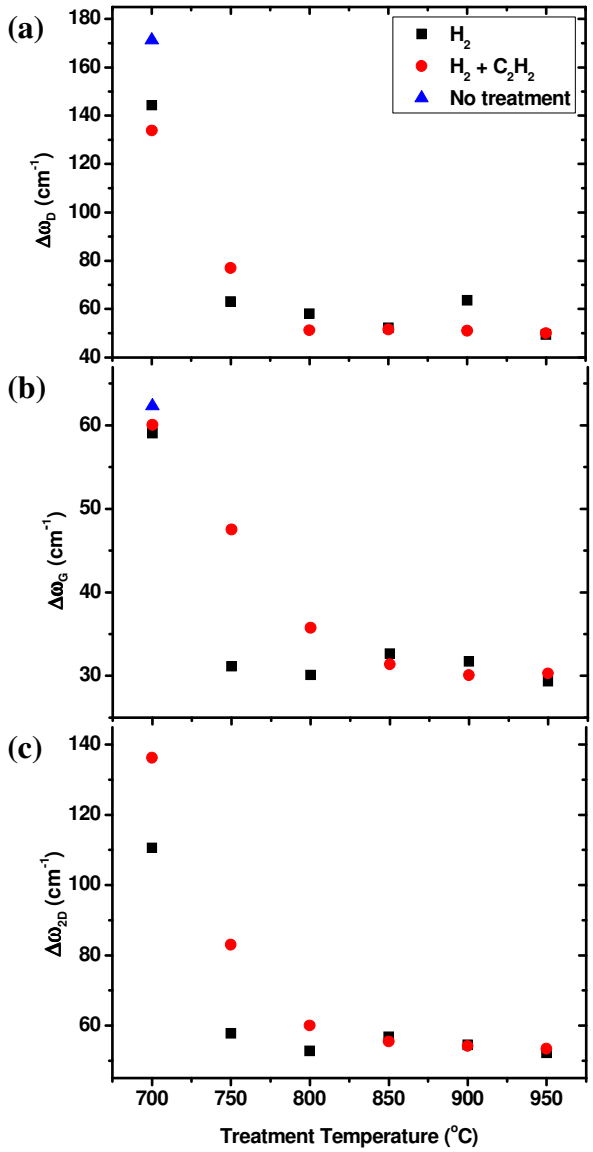

Figure 5.20 *Peak widths (a) $\Delta\omega_D$ (b) $\Delta\omega_G$ and (c) $\Delta\omega_{2D}$ as a function of treatment temperature*

5.4.2 XPS Analysis

XPS analysis was used to probe the surface of the PyC/Ni samples. This can be seen as complementary to the Raman spectroscopy analysis and gave information on the level of graphitisation, the presence of functional groups and the Ni content at the surface of the films. Films annealed in H_2 and C_2H_2+H_2 at 850 °C were probed as well as an untreated film.

A wide scan and C_{1s} core level spectrum of a PyC film with 3 nm of sputtered Ni is shown in Figure 5.21. It is evident that the metal deposition has a large effect on the PyC spectrum compared with those discussed in section 5.2. The strongest peak in the C_{1s} spectrum is seen at 285.25 eV which is associated with sp^3 bond formation[70]. This indicates that the physically aggressive sputtering action has induced additional defects on the graphitic nanocrystallites. The graphitic signal is located at 284.45 eV and is broadened due to induced disorder. This was fitted with a Doniac Sunjic function which gave an asymmetry factor of $\alpha = 0.191$ which is identical to that seen for PyC without Ni. Despite the fact that sputtering was carried out under high vacuum, additional oxygenated functionalities are seen in the spectrum. An additional peak centred at 283.6 eV is seen as a shoulder on the main peak. This implies the presence of Ni_3C[71]. The formation of this takes place through an endothermic reaction suggesting the Ni has a high energy when it impacts upon the PyC surface. The wide scan shows significant contributions from the various Ni core levels.

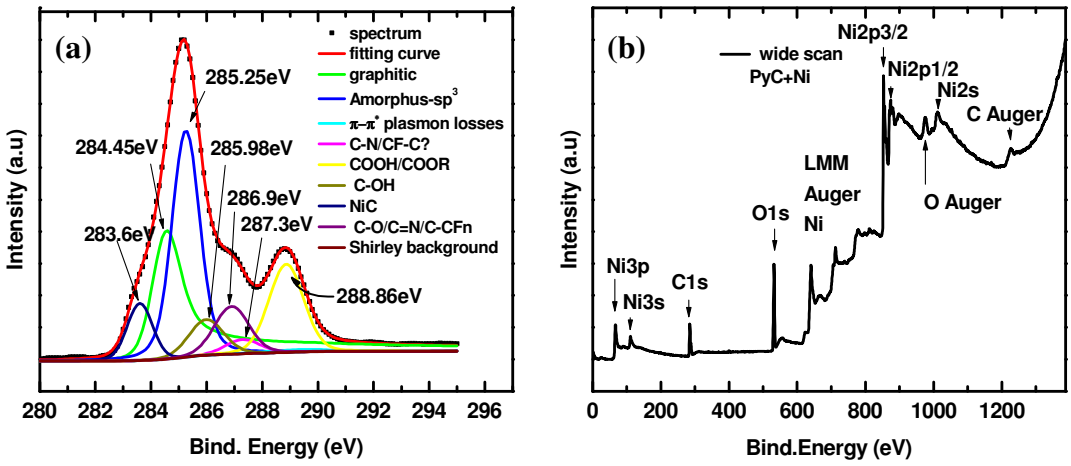

Figure 5.21 *XPS Spectra for Ni with 3 nm sputtered Ni (a) Fitted C_{1s} core levels showing significant contributions from sp^3 carbon and oxygenated functionalities (b) Wide scan showing assorted Ni peaks.*

Spectra of a PyC with 3nm of Ni post annealing in H_2 at 850 ^oC are shown in Figure 5.22. This treatment has a dual effect on the film. Firstly, the various functional groups seen for the PyC/Ni film without annealing are all removed. It is probable that the combination of H_2 and high temperature serves as a strong reducer stripping oxygen based functionalities from the surface. The peaks seen in the C_{1s} spectrum are a strong

graphitic peak (284.16 eV) and small contributions from Ni_3C (283.73 eV) and amorphous carbon (284.71 eV). The graphitic peak is sharper and Doniac Sunjic fitting gives a reduced asymmetry factor of $\alpha = 0.143$. This value is in good agreement with that reported for graphite[72] indicating that graphitisation occurs in the surface layers of PyC. Contributions from Ni are reduced in the wide scan suggesting a stripping of Ni from the surface or migration of the Ni into the sample.

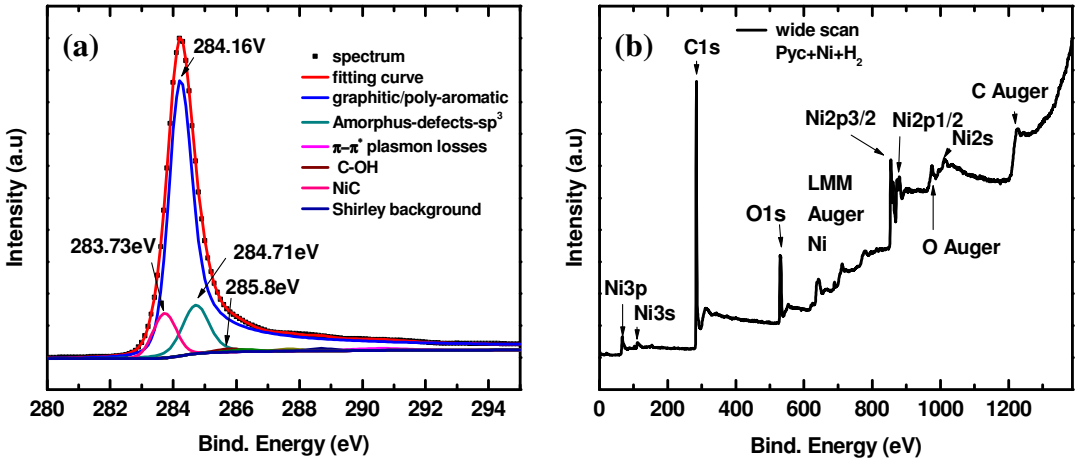

Figure 5.22 *XPS Spectra for Ni with 3 nm sputtered Ni post H_2 anneal at 850 ^oC (a) Fitted C_{1s} core levels showing sharp graphitic peak (b) Wide scan showing reduced Ni and O contributions.*

Spectra of PyC with 3nm of Ni post annealing in C_2H_2 + H_2 at 850 ^oC are shown in Figure 5.23. These are similar to the H_2 annealed spectra but the graphitic peak in the C_{1s} scan is sharper with an asymmetry factor, $\alpha = 0.132$ indicating further enhancement of graphitisation. The Ni contribution to the wide scan is further reduced suggesting that the Ni lies deeper in the sample. As the same temperature and dwell time were identical to that used for the H_2 anneal further migration of the Nickel into the PyC wouldn't be expected, thus suggesting the deposition of additional carbon under these conditions.

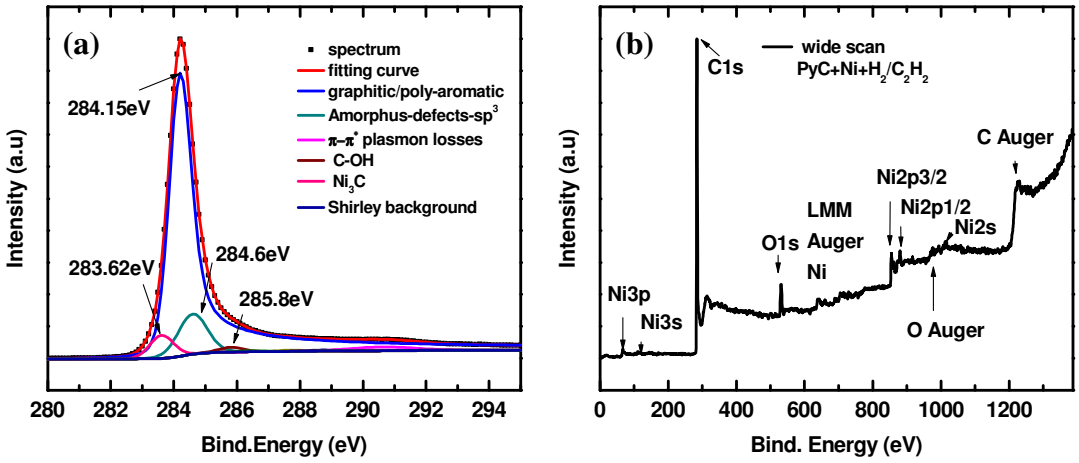

Figure 5.23 *XPS Spectra for Ni with 3 nm sputtered Ni post H_2 + C_2H_2 anneal at 850 ^oC (a) Fitted C_{1s} core levels showing sharp graphitic peak (b) Wide scan showing reduced Ni and O contributions*

5.4.3 AFM Analysis

PyC films were probed using AFM post Ni deposition. These films were seen to be rougher than pure PyC but were still very smooth (R_a ~ 1 nm). Furthermore, there was no obvious sign of Ni clustering on the surface of the films (see Figure 5.24). Films were too rough for AFM analysis post heat treatment.

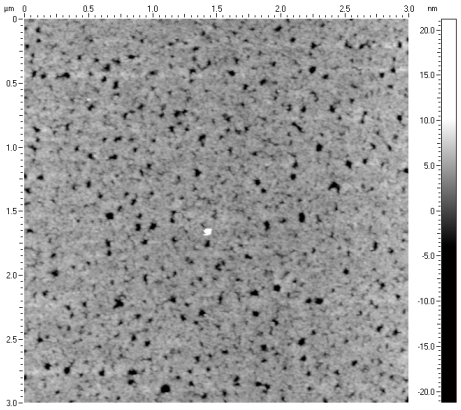

Figure 5.25 AFM image of PyC film with 3nm deposited Ni (scale 3 x 3 μm)

5.4.4 SEM Analysis

SEM analysis was used for imaging PyC films with Ni pre and post annealing treatments. Untreated films are shown in Figure 5.26. The top down view (a) shows that whilst overall the films are very smooth, they have some small pores which are also seen on the AFM images. Tilt view (b) shows a number of distinct regions on the films, a thin top layer of PyC and Ni, a thick PyC layer and then the underlying SiO_2 on Si substrate.

The appearance of the films post annealing treatments varied depending on the temperature and on the gaseous atmosphere used. Representative SEM images of H_2 treated films are shown in Figure 5.27. Flake like structures considerably rougher than the untreated films were observed.

Representative SEM images of anneals in C_2H_2 are shown in Figure 5.28. At lower temperatures (700 – 750 ^oC) tube like structures were seen to grow on top of the Ni/PyC layer. These look similar to the structures grown on PPF films as described in Chapter 4. As these were not seen with H_2 anneals it seems probable that they are grown from the C_2H_2 feedstock dissolving in the Ni which remains on the surface of the PyC films. At higher temperatures (800 ^oC and higher) the films looked similar to those produced with H_2 anneals.

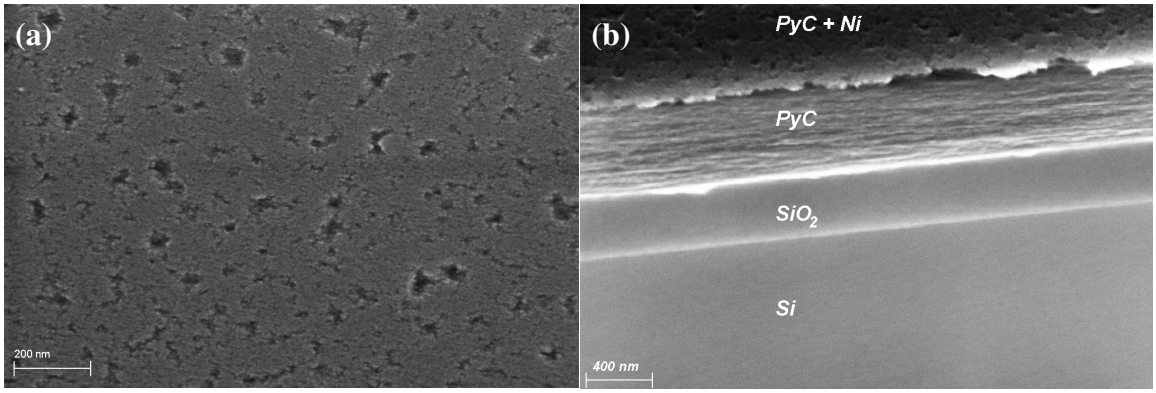

Figure 5.26 *SEM images of (a) top view and (b) tilt view on PyC films with evaporated Ni layer*

A tilt view SEM image of a film annealed in H_2 and C_2H_2 at 700 ^oC is shown in Figure 5.29(a). It is clear from this that additional structures grow on top of the Ni/PyC films. There is no obvious sign of Ni particles within the PyC layer, however at higher temperatures SEM images suggest that Ni migrates into the PyC (Figure 5.29(b)). Further migration would be expected at higher temperatures and this could be an explanation for why further structures aren't seen to grow at temperatures > 750 ^oC. This is also be supported by the XPS data which shows a considerably reduced Ni signal post treatments.

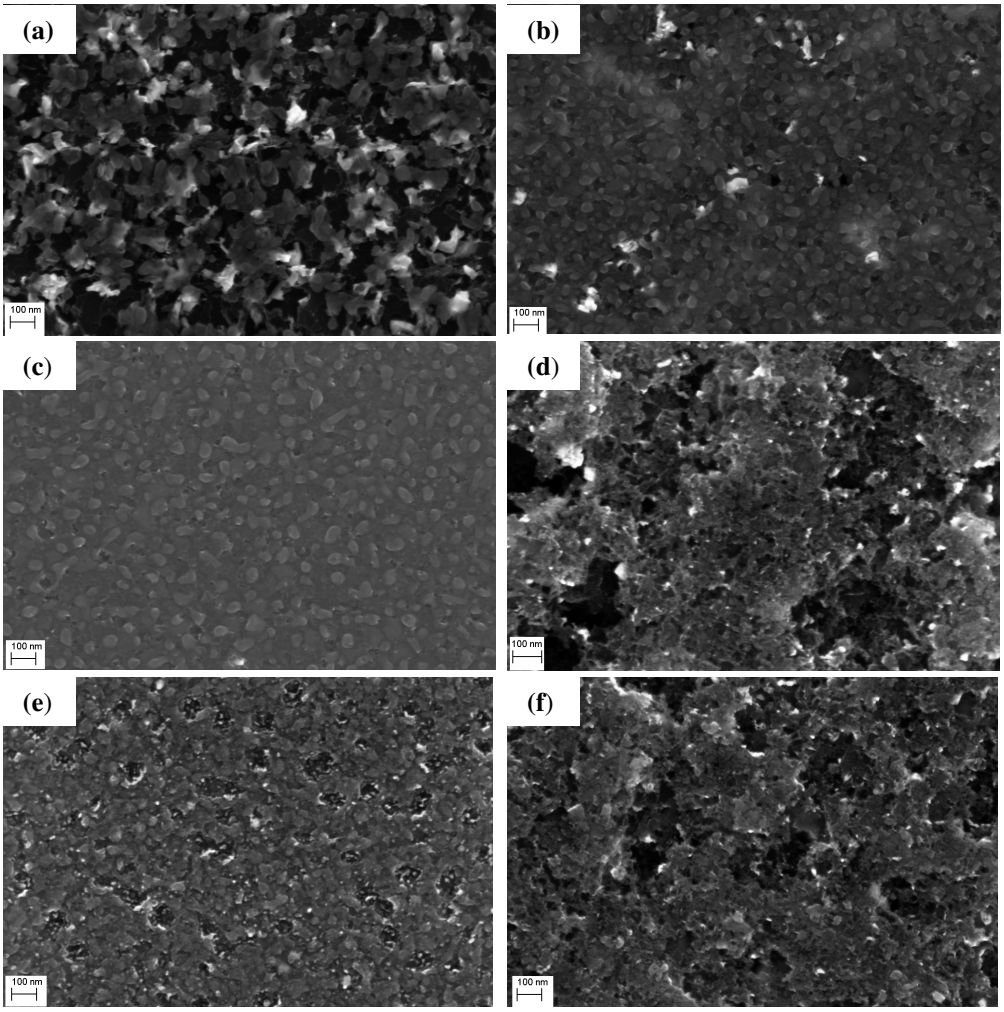

Figure 5.27 *SEM images of PyC/Ni films annealed in H_2 at (a) 700 ^oC (b) 750 ^oC (c) 800 ^oC (d) 850 ^oC (e) 900 ^oC (f) 950 ^oC. Scale bars all 100 nm*

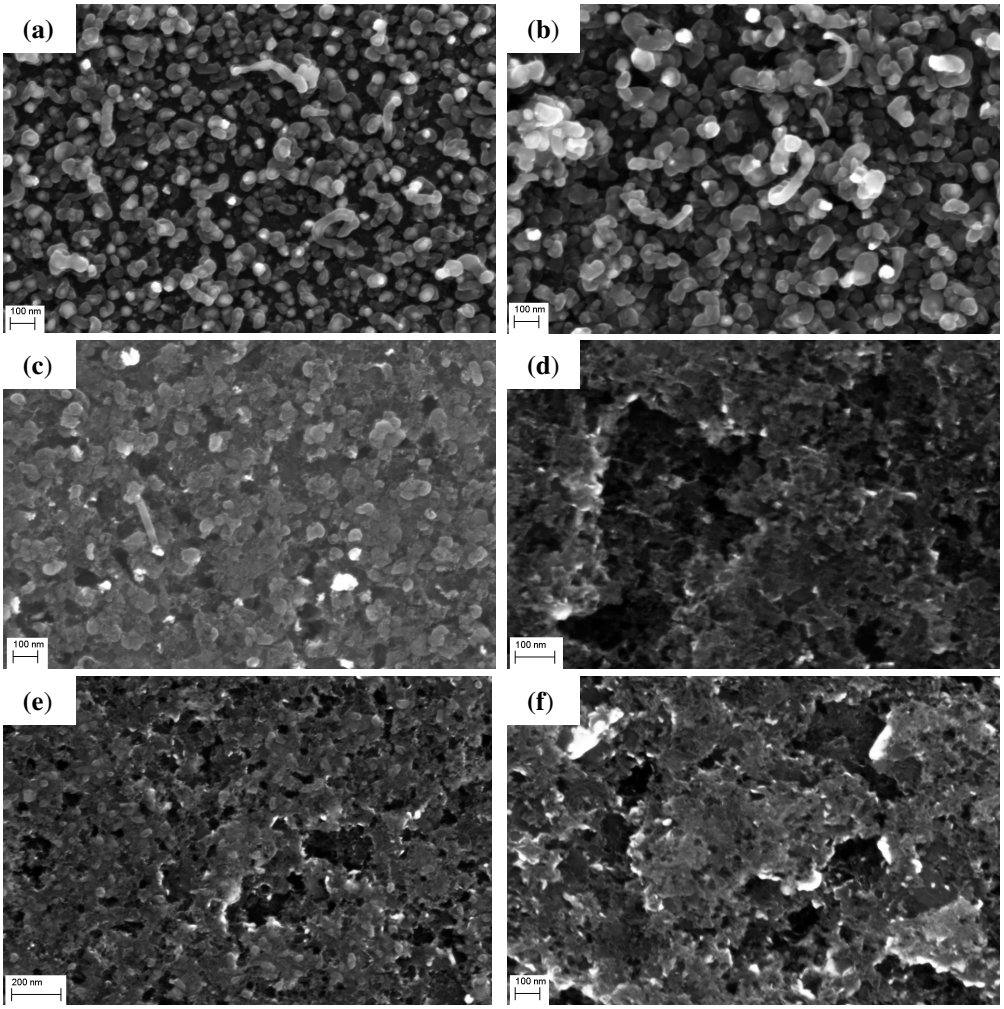

Figure 5.28 *SEM images of PyC/Ni films annealed in C_2H_2 at (a) 700 ^oC (b) 750 ^oC (c) 800 ^oC (d) 850 ^oC (e) 900 ^oC (f) 950 ^oC. Scale bars all 100 nm (except (e) 200 nm)*

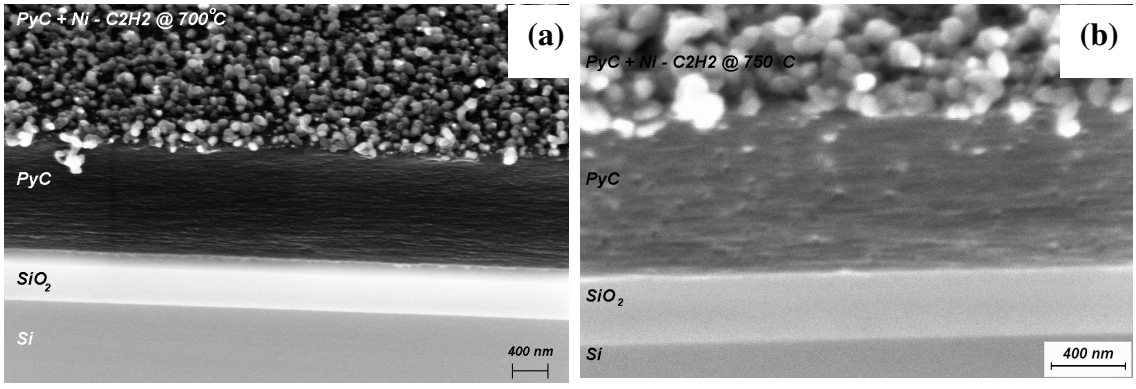

Figure 5.29 *Tilted SEM image showing PyC/Ni films annealed in C_2H_2 and H_2 at (a) 700 ^oC and (b) 750 ^oC. Scale bars 400 nm.*

5.4.5 Conclusions

The use of very thin Ni films in combination with heat treatments has been shown to graphitise PyC films. Raman spectroscopy showed a decrease in A_D/A_G and an increase in I_{2D}/I_G as well as a decrease in the *D*, *G*, and *2D* peak widths implying improved graphitisation and a reduction in defect levels. XPS analysis further implied improved graphitisation and also showed the removal of functional groups from the surface. The migration of Ni into the PyC upon treatment was also suggested. SEM imaging indicated the growth of additional structures with lower temperature treatments involving C_2H_2. Other treatments produced structures with flake like morphologies.

5.5 Conclusions

A process has been developed for the production of thin films of PyC on assorted substrates. The thickness of these films can be varied by varying the growth temperature, growth pressure and dwell time. The relationship between deposition rate and temperature implies that the deposition is a first order thermally activated process as described by the Arrhenius equation. An activation energy of 2.68 ± 0.15 eV was calculated for this process.

Four point probe measurements in combination with profilometry infer that the resistivity of the PyC films is ~ 2 x 10^{-5} Ωm. This combined with transmittance measurements gives values in the range of 0.8 – 1.1 for the conductivity ratio (σ_{DC}/σ_{op}) illustrating that PyC falls short of alternative materials for transparent electrode applications.

AFM analysis indicated that the films produced at 950 ^{o}C were incredibly smooth. Films produced at higher temperatures were considerably rougher. Raman spectroscopy indicated that the films were nanocrystalline and XPS showed the presence of amorphous carbon and oxygenated functionalities.

The deposition of PyC onto thin films of SWNTs was demonstrated. This allowed for good control over the thickness and hence bundle diameter produced. The deposition of PyC had a negative impact on the electrical properties of the films compared with films of just SWNTs. The mechanical and thermal properties of such films are of interest for further investigation.

The use of thin films of Ni and heat treatments to graphitise PyC films was established. Raman spectroscopy and XPS both indicated an improvement in the purity and

graphitic order of the films. High resolution TEM studies are planned to investigate the depth and level of ordering in the films. This would also be used to determine the exact location of Ni in the films post heat treatments. It is hoped that such a technique can be extended to thinner films of PyC for the production of ultrathin graphitic films.

References

1. Larouche, N. and B.L. Stansfield, *Classifying nanostructured carbons using graphitic indices derived from Raman spectra.* Carbon, 2010. **48**(3): p. 620-629.
2. Lopez-Honorato, E., et al., *Characterization of the anisotropy of pyrolytic carbon by Raman spectroscopy.* Carbon. **48**(3): p. 881-890.
3. Vallerot, J.M., et al., *Quantitative structural and textural assessment of laminar pyrocarbons through Raman spectroscopy, electron diffraction and few other techniques.* Carbon, 2006. **44**(9): p. 1833-1844.
4. Pfrang, A. and T. Schimmel, *Quantitative analysis of pyrolytic carbon films by polarized light microscopy.* Surface and Interface Analysis, 2004. **36**(2): p. 184-188.
5. Reznik, B. and K.J. Huttinger, *On the terminology for pyrolytic carbon.* Carbon, 2002. **40**(4): p. 621-624.
6. Koster, A., H.D. Matzner, and D.R. Nicholsi, *PBMR design for the future.* Nuclear Engineering and Design, 2003. **222**(2-3): p. 231-245.
7. Leomand, G.C., *Pyrolytic Carbon Nose for Hypersonic Vehicles*. 1973, Societe Nationale Industrielle Aerospatiale (Paris, FR): United States.
8. Wen, C.-Y. and G.-W. Huang, *Application of a thermally conductive pyrolytic graphite sheet to thermal management of a PEM fuel cell.* Journal of Power Sources, 2008. **178**(1): p. 132-140.
9. Bruckmann, H. and K.J. Huttinger, *Carbon, A promising Material in endoprosthetics 1. The Carbon Materials and Their Mechanical Properties.* Biomaterials, 1980. **1**(2): p. 67-72.
10. Pesakova, V., et al., *Biomechanical and biological properties of the implant material carbon-carbon composite covered with pyrolytic carbon.* Journal of Materials Science-Materials in Medicine, 2000. **11**(12): p. 793-798.
11. Reznik, B., D. Gerthsen, and K.J. Hüttinger, *Micro- and nanostructure of the carbon matrix of infiltrated carbon fiber felts.* Carbon, 2001. **39**(2): p. 215-229.
12. Zhang, W.G., Z.J. Hu, and K.J. Hüttinger, *Chemical vapor infiltration of carbon fiber felt: optimization of densification and carbon microstructure.* Carbon, 2002. **40**(14): p. 2529-2545.
13. Taylor, C.A. and W.K.S. Chiu, *Characterization of CVD carbon films for hermetic optical fiber coatings.* Surface and Coatings Technology, 2003. **168**(1): p. 1-11.
14. Aichmayr, G., et al. *Carbon / high-k Trench Capacitor for the 40nm DRAM Generation*. in *VLSI Technology, 2007 IEEE Symposium on*. 2007.
15. Graham, A.P., et al., *An investigation of the electrical properties of pyrolytic carbon in reduced dimensions: Vias and wires.* Journal of Applied Physics, 2010. **107**(11): p. 114316.
16. Raghavan, G., J.L. Hoyt, and J.F. Gibbons, *Polycrystalline Carbon - A Novel Material for Gate Electrodes in MOS Technology.* Japanese Journal of Applied Physics Part 1-Regular Papers Short Notes & Review Papers, 1993. **32**(1B): p. 380-383.
17. Becker, A. and K.J. Huttinger, *Chemistry and kinetics of chemical vapor deposition of pyrocarbon - II - Pyrocarbon deposition from ethylene, acetylene and 1,3-butadiene in the low temperature regime.* Carbon, 1998. **36**(3): p. 177-199.

18. Becker, A. and K.J. Huttinger, *Chemistry and kinetics of chemical vapor deposition of pyrocarbon - III - Pyrocarbon deposition from propylene and benzene in the low temperature regime.* Carbon, 1998. **36**(3): p. 201-211.
19. Becker, A. and K.J. Huttinger, *Chemistry and kinetics of chemical vapor deposition of pyrocarbon - IV - Pyrocarbon deposition from methane in the low temperature regime.* Carbon, 1998. **36**(3): p. 213-224.
20. Becker, A. and K.J. Huttinger, *Chemistry and kinetics of chemical vapor deposition of pyrocarbon - V - Influence of reactor volume/deposition surface area ratio.* Carbon, 1998. **36**(3): p. 225-232.
21. Benzinger, W., A. Becker, and K.J. Huttinger, *Chemistry and kinetics of chemical vapour deposition of pyrocarbon .1. Fundamentals of kinetics and chemical reaction engineering.* Carbon, 1996. **34**(8): p. 957-966.
22. Cohen, E.R., Lide, D.R., Trigg, G.L., *AIP Physics Desk Reference.* Springer, 2003: p. 396.
23. Doherty, E.M., et al., *The spatial uniformity and electromechanical stability of transparent, conductive films of single walled nanotubes.* Carbon, 2009. **47**(10): p. 2466-2473.
24. Bae, S., et al., *Roll-to-roll production of 30-inch graphene films for transparent electrodes.* Nat Nano, 2010. **5**(8): p. 574-578.
25. Schreiber, M., et al., *Transparent ultrathin conducting carbon films.* Applied Surface Science, 2010. **256**(21): p. 6186-6190.
26. De, S., et al., *Flexible, Transparent, Conducting Films of Randomly Stacked Graphene from Surfactant-Stabilized, Oxide-Free Graphene Dispersions.* Small, 2010. **6**(3): p. 458-464.
27. Zhang, J.M. and P.C. Eklund, *Optical transmission of graphite and potassium graphite intercalation compounds.* Journal of Materials Research, 1987. **2**(Copyright 1988, IEE): p. 858-63.
28. Dan, B., G.C. Irvin, and M. Pasquali, *Continuous and Scalable Fabrication of Transparent Conducting Carbon Nanotube Films.* ACS Nano, 2009. **3**(4): p. 835-843.
29. King, P.J., et al., *Improvement of Transparent Conducting Nanotube Films by Addition of Small Quantities of Graphene.* ACS Nano, 2010. **4**(7): p. 4238-4246.
30. Dressel, M. and G. Gruner, *Electrodynamics of Solids: Optical Properties of Electrons in Matter.* Cambridge University Press, 2002.
31. De, S. and J.N. Coleman, *Are There Fundamental Limitations on the Sheet Resistance and Transmittance of Thin Graphene Films?* ACS Nano, 2010. **4**(5): p. 2713-2720.
32. De, S., et al., *Silver Nanowire Networks as Flexible, Transparent, Conducting Films: Extremely High DC to Optical Conductivity Ratios.* ACS Nano, 2009. **3**(7): p. 1767-1774.
33. Meadows, P.J., E. López-Honorato, and P. Xiao, *Fluidized bed chemical vapor deposition of pyrolytic carbon - II. Effect of deposition conditions on anisotropy.* Carbon, 2009. **47**(1): p. 251-262.
34. Cancado, L.G., et al., *General equation for the determination of the crystallite size L-a of nanographite by Raman spectroscopy.* Applied Physics Letters, 2006. **88**(16).
35. Tuinstra, F. and J.L. Koenig, *Raman Spectrum of Graphite.* The Journal of Chemical Physics, 1970. **53**(3): p. 1126-1130.

36. López-Honorato, E., et al., *Characterization of the anisotropy of pyrolytic carbon by Raman spectroscopy.* Carbon, 2010. **48**(3): p. 881-890.
37. Bacsa, W.S., et al., *Raman scattering of laser-deposited amorphous carbon.* Physical Review B, 1993. **47**(16): p. 10931.
38. Ishida, H., et al., *An Application of Surface-Enhanced Raman Scattering to the Surface Characterization of Carbon Materials.* Appl. Spectrosc., 1986. **40**(3): p. 322-330.
39. Jawhari, T., A. Roid, and J. Casado, *Raman spectroscopic characterization of some commercially available carbon black materials.* Carbon, 1995. **33**(11): p. 1561-1565.
40. Darmstadt, H. and C. Roy, *Surface spectroscopic study of basic sites on carbon blacks.* Carbon, 2003. **41**(13): p. 2662-2665.
41. Dekanski, A., et al., *Glassy carbon electrodes: I. Characterization and electrochemical activation.* Carbon, 2001. **39**(8): p. 1195-1205.
42. Doniach, S. and M. Sunjic, *Many-electron singularity in X-ray photoemission and X-ray line spectra from metals.* Journal of Physics C: Solid State Physics, 1970. **3**(2): p. 285.
43. Mahan, G.D., *Excitons in Metals: Infinite Hole Mass.* Physical Review, 1967. **163**(3): p. 612.
44. Nozi, et al., *Singularities in the X-Ray Absorption and Emission of Metals. III. One-Body Theory Exact Solution.* Physical Review, 1969. **178**(3): p. 1097.
45. Cheung, T.T.P., *X-ray Photoemission of Carbon - Lineshape Analysis and Application to Studies of Coals.* Journal of Applied Physics, 1982. **53**(10): p. 6857-6862.
46. Carlo, S.R., A.J. Wagner, and D.H. Fairbrother, *Iron Metalization of Fluorinated Organic Films: A Combined X-ray Photoelectron Spectroscopy and Atomic Force Microscopy Study.* The Journal of Physical Chemistry B, 2000. **104**(28): p. 6633-6641.
47. Desimoni, E., et al., *XPS determination of oxygen-containing functional groups on carbon-fibre surfaces and the cleaning of these surfaces.* Surface and Interface Analysis, 1990. **15**(10): p. 627-634.
48. Ilangovan, G. and K. Chandrasekara Pillai, *Electrochemical and XPS Characterization of Glassy Carbon Electrode Surface Effects on the Preparation of a Monomeric Molybdate(VI)-Modified Electrode.* Langmuir, 1997. **13**(3): p. 566-575.
49. Karakuscu, A., et al., *White Luminescence from Sol–Gel-Derived SiOC Thin Films.* Journal of the American Ceramic Society, 2009. **92**(12): p. 2969-2974.
50. Eon, D. and et al., *High density fluorocarbon plasma etching of methylsilsesquioxane SiOC(H) low- k material and SiC(H) etch stop layer: surface analyses and investigation of etch mechanisms.* Journal of Physics D: Applied Physics, 2007. **40**(13): p. 3951.
51. Tsukasa, N., et al. *High-Speed Deposition of New Dielectric Film Having the Low Refractive Index for the Rewritable HD DVD Media*. 2005: Optical Society of America.
52. Zhang, W.G. and K.J. Hüttinger, *Densification of a 2D carbon fiber preform by isothermal, isobaric CVI: Kinetics and carbon microstructure.* Carbon, 2003. **41**(12): p. 2325-2337.
53. Tombrel, F., *Process for Producing Pyrolytic Carbon Impregnated Thermal Insulating Carbonized Felt*. 1971, Societe Le Carbone Lorraine (Paris, FR): United States.

54. Allouche, H., M. Monthioux, and R.L. Jacobsen, *Chemical vapor deposition of pyrolytic carbon on carbon nanotubes: Part 1. Synthesis and morphology.* Carbon, 2003. **41**(15): p. 2897-2912.
55. Li, X., et al., *Densified aligned carbon nanotube films via vapor phase infiltration of carbon.* Carbon, 2007. **45**(4): p. 847-851.
56. Kim, K.K., et al., *Dependence of Raman spectra G ' band intensity on metallicity of single-wall carbon nanotubes.* Physical Review B, 2007. **76**(20).
57. Musso, S., et al., *Improving macroscopic physical and mechanical properties of thick layers of aligned multiwall carbon nanotubes by annealing treatment.* Diamond and Related Materials. **17**(4-5): p. 542-547.
58. Kosaka, M., et al., *Annealing effect on carbon nanotubes. An ESR study.* Chemical Physics Letters, 1995. **233**(1-2): p. 47-51.
59. Nirmalraj, P.N., et al., *Electrical Connectivity in Single-Walled Carbon Nanotube Networks.* Nano Letters, 2009. **9**(11): p. 3890-3895.
60. Matuyama, E., *Graphitic Acid of Pyrolytic Carbon and Its Heat Treatment.* The Journal of Physical Chemistry, 1965. **69**(7): p. 2462-2464.
61. Guellali, M., R. Oberacker, and M.J. Hoffmann, *Influence of heat treatment on microstructure and properties of highly textured pyrocarbons deposited during CVD at about 1100 °C and above 2000 °C.* Composites Science and Technology, 2008. **68**(5): p. 1122-1130.
62. Taylor, C.A., M.F. Wayne, and W.K.S. Chiu, *Heat treatment of thin carbon films and the effect on residual stress, modulus, thermal expansion and microstructure.* Carbon, 2003. **41**(10): p. 1867-1875.
63. Hunn, J.D., G.E. Jellison Jr, and R.A. Lowden, *Increase in pyrolytic carbon optical anisotropy and density during processing of coated particle fuel due to heat treatment.* Journal of Nuclear Materials, 2008. **374**(3): p. 445-452.
64. Shiota, I. and O. Watanabe, *Compatability Studies Between Pyrolytic Carbon and Nickel.* Journal of Materials Science, 1979. **14**(5): p. 1121-1125.
65. Derbyshire, F.J., A.E.B. Presland, and D.L. Trimm, *Graphite formation by the dissolution--precipitation of carbon in cobalt, nickel and iron.* Carbon, 1975. **13**(2): p. 111-113.
66. Alsmeyer, Y.W. and R.L. McCreery, *Surface enhanced Raman examination of carbon electrodes: effects of laser activation and electrochemical pretreatment.* Langmuir, 1991. **7**(10): p. 2370-2375.
67. Lespade, P., et al., *Caracterisation de materiaux carbones par microspectrometrie Raman.* Carbon, 1984. **22**(4-5): p. 375-385.
68. Nakamura, K., M. Fujitsuka, and M. Kitajima, *Disorder-induced line broadening in first-order Raman scattering from graphite.* Physical Review B, 1990. **41**(17): p. 12260.
69. Yoshida, A., Y. Kaburagi, and Y. Hishiyama, *Full width at half maximum intensity of the G band in the first order Raman spectrum of carbon material as a parameter for graphitization.* Carbon, 2006. **44**(11): p. 2333-2335.
70. Diaz, J., et al., *Separation of the sp^3 and sp^2 components in the C1s photoemission spectra of amorphous carbon films.* Physical Review B, 1996. **54**(11): p. 8064.
71. Goto, Y., et al., *Formation of Ni3C Nanocrystals by Thermolysis of Nickel Acetylacetonate in Oleylamine: Characterization Using Hard X-ray Photoelectron Spectroscopy.* Chemistry of Materials, 2008. **20**(12): p. 4156-4160.

72. van Attekum, P.M.T.M. and G.K. Wertheim, *Excitonic Effects in Core-Hole Screening*. Physical Review Letters, 1979. **43**(25): p. 1896.

Chapter 6

Plasma Treatment of CVD Grown Nanocarbons

6.1 Introduction

Plasma treatment is a flexible technique with a broad range of applications including surface modification of polymers[1], improvement of hole injection in OLEDs[2] and etching and cleaning in semiconductor fabrication[3]. For implementation of CVD nanocarbons into assorted applications post growth processing is often required. This chapter deals with the use of remote plasma to treat various nanocarbon films. This can be used for functionalisation or etching depending on the parameters used.

The effect of O_2 plasma treatment on in house produced CNTs was investigated. This was seen to increase the defect levels and under certain conditions produced sheet like geometries. An O_2 plasma treatment was used to functionalise PyC films and the use of such films as electrochemical electrodes was demonstrated. Remote plasma treatment was used as this generates radicals without much contact between the plasma and the substrate leading to less physical bombardment of the substrate.

This chapter also introduces the growth of graphene by CVD. This took place under similar conditions to those used for the growth of PyC but is catalysed by the presence of a Ni layer. Conditions for the production of good quality graphene films are outlined. Following on from this, the effect of plasma treatment on such films is investigated using scanning Raman. The use of a nanosphere lithography based shadow mask in combination with plasma treatment was shown to be an effective route for the patterning of CVD grown graphene films.

6.2 Plasma Treatment of CVD Grown CNTs

Plasma treatment can be thought of as a multipurpose tool capable of modifying nanotube properties as well as physical etching. The functionalisation of CNTs is a massive field in itself and is a necessary step en route to many applications[4]. Plasma treatment has been shown to be an effective technique for the introduction of functional groups to the surface of CNTs removing the necessity for liquid phase processing. It can be thought of as a clean treatment, not reliant on the use of solvents, acids etc. Furthermore, compared with chemical methods it involves a much shorter reaction time.

Workers in the Charlier group investigated the effect of different plasma treatments on MWNT powders[5]. XPS studies identified the introduction of hydroxyl, carboxyl and carbonyl groups on treatment with O_2 plasma. N_2 plasma treatment led to the introduction of imine, amine, amide and nitrile groups whereas CF_4 plasma treatment led to the incorporation of assorted C-F groups. The incorporation of oxygenated functionalities onto the surface of CNTs has been shown to enhance their electrochemical performance[6]. O_2 plasma treatment has also been proposed as a method for purifying defective MWNT powders based on the lower bonding energy of sp^3 amorphous carbon deposits compared with the sp^2 MWNTs[7]. UPS studies have been used to show that under certain conditions an O_2 plasma can convert MWNTs from metallic to semiconducting[8].

6.2.1 O_2 Plasma Treatment of MWNT forests

In this study a combination of Raman spectroscopy and SEM are used to probe the effect of O_2 plasma treatment on CVD grown MWNT forests. This area has implications for a number of different CNT based applications. Firstly, in the case of vias selectively etching back the recess is an obstacle to large scale implementation. For electrochemical devices and electroanalytical sensing applications based on CNT forests plasma treatment has multiple impacts. Firstly, the introduction of functional groups can lend sensitivity to specific chemical groups/reactions. Secondly, controlled etching can lead to an enhanced surface area.

6.2.1.1 Sample Growth and Treatment

MWNT Forests ~ 10 μm in height were grown on 3 nm Co / 30 nm Ta catalysts on 300 nm SiO_2 on Si substrates in the Gero system. A growth temperature of 750 ^oC was used with a pressure of 10 Torr. The films were subjected to a 10 minute pre-treatment in H_2 and then a 10 minute growth step with a mix of H_2 and C_2H_2 (60 sccm each).

These forests were placed in the plasma chamber and treated with O_2 plasma under assorted conditions. A constant power of 1 kW was used for all runs but the O_2 flow (20 – 40 sccm) and the treatment time (30 s – 20 mins) were varied.

6.2.1.2 SEM Analysis

SEM imaging on the MWNT forests etched with 20 sccm O_2 flow indicated that there was no significant change in the height of the forests. Furthermore, these MWNTs exhibited no obvious sign of physical damage. In the case of the forests etched with 40 sccm flow there was an obvious change in the forest height noticeable from optical inspection with a 20 minute etch changing the coverage from a dense black forest to thin grey coverage.

SEM images of these MWNTs indicated considerable physical damage to the tubes. This can be attributed to the physical sputtering action of the plasma. Furthermore, some thin sheet-like structures were seen on the SEM images. It is probable that these are formed by the plasma unzipping the MWNTs. Similar results were reported for Ar plasma treatment of individual MWNTs for the productions of graphene nanoribbons (GNRs) by Jiao et al[9]. Fine tuning of this process could lead to the production of scaffolded graphene sheets with applicability for capacitors[10].

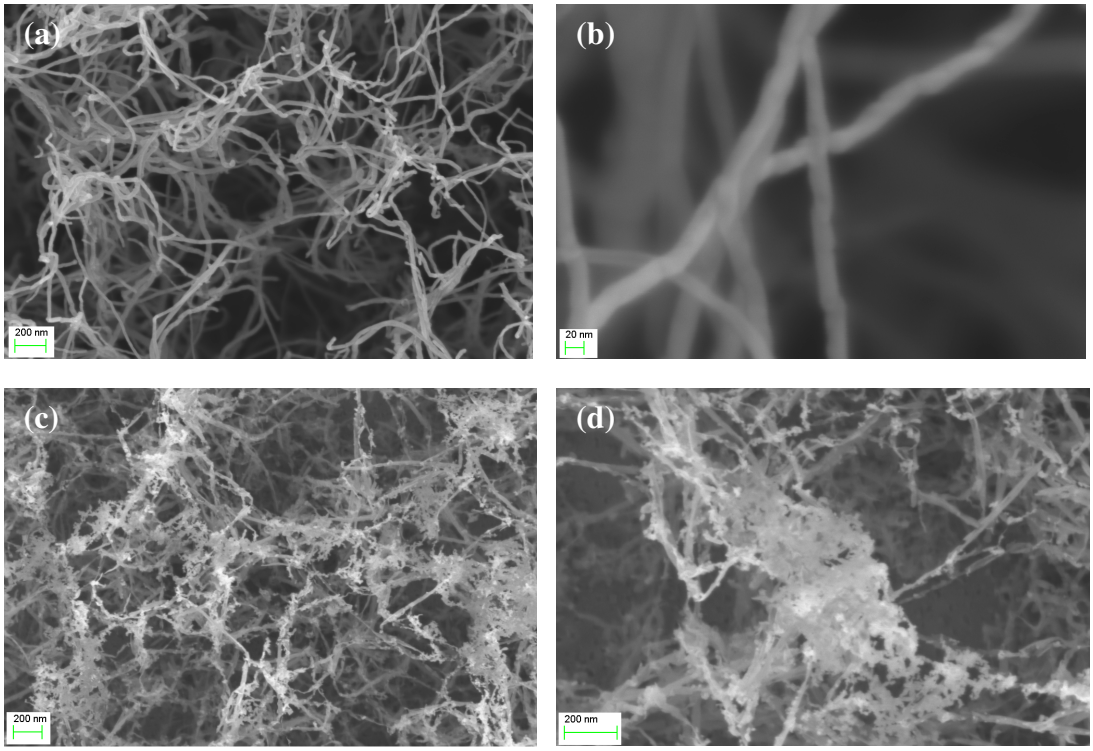

Figure 6.1 *SEM images of MWNT forests (a, b) untreated and (c, d) after 20 minute etch with 40 sccm O_2 flow showing damaged tubes and graphitic sheets.*

6.2.1.3 Raman Analysis

Raman spectroscopy was the principal tool used to investigate the effect of the plasma treatment. Five spectrum were taken for each sample and their average signal analysed (typically there was minimal variation in scans). The *D*, *G*, *D'* and *2D* bands were fitted with Lorentzian peaks.

Raman spectra for forests etched with 20 sccm and 40 sccm flows of O_2 are shown in Figure 6.2. It is clear from these that the relative intensity of the *D* band increases with increasing etch time. The integrated intensity (A_D/A_G) is seen to increase in a linear fashion with the etch time for both O_2 flow rates. The trends observed for the two flow rates differ somewhat and suggest plasma intensity significantly affects the functionalisation process. With the 20 sccm flow short treatment times lead to a decrease in the A_D/A_G ratio suggesting a selective removal of defective material (amorphous carbon) in the early stages of treatment. After this initial improvement the A_D/A_G ratio scales upwards in a linear fashion with etch time. With the 40 sccm flow this initial improvement is not seen and A_D/A_G scales upwards from the offset.

Literature models indicate that higher atom densities and etch rates are expected at higher pressures[11]. These results match closely those reported by Osswald e. al. for the oxidation of MWNTs by flash oxidation and chemical methods[12].

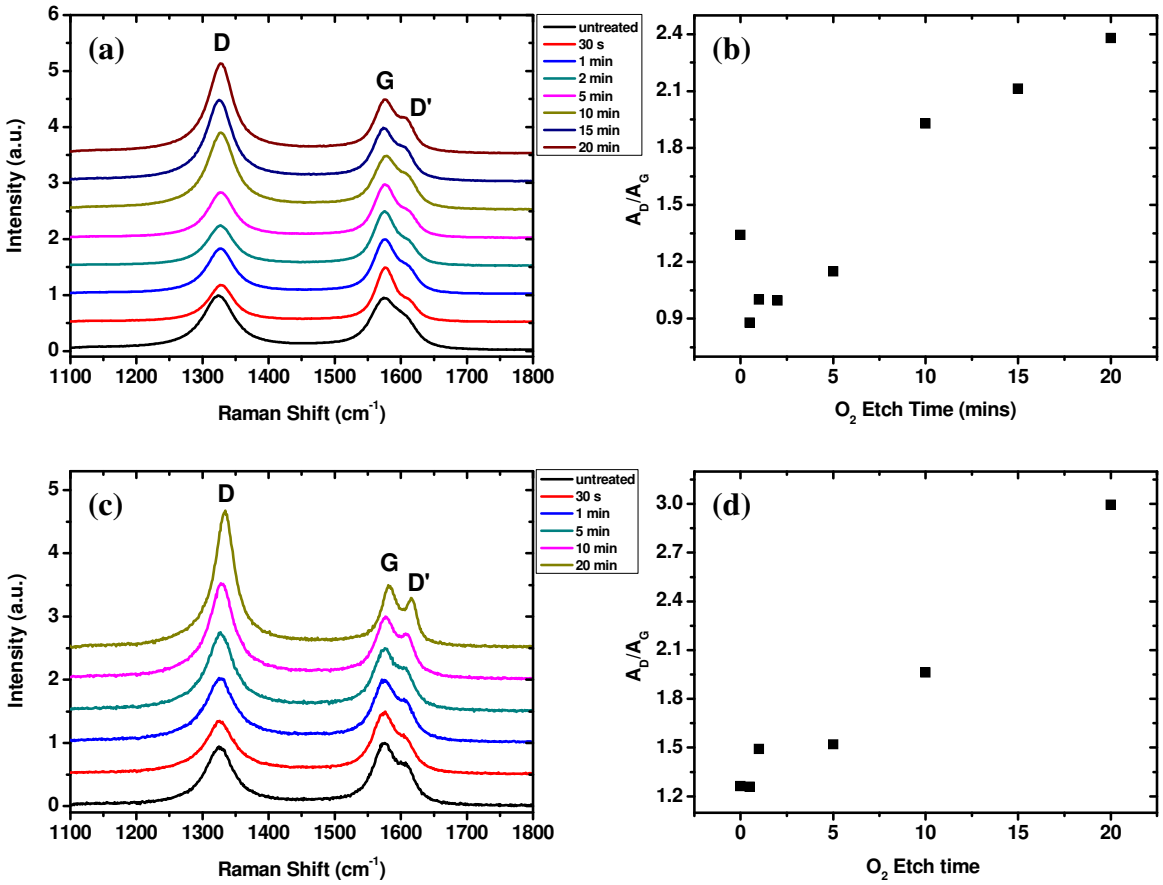

Figure 6.2 *Raman spectra and associated A_D/A_G ratios for (a, b) 20 sccm O_2 flow and (c, d) 40 sccm O_2 flow*

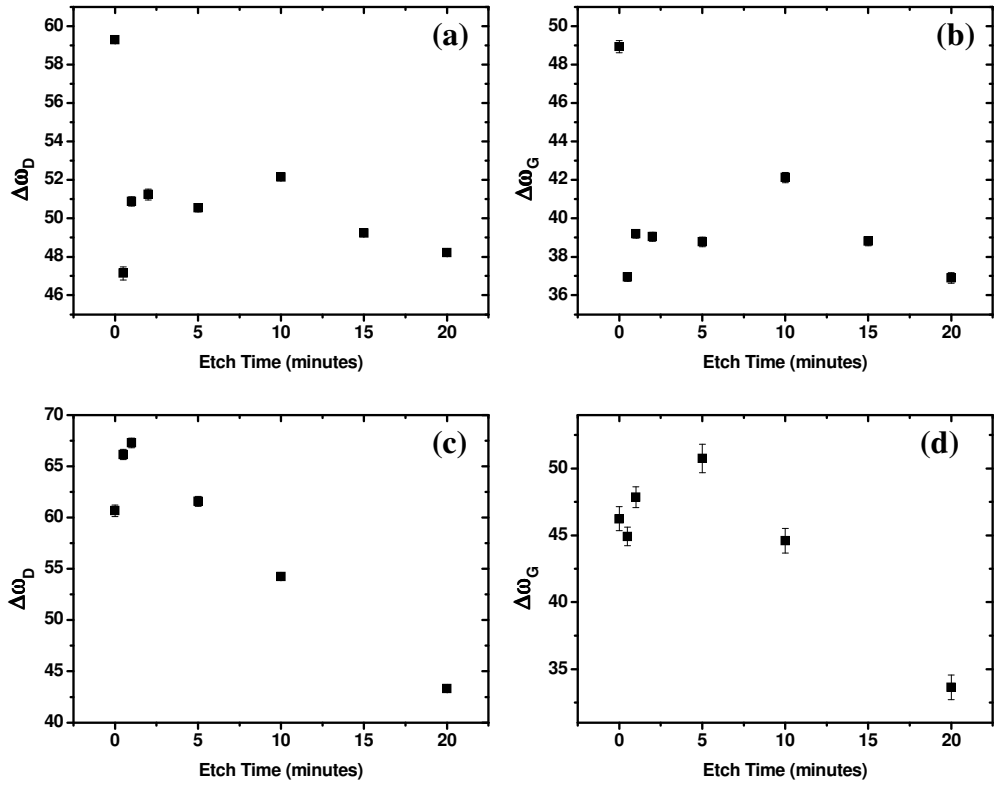

Figure 6.3 *Peak widths for (a, b) 20 sccm O_2 etch and (c, d) 40 sccm O_2 etch*

For the MWNT forests grown in Chapter 4 the peak widths of graphitic bands ($\Delta\omega_D$ and $\Delta\omega_G$) were seen to increase for growth at lower temperatures. This increasing peak width was linked to disorder and the presence of amorphous carbon. In the case of the O_2 treated MWNTs the peak widths do not broaden with increasing etch time (and A_D/A_G ratio). In fact for longer Etch times the peak width is seen to narrow. This suggests that the increase in the A_D/A_G is not related to the presence of amorphous carbon but is instead caused by well defined defects on the tubes.

6.2.2 Plasma Treatment of SWNTs

SWNT Forests grown on 0.4 nm CoFe / Al_2O_3 catalyst (as described in chapter 4) were removed from their growth substrate by sonication in IPA. These SWNTs were then drop cast onto native oxide covered Si pieces (~1cm^2) and used as substrates for assorted plasma treatments.

These SWNT films were treated with O_2, Ar, N_2 and H_2 plasmas. Flow rates of 20 sccm were used with powers of 0.5 and 1 kW and a treatment time of 1 minute.

Raman Analysis

Raman spectra for the treated SWNTs are shown in Figure 6.4. In each case the plasma treatment is seen to increase the relative *D* band intensity suggesting the plasma damages the SWNT structure. Also, the higher power treatment leads to a larger *D* band increase in each case. The defect inducing effect of the different plasmas is seen to scale in the order (O_2 > Ar > N_2 > H_2). Whilst the Ar ions are the heaviest generated they are chemically inert. Those produced from O_2 have a chemical reactivity increasing their defect inducing effect. The ions in the H_2 plasma are the lightest and would not be expected to induce many defects and as such give the smallest increase in defect levels.

The increase in *D* band is far more pronounced than that for similar conditions with the MWNT forests. This can be explained by considering the geometry of the tubes on the substrate. In the case of the MWNT Forests, growth is perpendicular to the substrate and the films are 10 μm thick. In this case the plasma will preferentially affect the tips and sides of the forest. The drop cast SWNTs lie parallel to the substrate and form thin films (< 1 μm) and the entire tube length is exposed to the plasma.

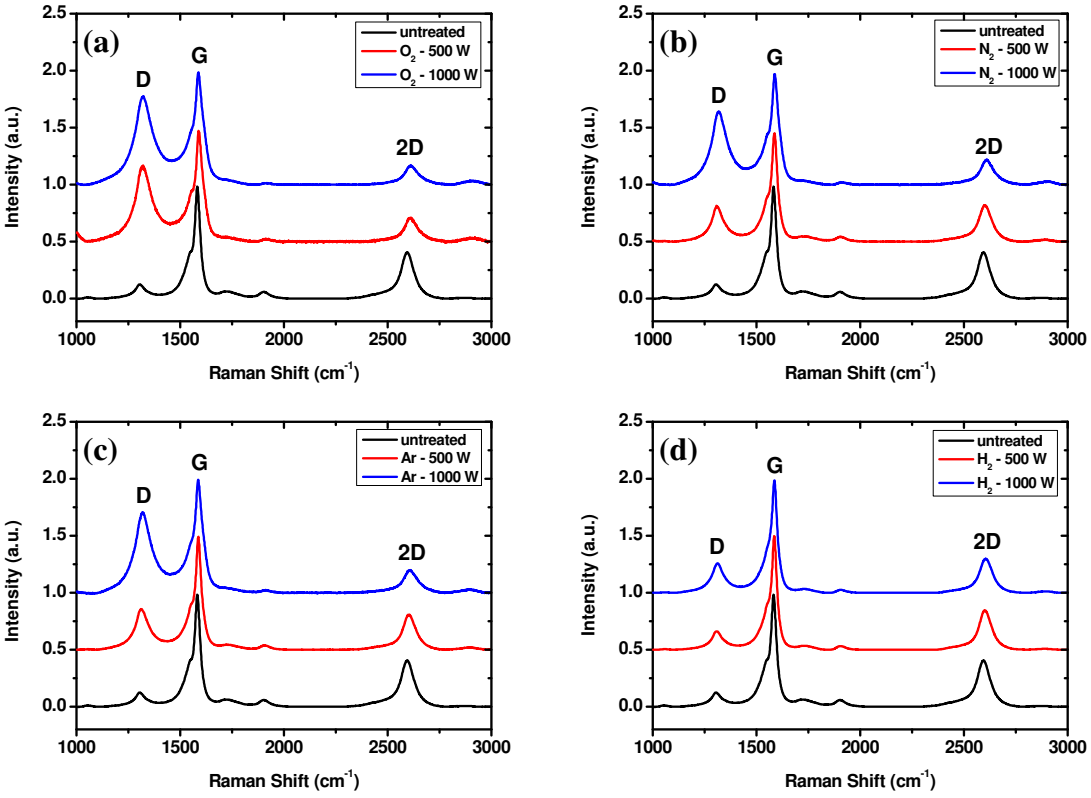

Figure 6.4 *Raman spectra for SWNTs treated with (a) O_2 (b) N_2 (c) Ar and (b) H_2 plasmas*

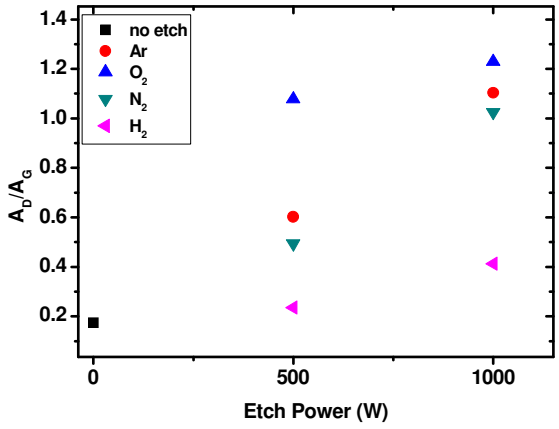

Figure 6.5 *Induced defect levels for different plasma treatments*

6.3 O_2 Plasma Treatment of PyC Films

Plasma treatment of PyC films has impact on a number of potential applications and can be used to create new devices. Firstly it offers a simple route for the incorporation of functionalities onto the surface of films. This can be used for surface and interface engineering where specific groups are required (e.g. sticking layers for ALD processes). Plasma treatment can also be used to increase the roughness of such films.

Functionalisation of PyC films is of interest for electrochemical electrodes, whereby specific groups can be used to introduce sensitivity to specific redox probes and analytes. Plasma etching has also been shown as a necessary step in the production of PyC liners for trench capacitors[13].

Here CVD grown films of PyC were treated using O_2 plasma. Etching of unpatterned films was undertaken in order to add functional groups to the surface of the films and thus enhance the electrochemical activity. The addition of functional groups was verified using XPS. Etching in combination with a NSL shadow mask was used to create hexagonal arrays. This simple approach to nano-structuring has implications for the production of tailored surfaces with increased surface areas. Well defined arrays of carbon nanodots could be of interest for future experiments in plasmonics.

6.3.1 Functionalisation of PyC films

6.3.1.1 Film Growth and Treatment

PyC films were grown by CVD on SiO_2 substrates as described in chapter 5. Films were grown at a temperature of 950 ^oC with a dwell time of 30 mins. A pressure of 20 Torr was used with a C_2H_2 flow rate of 180 sccm. Under these conditions films with thicknesses of ~ 400 nm were produced.

These films were exposed to O_2 plasma treatment at 1 kW for different exposure times. An O_2 flow rate of 20 sccm was used at a pressure of 0.8 Torr. A 10 minute treatment reduced the thickness of the film to ~ 150 nm indicating an etch rate of 25 nm/min. The films were characterised pre and post growth using Raman spectroscopy, XPS and electrochemical probes.

6.3.1.2 Raman Spectroscopy

Raman spectra of PyC films pre and post O_2 plasma treatment are shown in Figure 6.6. Both films have broad *D* and *G* bands indicative of the nanocrystalline nature of the material as discussed in chapter 5. Interestingly the spectrum of the etched material is effectively identical to that of the film as grown. There are a number of possible explanations for this. Firstly one must consider the penetration depth of the Raman laser in the PyC film. One can estimate this to be ~30 nm based on the appearance of peaks from the underlying SiO_2 substrate in thin PyC films and also from quoted literature values for the sampling depth of Raman lasers in carbon[14]. Carbonyl, carboxyl and hydroxyl groups are not strongly Raman active and would give a relatively weak signal when compared with the contribution from PyC. The presence of such groups would distort graphitic planes and could be expected to affect the *D* band intensity, however no obvious change is observed. This could be due to the fact that they are confined to the top surface of the film and do not contribute strongly to the overall signal. It is also possible that because the initial crystallite size is so small the additional functional groups have a relatively negligible affect on the *D* band.

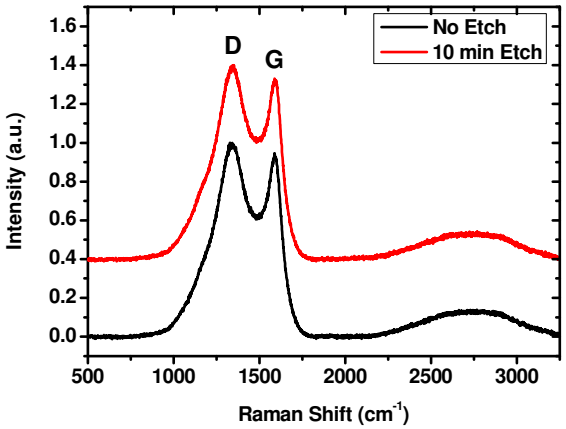

Figure 6.6 *Raman spectra of PyC film pre and post O_2 plasma treatment*

6.3.1.3 XPS Analysis

Unlike Raman spectroscopy XPS is very surface sensitive with a shallow sampling depth (1-2 nm) with the use of the Al *Kα* source. Furthermore, XPS gives an elemental fingerprint and is sensitive to the presence of oxygen at the surface of samples. XPS spectra of PyC films as grown and post O_2 plasma treatment are shown in Figure 6.7. It

is evident that the treatment leads to an increase in the O_{1s} signal as seen in the wide scan. The etching changes the shape of the tail on the C_{1s} peak indicating the presence of oxygen related functionalities [5, 7-8, 15].

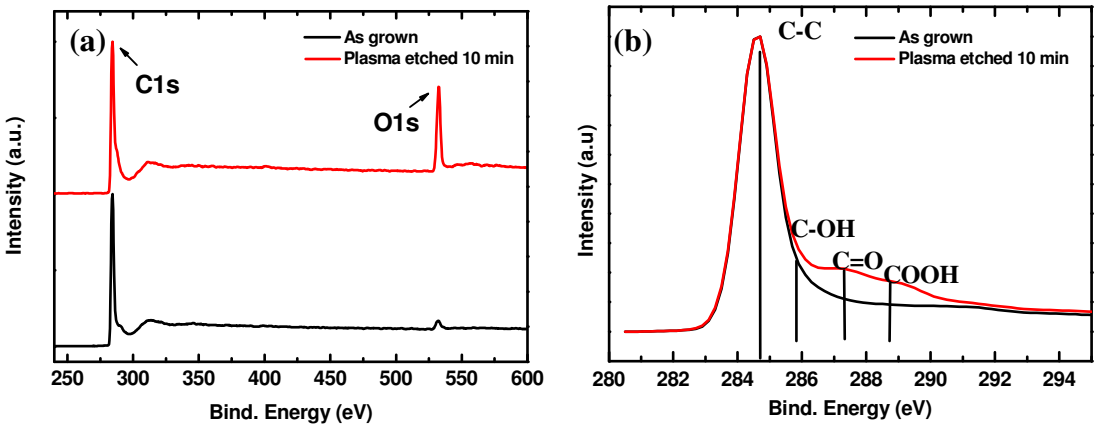

Figure 6.7 *(a) Wide scan XPS spectra showing increased oxygen content in etched sample* (b) *XPS spectra of C_{1s} core level of as grown and etched PyC films showing increased levels of oxygenated functionalities.*

6.3.1.4 Electrochemical Analysis

Carbon materials are one of the most widely studied materials in electrochemistry owing in particular to their low cost and wide applicability[16]. The effectiveness of carbon based electrodes is related to the presence of edge planes and defect sites[6, 17]. This has lead to much interest in CNT[6, 18] and more recently graphene[19-20] based electrodes. PyC, as another form of nanocarbon with a high density of edge planes is of interest for electrochemical characterisation. For films treated with an O_2 plasma electrochemical analysis offers an indirect route for probing the extent of functionalisation.

The electron transfer characteristics of as grown and O_2 treated PyC films were investigated by cyclic voltammetry using a $Fe(CN)_6^{3-/4-}$ redox probe. This was performed using a Ag/AgCl reference electrode. Voltammograms for as grown and treated films are shown in Figure 6.8(a). The peak current increased from 20 µA for the untreated films to 40 µA for the treated films. The peak separation was seen to decrease substantially from 350 mV for the as grown films to 80 mV for the treated films

implying a substantial improvement in the electron transfer rate. The improved electrochemical performance stems from two separate contributions. The etching process roughens the films giving a higher density of edge planes and defect sites, i.e. an increase in surface area. Meanwhile the presence of oxygenated functionalities on the surface of the film gives an increase in the electrochemical surface area. Electrochemical impedance spectroscopy (Figure 6.8(b)) indicated a decreased resistance to charge transfer in the case of O_2 treated films. Further information on the electron transfer characteristics and additional redox probes were detailed by Keeley et al [21].

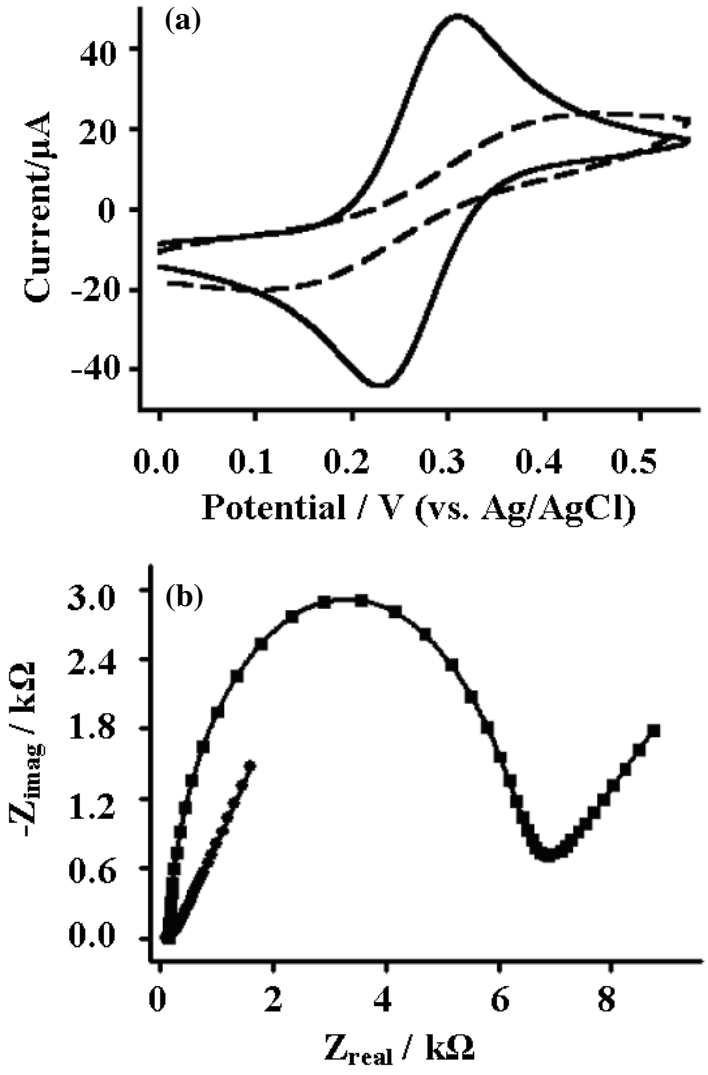

Figure 6.8 *(a) Voltammograms recorded for as grown (dashed) and O_2 treated (solid) PyC in 1mM $Fe(CN)_6^{3-/4-}$ in 1M KCl at 100 mVs^{-1}. (b) Nyquist plots for as grown (■) and O_2 treated (●) PyC for frequencies in the range 10^{-1} to 10^5 Hz. Adapted from [21].*

6.3.2 NSL Patterning of PyC Films

The O_2 treatments used in the previous section were seen to reduce the thickness of PyC films at a rate of ~25 nm/min. This implied that O_2 plasma treatment could be used for physical etching of PyC films. To this end shadow masks were prepared by drop casting a solution of nanospheres onto PyC films. The conditions used for the preparation of the etch masks were identical to those used for the preparation of patterned catalysts in chapter 4 (4.2.4.1). A schematic of this process is shown in Figure 6.9.

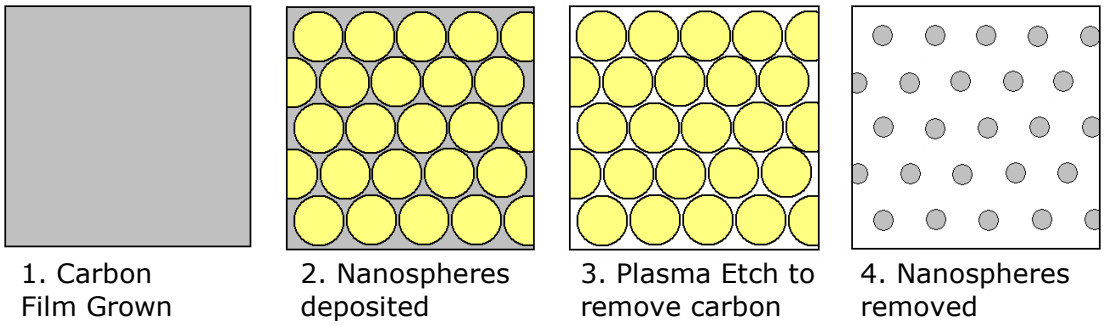

Figure 6.9 *Schematic for NSL shadow masked O_2 etching procedure*

NSL masked PyC films were etched with an O_2 plasma at a power of 1 kW. Following etching the polystyrene spheres were removed by mild sonication in DCM. AFM images of PyC films with 1 and 2 minute etches are shown in Figure 6.10. In both cases hexagonal arrays of raised domains are formed. The height of the domains formed after 1 minute of etching is ~ 23 nm. This is consistent with etch rates observed for unpatterned films. The diameter of these domains is ~ 300 nm. The heights of domains formed after the 2 minute etch are in the range 20 – 25 nm. The diameter of these is considerably smaller, in the range 100 – 150 nm; this can be attributed to the isotropic nature of the etching process giving a considerable under-etching.

Similar patterning and etching was carried out on HOPG and glassy carbon films by Friedrikson et al[22]. Etch rates of 0.19 and 0.65 nm/s were observed for HOPG and glassy carbon respectively. However, details on the etching parameters (plasma power, O_2 flow, pressure etc.) were not given in their paper and so the results cannot be compared directly with those presented here.

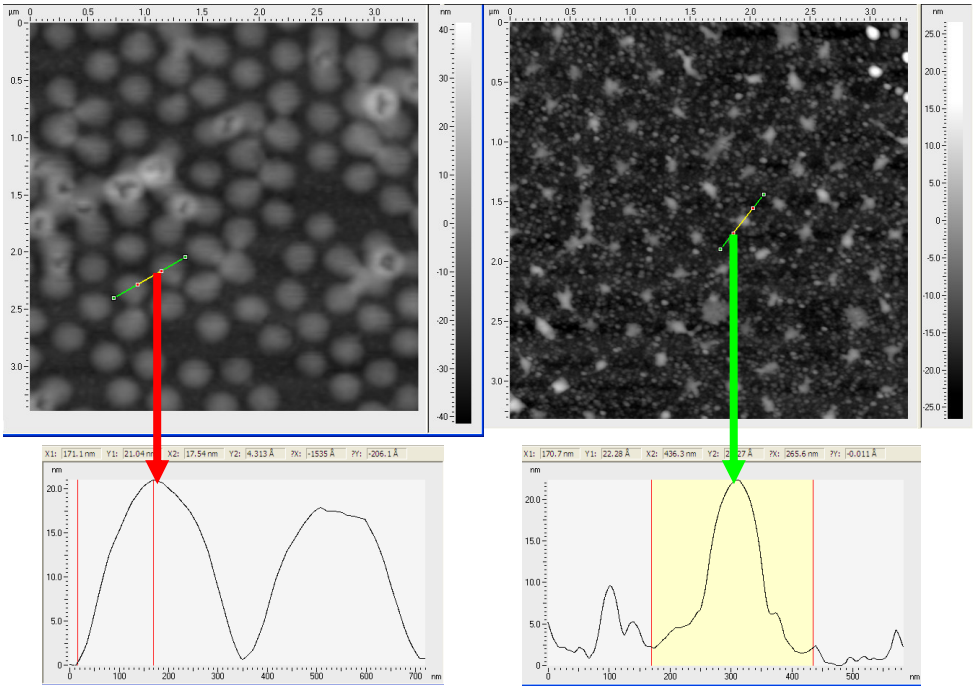

Figure 6.10 *AFM images of PyC films post NSL patterning and etching for (a) 60 s and (b) 120 s*

6.4 CVD Growth and Patterning of Graphene

The deposition of PyC films onto SiO_2 substrates was discussed in detail in Chapter 5. It was established that these films could be graphitised using heat treatments with Ni. Planar deposition of carbon onto Ni has also been studied for a long time. A number of groups have used Ni substrates for the deposition of PyC type films. Derbyshire et al. investigated gas phase deposition of carbon onto Ni foils. Depending on the growth parameters used uniform films or islands of graphitic deposit could be formed[23]. Similar studies were reported by Wada et al. who illustrated control over the morphology and graphitisation of the deposited carbon through modification of the active gas concentration[24]. Studies carried out on deposition of thin carbon films onto different substrates showed the production of graphite on Ni and PyC like deposits on Si, Al_2O_3 and quartz[25]. The graphite on Ni was seen to grow parallel to the underlying Ni forming domains 2 x 2 μm in area. These domains were separated by extrusions which were linked to the difference between the thermal expansion coefficient of the graphite and the underlying Ni.

In recent years focus has shifted towards the production of ultrathin films. Obrazstov et al. demonstrated the production of nanoscale graphitic films (1.5 ± 0.5 nm) on Ni substrates by CVD[26]. This constitutes 5 – 7 graphitic layers and so can be considered as few layer graphene (FLG). Subsequently numerous authors have reported the growth of graphene by CVD under similar conditions [27-30]. The principle growth model proposed for the growth of graphene on Ni surfaces is based on the dissolution of carbon into Ni followed by the segregation of graphitic material parallel to grains on the Ni surface. Isotopic labelling has suggested that this model is accurate for short dwell times[31].

The following section describes the growth of graphene by CVD on Ni substrates and its subsequent patterning using NSL masking and O_2 plasma etching.

6.4.1 CVD Growth of Graphene

6.4.1.1 Film Growth

Graphene films were grown by CVD in the Gero system. Ni films (300 nm) on SiO_2 were prepared by sputtering and used as the growth substrates. These films were introduced into the centre of the furnace and subjected to a pre-treatment in H_2 (60 sccm). The growth step involved a 50:50 mix of H_2:C_2H_2 (60 sccm each). Typically a growth pressure of 1 Torr was used with growth temperatures ranging from 750 ^oC – 950 ^oC. Dwell times in the range 30 s – 10 mins were used. Graphene films were transferred by immersion in HCl (5M) to dissolve the Ni and then subsequent dredging onto arbitrary substrates.

6.4.1.2 Temperature Dependence

In chapter 5 the lower temperature limit for appreciable PyC deposition was found to be ~ 850 ^oC. As the growth of graphene is catalysed process one could reasonably expect it to have a lower activation temperature. In practice the lower temperature limit has been found to be ~ 750 ^oC[32].

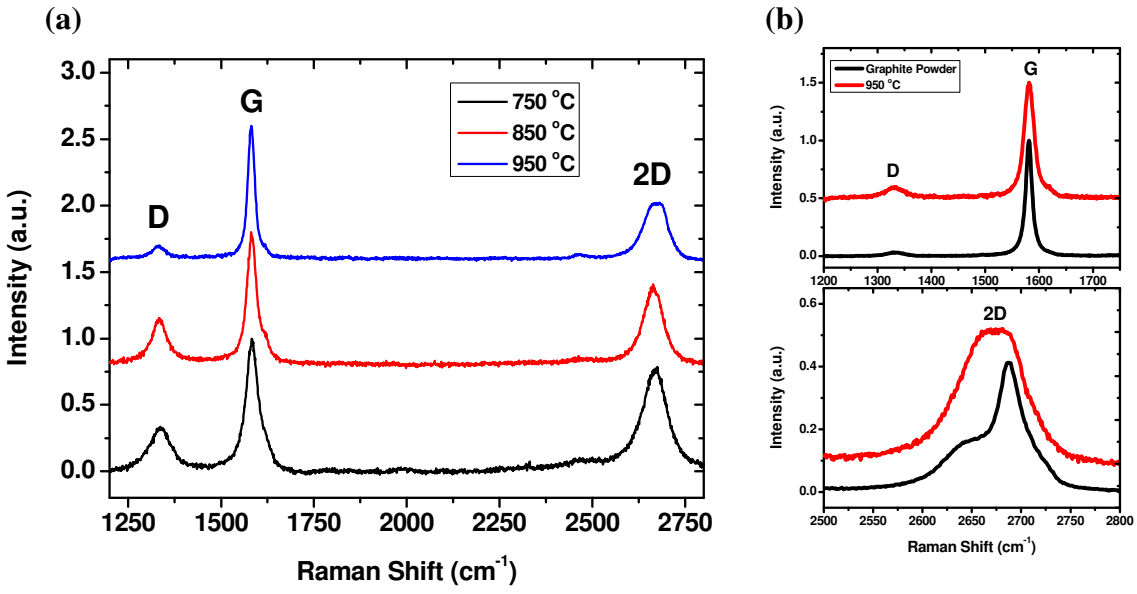

Figure 6.11 *(a) Raman spectra of films grown at different temperatures with a flow time of 5 minutes. (b) Comparison of D, G and 2D bands between graphite powder and films grown at 950 ^oC.*

Spectra of films grown at different temperatures are shown in Figure 6.11(a). In each case a dwell time of 5 minutes was used. It is clear from these spectra that an increase in growth temperature leads to a decrease in the *D* band intensity. In CVD graphene there are two primary contributions to the *D* band; lattice defects which are related to functional groups, missing atoms etc. and edge plane defects which stem from the extrusions seen between different graphitic domains.

A comparison between the film grown at 950 ^{o}C and graphite powder is shown in Figure 6.11 (b). The *2D* band shape of the CVD graphene film differs considerably from that of graphite. This can be attributed to various domains of few-layer graphene (FLG) of differing thicknesses contributing to the signal. It has been reported previously that these different thicknesses are due to different growth rates on different Ni crystal orientations [26, 33]. The *D* band for the CVD graphene is larger that that of graphite powder but this can be linked with the prevalence of edge sites. A SEM image of a graphene film grown at 950 ^{o}C is shown in Figure 6.12. This shows regions ~μm^2 in area separated by extrusions. The spot size on the Raman laser used is 3 – 5 μm^2 thus making contributions from these extrusions highly probable.

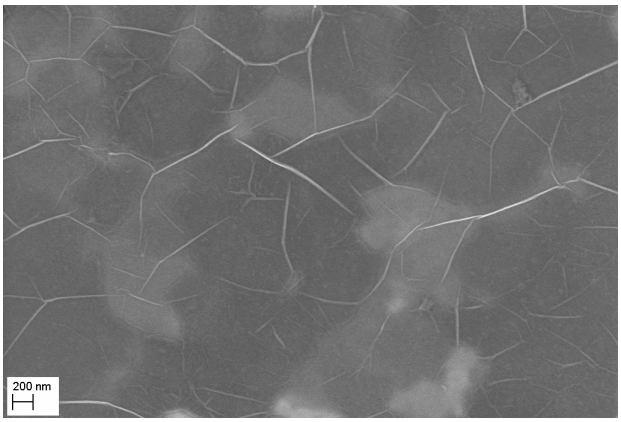

Figure 6.12 *SEM image of graphene film showing extrusions separating different domains*

6.4.1.3 Catalytic Action of Ni

The catalytic action of Ni was investigated by subjecting films of Ni, Ta and SiO_2 to identical growth conditions. A 32 minute growth step was used with a pressure of 5 Torr and a growth temperature of 950 ^{o}C. Raman spectra of the three films post growth are shown in Figure 6.13. The Ni film shows a clear graphitic signal, with well

defined *D*, *G* and *2D* bands. The SiO_2 film shows *D* and *G* bands indicative of the presence of carbon species; however the large *D* band and the absence of an appreciable *2D* band indicate that the deposit is highly disordered with a low level of graphitisation. This is somewhat similar to the PyC produced in chapter 5; however a larger A_D/A_G is seen implying a smaller crystallite size. The Ta film shows a signal similar to SiO_2 but its intensity is very low suggesting minimal deposition. These findings are in agreement with those previously reported by Johannson et al[25]. The minimal deposition observed on Ta validates some of the work in chapter 4. Firstly, it is evident that Ta is relatively inert and does not promote graphitic growth itself. Furthermore, the weaker signal observed on Ta when compared with SiO_2 suggests a lower deposition rate on Ta and explains why a better Raman signal is seen for Ta supported catalysts.

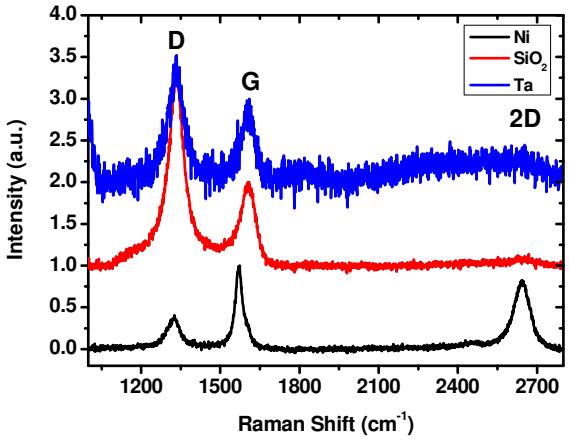

Figure 6.13 *Raman spectra of carbon films grown on different substrates at 950 °C*

6.4.1.4 Shorter Dwell Times

In order to produce thinner graphene films shorter dwell times were employed. Ten spectra from a film grown with a 2 minute dwell time are shown in Figure 6.14. As mentioned previously, CVD graphene films are non uniform due to differing growth rates on different Ni crystallites. This is evidenced in the Raman spectra with a monolayer graphene signal seen in one scan (spot 5) and the other nine exhibiting FLG signals. A comparison between this monolayer spectrum and powdered graphite is shown in Figure 6.15. The relative *D* band intensity is larger for the graphene but this can be attributed to contributions from the edge of the domain being probed. The real area of interest is the *2D* band where the monolayer has a single peak at ~ 2662 cm^{-1},

whereas the highest intensity in the graphite peak is seen at ~2688 cm^{-1}. Fitting a Lorentzian peak to this gives a FWHM of < 30 cm^{-1}. Furthermore the ratio of the *2D* to *G* band intensities (I_{2D}/I_G) is seen to be 2.75 which is much larger than that of graphite (~ 0.4). These observations are consistent with the presence of monolayer graphene.

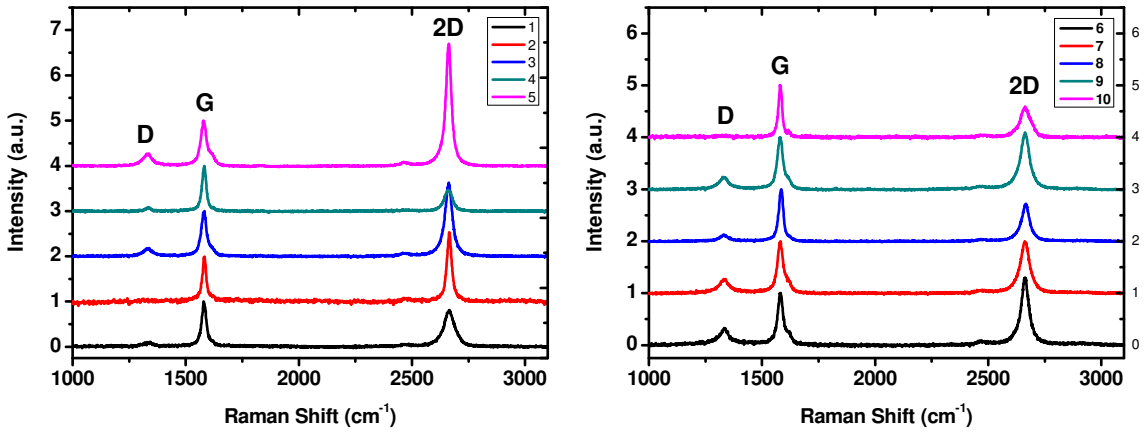

Figure 6.14 *Raman spectra of 10 different spots on sample grown at 950 °C with a dwell time of 2 minutes*

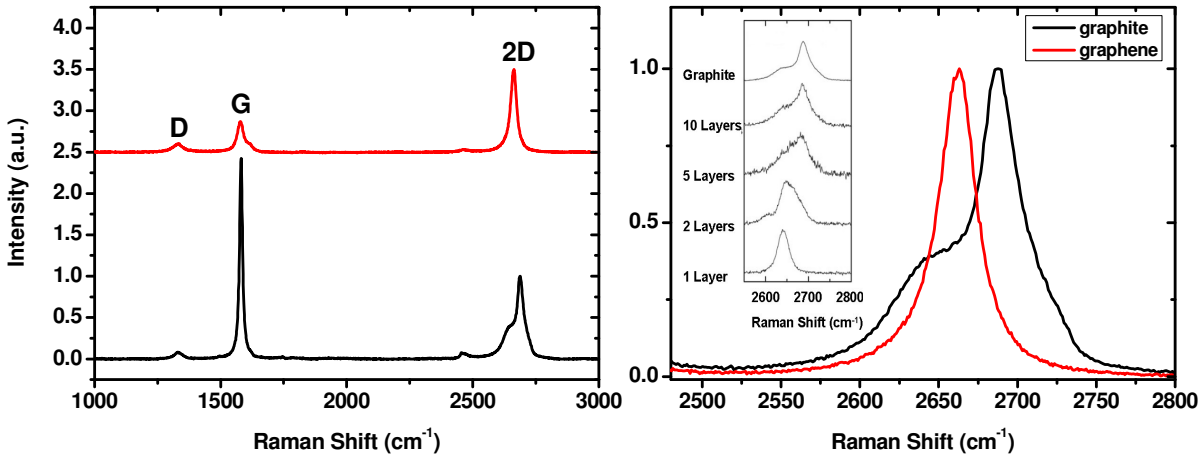

Figure 6.15 *Raman spectra of graphite powder and monolayer region of CVD graphene (a) Full spectrum (b) 2D band, inset shows the evolution of the 2D band with the addition of graphitic layers adapted from*[33].

Standard SEM imaging gives some indication of the thicknesses of different regions but the contrast is more apparent with the use of a STEM detector. The signal reaching the in-lens detector is dependent on the emission of secondary electrons and thus the

thickness of the sample being probed. Dark regions on the in-lens image correspond to thinner graphene domains. In STEM imaging mode the detector is located underneath the sample being probed. The intensity of the transmitted signal is reduced with increasing sample thickness and so bright regions on a STEM image are due to a high degree of electron transmission and indicate a thin sample region with high electron transparency. Images of the same region of a graphene film taken with an in-lens and STEM detector are shown in Figure 6.16. Here the darkest regions on the in-lens image overlap with the brightest regions on the STEM image. The high degree of electron transparency suggests that the brightest region on the STEM image corresponds to mono or bi-layer graphene.

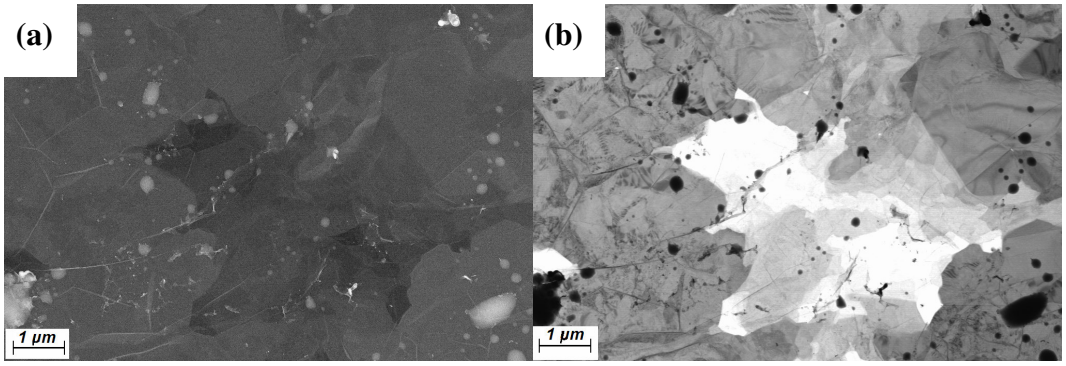

Figure 6.16 *SEM Images of the same area on a graphene film taken with (a) in lens detector and (b) STEM detector. Scale bar is 1 µm.*

6.4.2 O_2 Plasma Treatment of Graphene Films

The properties of graphene can be modified by post growth plasma treatments. It has been shown that and NH_3 plasma can be used to N dope CVD graphene during growth[34]. In the case of graphene produced by micromechanical cleavage it has been shown that O_2 plasma treatment can be used to make the graphene photoluminescent[35]. Scanning Raman spectroscopy is a powerful characterisation tool as it allows for two dimensional mapping of Raman active samples over large areas. This is useful for gauging the uniformity of samples and is used extensively for pharmaceutical quality control. Here scanning Raman was used to investigate the effect of O_2 plasma treatment on FLG samples. This allowed for the defect intensity to be probed and also gave information of the location of defects.

6.4.2.1 Sample Preparation and Treatment

Two FLG films prepared under identical growth conditions were transferred onto SiO_2 on Si substrates. One of these samples was treated with an O_2 plasma (flow = 20 sccm, P = 1000 W) for 30 s.

6.4.2.2 Raman Spectroscopy

Representative Raman spectra (spot scans) taken with a 633 nm laser of the FLG films pre and post O_2 etching are shown in Figure 6.17. These clearly indicate the high quality of the starting material with a negligible *D* band seen for most scans. The scans taken following plasma treatment show a large increase in the *D* band intensity and an increase in the *2D* band intensity indicative of increased defect levels.

The origin of defects in these samples was investigated using scanning Raman with an excitation wavelength of 633 nm. A scan area of 100 x 100 μm was probed taking 250 x 250 spectra in the x and y directions.

Raman maps generated for the *D*, *G* and *2D* band intensity for the untreated sample are shown in Figure 6.18 Bright areas on these maps indicate regions with a strong Raman signal. It is clear that the film is not continuous as flake-like morphologies are seen. This can be attributed to damage induced in the transfer process. It is also evident from the scale that the *G* band is considerably more intense than the *D* or *2D* bands as expected for FLG.

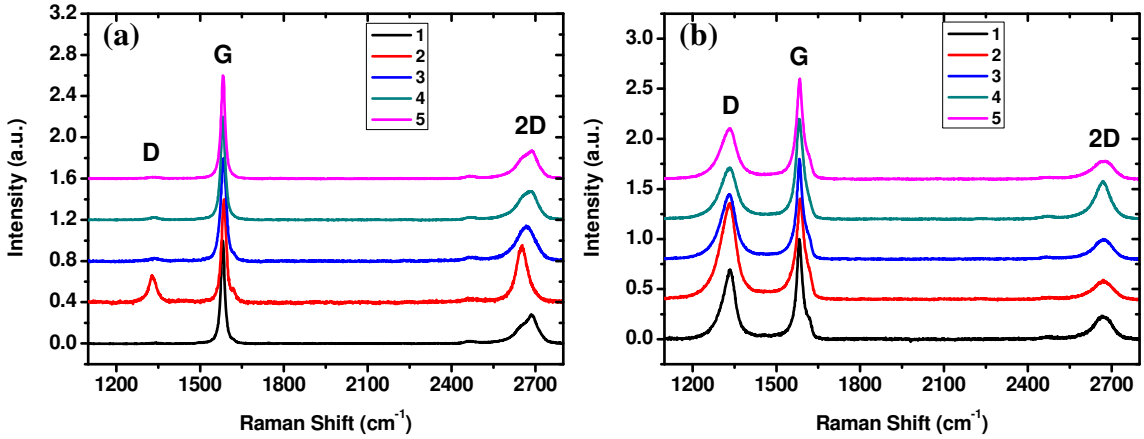

Figure 6.17 *Representative Raman spectra of FLG films (a) pre and (b) post O_2 plasma treatment.*

Contour maps were generated using the raw data from the Raman maps Figure 6.19. Those shown are zoomed in on the region highlighted on the Raman map and were chosen to be in a region where the flakes were in good focus. These clearly indicate a strong *G* band signal from the flakes seen. A low I_D/I_G ratio (0.06 – 0.12) is seen and the I_{2D}/I_G ratio is consistent with an FLG signal. Maps of I_D/I_G were generated by dividing the *D* band intensity matrix by the *G* band intensity matrix. At first glance this map is deceptive as it suggests that the most defective regions are those where no FLG is seen. This is merely an artefact of the process and by purely focusing on the regions which have a high intensity in the *G* band map it is evident that the entire flake exhibits a low I_D/I_G ratio.

Raman maps and generated contour plots for O_2 treated FLG are shown in Figure 6.20 and Figure 6.21 respectively. A number of differences between these and those for the untreated films are observed. The I_D/I_G ratio is seen to increase substantially across the entire sample. From this one can infer that the O_2 plasma is inducing defects throughout the FLG and that the *D* band is not wholly from edge plane contributions. The increasing defect levels are in fact underestimated as the mapping does not account for the emergence of the *D'* band.

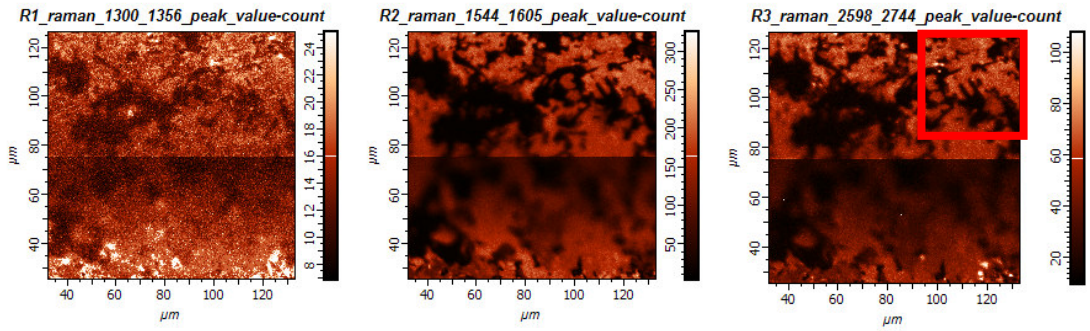

Figure 6.18 *Raman maps showing D, G and 2D band intensity for untreated FLG*

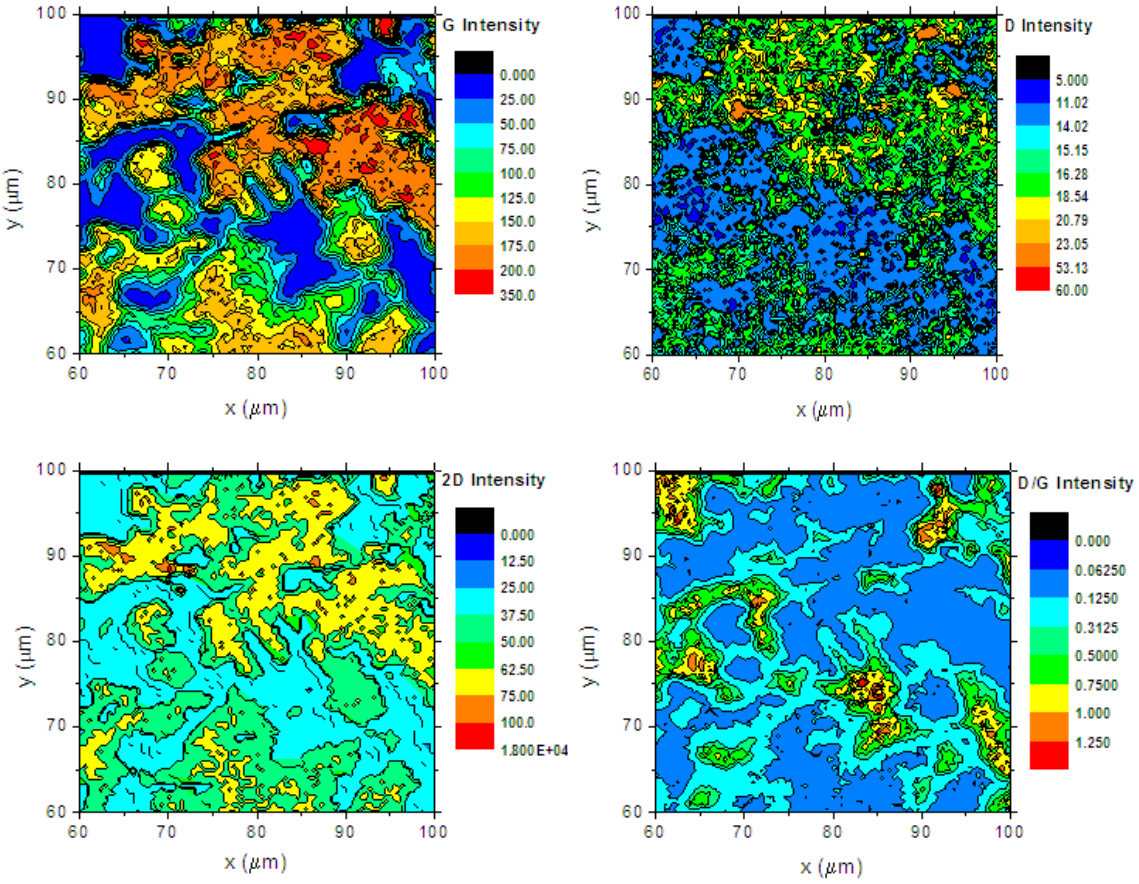

Figure 6.19 *Contour plots for untreated FLD showing D, G and 2D band intensities as well as* I_D/I_G

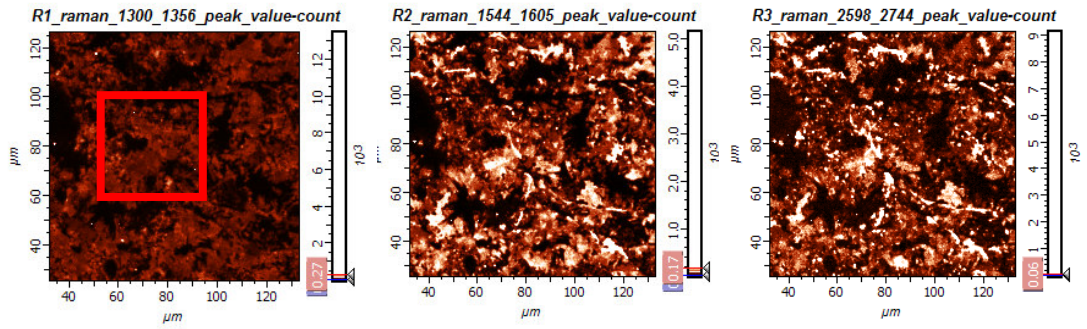

Figure 6.20 *Raman maps showing D, G and 2D bands for O_2 plasma treated FLG*

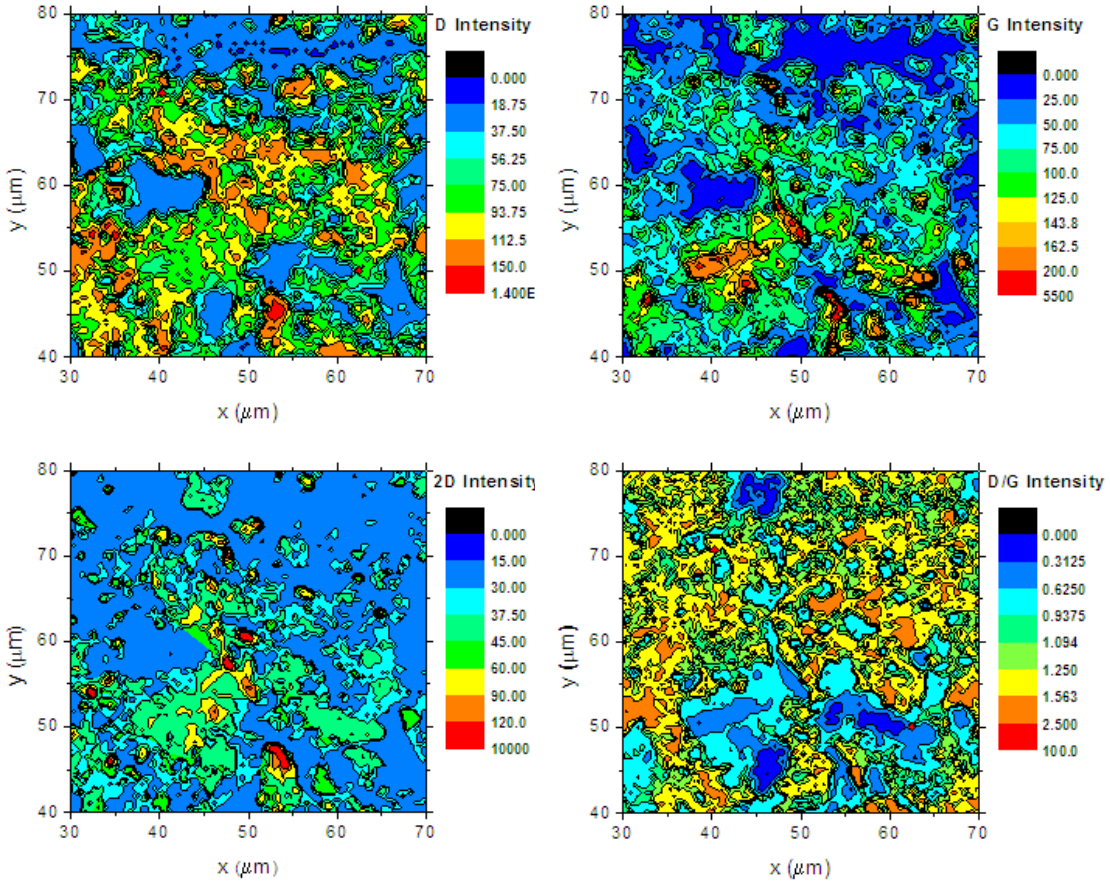

Figure 6.21 *Contour plots for O_2 plasma treated FLG showing D, G and 2D band intensities as well as I_D/I_G*

6.4.3 NSL Patterning of Graphene

In order to exploit the novel properties of graphene post growth processing steps are required. The use of nanowire etch masks with plasma etching for the production of GNRs has been reported[36]. This is particularly interesting as the edges of the GNR act as scattering sites and so the bandgap of the GNRs produced can be controlled by the diameter of the etch mask used.

Here a proof of concept is shown for the use of a NSL etch mask with O_2 plasma etching for the patterning of CVD FLG films. The graphene films were transferred to SiO_2 substrates and the NSL shadow mask was deposited as described in section 3.2.2. Etching was carried out with an O_2 plasma with an etch time of 30 s under the same conditions used in the previous section.

AFM images of the FLG films pre and post etching are shown in Figure 6.22. The untreated image shows domains ~μm^2 in area which is consistent with SEM images shown earlier. The post-etch image shows hexagonal patterning of the graphene film. The graphitic dots aren't cut out completely as seen for NSL patterned PyC films, however this can be attributed to the higher resistivity of the graphene to O_2 etching.

A higher magnification AFM image of the etched film is shown in Figure 6.23. This indicates that the etch depth is ~10 nm and the diameter of individual domains is ~ 200 nm.

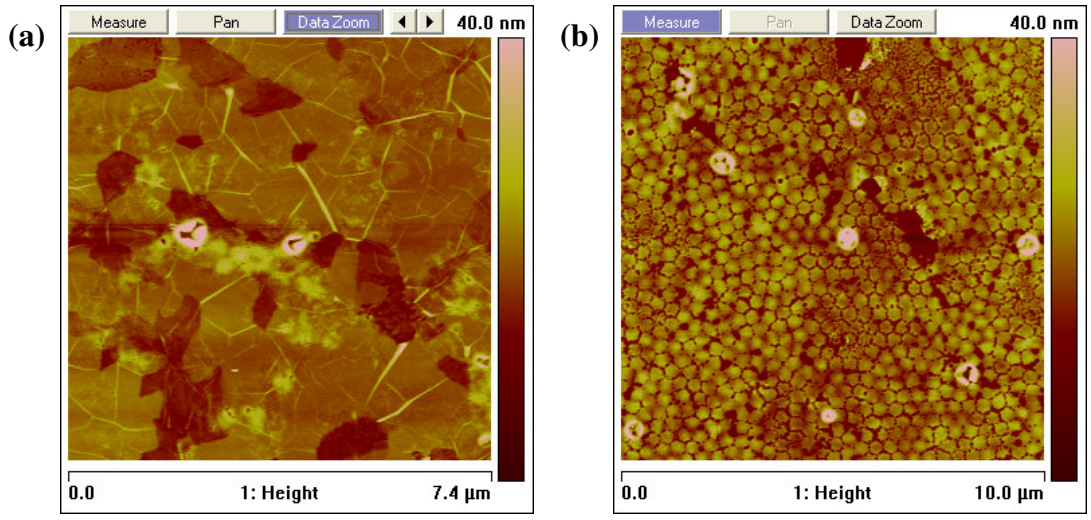

Figure 6.22 *AFM images of FLG (a) pre and (b) post NSL patterning and etching*

This simple approach to patterning could potentially be used for a number of applications. A porous graphene based mesh could be used for highly sensitive gas sensors where species adsorb at the defective edges. This has been theoretically assessed[37] (albeit with much smaller pore sizes). One can also envisage usage as templates for molecular assembly or selective membranes. Tuning of the etching parameters could be used to produce quantum dots based on nanoscale graphene crystals.

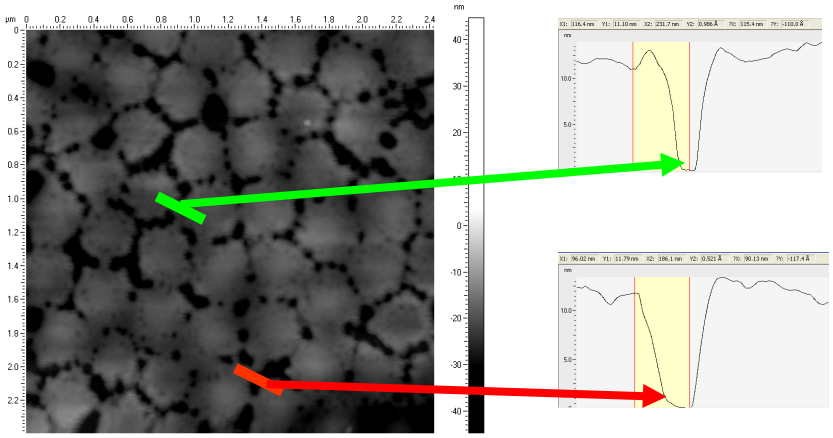

Figure 6.23 *High magnification AFM image showing an etch depth of ~ 10 nm on NSL patterned FLG*

Conclusions

O_2 Plasma etching has been used to introduce controlled levels of defects into MWNT forests. Increasing the O_2 flow leads to increased sputtering action and is seen to convert the MWNTs to thin graphitic sheets with long etch times. The defect inducing effect of different plasma sources on drop cast CVD SWNTs was also considered. These were far more susceptible due to the larger exposed surface area.

The effect of O_2 plasma treatment on PyC films was investigated. This was shown to be a very flexible process and was used for the production of electrochemical electrodes with enhanced performance and also for the production of hexagonal arrays of PyC nanodots.

The growth of graphene films on Ni substrates by a CVD process was described. Varying the dwell time allowed for the production of FLG or thinner films with regions of monolayer graphene. The catalytic activity of Ni was shown by inclusion of inert substrates in a number of runs. These showed the formation of thin PyC like deposits.

Scanning Raman analysis allowed for the mapping of FLG films transferred onto insulating substrates. This allowed for the imaging of defects on FLG films which were seen to stem from the middle of films as well as edge sites.

NSL patterning and O_2 plasma etching was shown to be a simple procedure for the patterning of FLG films. With optimisation this could be used for many potential applications.

References

1. Liston, E.M., L. Martinu, and M.R. Wertheimer, *Plasma Surface Modification of Polymers for Improved Adhesion - A Critical Review*. Journal of Adhesion Science and Technology, 1993. **7**(10): p. 1091-1127.
2. Wu, C.C., et al., *Surface modification of indium tin oxide by plasma treatment: An effective method to improve the efficiency, brightness, and reliability of organic light emitting devices.* Applied Physics Letters, 1997. **70**(11): p. 1348-1350.
3. Hartney, M.A., D.W. Hess, and D.S. Soane, *Oxygen Plasma-Etching for Resist Stripping and Multilayer Lithography* Journal of Vacuum Science & Technology B, 1989. **7**(1): p. 1-13.
4. Sun, Y.-P., et al., *Functionalized Carbon Nanotubes: Properties and Applications.* Accounts of Chemical Research, 2002. **35**(12): p. 1096-1104.
5. Felten, A., et al., *Radio-frequency plasma functionalization of carbon nanotubes surface O-2, NH3, and CF4 treatments.* Journal of Applied Physics, 2005. **98**(7).
6. Chou, A., et al., *Demonstration of the importance of oxygenated species at the ends of carbon nanotubes for their favourable electrochemical properties.* Chemical Communications, 2005(7): p. 842-844.
7. Xu, T., et al., *Surface modification of multi-walled carbon nanotubes by O2 plasma.* Applied Surface Science, 2007. **253**(22): p. 8945-8951.
8. Barinov, A., et al., *Imaging and Spectroscopy of Multiwalled Carbon Nanotubes during Oxidation: Defects and Oxygen Bonding.* Advanced Materials, 2009. **21**(19): p. 1916-1920.
9. Jiao, L., et al., *Narrow graphene nanoribbons from carbon nanotubes.* Nature, 2009. **458**(7240): p. 877-880.
10. Miller, J.R., R.A. Outlaw, and B.C. Holloway, *Graphene Double-Layer Capacitor with ac Line-Filtering Performance.* Science, 2010. **329**(5999): p. 1637-1639.
11. Tae Kim, M., *Pressure-dependence of etch rate in O2 discharges.* Thin Solid Films, 2001. **401**(1-2): p. 39-44.
12. Osswald, S., M. Havel, and Y. Gogotsi, *Monitoring oxidation of multiwalled carbon nanotubes by Raman spectroscopy.* Journal of Raman Spectroscopy, 2007. **38**(6): p. 728-736.
13. Aichmayr, G., et al. *Carbon / high-k Trench Capacitor for the 40nm DRAM Generation*. in *VLSI Technology, 2007 IEEE Symposium on*. 2007.
14. Alsmeyer, Y.W. and R.L. McCreery, *Surface enhanced Raman examination of carbon electrodes: effects of laser activation and electrochemical pretreatment.* Langmuir, 1991. **7**(10): p. 2370-2375.
15. Desimoni, E., et al., *XPS determination of oxygen-containing functional groups on carbon-fibre surfaces and the cleaning of these surfaces.* Surface and Interface Analysis, 1990. **15**(10): p. 627-634.
16. McCreery, R.L., *Advanced Carbon Electrode Materials for Molecular Electrochemistry.* Chemical Reviews, 2008. **108**(7): p. 2646-2687.
17. Rice, R.J. and R.L. McCreery, *Quantitative relationship between electron transfer rate and surface microstructure of laser-modified graphite electrodes.* Analytical Chemistry, 1989. **61**(15): p. 1637-1641.
18. Keeley, G.P. and M.E.G. Lyons, *The Effects of Thin Layer Diffusion at Glassy Carbon Electrodes Modified with Porous Films of Single-Walled Carbon*

Nanotubes. International Journal of Electrochemical Science, 2009. **4**(6): p. 794-809.
19. Tang, L., et al., *Preparation, Structure, and Electrochemical Properties of Reduced Graphene Sheet Films.* Advanced Functional Materials, 2009. **19**(17): p. 2782-2789.
20. Keeley, G.P., et al., *Electrochemical ascorbic acid sensor based on DMF-exfoliated graphene.* Journal of Materials Chemistry, 2010. **20**(36): p. 7864-7869.
21. Keeley, G.P., et al., *Thin film pyrolytic carbon electrodes: A new class of carbon electrode for electroanalytical sensing applications.* Electrochemistry Communications, 2010. **12**(8): p. 1034-1036.
22. Fredriksson, H., D. Chakarov, and B. Kasemo, *Patterning of highly oriented pyrolytic graphite and glassy carbon surfaces by nanolithography and oxygen plasma etching.* Carbon, 2009. **47**(5): p. 1335-1342.
23. Derbyshire, F.J. and D.L. Trimm, *Kinetics of the deposition of pyrolytic carbon on nickel.* Carbon, 1975. **13**(3): p. 189-192.
24. Wada, H., et al., *The Formation of Pyrolytic Carbon on a Nickel Sheet.* Japanese Journal of Applied Physics Part 2-Letters, 1989. **28**(2): p. L284-L286.
25. Johansson, A.-S. and J.-O. Carlsson, *Crystallinity, morphology and microstructure of chemical-vapor-deposited carbon films on different substrates.* Thin Solid Films, 1995. **261**(1-2): p. 52-58.
26. Obraztsov, A.N., et al., *Chemical vapor deposition of thin graphite films of nanometer thickness.* Carbon, 2007. **45**(10): p. 2017-2021.
27. Kim, K.S., et al., *Large-scale pattern growth of graphene films for stretchable transparent electrodes.* Nature, 2009. **457**(7230): p. 706-710.
28. Reina, A., et al., *Large Area, Few-Layer Graphene Films on Arbitrary Substrates by Chemical Vapor Deposition.* Nano Letters, 2009. **9**(1): p. 30-35.
29. Yu, Q.K., et al., *Graphene segregated on Ni surfaces and transferred to insulators.* Applied Physics Letters, 2008. **93**(11).
30. Kumar, S., et al., *Gas phase controlled deposition of high quality large-area graphene films.* Chemical Communications, 2010. **46**(9): p. 1422-1424.
31. Li, X., et al., *Evolution of Graphene Growth on Ni and Cu by Carbon Isotope Labeling.* Nano Letters, 2009.
32. Kumar, S., et al., *Low Temperature Graphene Growth.* ECS Transactions, 2009. **19**(5): p. 175-181.
33. Ferrari, A.C., *Raman spectroscopy of graphene and graphite: Disorder, electron-phonon coupling, doping and nonadiabatic effects.* Solid State Communications, 2007. **143**(1-2): p. 47-57.
34. Lin, Y.C., C.Y. Lin, and P.W. Chiu, *Controllable graphene N-doping with ammonia plasma.* Applied Physics Letters, 2010. **96**(13).
35. Gokus, T., et al., *Making Graphene Luminescent by Oxygen Plasma Treatment.* ACS Nano, 2009. **3**(12): p. 3963-3968.
36. Bai, J.W., X.F. Duan, and Y. Huang, *Rational Fabrication of Graphene Nanoribbons Using a Nanowire Etch Mask.* Nano Letters, 2009. **9**(5): p. 2083-2087.
37. Jiang, D., V. Cooper, and S. Dai, *Porous Graphene as the Ultimate Membrane for Gas Separation.* Nano Letters, 2009.

Chapter 7

Conclusions and Future Work

Work in this thesis covered the growth and characterisation of nanocarbon structures produced by catalytic and non-catalytic CVD methods.

MWNTs were grown on an array of different catalyst substrates. PLD was shown to be an effective method for the preparation of Fe catalysts. Flow rate modification allowed for the growth of forests and films of MWNTs on these catalysts. The incorporation of H_2 into growth recipes was used to enhance the catalyst activity producing much longer forests.

The use of a Ta layer was shown to be a viable route for the growth of MWNTs on conducting substrates. An investigation of growth parameters highlighted conditions for the production of tall forests of good quality MWNTs. Increasing the growth temperature improved the quality of nanotubes grown as seen in Raman spectra, where the intensity ratios and peak widths of *D* and *G* bands implied a lowering of defect levels. The tallest forests were produced at intermediate temperatures (700 ^{o}C) and high pressures (10, 20 Torr). Investigation of the catalyst showed the production of nanoparticles in the temperature range of 550 – 750 ^{o}C and a clustering of nanoparticles at 800 ^{o}C. TEM studies indicated that the MWNTs grown at 550 ^{o}C were defective and that those grown at higher temperatures were of good quality with well defined inner and outer diameters. Four different catalyst alloy systems were investigated and $Co_{90}Fe_{10}$ was seen to give the best quality growth. An investigation into the use of these MWNT forests on Ta underlayers as high surface area electrochemical electrodes is currently underway in the ASIN group in Crann, Trinity College Dublin (see Appendix A).

The use of PPF as a catalyst underlayer was also investigated. Under similar CVD growth conditions this produced structures with a larger mean and spread of diameter than those seen with a Ta underlayer. This suggested a different interaction between catalyst and substrate compared with Ta and SiO_2.

NSL was used as a simple route for the patterning of nanoscale catalyst features. Growth on these films was problematic by thermal CVD methods with the catalytic

activity being either too high or too low depending on the growth conditions used. PECVD on the other allowed for the production of well aligned structures. Characterisation suggested that these were CNFs rather than CNTs.

SWNT films were grown using similar CVD recipes with thinner catalyst films. The use of an Al_2O_3 layer was shown to be pivotal for this growth. Changing the reaction temperature was again seen to have a big impact on the quality of the samples produced. Examination of the RBM region of Raman spectra indicated that the SWNTs produced had contributions from small diameter SWNTs not seen in the spectra of some common commercial SWNTs. Different catalyst alloys were seen to give a different distribution of diameters in the SWNTs grown suggesting some degree of diameter selectivity. The growth of smaller diameter SWNTs was suppressed at higher growth temperatures.

By modifying the gas flow parameters SWNT forests were produced. High purity samples with heights greater than 100 μm were grown at a temperature of 850 ^{o}C and a pressure of 10 Torr. Both films and forests of SWNTs were transferred by immersion of the growth substrates in HF. In the case of forests this led to a densification of the SWNT material.

A flexible process was developed for the production of thin films of PyC. Control over the thickness and roughness of these films was achieved through varying the deposition temperature and dwell time. The relationship between deposition rate and temperature implied that the deposition was governed by the Arrhenius equation with an activation energy of 2.68 ± 0.15 eV. A combination of sheet resistance and thickness measurements was used to determine the resistivity of PyC films (~ 2 x 10^{-5} Ωm). Sheet resistance measurements in combination with transmittance measurements were used to calculate the conductivity ratio (σ_{DC}/σ_{op}). This was found to be in the range 0.8 – 1.1, making it unsuitable for use as a thin transparent conductor. Spectroscopic investigation of the films indicated that they were nanocrystalline in nature and contained contributions from amorphous carbon and oxygenated functionalities.

PyC CVD offered conformal coatings as demonstrated in deposition onto thin SWNT films. This had a negative impact on the electrical properties of SWNT films. Future measurement of the thermal and electrical properties of such films is of interest.

Catalytic graphitisation of PyC films was demonstrated using a Ni catalyst and heat treatments. Spectroscopic investigation showed an improvement in graphitic order and a decrease in impurity/defect levels. Furthermore, XPS studies implied a reduction in

the Ni intensity post treatment suggesting migration of the Ni into the sample. Future High resolution TEM studies could be used to investigate the depth and level of ordering in such films. It is hoped that the catalytic graphitisation technique can be extended to thinner films of PyC for the production of ultrathin graphitic films.

A series of different CVD nanocarbons were subjected to O_2 Plasma treatments. In the case of MWNT forests such treatments led to a pronounced increase in the Raman *D* band. This increase scaled linearly with treatment time suggesting a well controlled process for the introduction of functionalities. Under certain conditions MWNTs were flattened out into sheets suggesting a method for the production of GNR type structures.

Plasma treatment was shown to enhance the electrochemical properties of PyC films through the incorporation of oxygenated functionalities. Treated films were shown to be suitable for electroanalytical applications. Further work in this field could entail the use of other plasmas for the addition of different functional groups, sensitive to particular analytes.

The growth of thin graphitic and graphene films on Ni substrates by a CVD process was described. FLG and films with regions of monolayers were produced by varying the dwell time. The catalytic activity of Ni was shown by inclusion of inert substrates in a number of runs. These showed the formation of thin PyC like deposits. Transferred FLG samples were characterised using scanning Raman spectroscopy. This showed the high quality of the graphene films. Transferred FLG films were treated with O_2 plasma. This lead to increased defect levels as seen in an increased *D* band on Raman spectra obtained with spot scans. Scanning Raman analysis indicated the presence of defects in the middle of flakes as well as at the edges.

O_2 plasma etching was performed with a NSL shadow mask on PyC and graphene films. This simple procedure produced pattered nanoscale dots and with optimisation could be used for several potential applications.

Recent work in the field of CVD growth of graphene has shown high quality growth using Cu substrates rather than Ni. This can be used to produce monolayer graphene over large areas (see figure 7.1) which is a more promising material for future functionalisation and patterning.

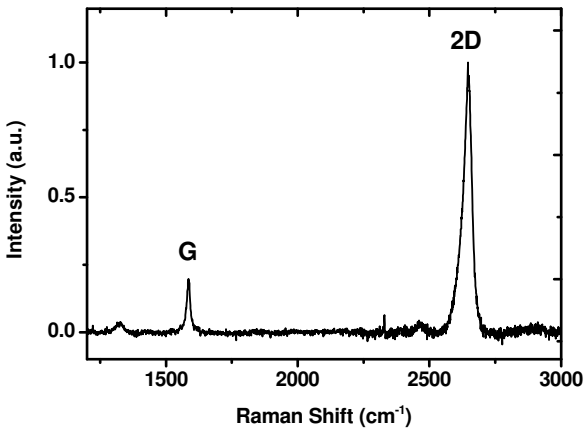

Figure 7.1 *Raman spectrum of graphene grown on Cu by CVD showing monolayer signal*

Appendix A

Preliminary Results on MWNT Electrodes

Cyclic voltammograms of two MWNT forests with different heights (both grown on Ta backed catalysts at 700 ^{o}C) are shown in Figure A.1. The 60 µm forest clearly has a much larger charging current (300 – 500 µA) compared with the 10 µm forest (70 – 100 µA). This gives a clear indication of the increased surface area in the taller sample. Several other tests with similar forests were in agreement with the data shown.

Such measurements are of interest not only for electrochemical electrodes but also as a way of measuring the density of CNT forests.

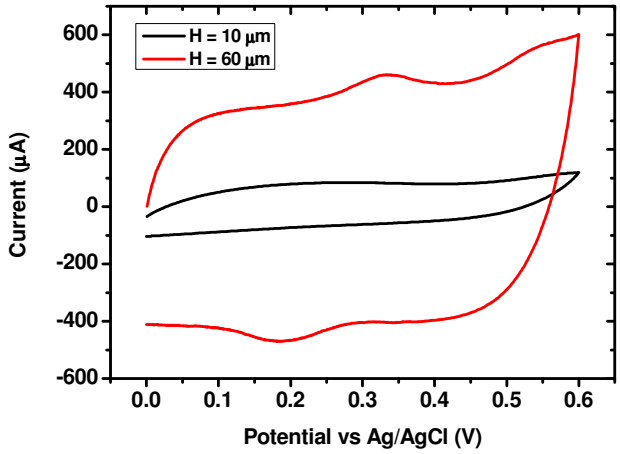

Figure A.1 *Cyclic Voltammogram for 60 µm and 10 µm MWNT forests recorded in 1M KCl at 100 mVs^{-1}.*

Appendix B

List of Publications

Published

"Growth of Carbon Nanotubes on Si Substrate Using Fe catalyst Produced by Pulsed Laser Deposition"

S. Krishnamurthy, T. Donnelly, N. Mc Evoy, W. J. Blau, J.G. Lunney, A.S. Teh, K.B.K.T. Teo, W.I. Milne

Journal of Nanoscience and Nanotechnology, Vol 8, 5478 – 5752, (2008)

"Low Temperature Graphene Growth"

S. Kumar, N. Mc Evoy, T. Lutz, G. P. Keeley, N. Whiteside, W. J. Blau, G. S. Duesberg

ECS Transactions, Vol 19, 175-181, (2009)

"Gas Phase Controlled Deposition of High Quality Large-Area Graphene Films"

S. Kumar, N. Mc Evoy, T. Lutz, G. P. Keeley, V. Nicolosi, C. P. Murray, W. J. Blau, G. S Duesberg

Chemical Communications, 46(9), 1422-1424, (2010)

"Thin Film Pyrolytic Carbon Electrodes: A New Class of Carbon Electrode for Electroanalytical Sensing Applications"

G. P. Keeley, N. Mc Evoy, S. Kumar, N. Peltekis, M. Mausser, G. S. Duesberg

Electrochemistry Communications, 12(8), 1034-1036, (2010)

In Preparation

"Optimisation of Aligned MWNT Growth on Ta underlayers for the Production of Electrochemical Electrodes"

N. Mc Evoy, H. Nolan, C. P. Murray, G. P. Keeley, N. Peltekis, W. J. Blau, G. S. Duesberg

To be submitted to the Journal of Physical Chemistry C

"CVD Growth of Pyrolytic Carbon: A flexible process for the production of thin conducting films"

N. Mc Evoy, N. Peltekis, S. Kumar, G. P. Keeley, W. J. Blau, G. S. Duesberg.

To be submitted to Carbon

"Catalytic Reordering of Pyrolytic Carbon"

N. Mc Evoy, N. Peltekis, S. Kumar, E. Rezvani, C. P. Murray, W. J. Blau, G. S. Duesberg

To be submitted to Applied Surface Science

Oral Presentation

"CVD Growth of Nanocarbons for Device Applications"

Invited Presentation, 216th ECS Meeting, Vienna, Austria, October 2009